

UNIVERSITÄT DER BUNDESWEHR MÜNCHEN
Fakultät für Elektrotechnik und Informationstechnik

A Multi-Channel Algorithm and Channel Modeling for Antenna Diversity of SiriusXM Vehicular Satellite Reception in Rayleigh-Scenarios

M. Sc. Ali M. Nassar
geboren in Foz de Iguaçu

Vollständiger Abdruck der von der Fakultät für Elektrotechnik und
Informationstechnik der Universität der Bundeswehr München zur
Erlangung des akademischen Grades eines

Doktor-Ingenieurs
(Dr.-Ing.)

genehmigten Dissertation.

1. Berichterstatter: Prof. Dr.-Ing. Stefan Lindenmeier
2. Berichterstatter: Prof. Dr.-Ing. Robert Weigel

Die Dissertation wurde am 04.02.2021 bei der Universität der Bundeswehr
München eingereicht und durch die Fakultät für Elektrotechnik und
Informationstechnik am 29.06.2021 angenommen.
Die mündliche Prüfung fand am 26.07.2021 statt.

Neubiberg, den 30. Juli 2021

Acknowledgements

I would like to thank Prof. Dr.-Ing. habil. Stefan Lindenmeier for giving me the opportunity to conduct the thesis at the Institute of High Frequency Technology and Mobile Communication at the Bundeswehr University in Munich. His constant advices and insightful ideas contributed a lot to the realization of this work. I would like to point out how exciting the research topics at the institute are because of the possibility to make things happen in real life out of the conducted theoretical research. Also many thanks for letting me participate in the teaching activities including various tutorials and labs which helped me in sharpening up my soft skills.

Moreover, thanks a lot to Prof. Dr.-Ing. habil. Wilfrid Pascher for the exciting time during the teaching activities of EMF (TET1) and ELW (TET2).

Special thanks to Dr.-Ing. Simon Senega for the various hints and fruitful technical discussions during our common work not only in the laboratory but also during the field measurements in the USA.

I would also like to thank Mr. Oliver Kindt and the whole workshop team for the realization of sophisticated prototypes which were used as demonstrators for laboratory analysis as well as test drive measurements.

My sincere thanks to all my wonderful colleagues for the friendly and inspiring working atmosphere at the institute and for providing a helping hand whenever it was needed especially M.Sc. Miguel Bueno Diez with whom I exchanged a lot of ideas during our common teaching activities.

Thanks to all the students who contributed to this work through their bachelor and master theses by performing numerous simulations and measurements.

And last but not least, my warmest thanks to my family. Thank you very much for your continuous encouragement and support.

Munich, Germany

Ali Nassar

Abstract

For almost two decades, satellite digital audio radio services (SDARS) have been covering the continental USA with digital quality signals to millions of subscribers. However, the destructive superposition of wave components due to multipath in Rayleigh fading scenarios deteriorates the signal-to-noise ratio (SNR) significantly, so that the common antennas need to be mounted at the best position on top of the car in order to prevent an unpleasant listening experience for subscribers because of audio mutes. For making possible also other more critical mounting positions multi-antenna diversity systems are investigated. First, a channel model to investigate the effects of dense foliage on the wave propagation in such scenarios is presented. Furthermore, a multi-channel scan-phase algorithm for the upper SiriusXM band is introduced. Moreover, an analysis of noise influence on the diversity performance for SDARS systems at 2.33 GHz and a method for correction of this influence in a diversity algorithm are introduced. Measurements with a compact scan-phase diversity module with an integrated circuit of small dimensions are presented applying this multi-channel algorithm ensuring the improvement of signal availability in comparison to single antennas.

Kurzfassung

Seit fast zwei Jahrzehnten decken digitale Satelliten-Radio Dienste (SDARS) die kontinentalen USA mit Signalen mit digitaler Qualität für Millionen von Abonnenten ab. Die destruktive Überlagerung von Wellenkomponenten durch Mehrwegeeffekte in Rayleigh-Fading Szenarien verschlechtert jedoch das Signal-Rausch-Verhältnis (SNR) erheblich, so dass die üblichen Antennen an der besten Position oben auf dem Fahrzeug montiert werden müssen, um ein unangenehmes Hörerlebnis für die Abonnenten aufgrund von Audio-Mutes zu vermeiden. Um auch andere kritischere Einbaupositionen zu ermöglichen, werden Mehrantennen-Diversity-Systeme untersucht. Zuerst wird ein Kanalmodell zur Untersuchung der Auswirkungen von dichtem Laub auf die Wellenausbreitung in solchen Szenarien vorgestellt. Ein mehrkanaliger Scan-Phase Algorithmus für das obere SiriusXM-Band wird eingeführt. Darüber hinaus wird eine Analyse des Rauscheinflusses auf Diversity für SDARS-Systeme bei 2.33 GHz und ein Verfahren zur Korrektur dieses Einflusses in einem Diversity-Algorithmus untersucht. Es werden Messungen mit einem kompakten Scan-Phasen Diversity-Modul mit einer integrierten Schaltung kleiner Abmessungen vorgestellt, bei denen dieser mehrkanalige Algorithmus zur Verbesserung der Signalverfügbarkeit im Vergleich zu Einzelantennen eingesetzt wird.

Contents

Abstract	v
Kurzfassung	vii
List of Abbreviations	xi
List of Symbols	xiii
1 Introduction and Thesis Overview	1
2 Satellite Digital Audio Radio Services	7
2.1 Satellite Transmission	7
2.2 Signal Reception in Mobile Multipath Scenarios	9
2.2.1 Multipath Fading Mitigation	10
2.3 Antenna Diversity Schemes	12
2.3.1 Selection Diversity	13
2.3.2 Scanning Diversity (Switch-Combining)	14
2.3.3 Phase Diversity (Equal Gain Combining)	15
2.3.4 Scan-Phase Diversity	16
2.3.5 Maximum Ratio Combining	17
3 Channel Modeling	19
3.1 Introduction	19
3.2 Channel Investigation Model	19
3.3 Simulated Test Drive	23
3.4 Measurement Campaign	26
4 Noise Calibration Method for SDARS	31
4.1 Noise Aspects	31
4.1.1 Noise in Electronic Systems	32
4.1.2 External Noise	36
4.2 Scan-Phase Diversity with Noise Calibration	40
4.3 Influence of Noise on Phase Calculation	44
4.4 Improving the Phase Calculation Accuracy	48
4.5 Examples of Diversity Performance in Test Drives	49
4.5.1 Test Drive Scenario	49
4.5.2 Signal Recorder / Playback Unit	52

4.5.3	Results	57
5	Multi-Channel Algorithm for Antenna Diversity	67
5.1	Concept Description	69
5.2	Mathematical Derivations	77
5.2.1	Antenna Sum	77
5.2.2	Single Antenna	80
5.3	Measures for Algorithm Calculations Acceleration	87
5.3.1	SiriusXM High-Band Test Cases	89
5.3.2	SiriusXM Low-Band Test Cases	94
5.4	Implementation	96
5.4.1	SAM D21 Micro-Controller	96
5.4.2	Micro-Controller PCB	98
5.4.3	Micro-Controller Programming	103
5.5	Measurements	106
5.5.1	SiriusXM High-Band	106
5.5.2	SiriusXM Low-Band	109
5.6	Satellite Monitoring	111
6	Measurements with the Diversity System IC Chip	115
6.1	Satellite Radio Diversity Circuit	116
6.1.1	Analysis of the RF Signal Path	116
6.2	Diversity Measurements with initial IC Versions	118
6.2.1	Laboratory Setup with IC + Level Detection Test Board	118
6.2.2	Laboratory Setup with IC + Compact Level Detection PCB	127
6.3	Diversity Measurements with the advanced IC Version	150
6.3.1	Laboratory Setup with external ADC	150
6.3.2	Laboratory Setup with internal ADC	152
7	Conclusions	163
A	Q-Function Table	168
B	Q-Function Plot	169
	Bibliography	171

List of Abbreviations

2D	2 Dimensional
3D	3 Dimensional
ADC	Analog-to-Digital Converter
ARM	Advanced RISC Machine
BE	Bit Error
CH	Channel
COFDM	Coded Orthogonal Frequency Division Multiplex
DCVSL	Differential Cascode Voltage Switch Logic
DFLL	Digital Frequency Locked Loop
DIV	Diversity
DSP	Digital Signal Processing
EIRP	Equivalent Isotropically Radiated Power
FCC	Federal Communication Commission
FEC	Forward Error Correction
FDPLL	Fractional Digital Phase-Locked Loop
GCLK	Generic Clock
GEO	Geostationary Orbit Satellite
GPIO	General Purpose Input Output
HEO	Highly Elliptical Orbit Satellite
I	In-phase
IC	Integrated Circuit
IF	Intermediate Frequency
LDO	Low-Dropout Regulator
LED	Light Emitting Diode
LHCP	Left Hand Circular Polarized
LNA	Low Noise Amplifier
LO	Local Oscillator
LOS	Line-of-Sight
LSB	Least Significant Bit
LUT	Look Up Table
MATLAB	Matrix Laboratory
MCU	Microcontroller Unit
MMD	Multi-Modulus Divider
MOSI	Master Output - Slave Input
MRC	Maximum Ratio Combining
MSB	Most Significant Bit
NLOS	Non-Line-of-Sight

PCB	Printed Circuit Board
PDF	Probability Density Function
PLL	Phase-Locked Loop
Q	Quadrature-phase
QPSK	Quadrature Phase Shift Keying
RAID	Redundant Array of Independent Discs
RCS	Radar Cross Section
REF	Reference
RF	Radio Frequency
RHCP	Right Hand Circular Polarized
RISC	Reduced Instruction Set Computer
RX	Receiver
SAW	Surface Acoustic Wave
SDARS	Satellite Digital Audio Radio Services
SMD	Surface Mounted Device
SNR	Signal-to-Noise Ratio
SPI	Serial Peripheral Interface
SWD	Serial Wire-Debug
TDM	Time Division Multiplex
TQFP	Thin Quadrat Flat Package
TX	Transmitter
UFBGA	Ultra Flat Ball Grid Array
USA	United States of America
USART	Universal Synchronous/Asynchronous Receiver/Transmitter
USB	Universtal Serial Bus

List of Symbols

Roman Characters

Character	Unit	Significance
\underline{a}	\sqrt{W}	Wave amplitude
\underline{A}_1	\sqrt{W}	Wave amplitude of the antenna 1 signal
\underline{A}_2	\sqrt{W}	Wave amplitude of the antenna 2 signal
\underline{S}	\sqrt{W}	Sum of wave amplitudes
\underline{T}	\sqrt{W}	Sum of wave amplitudes after rotating ant. 1 signal by 90°
$A_{m,eff}$	-	Antenna effective aperture
\underline{C}	-	Complex directional function of the antenna
$d_{1,i}$	m	Unobstructed distance between the satellite and vehicle
$d_{2,i}$	m	Distance between the scatterer i and vehicle
$d_{3,i}$	m	Distance between the satellite and scatterer i
f	Hz	Frequency
g_t	W	Satellite transmit gain
h	mm	Cylinder thickness
k	1/m	Wave number
\vec{n}_L	-	Normal vector
m	-	Number of diversity antennas
n	-	Number of scatterers
\underline{N}	\sqrt{W}	Noise
\underline{P}_1	W	Power level of the ant. 1 signal
\underline{P}_2	W	Power level of the ant. 2 signal
\underline{P}_S	W	Power level of the sum
\underline{P}_T	W	Power level of the sum, where ant. 1 signal is rotated by 90°
\underline{P}_N	W	Power level of the noise
P_{cur}	W	Current signal power
$p_{BE,I}$	-	Bit error probability in the I-channel
$p_{BE,Q}$	-	Bit error probability in the Q-channel
p_{eval}	-	Overall bit error probability
p_{total}	-	Bit error probability in the I- and Q-channel
p_t	W	Satellite transmit power
r	mm	Cylinder radius
S_{21}	-	Scattering parameter
\underline{S}_0	-	Projection on the S_0 -axis
\underline{S}_{90}	-	Projection on the S_{90} -axis

Character	Unit	Significance
\underline{S}_I	-	Projection on the S_I -axis
\underline{S}_Q	-	Projection on the S_Q -axis
t	s	Time
$x(t)$	m	Car's track position at instance t
Z_L	Ohm	Reference Impedance

Greek Characters

Character	Unit	Significance
α	degree	Phase difference between antenna 1 signal and the sum
β	degree	Phase difference between antenna 2 signal and the sum
δ	degree	Angle rotation from S to S'
$\Delta\alpha$	degree	Angle rotation from A_1 to A'_1
$\Delta\beta$	degree	Angle rotation from A_2 to A'_2
ϑ_i	degree	Angle of arrival of the incident scattered wave
ϑ_L	degree	Leaf's elevation angle from zenith
φ	degree	Phase difference between ant. 1 signal and ant. 2 signal
φ_L	degree	Leaf's Azimuth angle
ϑ_{sat}	degree	Satellites's elevation angle from zenith
ϵ_L	-	Leaf's Permittivity
σ	dBsm	Radar cross section
μ	-	Mean
η	-	Diversity efficiency

Constants

Constant	Definition	Value
c_0	Speed of light in vacuum	299,792,458 m/s
e	Euler's Constant	2.71828
j	Imaginary Unit	$\sqrt{-1}$
k_B	Boltzmann Constant	$1.38 \cdot 10^{-23}$ J/K
π	Ratio of a circle circumference to its diameter	3.14159

1 Introduction and Thesis Overview

An alternative to terrestrial signal broadcasting is being offered since almost two decades in the USA. Each of the two providers *Sirius Satellite Radio* and *XM Satellite Radio* launched a satellite digital audio radio service (SDARS). Both providers merged together a few years ago to form *SiriusXM Satellite Radio*, which offers numerous radio channels in digital quality to subscribers all over the continental USA and even in southern regions within Canada. In terrains with unobstructed reception to the transmission satellites, the signal-to-noise ratio (SNR) is considered sufficient. Nevertheless, there are some places which suffer from severe audio muting making the whole radio listening experience very unpleasant. This is especially occurring if the antenna is not mounted on the best point available on top of the vehicle roof. Fig. 1.1 illustrates a vehicle with two receiving antennas in such a scenario where destructive superposition of signal components at the receiver takes place due to multipath fading. Dense foliage plays an important role in the wave reflection and scattering. Another aspect which deteriorates the SNR is the shadowing effect caused by obstacles between the satellites and the vehicular receiver like for example tree trunks, buildings and hills.

In order to mitigate the negative effects of multipath fading in such scenarios, antenna diversity is deployed. Scan-phase diversity benefits from the advantages of signal superposition and selection via a non-complex system which makes use of a single RF cable and a single tuner unlike other state-of-the-art diversity schemes such as maximum ratio combining (MRC) [1]. A scan-phase diversity system has already been implemented in the Institute of High Frequency Technology and Mobile Communication at the Universität der Bundeswehr München for *Sirius Satellite Radio* service. The improvements in the SNR and audio availability of the diversity system optimized to one satellite were achieved by various system demonstrators [2], [3], [4], [5].

The precise modeling of propagation and scattering of electromagnetic waves through foliage for satellite reception is considered very challenging. The dielectric characteristics of foliage and the resulting overall shadowing attenuation are influenced by various factors and change with tree size and species. Other parameters like the orientation of the incident wave and the complex antenna characteristics in all polarizations contribute to further complexity of the modeling. For this reason, a channel model investigation and implementation is introduced in this thesis.

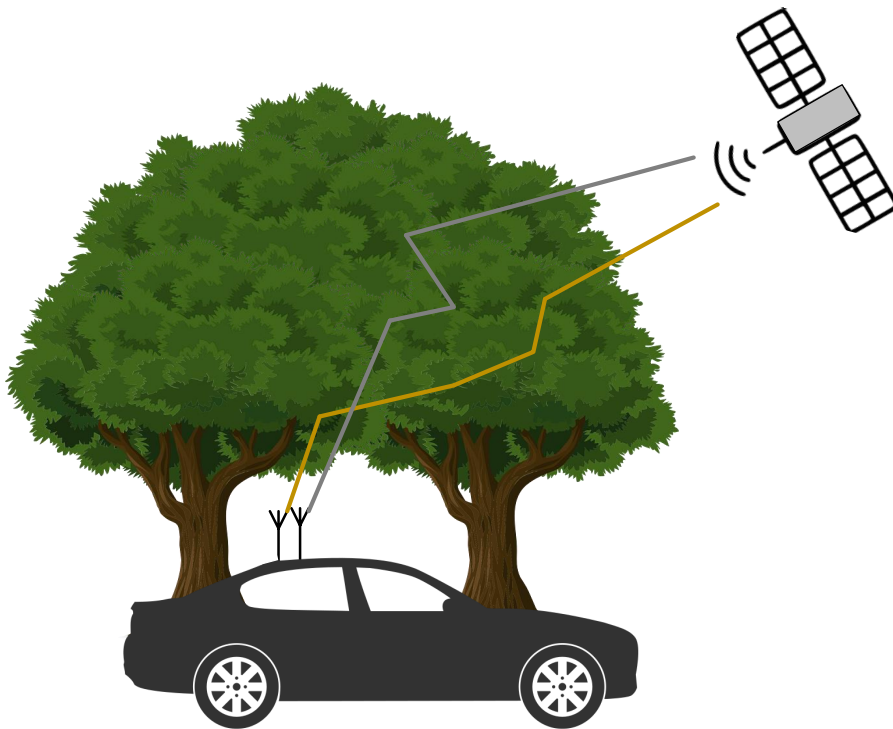


Figure 1.1: SDARS vehicular reception underneath dense foliage is degraded due to the multipath fading.

Moreover, a multi-channel scan-phase algorithm for vehicular antenna diversity of SiriusXM high band satellite reception is presented. The algorithm supports the frequency bands of distinct satellites according to their signal-to-noise ratio. For the reception optimization of frequency bands of the same satellite, but of different ensembles, the optimization is based on choosing the phase combination leading to the minimum estimated average bit error probability over both ensembles. In a further step to improve the diversity system performance, a three-antenna algorithm is introduced in this work which can be also expanded to a multi-channel application. The algorithms are tested in combination with various hardware system demonstrators, that were investigated with respect to their behavior in the field in combination with the different algorithms. Especially a new compact diversity system with integrated circuit is investigated.

The general structure of the thesis is outlined as follows:

In chapter 1, a general overview of the dissertation is provided.

In chapter 2, the actual state of the SDARS signal transmission is described in addition to the common techniques which are deployed in order to mitigate the effects of multipath in Rayleigh fading scenarios.

In chapter 3, a new channel model of SDARS wave propagation in areas underneath dense foliage is introduced. The model permits the time domain investigation of simultaneous satellite radio reception of multiple diversity antennas. It deals with multipath wave propagation in a Rician and Rayleigh fading scenario, shadowing by dense foliage and the characteristics of integrated vehicle antennas depending on the mounting position. The new channel model is evaluated through comparison with measured results. For this comparison, real scenario test drives are performed in order to record and analyze SDARS antenna signals. The histograms of the simulated signal amplitudes show very good agreement with the measured test drive results performed in the USA.

In chapter 4, a noise cancellation method for a fast scan-phase satellite radio antenna diversity system is investigated and optimized for SDARS application for significant improvement of audio availability at low signal-to-noise ratio conditions. An error analysis of phase and level detection in the diversity system in the presence of noise leads to a method of error correction based on a priori knowledge of the noise floor of the system. The corresponding noise correction is described and applied in a hardware example of an SDARS antenna diversity circuit for conditions of fast fading. Test drives, that have been performed in real fading scenarios in the USA, are described and the corresponding results are analysed statistically. Simulations of the scan-phase antenna diversity system show signal quality improvements in terms of higher availabilities and signal amplitudes. Measurement results of dislocated antennas (macro-diversity) as well as of a diversity antenna set on a single mounting position (micro-diversity) are presented. All available satellite signals are used in the comparisons of a diversity reception system with noise correction, the same system without noise correction and a single antenna reception system with each other. Using this new method in fast multipath fading driving scenarios underneath dense foliage with a low SNR of the antenna signals, a reduction in audio mute time by one order of magnitude compared to single antenna systems is achieved by the diversity system. The increased SNR due to the diversity system enables new unconventional mounting positions which would be severely impaired even if highly optimized single antennas are used.

Chapter 5 presents a new multi-channel algorithm for SDARS with scan-phase-antenna diversity at the SiriusXM high band. Considering reception via four different satellite frequency bands simultaneously, the algorithm controls not only microwave phase shifters but also switches of a diversity circuit in order to combine different antenna signals for a minimized overall bit error probability. On basis of a simple level detection, the in-phase and quadrature components are derived for all frequency bands and an overall bit error probability is es-

timated, which is minimized via the phase constellation and switching of the microwave diversity circuit. For the verification of the new algorithm, antenna signals of a micro-diversity antenna set are received in real scenario test drives underneath dense foliage which are fed into a scan phase diversity circuit. Even in unconventional antenna mounting positions the antenna diversity measurements with the novel multi-channel algorithm show a significant improvement of the audio reception quality in comparison to single antennas.

The audio mutes represented by black dots for both single antennas as well as the micro-diversity configuration with the new algorithm over a total time of 380 s are depicted in Fig. 1.2. The micro-diversity antenna set consisting of two loop antennas is mounted at one mounting position (front fender of the car). The presented recordings show a typical example of one of the five individual measurements, where the average results of these are shown in the average mute durations in Table 1.1. It can be clearly noticed how the number of mutes is reduced by the new algorithm in comparison to both single loop antennas which are mounted at the same position at the left side of the fender.

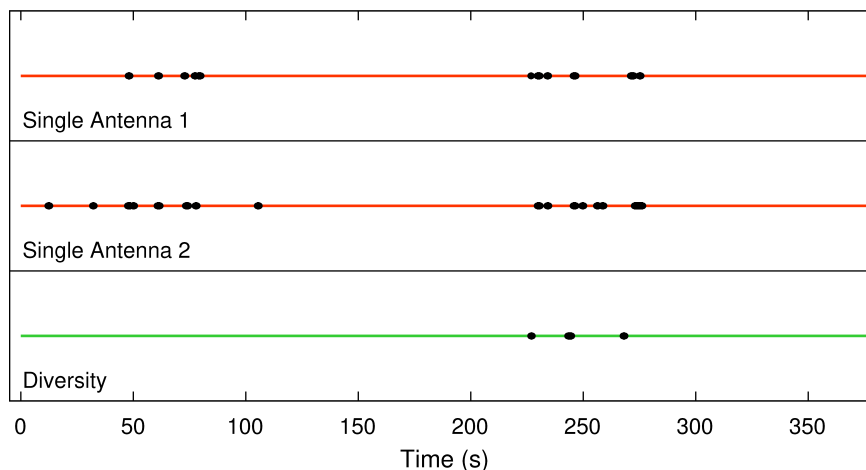


Figure 1.2: Measured audio mutes of individual measurements of the diversity antenna set's single antennas at one mounting point (front fender) in comparison to diversity with the multi-channel algorithm.

In chapter 6, measurements with a compact antenna diversity system with a new integrated circuit for automotive reception of SDARS at 2.3 GHz is introduced. For a scan phase antenna diversity with switching and phase alignment of up to three different antenna paths, the integrated circuit includes RF switches, phase-alignment and signal combining as well as the frequency conversion for level detection. This is the first integrated circuit for SDARS scan-phase antenna diversity, which possesses all the diversity functions except for level detection and digital signal processing. With the novel integrated circuit with a package size

Table 1.1: Comparison of average audio mute durations (each over five measurements) in a real fading scenario recorded on test drives in the USA for the cases of single antennas as well as antenna diversity. The diversity antenna set was mounted on the car's front fender.

	Audio Mutes [s]	Duration [s]	Availability [%]
Aver.(Ant1,2)	15.87	380	95.82
DIV SAT1A	1.88	380	99.50
DIV SAT1B	5.34	380	98.59
New Algorithm	2.43	380	99.36

of only 9 mm by 9 mm a compact hardware demonstrator is realized. The diversity circuit is independent of the radio and offers the same interface to the radio as one conventional single antenna. In laboratory measurements characteristic values of the RF signal paths like variable phase shift and gain are determined. In addition, the new compact diversity circuit is also evaluated in a real fading scenario on a single side mirror of the test vehicle showing a significant reduction of audio mutes by the diversity system compared to single antenna reception under same circumstances.

Moreover, a three-antenna algorithm is introduced with its derivation and measurements. Table 1.2 shows the results. The three single patch antennas have an audio mute duration of 11.71s, 14.03s and 12.85s respectively which leads to an average audio mute duration of 12.87s for an overall test duration of 380s. Initial investigations show that by applying the three antenna algorithm the mute duration dropped to 0.1s only. In other words, the signal availability increased from 96.61% to 99.99% which is basically a flawless audio reception underneath dense foliage. This shows that even at critical mounting positions the diversity yields a perfect reception quality where a single antenna would lead to an unacceptable listening experience.

Table 1.2: Diversity with 3 reference patch antennas on the hood of the car.

	Audio Mutes [s]	Duration [s]	Avail. [%]
Ant. 1	11.71	380	96.92
Ant. 2	14.03	380	96.31
Ant. 3	12.85	380	96.62
Aver. (1,2,3)	12.87	380	96.61
Diversity	0.1	380	99.99

The last chapter gives a final overview of the achieved results and concludes the presented work.

2 Satellite Digital Audio Radio Services

In this chapter, the actual state of satellite transmission of the lower and upper SDARS bands is described in addition to the challenges of radio reception in multipath scenarios with mobile receivers. Furthermore, different common solution approaches for reception improvement in such scenarios are depicted.

2.1 Satellite Transmission

Satellite digital audio radio services (SDARS) offer a number of advantages compared to terrestrial analog or digital broadcasting systems. It is mainly possible to ensure the coverage of larger geographical areas by using only few transmitters. This is of decisive importance, especially with regard to countries such as the USA, which possess continental dimensions. The construction and operating of the transmission of terrestrial broadcasting systems are in such large regions not the most suitable option due to the high operational and maintenance costs of base-stations all over the country.

To solve this problem, satellites are used as transmitters instead of fixed ground-based transmitting antennas as is conventionally the case. This means that the satellite signals can be received not only all over the country but also a several hundred kilometers overseas.

For this reason, the Federal Communication Commission (FCC) allocated in the S-band (2 GHz to 4 GHz [6]) two frequency bands each with a bandwidth of 12.5 MHz for two providers Sirius and XM [7], [8]. Nevertheless, both providers merged together to form Sirius XM Radio and today they occupy the entire 25MHz band between 2.320 GHz and 2.345 GHz. There are currently over 9 millions of users [9]. It is now possible for the provider in 48 states in the USA and in southern regions inside Canada, to offer an entertainment program of over 65 music channels in addition to more than 70 speech and information channels in CD-like sound quality.

The frequency band allocation of SiriusXM is illustrated in Fig. 2.1. The lower side band (Sirius) has its center frequency at 2.32625 GHz while the upper side band (XM) has its center frequency at 2.33875 GHz.

2 Satellite Digital Audio Radio Services

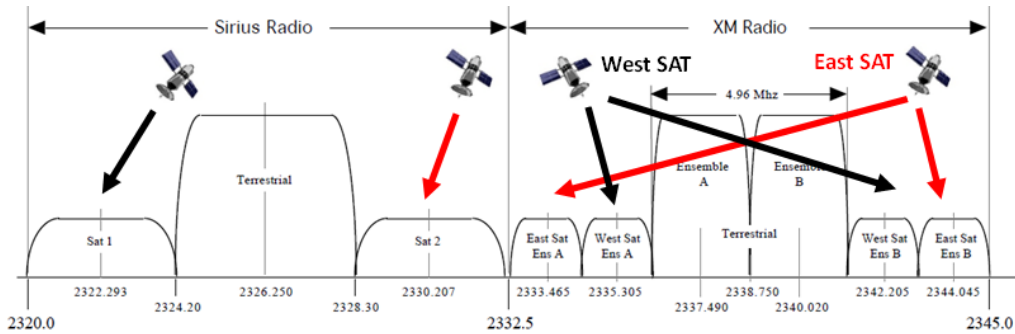


Figure 2.1: The frequency assignment in MHz of SDARS (SiriusXM) in the S-band

The lower side band system is based on three highly elliptical orbit (HEO) satellites and one geostationary orbit (GEO) satellite. The GEO satellite transmits RF signals, which are modulated by means of quadrature phase shift keying (QPSK) [10], [11], at 2.322293 GHz whereas the HEO satellite transmits at 2.330207 GHz with 4.1685s delay.

Each HEO satellite needs about 24 hours for a periodic cycle on its elliptical orbit. This means that a HEO satellite is always active eight hours over North America before it and will be replaced by another HEO satellite. In other words, always a GEO satellite and a HEO satellite are actively transmitting. In urban areas where the satellites are shaded by skyscrapers, additional terrestrial repeaters are installed. They transmit at 2.32625 GHz using coded orthogonal-frequency division multiplexing (COFDM) modulation.

Concerning, the upper side band system is made up of two active GEO satellites. Each GEO satellite transmits RF signals, which are QPSK modulated [12] within two ensembles A and B, where each one carries half the total system capacity.

The east satellite supplies the outer two satellite bands at 2.333465 GHz and 2.344045 GHz with the ensembles A and B respectively. The west satellite supplies the inner two satellite bands at 2.335305 GHz and 2.342205 GHz with the ensembles A and B respectively. Terrestrial repeaters transmitting at 2.337490 GHz for ensemble A and 2.340020 GHz for ensemble B are also installed in urban areas like the lower side band systems. In other words, a subscriber located in New York will definitely make more use of the east satellite, and a subscriber situated in San Francisco will benefit more from the west satellite.

2.2 Signal Reception in Mobile Multipath Scenarios

Electromagnetic waves usually propagate unimpaired in free space. This means that only one signal arrives at a receiver situated at a given position. In a multipath scenario, on the other hand, several wave components of different amplitude and phase may overlap additionally. Fig. 2.2 depicts a typical multipath scenario underneath dense foliage.

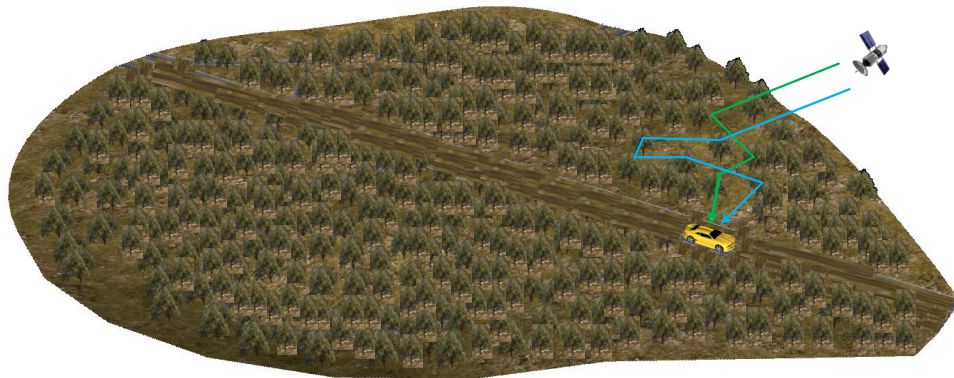


Figure 2.2: Multipath fading scenario caused by dense foliage

The individual parts of the received electromagnetic waves are caused by the reflection and diffraction on objects. Due to the different path lengths from the transmitter to the receiver, the incoming signals have different phases. Depending on the number, arrangement, reflectivity, attenuation, etc. of these objects, destructive superposition can occur, so that the receiver does not find the required signal-to-noise ratio at certain locations. On the other hand, good reception conditions can prevail with constructive superposition.

In the case of terrestrial broadcasting, the signal is reflected, for example, by mountains or houses. Diffraction effects at mountain tops or hills also lead to other propagation paths. Not only the line-of-sight (LOS) signal received directly arrives at the receiver, but also signal components with different amplitude and phase. However, there are also reception situations without radio LOS between transmitter and receiver, so that only reflected signals are received. The superposition of all these signal components at the receiver in variable phase constellations leads to local fluctuations of the signal strength, the so-called fading. If a mobile receiver moves through such a scenario, its movement produces signal strengths that vary over time. The SNR fluctuation at the mobile receiver might lead to audio mutes.

A characteristic feature of multipath scenarios is the probability density of the amplitude of the incident wave components. It describes the probability with which the amplitude of a signal component has a certain value. The Rayleigh distribution is of particular importance for the considerations in this dissertation, as is, to a limited extent, its generalization, the Rice distribution.

2.2.1 Multipath Fading Mitigation

Despite the negative effects of multipath fading, satellite radio systems must ensure an audio availability that is still acceptable to the subscriber. For this reason it is necessary to take measures to mitigate the loss of information as much as possible. Signal coding schemes play a central role here in combination with different diversity methods.

2.2.1.1 Signal Coding Schemes

Several signal coding methods to correct transmission errors are used by satellite radio services. They include the following schemes:

Forward Error Correction (FEC)

By adding redundant information to the digital source encoding before the signal is transmitted, the receiver is able to correct errors that occur during transmission [13], [14], [15]. This procedure is called Forward Error Correction (FEC). Individual bits that have been falsified by transmission errors can be detected and corrected by the added redundant data. The calculation of the redundant data is usually done via a block with a certain number of bits, which makes the FEC a block-based method. The number of bits that are detected as erroneous and the number of bit errors that can be corrected are essential features of an FEC. However, the effective transmission rate of the user data decreases due to the additional data sent, which does not contain any new information.

Interleaving

The mechanisms of the FEC are not very suitable for securing the transmission against errors that interfere with several sequential bits (burst errors). These burst errors distort an above-average number of bits in a data block, while other blocks are not disturbed. Since the number of correctable bit errors can only be increased by adding redundancy, applying FEC for the relatively rare burst errors is inefficient. Interleaving is better suitable for this purpose, where the bits of different blocks are swapped (interleaved) according to a known pattern.

2.2.1.2 Transmission Diversity Schemes

The diversity principle describes the use of redundancy with the help of several parallel transmission channels to overcome the disturbances in one or more of the used channels. These channels can differ from each other by different characteristics, which usually determine the name of the diversity method. Combinations of the described diversity methods with each other as well as combinations with other methods not mentioned below are also possible.

Frequency Diversity

The use of different frequencies for the transmission of signals of the same content is generally referred to as frequency diversity. The same information is transmitted on different frequencies from the transmitter to the receiver. This diversity method takes advantage of the fact that the propagation conditions are generally frequency-dependent. This usually results in statistically independent interference, where one can make use of the other transmission channel. In the Sirius Satellite Radio service, two satellites transmit the signals on one frequency each (2.233393 GHz and 2.330207 GHz). With XM Satellite Radio, each satellite (east and west) transmits on two different frequencies as illustrated in Fig. 2.1.

Time Diversity

Time diversity describes the procedure of applying different time delays to several data streams before sending them. If an event occurs on the transmission channel that disrupts all signals simultaneously, the receiver can ideally still process the user data. If the receiver uses the time delays of the signals, it can override the disturbances by evaluating the respective undisturbed contents. With satellite radio services, time diversity is implemented by delaying one of the satellite signals for a certain period of time Δt ($\Delta t = 4.1685$ s for Sirius Satellite Radio). This is sufficient, for example, to inadvertently overreach the short-term loss of the satellite signal for the user when driving under a bridge (as long as the duration of the shading does not exceed the delay time of the signals).

It is worth mentioning that the difference between interleaving and time diversity is that in the case of interleaving the bits of a data stream are re-sorted, while in time diversity two data streams carry the same content with different delays. Both methods can be combined, where long signal loss can be overcome by time diversity, and a long sequence of short burst errors can be overcome by time interleaving of the data streams.

Space Diversity

Space diversity refers to the method of using different physical transmission channels by spatially separating the respective antennas from the transmitter or receiver. The satellite radio services achieve this by using several satellites in different orbital positions. Two satellites transmitting simultaneously from different spatial positions enable the receiver to receive signals from different angles and directions. With this method, the probability that an obstacle blocks or at least disrupts all transmission paths can be reduced.

Polarization Diversity

Signals with different polarizations are deployed in polarization diversity. In urban regions nowadays, not only LHCP satellite signals but also terrestrial signals are received by the same satellite antennas which are slightly compatible to vertical polarization. In other words, both channels (terrestrial and satellite) are received. The LHCP and vertically polarized signals also possess different modulation schemes. The satellite signals are QPSK modulated and the terrestrial repeaters transmit the signals using COFDM.

Despite the application of all these measures mentioned above, there are still scenarios left where reception quality is unacceptable, especially if antennas are mounted in non-optimal positions on or in the vehicle. For prevention of such situations antenna diversity solutions have been proposed [2], [3], [4], [5].

2.3 Antenna Diversity Schemes

Especially for critical antenna positions the fadings of the received signal are so strong, which leads to bit errors in the received data stream up to the total loss of data blocks. Measures for channel coding and transmission have already been described in the previous sections. While the described methods so far have to be implemented on the transmitter or system side, the availability of the signal at the receiver can also be increased.

Diversity reception systems are used in mobile receivers in numerous modern radio transmission and communication services. They are used to avoid the signal loss by using several antennas. Today, antenna diversity systems are used commercially for radio and television reception in vehicles, Wi-fi, mobile phones and much more. The method is based on the fact that the simultaneous loss of all antenna signals becomes increasingly unlikely as the number of antennas increases, and as long as the antennas are decoupled from each other, so that their reception is statistically independent from each other. For N statistically independent antenna signals with the same failure probability p , the probability for

the simultaneous loss of all signals is only $p_{\text{total}} = p^N$ [16].

In the further course of this chapter, examples of the application of the diversity principle are shown using M multiple antenna signals. The use of statistically independent propagation paths can generate considerable profits. Provided that the antenna signals are as uncorrelated as possible, they can then be combined or selected to provide the receiver with a good reception signal [17], [18].

Now, different antenna diversity methods are depicted in comparison to each other.

2.3.1 Selection Diversity

With this method, the received signal with the maximum available signal-to-noise ratio SNR_{max} is always used for evaluation. For this purpose, the signal-to-noise ratios $(S/N)_n$, where $n \in [1, M]$, of all M antenna signals must be compared to each other.

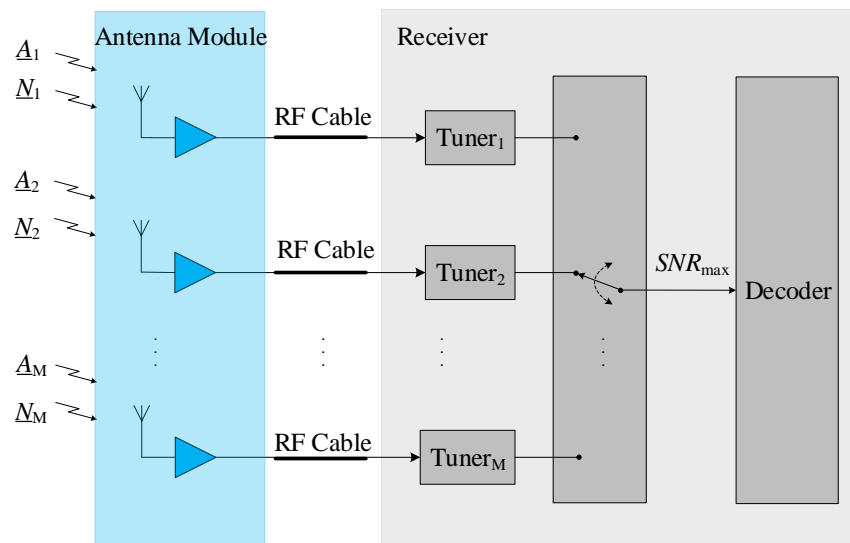


Figure 2.3: Schematic representation of a selection diversity system

For each received antenna signal a separate tuner and a separate RF cable leading through the car are required. Therefore, selection diversity is considered one of the methods with the most effort after maximum ratio combining. Fig. 2.3 depicts the schematic representation of a selection diversity system.

2.3.2 Scanning Diversity (Switch-Combining)

Scanning Diversity, also called switch-combining, measures the received levels of the individual antennas one after the other or in parallel and compares them with each other. This technique has been utilized for the VHF reception in vehicles [19]. The antenna with the highest level or SNR is then selected and connected to the receiver. Depending on the desired switching behavior, the best signal can be continuously searched for or in alternative, only at measurements when it drops below a certain threshold [20]. By switching the antenna signals, phase shifts occur in the received signal, since the antenna signals must be as uncorrelated as possible for use in the diversity system. Due to the phase modulation used in the satellite radio signals, this would lead to bit errors.

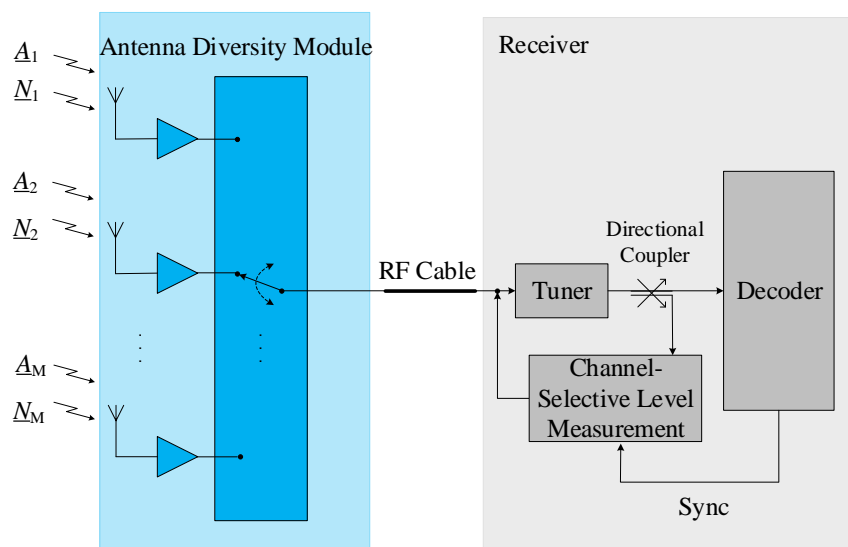


Figure 2.4: Schematic representation of a scanning diversity system

For this reason, the switching operations must be carried out quickly to reduce the number of errors that may occur during the switching process. Furthermore, to synchronize the phases in the receiver to the transmitted signal, so-called reference phase symbols are embedded at regular intervals. By synchronizing the switching with this reference phase symbol, the occurring bit errors can be minimized [21]. In all diversity systems, the level measurement unit must be channel-selective, since broadband optimization of all signals at the same time is not possible. Fig. 2.4 depicts the schematic representation of a scanning diversity system.

The simple design of the switching diversity - no signal addition is possible and therefore no phase detection and adjustment is required - enables a cost-effective overall system. Only one measurement path and one RF cable from

switch to receiver are required. The control signal for the antenna switch can be routed back on the same cable without interfering with the antenna signals [21]. Switching between the antenna signals causes interference in the signal to the receiver for the very short testing time between start of switching and arrival of the reference phase signal.

However, these interferences are only relevant to a small extent and are far outweighed by the improvement of the received signal by the diversity system [22]. A major advantage of a scanning diversity system is the presence of only one receiver and one RF cable connecting the antenna side to the receiver. A disadvantage is that the antenna part with its switches can be only steered in cooperation with the radio which has to provide the information about the reference phase signal.

2.3.3 Phase Diversity (Equal Gain Combining)

In phase diversity, unlike scanning diversity, the antennas are always combined. There is no weighting or switching off of single antennas. This technique has been utilized for the VHF reception in vehicles [23, 24]. To constructively superimpose the antenna signals, the corresponding phases must first be aligned. Phase shifters are integrated into each signal path for this purpose. Phase detection and rotation as well as signal addition can be performed in both the analog and the digital part of the received path.

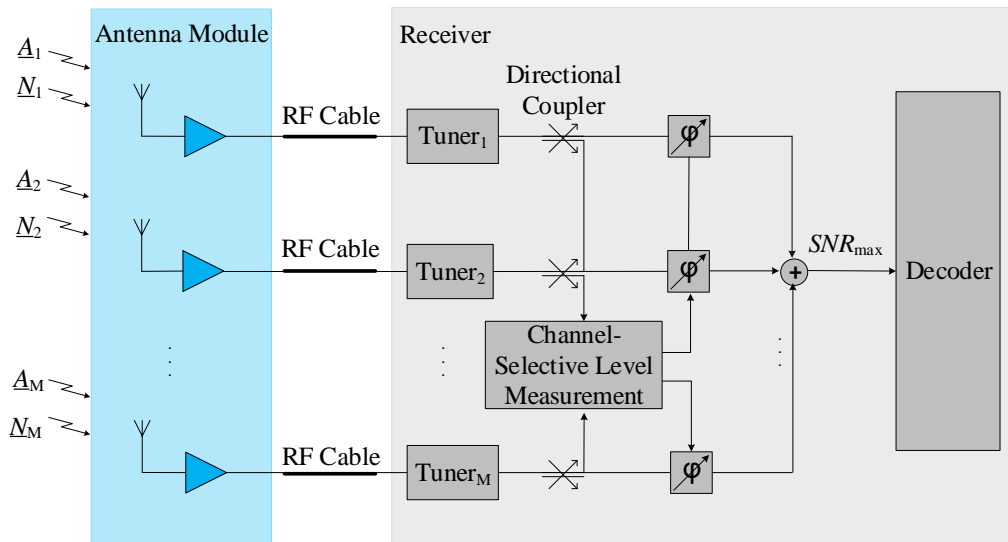


Figure 2.5: Schematic representation of an equal gain combining diversity system

Phase detection must be performed for optimal system performance before addition. As a result, each antenna signal must be connected to the tuner with its

own RF cable. Moreover, each signal requires its own tuner, since phase measurement and adjustment must be performed before the signals are superimposed. The advantage of this system is the possibility to achieve a higher signal level than that of the best single antenna by the constructive superposition of signals. The disadvantage is that in the relevant cases, where one antenna signal is low, the noise of its amplifier leads still to a decrease in SNR. Fig. 2.5 depicts the schematic representation of an equal gain combining diversity system.

The applicability of phase diversity is limited to signals with sufficiently small bandwidth. Broadband signals do not show a constant phase difference over the signal bandwidth in the multipath scenario, so that the constructive superposition is not possible in the entire frequency range. The sub-bands of the satellite radio services are sufficiently narrow-band (maximum of about 4 MHz for Sirius Satellite Radio), so that phase diversity can be applied.

A comparison with the maximum ratio combining shows that phase diversity is a simplified version, where the possibility of individual weighting of the individual signals is eliminated. Therefore, antenna signals with a low signal-to-noise ratio are also included in the combination. This may lead to the opposite of the desired effect: a deterioration of the overall signal.

2.3.4 Scan-Phase Diversity

Fig. 2.6 depicts the schematic representation of a scan phase diversity system. Phase shifters enable the constructive superposition of several antenna signals, while an antenna selection is carried out with the help of the switches. Phase shifters and switches are integrated in the each signal paths for this purpose. A combiner permits the signal addition.

Due to the possibility of signal superposition, scan-phase diversity improves the SNR by up to 3 dB in all the moments where identical single antenna levels appear. In contrast to the MRC system, however, no continuous signal weight is possible. Only a level measurement unit is required to determine the optimum system settings. A direct phase measurement is not necessary at all. The measurement can be carried out after the superposition of the antenna signals.

As in the case of scanning diversity, only one cable is required to connect to the receiver. A single signal path in the receiver is therefore sufficient. A scan-phase diversity system can therefore replace a single antenna as a stand-alone solution without modification or replacement of other receiving components.

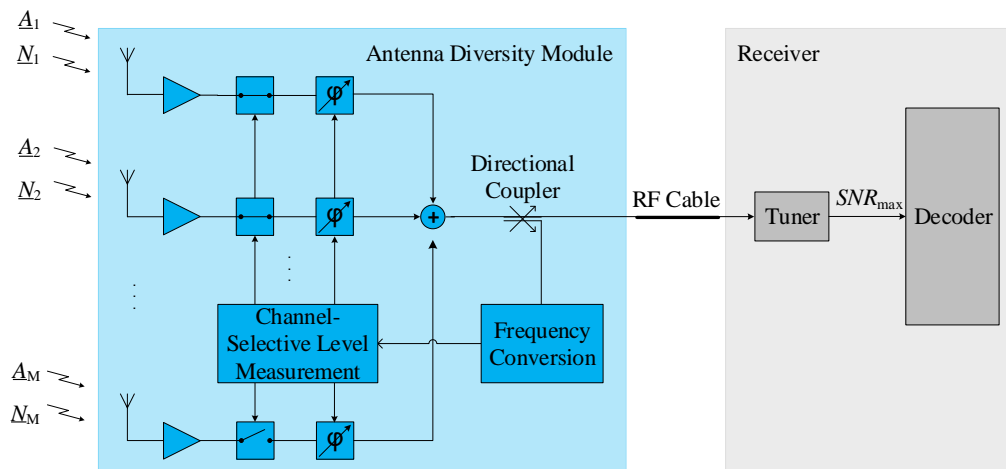


Figure 2.6: Schematic representation of a scan phase diversity system

2.3.5 Maximum Ratio Combining

Like (scan)-phase diversity, Maximum Ratio Combining (MRC) offers the possibility to constructively superimpose signals. For further optimization of the SNR, the signals are weighted with continuously adjustable amplification and attenuation factors. This measure allows the SNR of the combined signal to be optimized, which is where the name of the method comes from. The weighting of the signals can, for example, be done with amplifiers, which provide an adjustable amplification for each path.

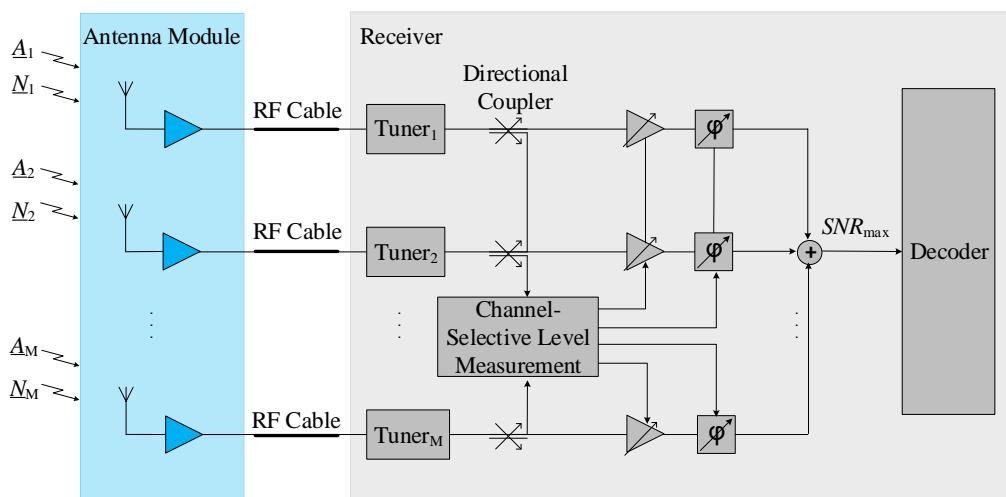


Figure 2.7: Schematic representation of maximum ratio combining

The weighting factors and the phase settings are determined on the basis of the SNR of all individual antennas as well as their phase position relative to each other. Figure 2.7 shows a simplified schematic representation of a MRC system. As can be seen from this, each antenna signal requires its own receive path and its own cable to connect to the receiver. Since the level and phase detection can only take place in the IF, a separate tuner is necessary for each signal. A representation of maximum ratio combining for analog services can be found, for example, in [25], where the combination of maximum ratio combining with several switchable antenna signals is discussed.

The performance of a conventional maximum ratio combining diversity system is therefore relatively expensive to buy. Scanning diversity is only performing if the radio is cooperative.

These challenges show the necessity to implement a cost efficient diversity circuit which eliminates the disadvantages of a switched or scanning diversity system and offers almost the performance of a maximum ratio combining diversity. At the same time, the effort should be less than in the case of the traditional maximum ratio combiner. Scan-phase diversity offers such a cost efficient system with very high performance. It can be implemented with a lean unidirectional RF-interface by a simple RF-cable, where no back-signal of the radio is required.

3 Channel Modeling

For investigation of antenna diversity techniques in a fading scenario, a method for computer aided modeling of the typical multipath reflection scenarios is required. For this reason, a new channel model of wave propagation in regions underneath dense foliage is presented. The model investigates the simultaneous SDARS reception of multiple diversity antennas in the time domain. It takes into consideration multipath wave propagation in a Rayleigh and Rician fading scenario, shadowing by dense foliage and the characteristics of integrated car antennas depending on the mounting position.

3.1 Introduction

SDARS signals covering the continental USA as well as southern regions inside the Canadian territory are widely spread also in regions underneath dense foliage. In such areas, multipath propagation may impose additional challenges to ensure full SDARS signal coverage [18, 26]. In order to guarantee highest reception quality and to make use of new hidden antenna positions in the car if the ideal exposed position (car rooftop) [27] cannot be utilized, antenna diversity is deployed [28, 22, 29].

For a fast analysis of the behaviour of various diversity systems in a Rayleigh or Rice scenario underneath dense foliage, a new channel model is presented, investigated and validated by field measurements which were performed in the USA. This facilitates the prediction of various diversity system aspects such as the diversity efficiency as well as the overall performance of the whole SDARS receiving system and its antennas before being deployed in test drives.

3.2 Channel Investigation Model

The precise modeling of electromagnetic wave propagation and scattering through foliage for satellite reception is considered a challenging mission. The dielectric characteristics of foliage and the resulting overall shadowing attenuation depend on many factors and change with tree size and species.

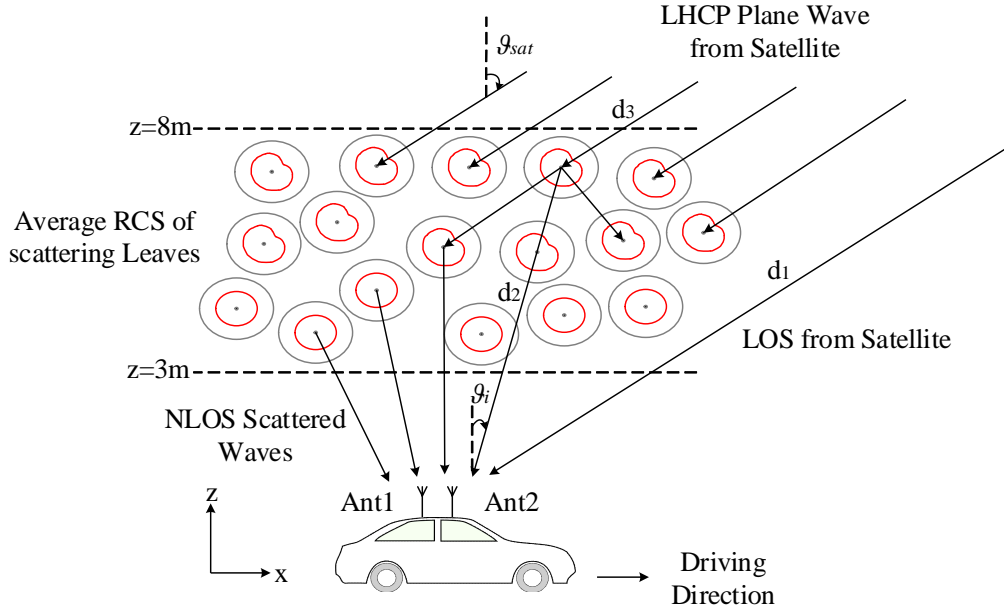


Figure 3.1: Simulated test drive scenario underneath dense foliage utilizing the average RCS of a leaf.

Other parameters such as the complex antenna characteristics in all polarizations and the orientation of the incident wave contribute to further modeling complexity. Fig. 3.1 illustrates a simulated test drive underneath dense foliage. A satellite transmits an incident left hand circular polarized (LHCP) plane wave which is not only attenuated but also reflected and obstructed through the propagation channel due to thick foliage along the driving path [30].

The foliage leaves behave as statistically distributed scatterers in a layer of roughly about 4 m - 8 m of thickness. Each single leaf yields a scattering characteristics that depends on the angle of the incident wave as shown in the red curves in Fig. 3.1. The signal is received by the car through its multiple antennas to make use of antenna diversity.

A single leaf constituted of lossy dielectric material is modeled as a very thin cylinder with radius r and thickness h in an orthogonal coordinate system (x, y, z) in order to obtain a simple statistical model of the leaves' scattering characteristics. Its azimuth and elevation angles are denoted by φ_L and ϑ_L respectively.

The geometrical representation of the leaf with its normal vector n_L is depicted in Fig. 3.2. The LHCP plane wave transmitted by a satellite with an elevation angle of ϑ_{sat} and azimuth angle which we define to be zero illuminates the leaf. The radar cross section (RCS) $\sigma(\vartheta)$ of a single leaf is analyzed as a function of the direction angle of the incident wave in order to investigate the aspect of the

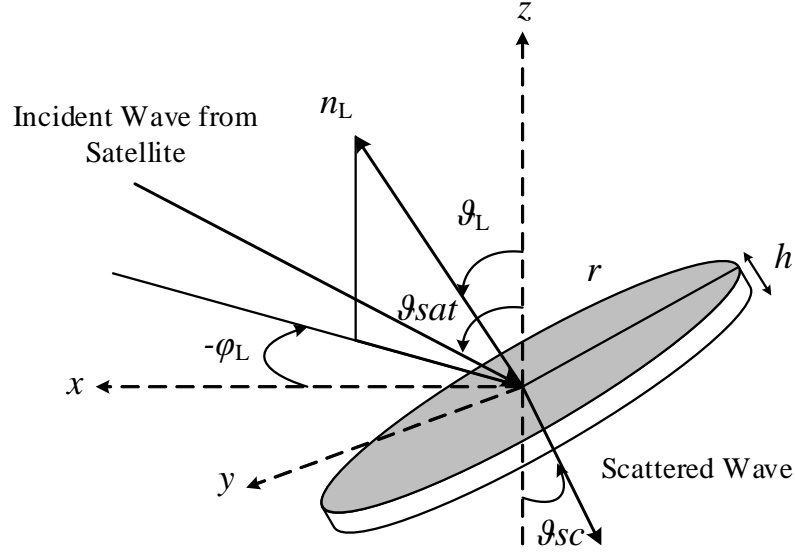


Figure 3.2: One single leaf modeled as a thin cylinder with thickness h , radius r , normal vector n_L , azimuth φ_L and elevation ϑ_L .

leaf's surface direction with respect to the incident plane wave for signal reception. In a first approach according to [31], a leaf with a radius of $r = 35$ mm, a thickness of $h = 0.2$ mm and permittivity $\varepsilon_L = 31 - j8$ is chosen. A LHCP plane wave propagates with an elevation angle of $\vartheta_{\text{sat}} = 60^\circ$ from zenith at 2.332 GHz in an example of SDARS reception [30].

Fig. 3.3a illustrates the set of curves of the RCS $\sigma(\vartheta)$ of simulated leaves with the orientation ϑ_L varying between -90° and $+90^\circ$ in 5° steps, while $\varphi_L = 0$. It can be clearly noticed that the scattering in all possible cases yields a similar pattern with a maximum in the forward scattering region of the leaf. This indicates a characteristics which is almost independent of the orientation of the leaves (ϑ_L , φ_L).

Fig. 3.3b depicts the average RCS $\sigma_L(\vartheta)$ of the 37 different outcomes. The average lies at around -38 dBsm (decibel relative to one square meter) in the forward scattering direction. This enables to choose only the average RCS $\sigma_L(\vartheta)$ to be used in a virtual test drive underneath thick foliage without regard of the leaf orientation.

The impact of the leaf size on the RCS behaviour is further investigated by changing the thickness and the radius while maintaining the foliage permittivity $\varepsilon_L = 31 - j8$. Leaves with r varying between 25 mm and 50 mm and $h = 0.2$ mm are simulated in all possible ϑ_L orientations. Fig. 3.4 illustrates their corre-

3 Channel Modeling

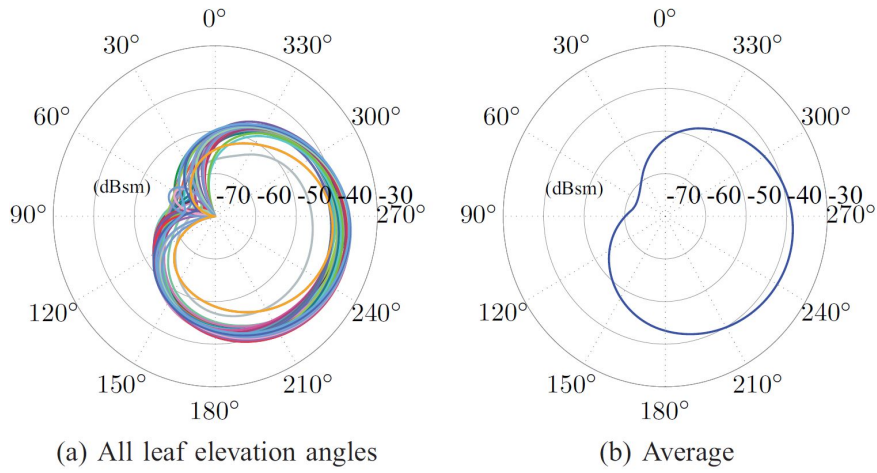


Figure 3.3: RCS of one single leaf with $r=35$ mm and $h=0.2$ mm hit by an incident LHCP plane wave with an elevation of $\vartheta_{\text{sat}} = 60^\circ$ from zenith at 2.332 GHz.

sponding average RCS after being excited by the same LHCP plane wave as in the previous scenario. It can be observed that only the absolute values of the RCS change with the size of the leaves. Values of about 13 dB more RCS are obtained at a radius of 50 mm compared to smaller leaves with a radius of only half the size. Varying the radius of the leaf does not highly affect the unique shape of the average RCS over the angle of incident waves [30].

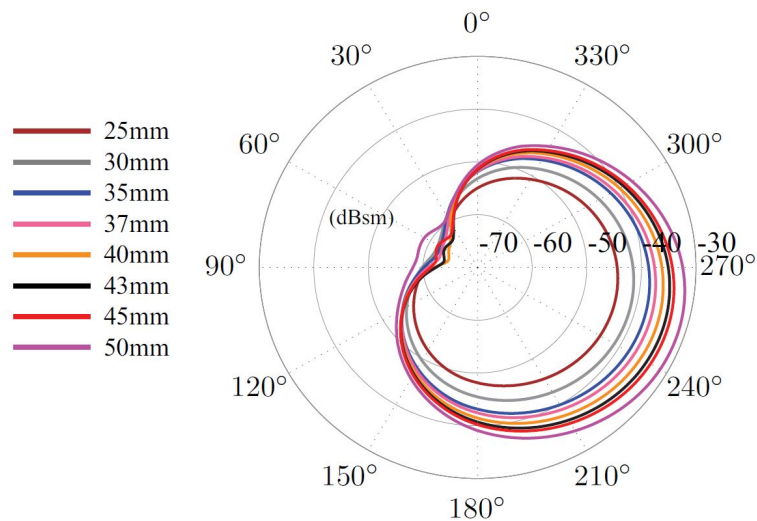


Figure 3.4: The average RCS of foliage with variable r and $h=0.2$ mm hit by an incident LHCP plane wave with 60° elevation from zenith at 2.332 GHz.

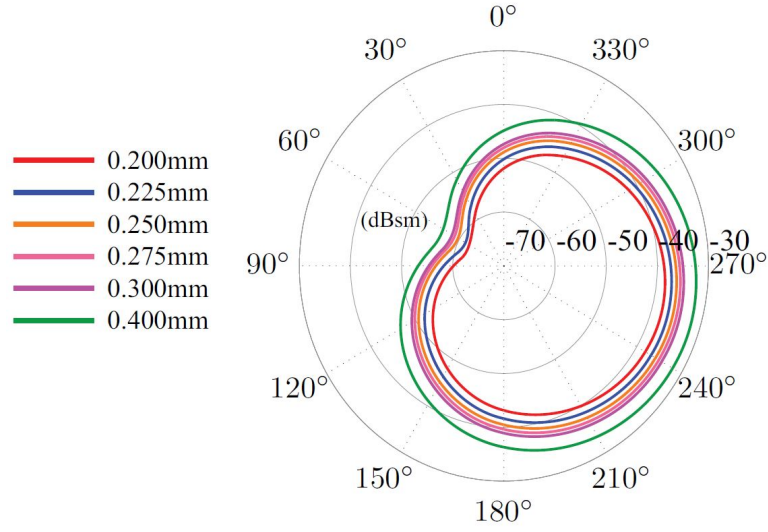


Figure 3.5: The average RCS of foliage with variable h and $r=35$ mm excited by an incident LHCP plane wave with 60° elevation from zenith at 2.332 GHz.

The foliage thickness is investigated for values of h varying between 0.2 mm and 0.4 mm with $r = 35$ mm and the same LHCP plane wave excitation as before. Fig. 3.5 depicts the average RCS for six different dimensions of h .

It is noticed that the average RCS value increases from -38 dBsm to -32 dBsm as h is incremented from 0.2 mm to 0.4 mm respectively. Changing the foliage thickness also does not modify the unique shape of the average RCS. The RCS $\sigma(\vartheta, h)$ for $r = 35$ mm as a function of the thickness h and a constant factor $k = 20.1$ can approximately be calculated as follows:

$$\sigma(\vartheta, h) \approx \sigma_L(\vartheta) + k \cdot \log_{10} \left(\frac{h}{0.2\text{mm}} \right) (\text{dB}) \quad (3.1)$$

where $\sigma_L(\vartheta)$ denotes the average RCS according to Fig. 3.3b.

3.3 Simulated Test Drive

By use of the characteristics according to equation (3.1), the scattering effects of several hundred scatterers are superimposed in the time domain in order to create an efficient model of the driving scenario as illustrated in Fig 3.1. For this reason a geostationary orbit (GEO) satellite as well as an active highly elliptical orbit (HEO) satellite operated by the SDARS provider are taken into consideration for the transmitting side.

3 Channel Modeling

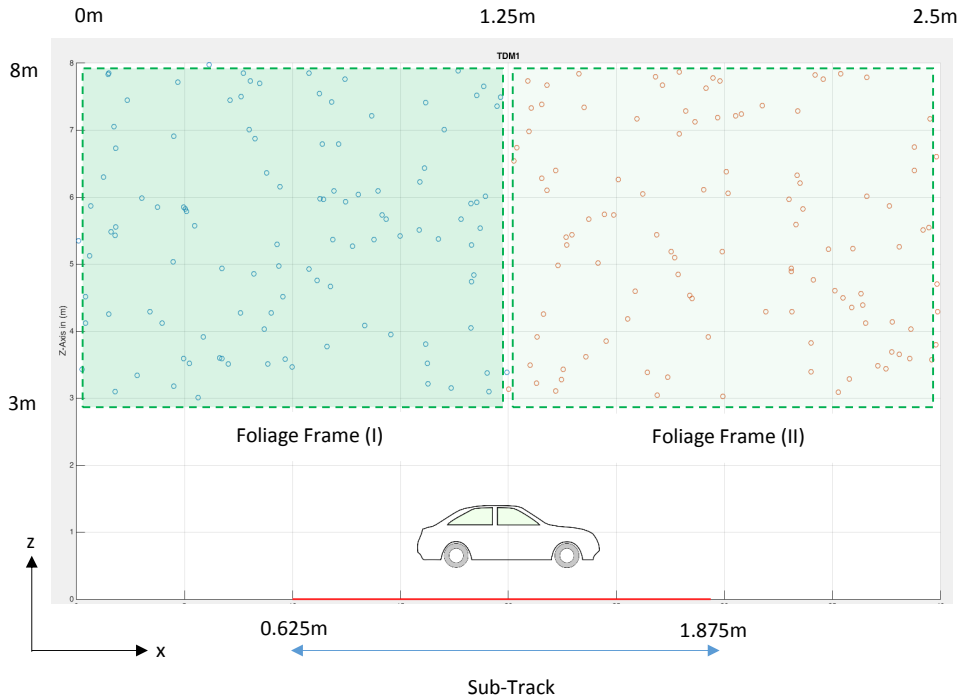


Figure 3.6: 2D illustration of the simulated sub-track. The virtual test drive consists of multiple sub-tracks.

Satellite parameters such as frequency, elevation, altitude and equivalent isotropically radiated power (EIRP) [32, 33] used in the simulation are shown in Table 3.1. The signals of both satellites are LHCP and QPSK-modulated.

Regarding foliage, scatterers with $r=35$ mm, $h=0.2$ mm and $\epsilon_L = 31 - j8$ are randomly distributed along a 65 m long driving path. Dividing the overall driving path into multiple sub-tracks accelerated the simulation processing. Fig. 3.6 illustrates how a sub-track was simulated. The leaves are located 20 m to each side of the road with a height of 5 m [30].

In the simulation every leaf is represented by its average RCS shown in Fig. 3.3b. As we move from the top of the foliage towards the vehicle, the scatterers display a slight modification in the behaviour and become almost isotropic due to internal reflections within the foliage. This is due to the increasing variance of the incident angle that is spread more at deeper layers in the dense foliage.

Different antennas are taken into account in order to evaluate diversity systems in the simulation. The vehicular receiver with a driving velocity of 40 km/h (25 mph) receives the signal through its multiple SDARS antennas. It makes use

of the scan-phase diversity algorithm in order to improve the signal quality [34]. Fig. 3.7 shows the measured radiation characteristics of both LHCP diversity antennas which are considered in the simulation.

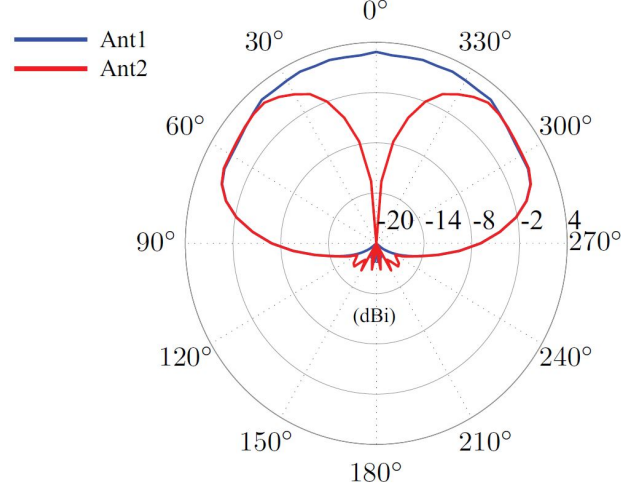


Figure 3.7: The measured radiation of both utilized LHCP antennas at 2.332 GHz.

One of the antennas possesses a directive beam towards zenith and the other one is tailored to the reception of signals transmitted via the GEO satellite for low elevation angles above horizon. $A_{m,\text{eff}}$ is the effective aperture of both utilized diversity antennas $m \in \{1, 2\}$ depending on the angle of arrival ϑ_i of the incident scattered wave. While at the time t , the vehicle is moving through the track position $x(t)$, the direction $\vartheta_i(t)$ of the incident scattered wave is modified [35]. The satellites transmit their signals with the transmit power p_t and gain g_t . In case the wave amplitude is defined at the receiving antenna m at LOS for its optimum orientation with [36]

$$a_{m,0} = \sqrt{\frac{2 \cdot p_t \cdot g_t \cdot A_{m,\text{eff}}}{4 \cdot \pi \cdot d_1^2}}, \quad (3.2)$$

the wave amplitude of the superposition of all scattered and LOS components is obtained with

$$\underline{a}_m = \underline{C}_m(\vartheta_{\text{sat}}) \cdot a_{m,0} \cdot e^{-jk d_1} + \sum_{i=1}^n \underline{C}_m(\vartheta_i) \cdot a_{m,0} \cdot \sqrt{\frac{\sigma_L(\vartheta_i)}{4 \cdot \pi \cdot d_{2,i}^2}} \cdot e^{-jk(d_{2,i} + d_{3,i})} \quad (3.3)$$

where n is the number of scatterers and $\underline{C}_m(\vartheta)$ is the complex directional function of the receiving antenna m . The average RCS of the leaf is represented by

Table 3.1: The utilized parameters of both satellites in the simulation

	GEO	HEO
Altitude (km)	37670	43600
Frequency (GHz)	2.322293	2.33021
Elev. from zenith ($^{\circ}$)	50 – 60	20 – 30
EIRP (dBW)	71.25	65.81

$\sigma_L(\vartheta_i)$, and k denotes the wave number. The unobstructed distance between the satellite and the car is denoted by d_1 . For every time t , we obtain from the position $x(t)$, the arrival angles $\vartheta_i(t)$ and the corresponding distances $d_{2,i}$ between the scatterer and the car as well as the distances $d_{3,i}$ between the satellite and the scatterer. Therefore, the time history of the carrier phase and level of the antenna signals for both diversity antennas $m \in \{1, 2\}$ is obtained from the real part of \underline{a}_m .

By this way, we obtain for both diversity antennas also the probability density functions (PDFs) of the simulated signal amplitude relative to its mean as illustrated in Fig. 3.10. The PDFs are related to the GEO satellite as the signal transmitter. The histograms are both Rice- and Rayleigh-distributed due to the presence of LOS and NLOS parts respectively. The NLOS component, which is caused by multipath propagation, varies depending on the density of foliage. In the simulation, 80% of the whole track shows NLOS transmission behaviour.

3.4 Measurement Campaign

For comparison with the results of the virtual test drive, a measurement campaign is performed in order to evaluate the introduced channel investigation model and to verify possible improvements in the signal reception quality with the utilized scan-phase antenna diversity system. The field measurements have been performed in the USA in a dense tree-sided test track.

Multiple test antennas, including the ones utilized in the simulation, are mounted on the rooftop of the vehicle. The scan-phase diversity system and the SDARS signal recording equipment are installed and placed in the car's trunk. The recording unit can record up to four signals simultaneously in the time domain [37]. The recorded signals can then be played back anytime in order to conduct further laboratory investigations of many aspects with the goal of achieving optimizations.



Figure 3.8: Examples of the leaf species scattered around the test drive path.

Fig. 3.8 depicts distinct leaves from different species of trees which were collected around the test track during the field measurement campaign. For dimension comparison, a quarter dollar coin with a diameter of 2.426 cm is utilized and compared to two sample leaves as can be seen in Fig. 3.9.

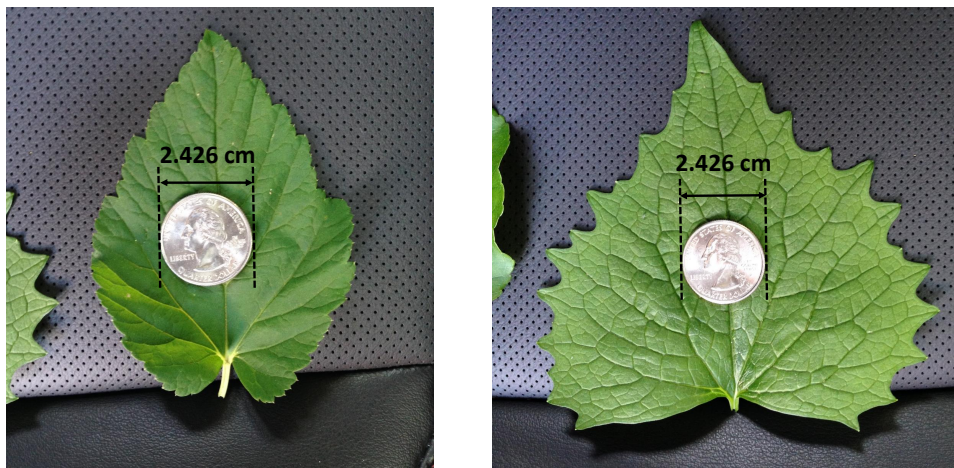


Figure 3.9: Two Leaves compared to a quarter US dollar.

By using the post-processing software tool, the signal amplitude distribution is determined. The results indicate that the signal levels are Rayleigh-distributed for most of the time during the test drive. Very short time intervals of LOS reception can however be observed especially in road parts where the foliage is not considered so dense. A combination of a Rayleigh and Rice distribution is obtained. This fulfills the criteria in order to perform field measurements in the track where NLOS reception is dominant over LOS.

The histograms of the measured relative signal amplitude with respect to the mean amplitude for both SDARS antennas with the GEO satellite as transmitter are illustrated in Fig. 3.11.

By comparing the histograms of the SDARS antennas 1 and 2 in both the simulation and measurement, the effective peaks of the Rayleigh distribution yield the values 0.75 and 0.77 for antenna 1 and the values 0.79 and 0.8 for antenna 2 respectively [30].

Additionally, the results of the measurement and simulation are compared with a theoretical Rayleigh and Rice distribution showing that there is a strong share of the Rayleigh fading scenario and another one with more LOS-share with a rician fading scenario.

This shows that deviations between the simulated model and the measurement are only between 0.01 and 0.02. Regarding the maxima of the LOS component, represented by the Rice distribution, antenna 1 has the values 0.59 and 0.58 in the simulation and measurement respectively. The second antenna yields the values 0.46 and 0.45. The deviation in the LOS scenario is only 0.01.

It can be clearly observed that there is a very good agreement between the histograms of the simulated test drive and the field measurements for both SDARS diversity antennas. This validates the introduced channel model as a suitable one to conduct fast analysis of the behaviour of different diversity systems and to predict the performance of satellite antennas in various mounting positions before performing field measurements.

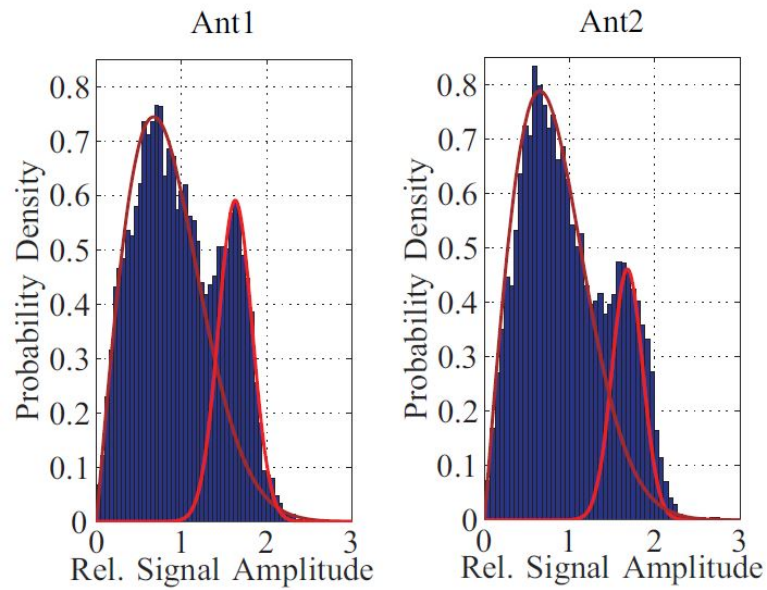


Figure 3.10: PDF of the simulated relative signal amplitudes and comparison with Rice and Rayleigh distributions.

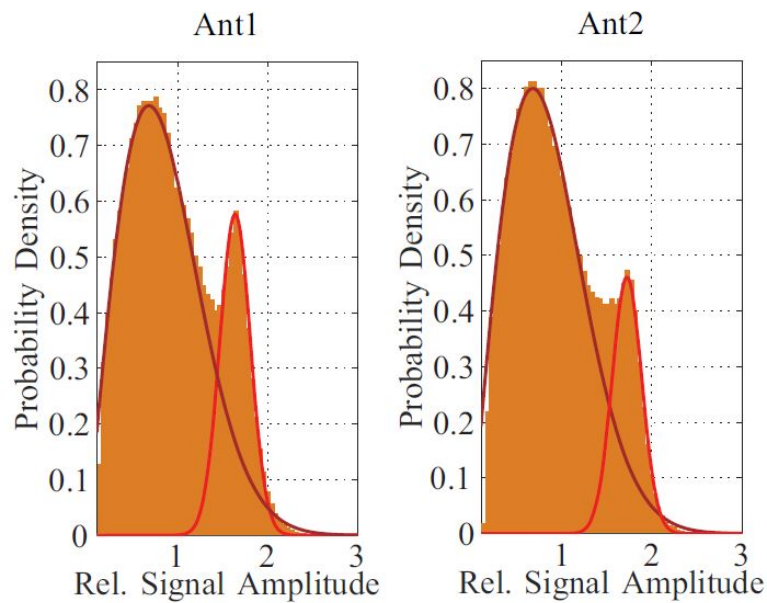


Figure 3.11: PDF of the measured relative signal amplitudes and comparison with Rice and Rayleigh distributions.

4 Noise Calibration Method for SDARS

In this chapter, a noise cancellation method for a fast scan-phase satellite radio antenna diversity system is investigated and optimized for application in SDARS antenna diversity in order to significantly improve the audio availability at low signal-to-noise ratio conditions. An error analysis of both level and phase detection within the diversity system in the presence of noise leads to a method of error correction based on a priori knowledge of the system's noise floor [38, 29]. The corresponding noise calibration is described and applied in the steering algorithm of a hardware example of an SDARS antenna diversity circuit for fast fading conditions. In other words, the algorithm's functionality is extended to include the noise calibration method for further SNR improvement in diversity systems. All available satellite signals are taken into consideration in the comparisons of a diversity reception system with noise cancellation, the same system without noise cancellation and a single antenna reception system with each other. Applying the noise calibration method in fast multipath fading driving scenarios located underneath dense foliage with a low signal-to-noise ratio of the antenna signals, a reduction in audio mute time by one order of magnitude compared to single antenna systems is achieved due to the diversity system in real-life scenarios. The improved SNR enables new unconventional mounting positions which would be severely impaired even if highly optimized single antennas are used.

4.1 Noise Aspects

Before starting with the investigation of the noise calibration method on the SDARS algorithm, it is worth highlighting the main noise aspects especially how it is generated and why it makes sense to mitigate its effects. Radio noise is defined as an electromagnetic phenomenon varying with time. It possesses components in the radio-frequency range, apparently not conveying information and which may be superimposed on, or combined with, a desired signal. The noise for a receiving system is composed of multiple noise sources at the receiving terminal. Not only external noise but also internal noise, which is generated within the receiver, must be taken into consideration while designing and implementing a system. Noise is considered a random process, that is why its instantaneous values are impossible to predict, and the only way to deal with it is by making use of statistics. Noise has a probability distribution, which shows with which probability a certain value is to be found at a given moment.

4.1.1 Noise in Electronic Systems

Communication systems receive not only the wanted signal but also additional unwanted noise, which interferes with the original transmitted signal. The noise effects can be mitigated to a certain extent, even though it is impossible to totally eliminate noise in electronic devices. The amount of noise, as a superposition of all available noise sources, is of crucial importance for input stages of electronic systems (usually realized by a low noise amplifier). The principal types of noise found in electronic components are listed below:

- **Thermal noise** is a very common noise source found within an amplifier network, which results from a fluctuation in voltage or current caused by the random thermal vibration of the charge carriers in any conducting medium at a temperature above absolute zero. It is also referred to as Johnson or Nyquist noise, because J. Johnson first observed it and H. Nyquist explained its origins [39].

Thermal noise possesses the characteristics of white noise (and therefore sometimes is also called white noise) up to very high frequencies. The spectrum of white noise has a constant spectral power distribution over the frequency. In other words, if we take into consideration two bands with identical widths, but situated at two distinct frequencies, the noise power in these bands is equal. Hence, the the amplitude of the thermal noise can be modeled with a zero mean Gaussian probability distribution.

Since the thermal noise is found in any conductive material above 0 K, it is the sensitivity limit of any receiving system. The available thermal noise power N_{th} is independent of the resistivity of the conductor in which it arises:

$$N_{th} = k \cdot T \cdot B, \quad (4.1)$$

where k is the Boltzmann constant, T the absolute temperature and B the bandwidth. The internal Root Mean Square (RMS) noise voltage source is described by the Nyquist equation [40] as follows:

$$\overline{v_{th}^2} = 4 \cdot k \cdot T \cdot B \cdot R, \quad (4.2)$$

where R is the value of the resistance.

In addition to thermal noise, resistors show some amount of extra noise, which is not related to the thermal noise and which is caused by discontinuities in the structure of the resistor [41]. Metal thin-film resistors have less excess noise in comparison to carbon ones, due to the homogenous

structure. Nevertheless, the resistor excess noise is an aspect for frequencies below 100 kHz. Therefore, it will not be further considered in this work.

- **Shot noise** is related to a discrete structure of electricity and to the individual carrier injection through a pn -junction. It is generated in the pulsed character of the current (determined by the discrete nature of the charge carriers, electrons and holes) flowing through a potential barrier, as the one of the pn -junction or the charge-free space in a vacuum tube.

Like the thermal noise, shot noise is also considered a white noise and has a Gaussian distributed amplitude. The RMS noise current source is given by [42]:

$$\overline{v_{\text{th}}^2} = 2 \cdot q \cdot I \cdot B, \quad (4.3)$$

where I is the forward junction current and q the electron charge. Shot noise is particularly observable in active devices and semiconductors, such as tunnel junctions and Schottky barrier diodes.

- **Flicker noise** is observed in almost every electronic device. It shows an inverse frequency power density curve ($1/f$ characteristic). The flicker is also called as $1/f$ noise, pink noise and low-frequency noise. It is found both in semiconductor devices and vacuum tubes. In semiconductors, it is produced by generation and recombination phenomena, caused by defects and impurities. Flicker noise is also found in carbon resistors, due to the granulated-nature of the current path, whereas in metal film resistors it is often negligible.

Flicker noise usually occurs as a resistance fluctuation and the corresponding noise spectral density function can be expressed as follow [42]:

$$S_{\text{fl}}(f) = K/f, \quad (4.4)$$

where K is a process-dependent constant and f the considered frequency.

4.1.1.1 Noise Figure

In an antenna amplifier, the noise figure and output noise voltage are used as parameters of the noise contribution. H. Friis introduced the noise figure concept in order to describe the degradation in SNR by the receiver [43]. This enables to compare the sensitivity of a real amplifier to an ideal, loss-less and noiseless amplifier with the same bandwidth and input termination. In wireless communication systems, the noise factor F describes the noise performance of a device and relates the SNR available at the input to the SNR at the output [44]:

$$F = \frac{SNR_{in}}{SNR_{out}} \geq 1. \quad (4.5)$$

The logarithmic noise figure F_{dB} can be calculated out of the noise factor F as follows:

$$F_{dB} = 10 \cdot \log(F). \quad (4.6)$$

For a cascaded system, the total noise factor F_{cas} can be calculated by means of the Friis formula [43]:

$$F_{cas} = F_1 + \frac{F_2 - 1}{G_1} + \frac{F_3 - 1}{G_1 \cdot G_2} + \dots + \frac{F_n - 1}{G_1 \cdot G_2 \dots G_{n-1}}, \quad (4.7)$$

where G_i and F_i ($1 \leq i \leq n$) are the respective gain and noise factor of the n stages. This equation shows that the first stage amplifier clearly affects the noise factor. Furthermore, it shows that the overall noise contribution of a cascaded system can be reduced by increasing the gain (G_1) of the low-noise (F_1) first amplifier stage. In other words, the first stage dominates the total noise factor and therefore it is necessary for low-noise applications to maximize G_1 and to minimize F_1 .

The figure below shows a system with n cascaded amplifiers possessing the amplifier gain G_i , amplifier noise $N_{a,i}$ and noise figure F_i ($1 \leq i \leq n$).

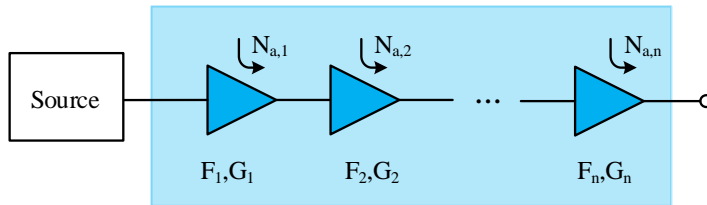


Figure 4.1: A system with n cascaded amplifiers

4.1.1.2 Noise Temperature

The concept of noise temperature can be utilized to describe the circuit noise performance or to simplify noise calculations. This is not a common physical temperature, but it is defined as the virtual temperature a passive network must possess in order to display an available noise power equal to the one of the port to be described, at a specific frequency [45]. For example, we can state that an antenna has a noise temperature of 400 K at a given frequency. This means that the available noise power at the antenna port is the same as the one of a R_A resistance (the real part of the antenna impedance) heated at 400 K.

A noisy two-port can be also described in terms of effective noise temperature T_e . It is the temperature the source resistance would possess, so that the noiseless two-port exhibits the same amount of output noise as the actual two-port [46]. In other words, the noise contributed by the two-port is not only the result of an internal cause, but it is externalized and attributed to the source resistance.

As the noise floor limits the detection of weak signals (with very low power) and the distortion products limit the upper level of detectable power, the output noise voltage of an amplifier circuit is an additional measure to describe the noise behavior of an amplifier. Any source of white noise can be modeled as a thermal noise source with an equivalent noise temperature. Components and systems can then be characterized by this temperature. Given the noise factor F of a component or a system, the corresponding equivalent noise temperature T_e is defined as [44, 45]:

$$T_e = (F - 1) \cdot T_0, \quad (4.8)$$

where T_0 represents the ambient noise temperature of around 290 K. Using the equivalent noise temperatures of the components, the amount of noise voltage at the output port of the considered system can be calculated by the square root of v_{th} , thus being dependent on the Intermediate Frequency (IF) bandwidth B :

$$\overline{v_{out}} = \sqrt{4 \cdot k \cdot T_e \cdot B \cdot R}. \quad (4.9)$$

4.1.1.3 Signal-to-Noise Ratio

In both analog and digital communication systems, the SNR is a measure of the wanted signal power strength S relative to the overall undesired noise N :

$$SNR = \frac{S}{N}. \quad (4.10)$$

If the incoming signal strength is V_s (in μV) and the noise level is V_n (in μV), the SNR in decibels is calculated as follows:

$$SNR_{dB} = 20 \cdot \log(V_s/V_n) \quad (4.11)$$

$$= 10 \cdot \log(S/N). \quad (4.12)$$

The minimum detectable signal gives an output SNR of 0 dB ($V_s = V_n$). In this case, the received signal is almost undetectable because the noise level severely competes with it. V_s must be greater than V_n in order to be detectable, which gives a positive SNR value. If all levels are expressed in decibels, the formula can be simplified to:

$$SNR_{dB} = S_{dB} - N_{dB}. \quad (4.13)$$

The power levels may also be expressed in dBm (relative to 1 mW) or to some other standard by which the levels can be compared.

The SNR value is an essential measure for the receiver sensitivity. Receiving systems always have a specified sensitivity which is related to the minimum signal strength $V_{s,min}$ at the input required to achieve a reasonable SNR . The sensitivity of receiving systems has a large impact on the overall quality of the received service.

4.1.2 External Noise

Not only the noise generated in the receiver itself limits the performance and quality of radio reception, but also the external noise collected by the receiving antenna. So the characteristic of the radio channel plays a major role in this aspect. The main external noise sources include [47]:

- **Man-made noise** or artificial noise which is the electrical noise generated by sources such as automobile/aircraft ignition, electrical motors, switch gears, industrial equipment and various other heavy electrical machines. This type of noise is contributed by the arc discharge which takes place during operation of these machines. Urban environments generate more artificial noise than rural areas. When it comes to vehicular radio reception, the vehicle is considered a major source of man-made noise, since the antenna is situated in the immediate vicinity of noise generators. The disturbances have their origins in the engine ignition pulses and in all the digital electronic equipment within the vehicle. Some components such as microprocessors are particularly problematic, because they deploy digital signals with abrupt slopes, which exhibit broad spectra and are subject to electromagnetic compatibility issues.

- **Natural noise** which includes several sources caused by nature. Atmospheric noise is for instance caused by natural atmospheric processes, particularly lightning discharges in thunderstorms. The sum of all lightning flashes results in atmospheric noise. In addition to that, there is cosmic noise which is observed at frequencies beyond 15 MHz when highly directional antennas point towards the sun or to certain other regions of the sky. Celestial objects, which are situated far away from Earth, emit electromagnetic waves in their full spectrum, including RF waves.

The following three figures 4.2, 4.3 and 4.4 specify the expected values of F_a (the external noise figure) in the frequency range 0.1 Hz to 100 GHz along with the effective antenna temperature t_a due to external noise [47].

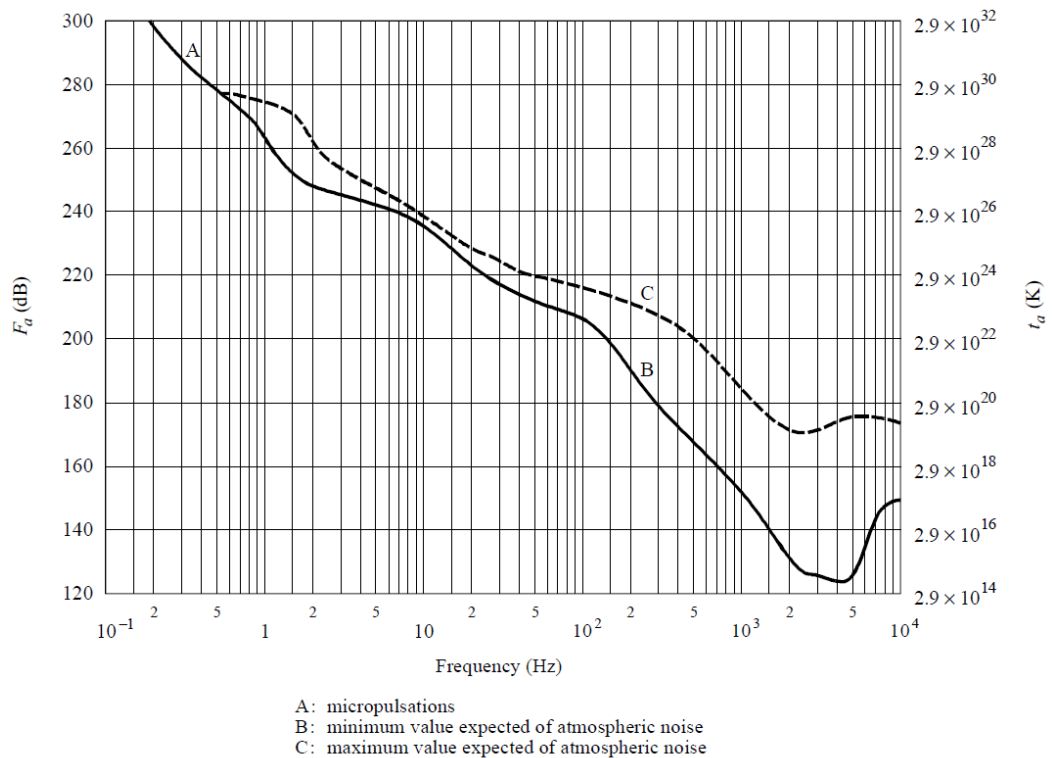


Figure 4.2: External noise factor and effective antenna temperature from 0.1 Hz to 10 kHz

Figure 4.2 covers the frequency range 0.1 Hz to 10 kHz. The solid curve is the minimum expected hourly median values of the external noise figure F_a based on measurements (taking into consideration the whole Earth surface, all seasons

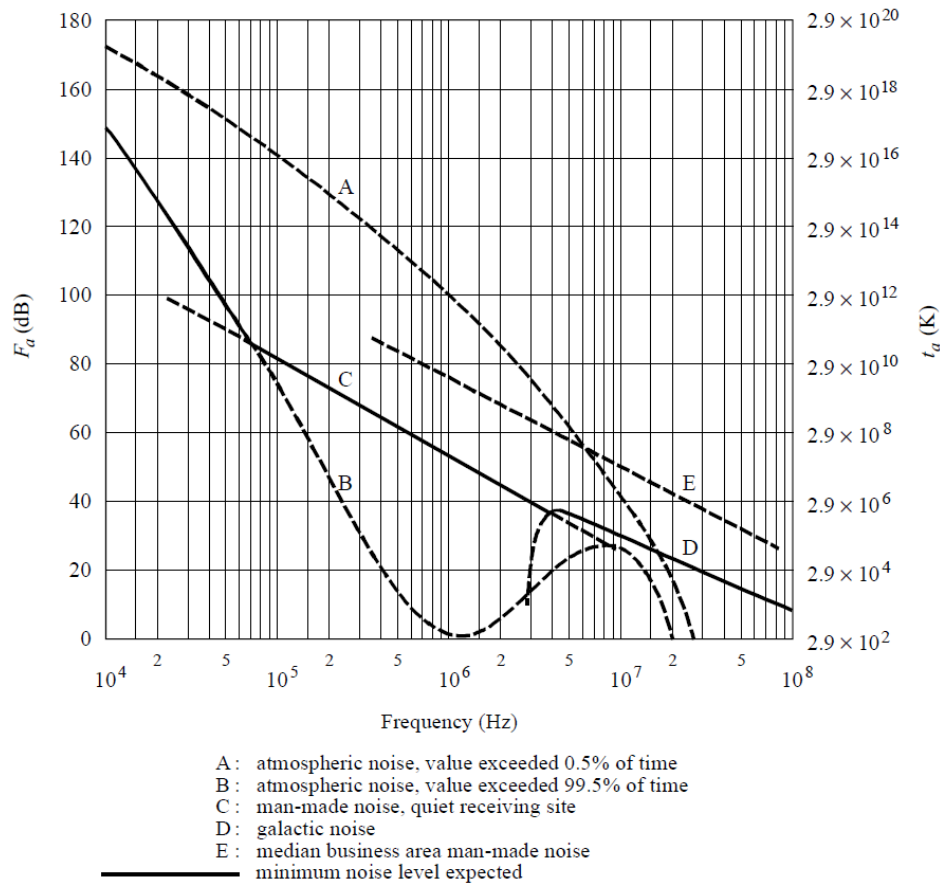


Figure 4.3: External noise factor and effective antenna temperature from 10 kHz to 100 MHz

as well as times of day) and the dashed curve exhibits the maximum expected values. It is worth mentioning that in this frequency range there is very little diurnal, seasonal, or geographic variation.

Figure 4.3 covers the frequency range 10 kHz to 100 MHz for various sources of noise. The minimum expected noise is represented by the solid curves. For atmospheric noise due to lightning, the minimum values of the hourly medians expected are taken to be those values exceeded 99.5% of the time and the maximum values are those exceeded 0.5% of the time. This type of noise decreases with frequency and is lower during the day [48]. Concerning the man-made noise, it decreases with frequency [49]. The cosmic noise becomes important for frequencies higher than 20 MHz.

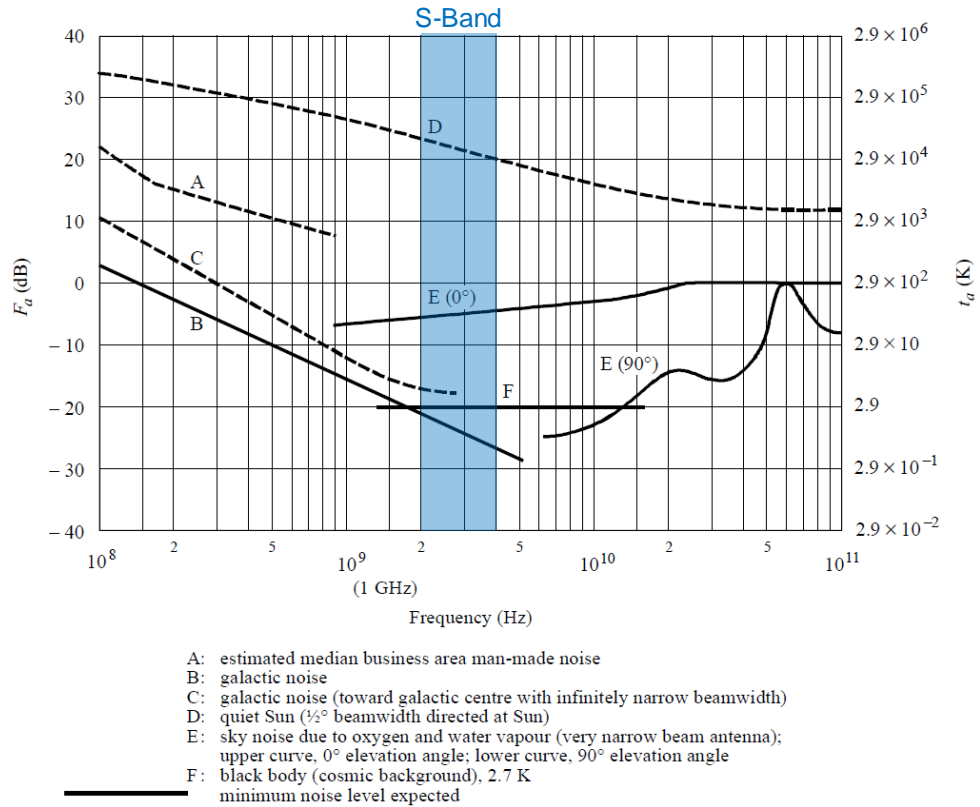


Figure 4.4: External noise factor and effective antenna temperature from 100 MHz to 100 GHz

Figure 4.4 covers the frequency range 100 MHz to 100 GHz. The minimum noise is given by solid curves, while some other noises of interest are given by dashed curves. The majority of the results shown in the figure is for omni-directional antennas (except as noted on the figures). For directional antennas, however, studies have indicated that at HF (for example), for atmospheric noise from lightning for very narrow beam antennas, there can be as much as 10 dB variation (5 dB above to 5 dB below the average F_a value shown) depending on antenna pointing direction, frequency and geographical location. For galactic noise, the average value (over the entire sky) is given by the solid curve labeled galactic noise.

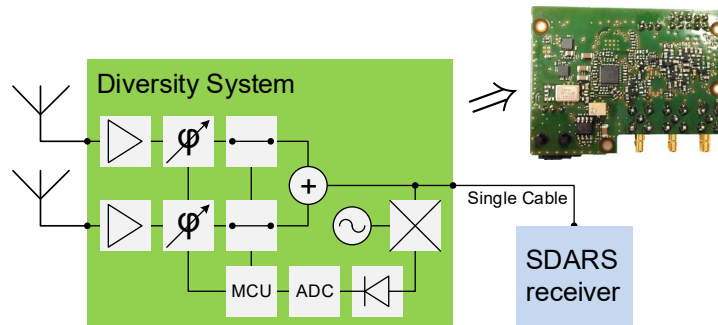


Figure 4.5: Diversity system block diagram and printed circuit board of the hardware demonstrator which was utilized during the measurements. The printed circuit board is 60mm by 45mm in size

4.2 Scan-Phase Diversity with Noise Calibration

As has been mentioned in the previous chapters, antenna diversity systems in combination with antennas [50, 51, 52, 53, 54] that provide statistically independent output signals allow for remarkable improvements of the received signal level in comparison to a single antenna [55, 56, 57]. Scan-phase antenna diversity systems have proven to be extremely efficient because they extend the capabilities of comparatively simple scanning diversity systems by also enabling phase detection as well as phase-aligned superposition of antenna signals [1, 58] while still working with a one standard antenna receiver with only a single RF cable. This aspect is of significant importance for car manufacturers since often cables with a length of several meters have to be led through the car towards the radio. Using scan-phase diversity, the same simple interface between the antenna part and the radio can be utilized like for a single antenna while keeping the radio unmodified. A block diagram is depicted in Fig. 4.5. Next to it, an example of a hardware demonstrator is also shown.

In multipath fast fading environments the utilization of several receiving antennas in combination with a scan-phase antenna diversity system has been inspected and proved the significant reduction of audio muting compared to single antennas [59, 4, 60]. In [61, 62] measurements are presented which confirm that even at critical and unconventional mounting positions (e.g. on the dashboard or in a single side mirror) the scan-phase antenna diversity achieves excellent improvements of audio availability compared to single antenna systems.

The impact of noise on the accuracy of both the level detection and the phase calculation of a diversity algorithm is described. In order to enhance the satellite signal availability even in scenarios with very low SNR, it is shown how a priori knowledge of the system's noise floor is applied. The corrections are applied to the results of level measurement that are utilized for the determination

of the phase differences of the antenna signals. The noise cancellation method is applied and verified in real test drive scenarios underneath thick foliage. While even a scan-phase antenna diversity system without the noise calibration method yields already an improvement of the audio quality in comparison with a single antenna, the additional noise correction method leads to a significantly higher audio mutes reduction of more than one order in magnitude.

A scan-phase antenna diversity system contributes to the enhancement of the reception quality in terms of a reduction of the mute duration in fading scenarios [1]. In the blockdiagram depicted in Fig. 4.5 it can be seen that the diversity system consists of RF switches and phase shifters which allow for selecting, phase-aligning and combining the antenna signals. Afterwards, a small share of the output signal is down-converted in frequency and bandpass filtered. Then, a logarithmic detector generates a voltage that is considered proportional to the signal level (the channel selective logarithmic detector is the block with the diode symbol in Fig. 4.5). These level measurement results are read by a simple micro-controller unit (MCU), which also executes the diversity algorithm in periods of $200 \mu\text{s}$ [60], [63].

Due to the fact that RF signals from the satellites are QPSK-modulated the ideal signal phase changes in steps of 90° . Hence, bit errors are generated only after the signal phase is distorted enough to be shifted into a different quadrant of the complex signal plane which is equivalent to a phase shift of more than 45° . The phase distortions can be corrected by phase shifters with controllable steps of 90° . The diversity demonstrator possesses phase shifters with an even finer step width of 45° .

The elementary calculations of the scan-phase antenna diversity algorithm are described in the following [64, 65]. In each period of the algorithm, four different test constellations with distinct combinations of antenna signals are set in order to measure the power levels from which the phase differences are determined. Fig. 4.6 illustrates a representation of an arbitrary signal constellation. The terms \underline{A}_1 and \underline{A}_2 are the wave amplitudes of the signals of antenna 1 and 2 respectively, \underline{S} is the sum of these amplitudes and \underline{T} is the sum after rotating antenna signal \underline{A}_1 by 90° in phase [65]. The phase difference between \underline{A}_1 and \underline{S} is denoted by the angle α . Angle β describes the phase difference between \underline{A}_2 and \underline{S} .

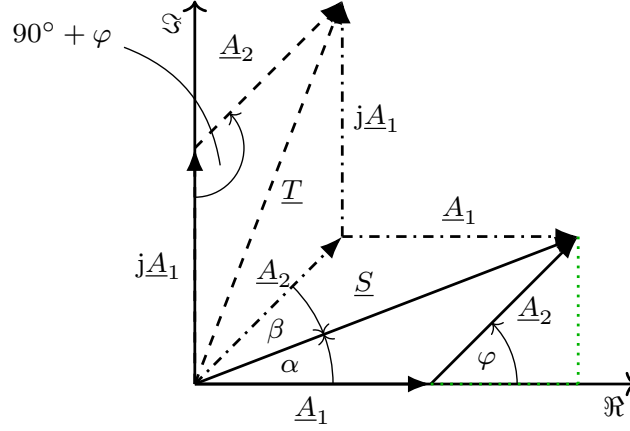


Figure 4.6: Signal constellation of two single antennas \underline{A}_1 and \underline{A}_2 showing the four test cases of the scan-phase antenna diversity algorithm in the complex plane

The calculation of mutual phase differences in addition to the antenna selection are only based on power level measurements of the four test cases with the power levels

$$P_S \sim |\underline{A}_1 + \underline{A}_2|^2 = S^2 \quad (4.14)$$

$$P_1 \sim |\underline{A}_1|^2 = A_1^2 \quad (4.15)$$

$$P_2 \sim |\underline{A}_2|^2 = A_2^2 \quad (4.16)$$

$$P_T \sim |j\underline{A}_1 + \underline{A}_2|^2 = T^2. \quad (4.17)$$

The absolute values of the mutual phase differences α and β are calculated from the levels P_1 , P_2 and P_S based on trigonometric considerations [64, 65]. The fourth test case is crucial since it calculates the sign of the phase differences which are important for a correct phase alignment. The law of cosines can be applied if we consider for example the determination of the angle α according to

$$2A_1S \cos(\alpha) = S^2 + A_1^2 - A_2^2. \quad (4.18)$$

Moreover, the following is derived

$$\begin{aligned} T^2 &= A_1^2 + A_2^2 - 2A_1A_2 \cos(180^\circ - (90^\circ - \varphi)) = \\ &= A_1^2 + A_2^2 + 2A_1A_2 \sin(\varphi). \end{aligned} \quad (4.19)$$

In Fig. 4.6 (green dotted line) it can be noticed that

$$S \sin(\alpha) = A_2 \sin(\varphi). \quad (4.20)$$

Table 4.1: Evaluating phase differences of two signals from the four measured test cases for angle steps of 45° resolution ($\varepsilon < 22.5^\circ$)

Range of α	conditions (all have to be met)
$0^\circ \pm \varepsilon$	$N_a < D_u$ $D > 0$
$45^\circ \pm \varepsilon$	$N_a > D_u$ $N_a < D_o$ $N > 0$ $D > 0$
$90^\circ \pm \varepsilon$	$N_a > D_o$ $N > 0$
$135^\circ \pm \varepsilon$	$N_a > D_u$ $N_a < D_o$ $N > 0$ $D < 0$
$180^\circ \pm \varepsilon$	$N_a < D_u$ $D < 0$
$225^\circ \pm \varepsilon$	$N_a > D_u$ $N_a < D_o$ $N < 0$ $D < 0$
$275^\circ \pm \varepsilon$	$N_a > D_o$ $N < 0$
$315^\circ \pm \varepsilon$	$N_a > D_u$ $N_a < D_o$ $N < 0$ $D > 0$

In combination with (4.19) the following is obtained

$$2A_1 S \sin(\alpha) = T^2 - A_1^2 - A_2^2. \quad (4.21)$$

The expression $\tan(\alpha)$ is obtained through dividing (4.21) by (4.18). Therefore, the angle α can finally be expressed via the measured power values by

$$\alpha = \arctan\left(\frac{P_T - P_1 - P_2}{P_S + P_1 - P_2}\right) = \arctan\left(\frac{N}{D}\right), \quad (4.22)$$

where the four-quadrant arctan-function must be evaluated by taking into consideration the signs of both the denominator $D = P_S + P_1 - P_2$ and the numerator $N = P_T - P_1 - P_2$ [66]. The angle β can also be determined respectively. Since the phase shifter possesses a stepped topology, there is a necessity to evaluate the arctan-function in the MCU which takes between $80 \mu\text{s}$ and $130 \mu\text{s}$ depending on the input values. The following analysis is utilized in order to calculate the optimum settings for the phase shifters with a step width of 45° . The analysis makes use of the variables $N_a = |N|$, $D_a = |D|$, $D_u = D_a/\sqrt{2}$, and $D_o = D_a \cdot (1 + \sqrt{2})$. It is also based on the fact that $\tan(22.5^\circ) = 1/\sqrt{2}$ and $\tan(67.5^\circ) = 1 + \sqrt{2}$. The phase evaluation is performed according to the values listed in Table 4.1.

The advantage of this phase detection algorithm is avoiding the time-consuming arctan function in the small MCU. It is replaced by only a small number of very simple instructions, each of which is executed within one or a few MCU clock cycles. The maximum total measured time in order to calculate one phase value according to this algorithm in the hardware demonstrator is $35 \mu\text{s}$. This is a significant time reduction in comparison to the $130 \mu\text{s}$ which are needed by the arctan function.

4.3 Influence of Noise on Phase Calculation

The diversity system must process low-power received signals due to the high free-space path loss of approximately 190 dB from the GEO-satellite to the receiving antenna. Fig. 4.8 illustrates the spectrum of such a noisy received signal relative to the line-of-sight (LOS) level [66]. It is worth mentioning that multiple aspects of the overall reception system also contribute to low signal power or high noise power, both of which result in lower SNR values. Unconventional antenna mounting positions can result in distorted antenna patterns and reduced antenna gain and/or efficiency in case the ideal rooftop mounting of the SDARS antenna(s) is not possible. The combination of multiple antennas help in mitigating such individual antenna impairments. Nevertheless, these low signal powers necessitate in a high level detection accuracy even in cases of very low SNR close to 0 dB.

Non-linearities in the detection circuitry can also be corrected when applying the noise cancellation method. As it will be shown later, these non-linearities are particularly noticeable close to the lower end of the logarithmic amplifier's dynamic range. In other words, the diversity hardware itself can be simplified by correcting non-linear and noisy input levels through reducing the gain of the level detection circuit or alleviating noise figure specifications both of which can result in reduced hardware effort.

A critical noise power PN_{crit} above which phase distortions due to an erroneous calculation of the phase changes for signal optimization exceed 45° is now derived. This value is of significant importance for the QPSK-modulated signals above which the probability of bit errors increases. The complex signal vectors of \underline{A}_1 , \underline{A}_2 and their superposition \underline{S} are illustrated in Fig. 4.7 [66]. The black vectors depicted in the figure represent the wave amplitudes of which we assume that a phase aligned superposition will optimize the reception quality by perfectly aligning them at the phase of the current superposition \underline{S} .

As a matter of fact, the ideal sum of both individual signals (signal amplitude) would be available to the receiver while getting rid of phase distortions $\Delta\gamma > 45^\circ$ which would cause bit errors due to the phase modulation of the SDARS signals. Deviating phase results are calculated with the impact of noise on the level measurements. This results in an inferior alignment with lower amplitude and even phase deviations from the previous signal phase. In the case illustrated in Fig. 4.7, the angle γ of \underline{S} equals α .

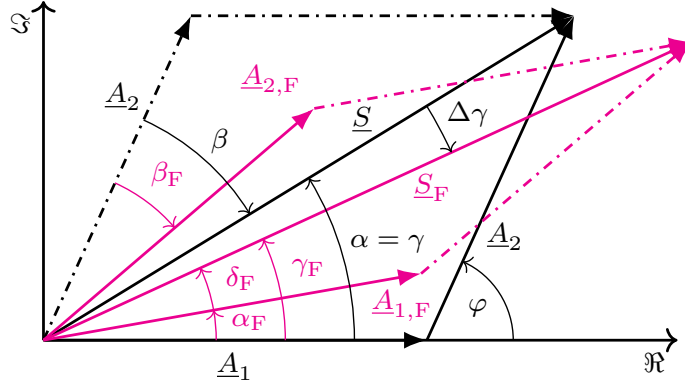


Figure 4.7: Complex signal diagram with correct (black) and erroneous (red) summed signals due to noise-influenced phase calculations (e.g. low signal-to-noise ratio signals)

An erroneous calculation leading to phase distortions of the diversity signal takes place in case all signal levels are superimposed with the noise power PN [66]. As a result, the calculation of the phase α modifies from (4.22) to

$$\alpha_F = \arctan\left(\frac{P_T - P_1 - P_2 - PN}{P_S + P_1 - P_2 + PN}\right). \quad (4.23)$$

It can be observed in Fig. 4.7 that there is such a case in red color. The antennas 1 and 2 are phased with angles α_F and β_F respectively instead of the optimal values. This leads to a new superposition of antenna signals with a phase derivation $\Delta\gamma$ to the previous case. We can calculate the phase distortion of the superposition of the antenna signals as follows

$$\Delta\gamma = \gamma_F - \gamma = \gamma_F - \alpha = \alpha_F + \delta_F - \alpha \quad (4.24)$$

utilizing the results of (4.22) and (4.23). With the power $P_{S,n}$ of $\underline{S}_F = \underline{A}_{1,F} + \underline{A}_{2,F}$ and $P_{T,n}$ accordingly the angle δ_F is calculated according to

$$\delta_F = \arctan\left(\frac{P_{T,n} - P_1 - P_2}{P_{S,n} + P_1 - P_2}\right). \quad (4.25)$$

The new power $P_{S,n}$ of the erroneous signal sum is

$$P_{S,n} = P_1 + P_2 + 2 \cdot \sqrt{P_1 \cdot P_2} \cdot \cos(\varphi - (\alpha_F + \beta_F)). \quad (4.26)$$

The derivation of the power $P_{T,n}$ is performed accordingly [66]. Actually, bit errors can be avoided in case phase distortions do not exceed a critical value of $|\Delta\gamma| < 45^\circ$ so that a critical noise power PN_{crit} can be calculated at which the following condition is met

$$\Delta\gamma|_{PN=PN_{\text{crit}}} = 45^\circ. \quad (4.27)$$

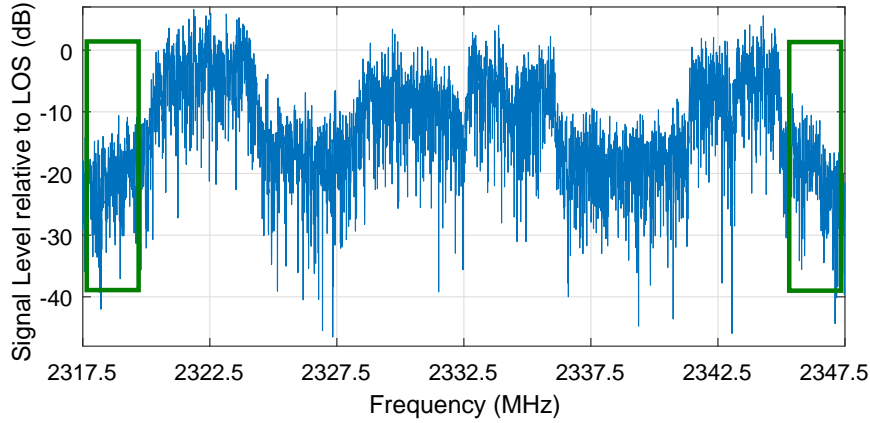


Figure 4.8: Signal spectrum of a noisy satellite radio received signal normalized with respect to the LOS level. Out-of-band noise levels can be measured in the frequency bands indicated by green rectangles

The noise power PN_{crit} depends on the signal constellation in terms of not only the ratio of both antenna signals' powers but also their phase difference φ at the beginning of the measurements [66]. The resulting phase distortion can be calculated according to

$$\begin{aligned} \Delta\gamma = & \arctan\left(\frac{P_T - P_1 - P_2 - PN}{P_S + P_1 - P_2 + PN}\right) \\ & + \arctan\left(\frac{\sqrt{P_1 \cdot P_2} \cdot \sin(\varphi - (\alpha_F + \beta_F))}{P_1 + \sqrt{P_1 \cdot P_2} \cdot \cos(\varphi - (\alpha_F + \beta_F))}\right) \\ & - \arctan\left(\frac{P_T - P_1 - P_2}{P_S + P_1 - P_2}\right) \end{aligned} \quad (4.28)$$

where both α_F and β_F are considered functions of the noise power PN . Regarding the power ratio of the individual antennas, it only needs to be considered in a certain range around 0 dB (equally strong antenna signals). This can be shown by calculating the signal-to-noise ratio of the output signal from input signals with differing SNR values. If equation (4.28) is numerically evaluated for the critical noise power PN_{crit} where (4.27) is true, a range of $-7.7 \text{ dB} \leq P_1/P_2 \leq +7.7 \text{ dB}$ (which corresponds to an amplitude imbalance of $|\underline{A}_2| < |\underline{A}_1| \cdot (\sqrt{2} - 1)$) is considered sufficient [66].

At more extreme power ratios, which exceed the absolute value of $|\pm 7.7| \text{ dB}$, the antenna with the lower power will be switched off due to the noise contribution of the antenna signal with the lower SNR to the combined signal. The entire range of phase differences $0^\circ \leq \varphi < 360^\circ$ is considered here for completeness even if values close to 180° are extremely unlikely because of the continuous operation of the fast scan-phase diversity system [66]. Fig. 4.9 illustrates the result

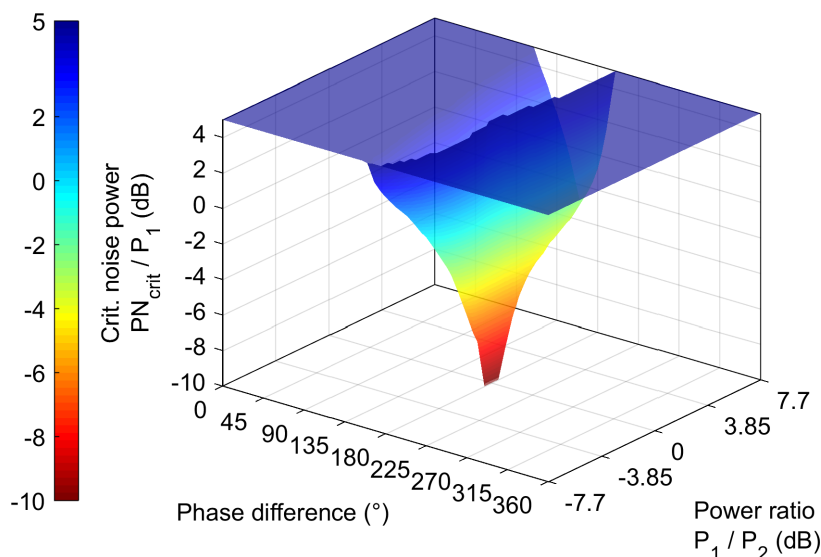


Figure 4.9: Critical noise power ratio PN_{crit}/P_1 for various power ratios P_1/P_2 and phase differences φ of both antenna signals. The values are bound within the depicted axis limits

of this analysis and indicates that the highest influence of the noise power PN on the error of the calculated phase values arises around a phase difference of $\varphi = 180^\circ$ for similar signal levels of both antenna signals. This is expected due to the cancellation the signal sum in such a case, where even small distortions of the measured level caused by noise will lead to large phase calculation errors. A detailed illustration for several phase differences φ between the two antenna signals around 180° is depicted in Fig. 4.10 [66].

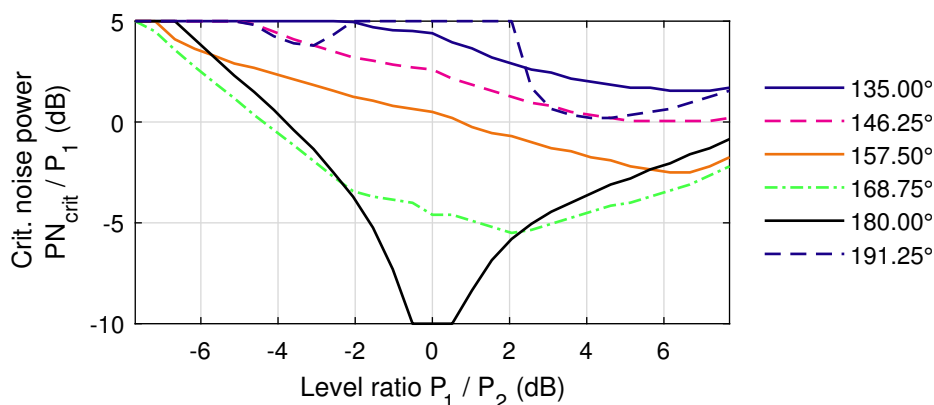


Figure 4.10: Critical noise power ratio PN_{crit}/P_1 for phase differences φ of the individual antenna signals close to the angle 180°

4.4 Improving the Phase Calculation Accuracy

The noise level information is obtained from laboratory measurements of the system's noise floor. Performing out-of-band noise measurements could be applied in frequency ranges where external noise received by the antenna cannot be neglected with the aim of supplementing the measured noise influences of the circuit itself as it is illustrated in Fig. 4.8, but this is not implemented yet. In order to pre-calculate the noise correction values, the level detection results are logged for known input levels of a sinusoidal signal within the satellite signal's frequency band [66].

Signal levels for a level sweep in addition to corrected measurement results are depicted in Fig. 4.11. Basically, a constant noise power can simply be subtracted in systems comprising a power measurement in linear values (equal or proportional to Watts) in order to gain the wanted signal power without noise. Nevertheless, a more complex calculation must be used since the level detection in the discussed diversity demonstrator yields logarithmic measurement results. The values, which are measured, are matched to an extrapolated linear characteristic. This characteristic is determined from measurements at high input levels where distortions from noise are negligible. This is considered equivalent to reading the value of the "ideal value" from Fig. 4.11 for the measured value of "signal + noise (uncal.)" [66].

A pre-calculated lookup-table is utilized to convert the measured levels to corrected values in order to guarantee a low processing time and since memory usage is no significant issue. The non-linearities in the level detection characteristic (e.g. the small bump in the blue line at -74 dBm) are corrected as well in the calibrated measurement result (dashed magenta line) as can be observed in Fig. 4.11 [66]. The measured and corrected logarithmic values to their corresponding linear powers, which are used in the phase calculations, are converted through another lookup-table. This correction is applied with the assumption that noise contributions to the received signal are constant. It is planned to extend this functionality in the future by conducting additional measurements of out-of-band noise levels within the frequency bands indicated in Fig. 4.8. With this information, variations in external noise sources presented in section 4.1.2 in addition to temperature-induced deviations from the pre-determined values will be accounted for.

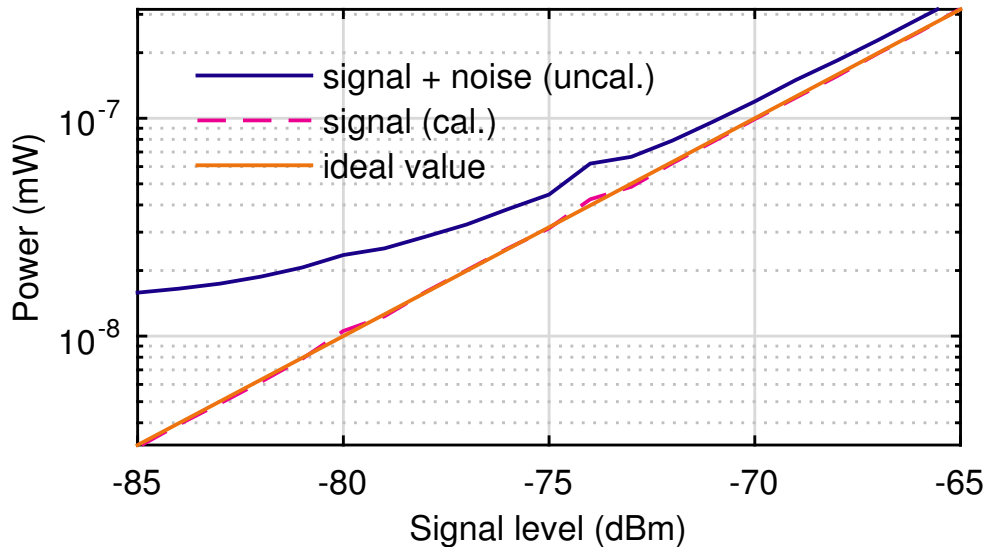


Figure 4.11: Measured level value converted to power: The uncalibrated and calibrated results are compared to ideal value

4.5 Examples of Diversity Performance in Test Drives

After describing the general noise aspects, the noise influence on the phase calculation and the purpose why a noise cancellation method leads to improvements in the phase calculation accuracy, examples of diversity performance in real-scenario test drives in the United States are introduced. First, the test drive scenario and the corresponding mute recording system setup are described. Afterwards, the recording and playback unit which was utilized during the measurement campaigns is introduced. It is also verified that the recorded signals, which are used in the laboratory for further investigations, possess the same behaviour as the ones in the field. Finally, test drive results showing significant improvement through the antenna diversity system are presented.

4.5.1 Test Drive Scenario

The field measurements and signal recordings for further laboratory investigations were conducted on a test track with real fading scenario conditions. The test track is an almost circular set of roads in hilly terrain underneath dense foliage of broad-leaf trees spread with a minor number of coniferous trees in the north-eastern USA. A map showing the track in addition to the photograph of a typical scene along the test track are illustrated in Fig. 4.12. Some track impressions are shown in Fig. 4.13. The diversity system as well as the recording/playback unit are installed in the car's trunk as be observed in Fig. 4.14. The overall length of the test track is approximately 2.15 km. For a single mea-

4 Noise Calibration Method for SDARS

surement result two drives around the track are considered. The measurement campaigns took place with a driving speed of 40 km/h. This results in a total time of about 390 – 400s per test drive, of which 380 s are actually taken into consideration for analysis in order to allow for the initial synchronization of the SDARS receiver in a newly started playback. Measurements were conducted in two directions (clockwise and counter-clockwise) throughout the circular track. An example of antennas mounted on the test vehicle are illustrated in Fig. 4.15.

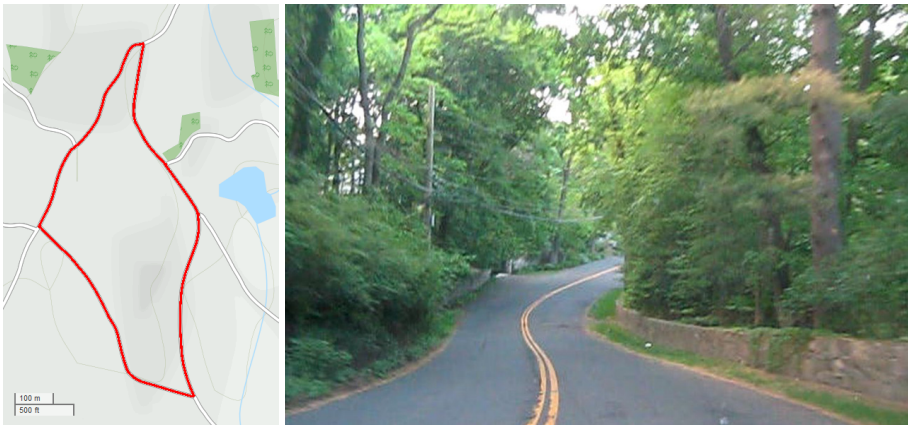


Figure 4.12: Left: Test track underneath dense foliage in the north-eastern USA (map background ©OpenStreetMap contributors). The total length of the track is approximately 2 km. Right: Photograph of a section of the test track.



Figure 4.13: Impressions from the dense-foliage track, where the field measurement campaigns were performed

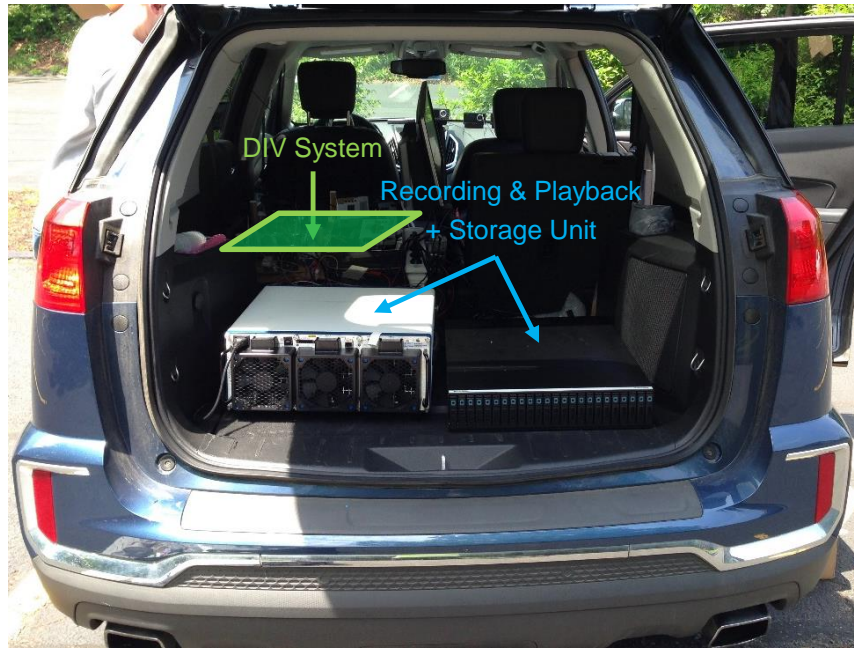


Figure 4.14: Installed equipment inside the test vehicle's trunk



Figure 4.15: Antenna mounting positions of the measured antenna sets on the front fender(s). Big photograph: Two dislocated off-the-shelf commercial patch antennas (red circles). Image inset: Diversity antenna set (green circle) with two output signals on a single mounting position

4.5.2 Signal Recorder / Playback Unit

The recording / playback equipment enables the simultaneous recording of up to four antenna signals in addition to playing back those recorded signals in order to perform repeated measurements of different hardware prototypes as well as diversity algorithms [67, 68]. The equipment is based on a commercial RF-signal record and playing platform including four Vector Signal Transceivers (VST) which can record up to 80 MHz of bandwidth in a frequency range up to 6 GHz [69].

With the purpose of reducing the SNR of the recording and playback equipment, Pre-amplifiers with a gain of 20 dB and a noise figure of 0.6 dB, which are specifically designed for SDARS applications, are utilized. Even though all available SiriusXM bands have a total bandwidth of 25 MHz, a bandwidth of 30 MHz has actually been recorded with a hybrid analogue down-conversion to an intermediate frequency of 20 MHz followed by a digital down-conversion to the baseband, all in the VSTs.

In order to better detect the received SDARS signals before recording them during the field measurements, a two-stage-amplification was included between the antenna and the recording unit according to the setup shown in Fig. 4.16. The received signal is amplified with 27 dB via a low-noise-amplifier, then attenuated by 6 dB before being amplified again by 27 dB. The input signal is then down-converted before being further digitally processed and stored for future playbacks at any time. During the measurement campaign, the RF-signal recorder is installed in the trunk of the car as already shown in Fig. 4.14.

In order to compensate the amplification of the second LNA in Fig. 4.16, an attenuator with 20 dB attenuation is added to the PXI playback unit output. Fig. 4.17 illustrates the utilized setup to playback the signals in the laboratory. Before being played back at the output of the playback unit, the stored signal undergoes frequency up-conversion. Then, it is possible to perform an audio mutes analysis with a diversity system and compare it with reference antennas in order to prove the significant improvements due to diversity. In Fig. 4.18 a photograph of an exemplary laboratory setup is shown including the RF recording/playback unit in addition to a diversity system hardware demonstrator used for SDARS audio mutes analysis.

4.5 Examples of Diversity Performance in Test Drives

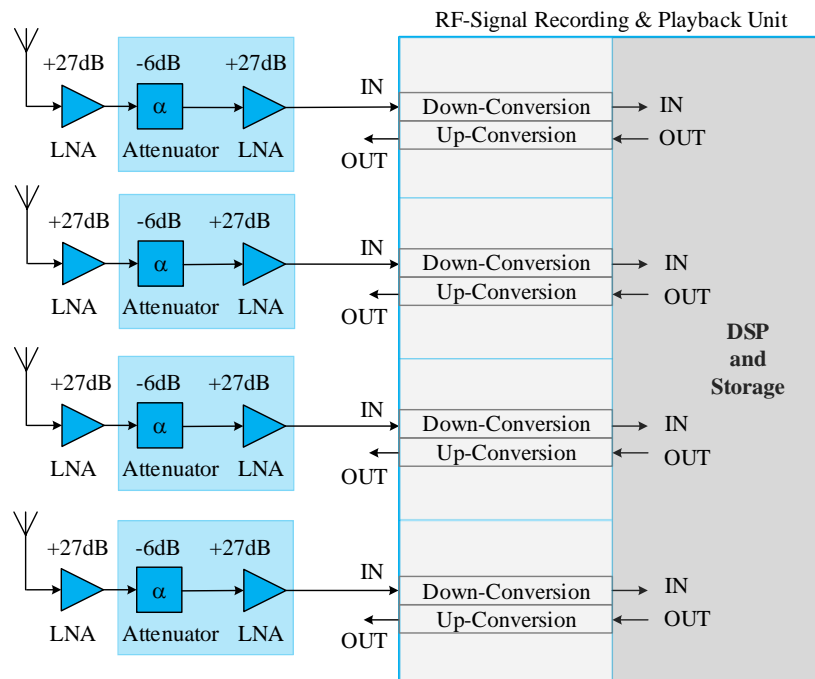


Figure 4.16: Setup to record SDARS signals during the measurement campaign

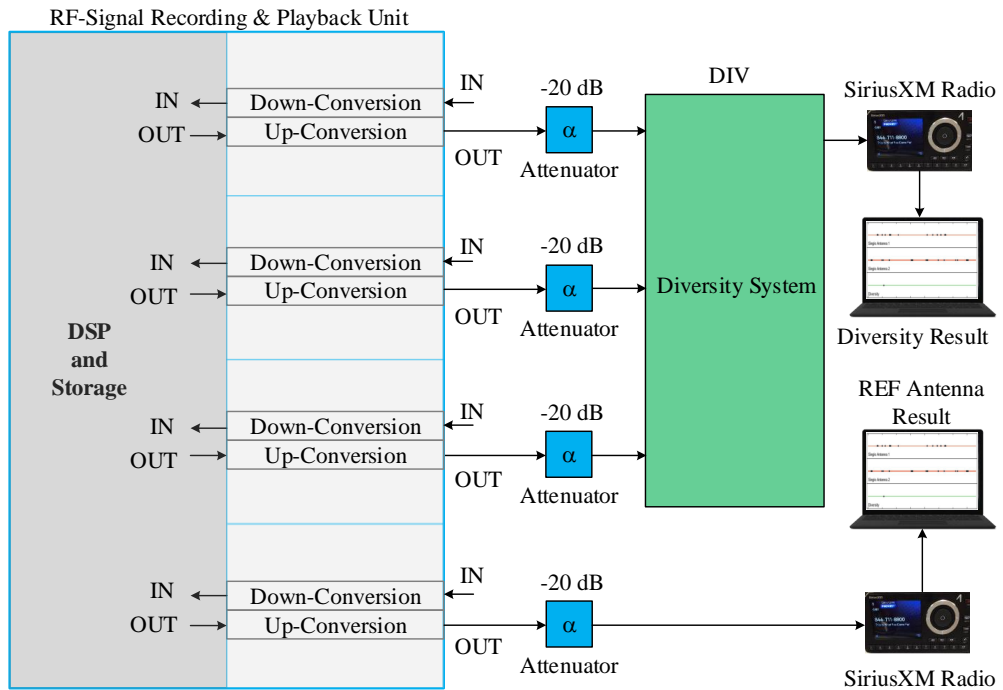


Figure 4.17: Setup to playback SDARS signals in the laboratory

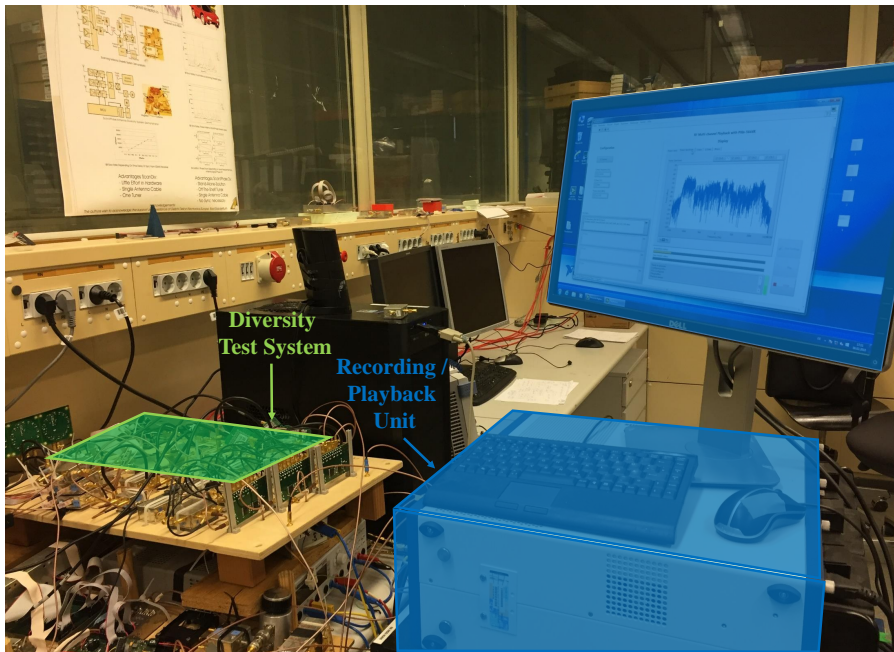


Figure 4.18: Setup for recording/playback of the laboratory measurement campaigns

Results Verification:

In order to verify that the measurements performed in the laboratory yield results equivalent to the ones obtained during the field measurement campaigns, investigations have been conducted to prove this aspect. Four field measurements from the USA are directly compared to their corresponding playback signals in the laboratory. It is worth mentioning that a test drive measurement with two laps has a total time of around 400s, of which approximately 380 s – 390 s are actually taken into consideration for analysis in order to allow for the initial synchronization of the SDARS receiver in a newly started playback in the laboratory.

Table 4.2 shows the comparison between a field measurement and corresponding laboratory playback signal of a single diversity loop antenna mounted on the vehicle's dashboard. For this case, the direction of the test drive is counter-clockwise and TDM2 is suppressed. The average value of two laboratory measurements is taken into consideration. For a total lab test duration of 390 s, the two laboratory measurements yield 88.30 s and 89.15 s respectively for the audio mutes duration, which results in an average value of 88.73 s. This value is comparable with the field-measured value of 88.35 s over 405 s.

4.5 Examples of Diversity Performance in Test Drives

Table 4.2: Comparison between a field measurement and corresponding laboratory playback signal of a single diversity loop antenna mounted on the dashboard with TDM2 suppressed. The direction of the test drive is counter-clockwise.

	Audio Mutes [s]	Total Test Duration [s]
Lab Signal (aver.)	88.73	390
Field Signal	88.35	405

Table 4.3 shows the comparison between a field measurement and corresponding laboratory playback signal of a single diversity loop antenna mounted on the vehicle's dashboard. For this case, the direction of the test drive is counter-clockwise and TDM1 is suppressed. The average value of two laboratory measurements is taken into consideration. For a total lab test duration of 380 s, the two laboratory measurements yield 301.65 s and 302.25 s respectively for the audio mutes duration, which results in an average value of 301.95 s. If we halve this value, it is comparable with the field-measured value of 150.15 s over 201 s.

Table 4.3: Comparison between a field measurement and corresponding laboratory playback signal of a single diversity loop antenna mounted on the dashboard with TDM1 suppressed. The direction of the test drive is counter-clockwise.

	Audio Mutes [s]	Total Test Duration [s]
Lab Signal (aver.)	301.95	380
Field Signal	150.15	201

Table 4.4 shows the comparison between a field measurement and corresponding laboratory playback signal of a single diversity loop antenna mounted on the vehicle's dashboard. For this case, the direction of the test drive is clockwise and TDM1 is suppressed. The average value of two laboratory measurements is taken into consideration. For a total lab test duration of 380 s, the two laboratory measurements yield 298.1 s and 298.65 s respectively for the audio mutes duration, which results in an average value of 298.38 s. If we halve this value, it is comparable with the field-measured value of 148.5 s over 201 s.

Table 4.4: Comparison between a field measurement and corresponding laboratory playback signal of a single diversity loop antenna mounted on the dashboard with TDM1 suppressed. The direction of the test drive is clockwise.

	Audio Mutes [s]	Total Test Duration [s]
Lab Signal (aver.)	298.38	380
Field Signal	148.5	201

Table 4.5 shows the comparison between a field measurement and corresponding laboratory playback signal of a single diversity loop antenna mounted on the vehicle’s dashboard. For this case, the direction of the test drive is clockwise and no band is suppressed. One laboratory measurement is taken into consideration. For a total lab test duration of 390 s, the laboratory measurement yields 22.90 s for the audio mutes duration. If we halve this value, it is comparable with the field-measured value of 11.15 s over 203 s.

Table 4.5: Comparison between a field measurement and corresponding laboratory playback signal of a single diversity loop antenna mounted on the dashboard without any band suppressed. The direction of the test drive is clockwise.

	Audio Mutes [s]	Total Test Duration [s]
Lab Signal	22.90	390
Field Signal	11.15	203

Table 4.6 shows the comparison between a field measurement and corresponding laboratory playback signal of a reference patch antenna mounted on the vehicle’s front right fender. For this case, the direction of the test drive is clockwise and TDM2 is suppressed. The average value of two laboratory measurements is taken into consideration. For a total lab test duration of 380 s, the two laboratory measurements yield 69.75 s and 72.4 s respectively for the audio mutes duration, which results in an average value of 71.07 s. If we halve this value, it is comparable with the field-measured value of 35.2 s over 199 s.

Table 4.6: Comparison between a field measurement and corresponding laboratory playback signal of a reference patch antenna mounted on the vehicle’s front right fender with TDM2 suppressed. The direction of the test drive is clockwise.

	Audio Mutes [s]	Total Test Duration [s]
Lab Signal (aver.)	71.07	380
Field Signal	35.2	199

4.5.3 Results

For various mounting positions and SDARS reception antennas RF signals have been recorded and measured. Two commercial SDARS patch antennas mounted in a dislocated way on both front fenders in addition to a micro-diversity set in a single mounting volume are analysed. A picture illustrating the antenna positioning is depicted in Fig. 4.15. One can notice that both antennas are tilted away from the driving direction of the vehicle. This results in impairments not only on antenna pattern roundness but also on gain and/or received SNR which are unavoidable when unconventional antenna mounting positions are utilized because of the available antenna mounting volume, the shape and size of the available ground plane as well as shadowing caused by the car body itself in any mounting position other than on the rooftop [66].

The statistical properties of the reception scenario are shown through an analysis of the recorded signals of the patch antennas. A plot of the patch antenna signal levels over time of the received signal transmitted by a geostationary satellite is illustrated in Fig. 4.19. It can be observed that two laps of driving along the exact same test drive track have been recorded. In both recording halves, slow fading effects can be noticed. These effects result from obstructions along the track due to the high foliage trees and hilly terrain. If the depicted level plots are inspected closer further differences can be observed. Multipath propagation is responsible for the fast fading behaviour in the dense foliage environment. This contributes to high relative frequencies of low signal levels as the probability density plot of the recorded antenna signal amplitudes shows in Fig. 4.20 [66].

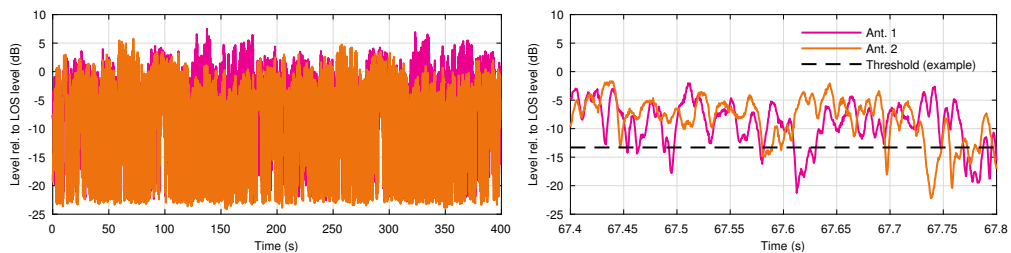


Figure 4.19: Left: Single antenna signal levels of the SDARS received signals from the geostationary satellite relative to the mean LOS signal level along two rounds on the test track. Right: Detailed view of the single antenna signal levels and exemplary threshold for the analysis of the ratio of signal levels below the respective threshold

The statistical behaviour of a simulated scan-phase diversity system is inspected taking into consideration a range of additional noise influences on measured levels which are used in the phase calculation. Fig. 4.20 shows the analysis of the diversity system's output signal amplitude. Simulations of an ideal system, where the noise power $PN = 0$, have been performed. These simulations were

compared to results from simulations including noise influences in the range of $-20\text{ dB} \leq PN/P_{\text{LOS}} \leq +30\text{ dB}$ in order to take into consideration different levels of external and internal (relative to the diversity circuit) noise contributions. The diversity system's phase shifters were considered with a step size 45° in all simulations. It can be noticed that the simulated scan-phase antenna diversity system with low noise powers PN – which is equivalent to systems that apply the noise cancellation method – indicate enhancements of the signal amplitude statistics in two distinct aspects [66].

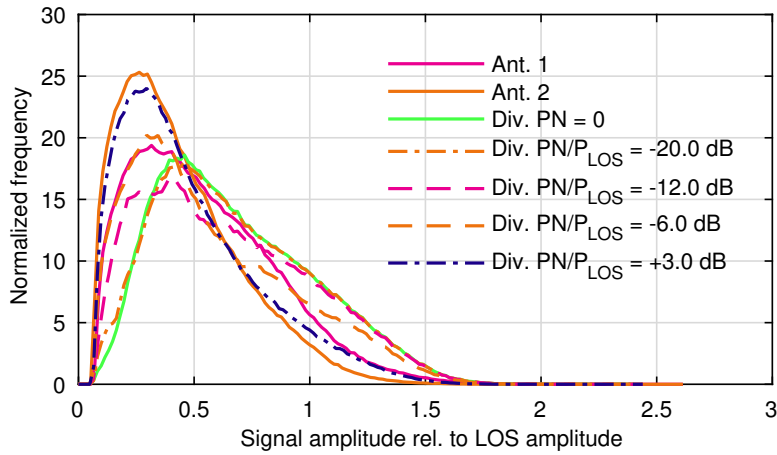


Figure 4.20: Normalized histogram of the signal amplitudes of the GEO satellite's signal received by two single antennas in a fading scenario in addition to a simulated scan-phase antenna diversity system with noise power PN in the level detection path

First of all an improvement in the average signal amplitude is observed in comparison to those of the two single antenna input signals. Secondly signals with very low amplitudes occur less often due to the fact that the antenna diversity system avoids signals with very low signal amplitudes by switching them off completely. This results in the improvement of the output signal SNR since the noise influence by this antenna cannot enter the signal path to the receiver. In the case of higher noise powers PN the results of the phase calculation differ from the true noiseless value. This value leads to a suboptimal phase alignment of the antenna signals. The histogram shows similarities between the ideal case $PN = 0$ and the case where $PN/P_{\text{LOS}} = -20\text{ dB}$ [66]. Deviations from the ideal results are observed for the ratio $PN/P_{\text{LOS}} = -12\text{ dB}$.

The probabilities of recorded single antennas' levels which lie below a threshold value have been inspected. The level plot on the right hand-side of Fig. 4.19 depicts an example of such threshold analysis. By considering the GEO satellite, the probabilities have been determined for a single frequency. Regarding the respective probabilities for both frequencies of the SDARS system, an estimation is performed based on the fact that the signal levels of both frequencies

are fading independently but with the same probability. Hence the squared probability values of the single frequency results correspond to the estimated two-frequency fading probability and are illustrated in Fig. 4.21 [66].

The results of an investigated scan-phase antenna diversity system simulation are shown in Fig. 4.21. As an example, if a threshold of -13.2 dB below the average LOS level would correspond the distinction between an available signal and an audio mute then both single reception antennas would show probabilities to fall below this threshold of approximately 1.56% and 3.85% respectively. Lower probabilities depending on the noise power PN are achieved if the scan-phase antenna diversity system is applied on these two antenna signals. A probability value of around 0.86% is determined for $PN/P_{LOS} = -12$ dB [66].

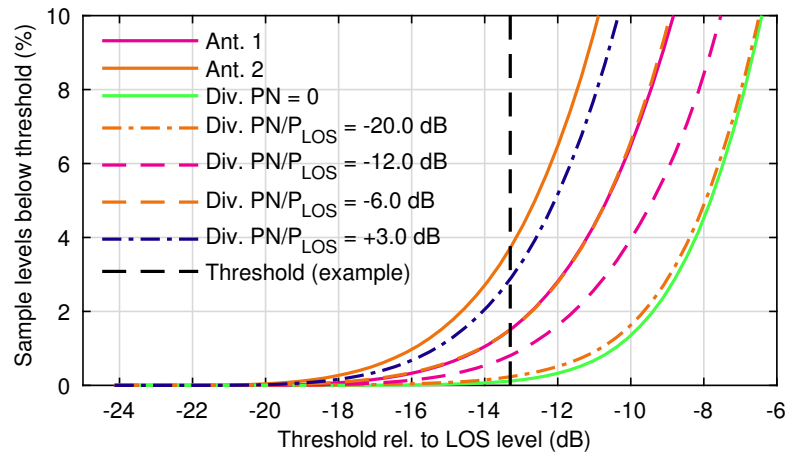


Figure 4.21: Estimated fading probability (level falls below the respective threshold) of a two-frequency satellite signal of two single antennas in addition to a simulated scan-phase antenna diversity system with noise power PN in the level detection path

A mute ratio of 0.11% based on the signal levels is achieved by an ideal diversity system with $PN = 0$. This clearly confirms the advantage of applying the noise cancellation method. Measurements of the audio availability improvements achieved by the diversity system can be conducted in the laboratory by means of the RF signal recording and playback equipment introduced in section 4.5.2. The audio availability of not only both single antennas but also of the scan-phase antenna diversity system has been measured utilizing these recorded RF signals. The audio availability of distinct diversity algorithms can be repeatedly measured taking into consideration real RF satellite signals from fading scenarios without the ambiguity of repeated test drives even on the same track. Such ambiguity might arise due to the exact driving track on the road, weather conditions etc...

The diversity measurements are performed using all available satellite signals and unmodified receivers. They investigate the audio availability with and without the calibration of noise influences on the level detection accuracy. Table 4.7 lists the average results of five individual measurements (each with a duration of 380 s) for the test scenario with dislocated patch antennas on the vehicle fenders as shown in the main photo of Fig. 4.15 [66]. The black dots in Fig. 4.22 represent the occurrence of audio mutes for the two single antennas and both diversity configurations. The shown recordings represent individual measurements which have been chosen to closely match the average mute durations in Table 4.7. The results show that the diversity system contribute to a significant reduction of the audio mutes by a factor of approximately 4 from an average of 12.2 s of the single antennas to 3.34 s. Measurements from more complex system demonstrators yield higher improvement factors of around one order in magnitude. This is achieved with more gain and lower noise figures of the level detection circuit due to the non-linearities at low signal levels. Applying the noise cancellation method on the level detection further enhances these results by reducing the mute time to 0.29 s which is by a factor of around 40 lower than the single antenna thus rendering a more complex hardware unnecessary.

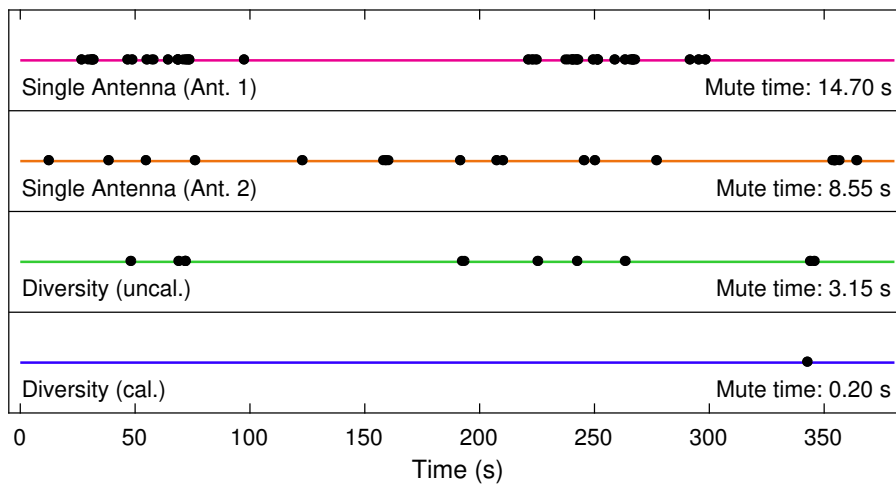


Figure 4.22: Measured audio mutes of respective individual measurements of the single dislocated off-the-shelf patch antennas (refer to main photo of Fig. 4.15) and scan-phase diversity demonstrator from Fig. 4.5 with and without calibration. All available satellite signals have been used by the receiver.

In addition to the dislocated antenna mounting positions previously described in the main photo of Fig. 4.15, a micro-diversity antenna set with two SDARS antennas in a single mounting volume on the left front fender was also inspected as can be seen in Fig. 4.23. Fig. 4.24 illustrates the realized gain over the elevation angle Θ averaged over all azimuth angles Φ . These antennas were mounted on a circular ground plane with bent edges with an overall diameter of 1.2 m and

4.5 Examples of Diversity Performance in Test Drives

Table 4.7: Comparison of average audio mute durations (each over five measurements of the respective setup) from all available satellite signals in a real fading scenario recorded on test drives in the USA: Conventional single antenna reception system and the compact diversity system on a single printed circuit board

	Audio Mutes [s]	Test Duration [s]	Availability [%]
Antenna 1	15.0	380	96.05
Antenna 2	9.32	380	97.55
Diversity (uncal.)	3.34	380	99.12
Diversity (cal.)	0.29	380	99.92

measured in an anechoic chamber. Ant. 1 yields a realized gain which perfectly meets the specifications of the SDARS service providers in such a mounting position. Ant. 2 has its highest realized gain at an elevation angle Θ of 50° from zenith where geostationary satellites are located relative to the receiving antennas. For this reason, Ant. 2 is considered a perfect complement for Ant. 1 in a diversity antenna set [66]. Mounting the antenna set at the exact hidden mounting position of an antenna in series production is impossible since the test vehicle was not allowed to be modified itself. As can be observed in Fig. 4.23, the antenna set was instead mounted on the outside of the vehicle's chassis on a flat small rectangular ground plane with a side length of 16 cm and a slant angle of approximately 20° .



Figure 4.23: Micro-diversity antenna set (green circle) with two output signals on a single mounting position

Antenna characteristics vary dramatically in critical mounting situations where even higher tilt angles, smaller ground planes and hidden mounting positions are chosen. Moreover, the average gain at the elevation angle of the satellite position may decrease by several dB. Even a curved rooftop, where a large metallic ground plane is present, can change the pattern of SDARS antennas at that position as shown in [70].

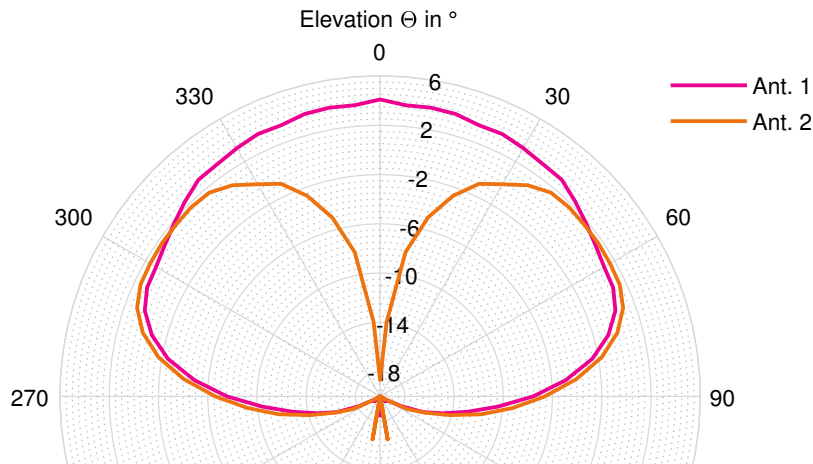


Figure 4.24: Measured average realized gain of the two single antennas of the diversity antenna set on one mounting position (averaged over all azimuth angles Φ). The measurements were conducted in an anechoic chamber, the antenna was mounted on a circular ground plane of 1.2 m diameter.

No plastic car-body cover was utilized here. Moreover, the ground plane was larger, and the angle was not steep enough. In order to take this aspect into consideration, the SNR at the input of the diversity circuit is in a further measurement reduced in a way which is equivalent to a slight decrease in antenna gain by 0.6 dB.

This is accomplished by inserting an attenuator, an amplifier and a further attenuator at each of the two input ports of the antenna diversity circuit. These components contribute to no additional gain with deviations of less than 0.3 dB, but a decrease in SNR which corresponds to a decrease of 0.6 dB at the air interface. Fig. 4.25 depicts the measured audio mutes for the single antennas as well as for diversity with and without noise cancellation.

In an impaired playback configuration, the average mute time of the single antennas of the diversity set is 3.2 s. Without applying the noise cancellation method, the antenna diversity system reduces this an average mute time of 0.88 s, which is by a factor of 3.6 lower than the single antennas' average result. After applying the introduced noise cancellation method, the mute time is further reduced to an average of only 0.38 s, which is a factor of 8.4 lower than the single antenna system [66]. The occurring mutes during a single measurement of the respective single antennas, which closely match the average values, are shown in Fig. 4.25 (top two measurements with signals unimpaired by a reduced SNR).

With SNR reduction, the diversity set's single antennas yield an average mute duration of 12 s using all available satellite signals. A comparison to the availability of the dislocated commercial antennas (refer to Table 4.7) in a similar

4.5 Examples of Diversity Performance in Test Drives

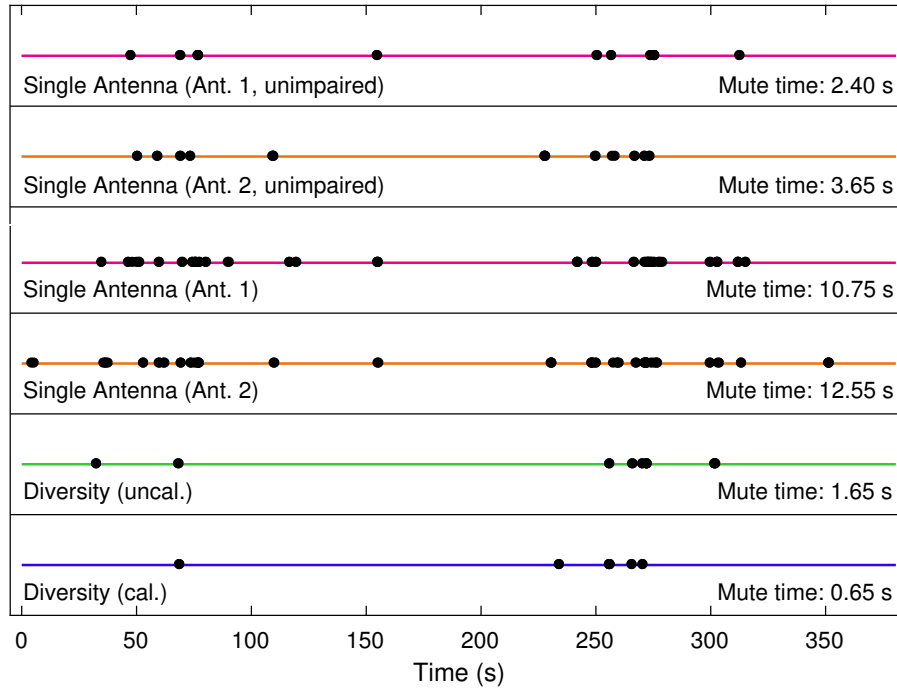


Figure 4.25: Measured audio mutes of respective individual measurements of the microdiversity antenna set's single antennas at one mounting point (refer to Fig. 4.23) and scan-phase diversity demonstrator from Fig. 4.5 with and without calibration. All available satellite signals have been used by the receiver. The top two measurements show the original recorded data without SNR reduction. The lower four measurements are taken with reduced SNR in order to model antenna impairments of a hidden mounting position with a small ground plane and slant angle.

mounting position (vehicle's fender) shows matching values, which validates the impairment. An overall average mute duration of 1.71 s is achieved by the diversity system. This is an improvement by a factor of 7. The application of the noise cancellation method further reduces the average mute time to only 0.76 s which is by a factor of 15.8 better than the average of both single antennas [66]. Fig. 4.25 depicts the occurrence of audio mutes from individual tests, which represent the average results as closely as possible. If we compare the unimpaired single antenna results with the availability of the diversity signal even after reducing the SNR of the input signals, we can clearly observe that the diversity system more than compensates for the SNR reduction.

This diversity efficiency parameter [71] can also be utilized to compare different measurement set-ups and diversity methods according to:

$$\eta = \frac{\log_{10}(t_{\text{mutes}}/t_{\text{total}})_{\text{DIV}}}{\log_{10}(t_{\text{mutes}}/t_{\text{total}})_{\text{REF}}}. \quad (4.29)$$

The denominator contains the values of the best reference antenna and the numerator the values of the diversity system. The total duration t_{total} of the performed measurement is the same for both quotients.

In the following, additional measurements directly performed in the field (not in the laboratory) using the exact same diversity hardware demonstrator as above are presented. A different antenna position namely the dashboard is taken into consideration. Even though this position is considered unconventional, the diversity system demonstrated a significant improvement in comparison to single antennas at this position even without applying the noise cancellation method. The improvement achieved through diversity is almost comparable to mounting the antennas on the roof of the vehicle.

Micro-Diversity Measurement (Sirius):

A micro-diversity antenna set made up of two loop antennas has been mounted on the dashboard the test vehicle as shown in Fig. 4.26. Standard after-market receivers for SiriusXM Satellite Radio have been used for the measurements. The diversity algorithm has been optimized for the Sirius TDM1 band.



Figure 4.26: A micro-diversity antenna system mounted on the dashboard

Measurements of the audio signal availability were taken for the two antennas of the micro-diversity set as individual single antennas and of the antenna diversity system. As the results given in Table 4.8 show, the mutes duration dropped from 14.70s to 1.60s showing an improvement in the audio availability from 92.65% up to 99.20%. This corresponds to a diversity efficiency of 1.85 when taking the average of the single antennas as reference (92.65% availability) into consideration.

Table 4.8: Average total audio mute duration of the single antennas as well as of the diversity system using the same input signals in a fading scenario.

	Audio Mutes [s]	Duration [s]	Avail. [%]	Mute Rate [%]
Single Ant.	14.70	200	92.65	7.35
DIV	1.60	200	99.20	0.80

Micro-Diversity Measurement (XM-SAT1A):

A micro-diversity antenna set made up of two loop antennas has been mounted on the dashboard the test vehicle as shown in Fig. 4.27. Standard after-market receivers for SiriusXM Satellite Radio have been used for the measurements. The diversity algorithm has been optimized for the XM-SAT1A band.



Figure 4.27: A micro-diversity antenna system mounted on the dashboard

Measurements of the audio signal availability were taken for the two antennas of the micro-diversity set as individual single antennas and of the antenna diversity system. As the results given in Table 4.9 show, the mutes duration dropped from 11.70s to 2.10s showing an improvement in the audio availability from 94.15% up to 98.95%. This corresponds to a diversity efficiency of 1.60 when taking the average of the single antennas as reference (94.15% availability) into consideration.

Table 4.9: Average total audio mute duration of the single antennas as well as of the diversity system using the same input signals in a fading scenario.

	Audio Mutes [s]	Duration [s]	Avail. [%]	Mute Rate [%]
Single Ant.	11.70	200	94.15	5.85
DIV	2.10	200	98.95	1.05

5 Multi-Channel Algorithm for Antenna Diversity

After presenting the investigations and optimizations of the noise cancellation method for application in SDARS antenna diversity in chapter 4, a new multi-channel algorithm for SDARS with scan-phase-antenna diversity is introduced in this chapter.

Considering the simultaneous reception through four different satellite frequency bands, the algorithm steers phase shifters as well as switches of a diversity circuit in order to combine distinct antenna signals for a minimized overall bit error probability. By means of a simple level detection, not only the in-phase but also the quadrature components are derived for all frequency bands and an overall bit error probability is estimated, which is minimized through the switching and phase constellation of the diversity circuit. In order to verify the validation of the algorithm, antenna signals of a micro-diversity antenna set are received in real scenario test drives underneath dense foliage which are fed into a scan phase diversity circuit. The antenna diversity measurements with the multi-channel algorithm show a significant improvement of the reception quality in comparison to single antennas even in unconventional antenna mounting positions.

Two satellites in geostationary orbit (GEO) are operated in order to guarantee the coverage of SDARS signals within the SiriusXM high band ranging between 2.3325 GHz and 2.3450 GHz [9]. Each GEO satellite transmits QPSK-modulated RF signals within two ensembles *A* and *B*. Each ensemble carries half the total system capacity. In order to mitigate the effects of multipath propagation in NLOS locations and to make use of hidden and unconventional antenna positions in the vehicle, antenna diversity has shown its numerous advantages in various scenarios for satellite reception at the SiriusXM low band at 2.320-2.3325 GHz [72],[1],[62]. Furthermore, the SDARS service provide may utilize the gain in the SNR via diversity to expand the coverage area and to offer further content for the subscribers.

Fig. 5.1 illustrates not only a block diagram of the micro-diversity antenna system but also the photographs of a possible implementation of the hardware. The hardware consists of an antenna diversity integrated circuit [73] as well as a level detector and a micro-controller unit (MCU). The antenna diversity circuit is capable of combining and phase aligning up to three antenna signals, which

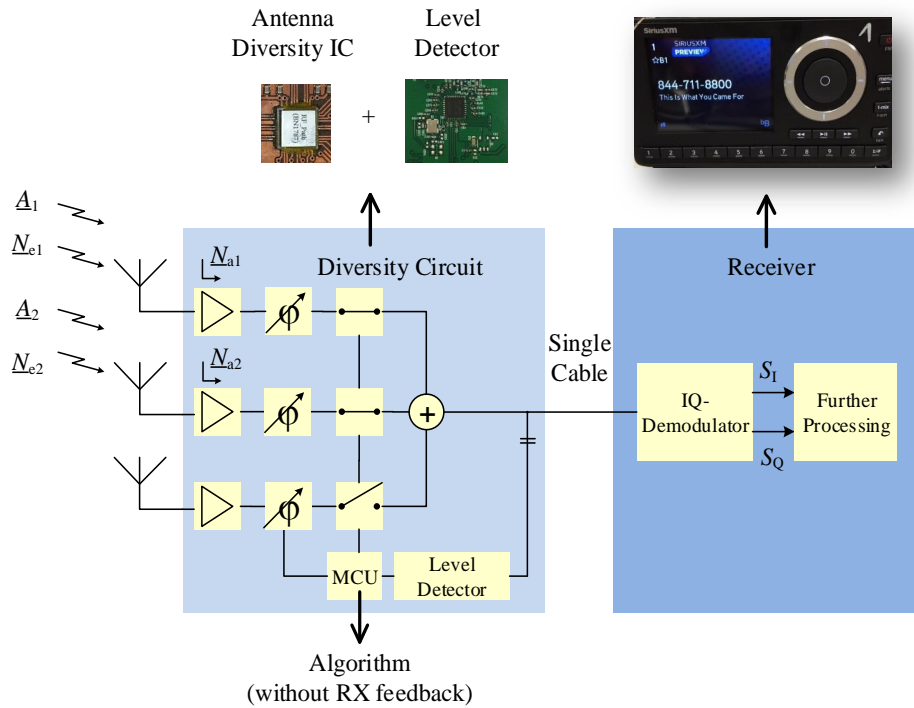


Figure 5.1: Diversity system block diagram (two out of three antenna paths are shown) as well as a possible hardware implementation (consisting of an antenna diversity IC in addition to a level detector and a microcontroller unit).

are pre-amplified by a low-noise amplifier stage (LNA). Their phases are calculated in different test cases through a simple level detector and MCU for digital signal processing as presented in [65]. Only one cable connects the output of the diversity circuit to the SDARS receiver which demodulates the received QPSK signals.

In this chapter, an algorithm is introduced for steering the phase shifters and switches, which optimizes phases and switching states of the different antenna paths in order to minimize the bit error probability with respect to all four satellite frequency bands. The multi-channel algorithm supports the frequency bands of different satellites according to their SNR. Moreover, it estimates the overall bit error probability over the two ensembles A and B in order to find the optimum state of phase shift and switching.

5.1 Concept Description

The multi-channel algorithm determines which antenna phase combination contributes to the minimum estimated bit error probability over both ensembles of the most suitable satellite according to the flowchart depicted in Fig. 5.2 [74].

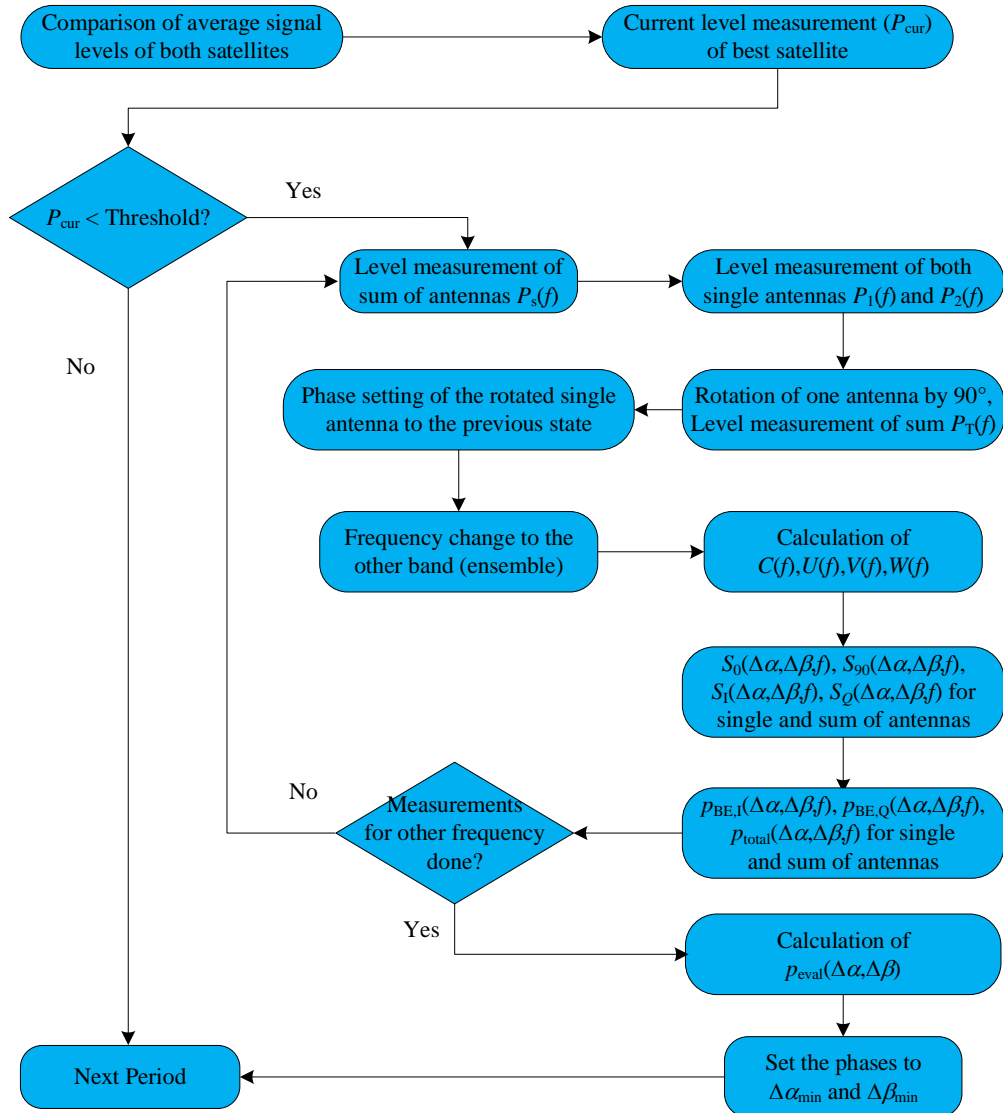


Figure 5.2: A flowchart of the multi-channel algorithm for vehicular antenna diversity of SiriusXM satellite reception.

The average signal levels of both satellites in LOS conditions are compared to predict which of the SiriusXM high band satellites has to be supported. This permits the detection of the user's geographic location, so that the algorithm

5 Multi-Channel Algorithm for Antenna Diversity

can then accordingly optimize the ensemble of the satellite with the best SNR. Afterwards, the current signal level (P_{cur}) of the most suitable satellite is measured and compared to a threshold which is pre-defined. A timeline illustrating two complete diversity periods (marked in dark blue) taking into consideration both frequencies f_A and f_B is depicted in Fig. 5.3.

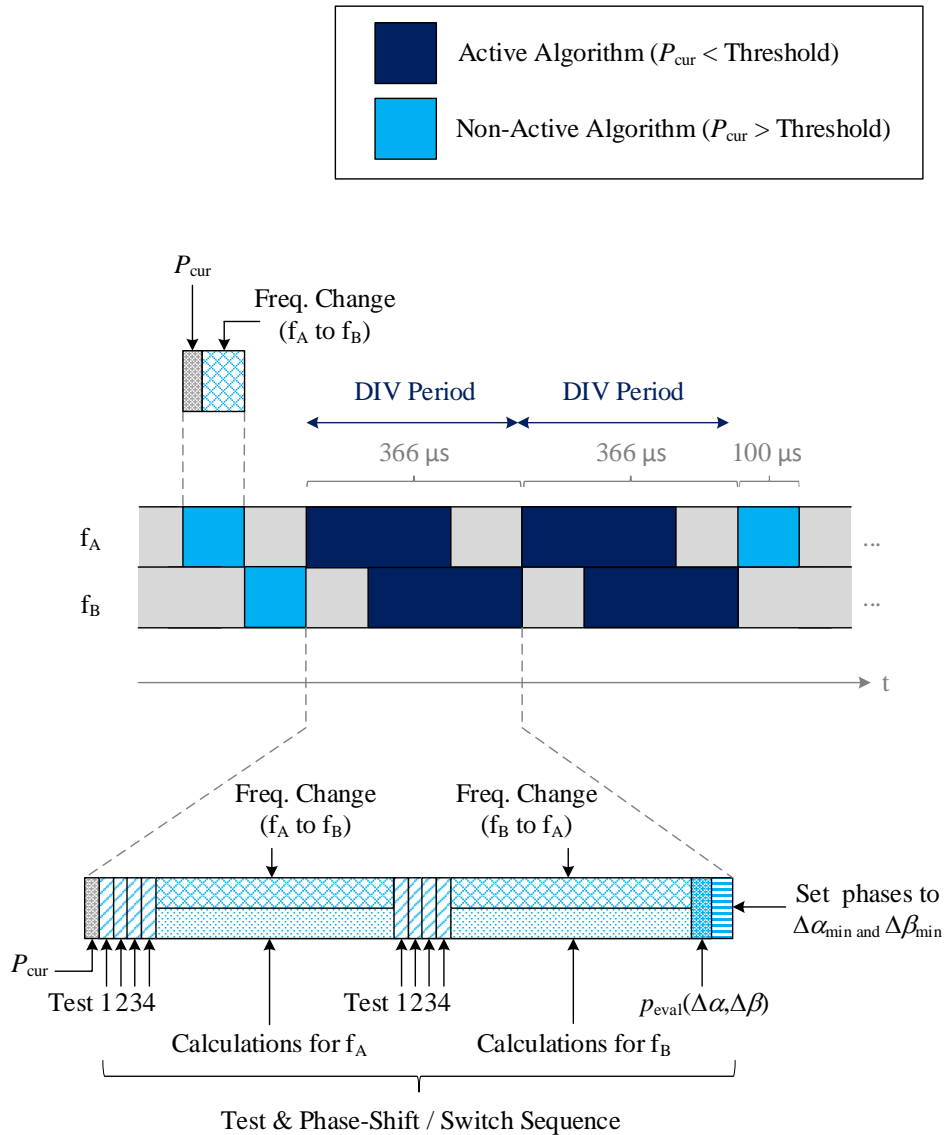


Figure 5.3: The timeline showing two complete diversity periods ($P_{\text{cur}} < \text{Threshold}$) taking into consideration both frequencies.

If the signal level P_{cur} exceeds the threshold, there is no need for any phase alignment or switching of the antennas. In other words, the multi-channel algorithm is not activated in this particular case. Otherwise, the multi-channel algorithm is activated, and a series of four test constellations takes place. The aim of the test constellations is to measure the power levels of the preferred satellite at the center frequencies f_A and f_B of the ensembles A and B.

In the timeline illustrated in Fig. 5.3, each light blue block which represents the case where the multi-channel algorithm is not activated, since the signal level exceeds the threshold, has a duration of $100\mu\text{s}$. After measuring the signal level and verifying the comparison to the threshold, the frequency change takes place. Around $60\mu\text{s}$ are needed till the local oscillator and active mixer are set correctly so that the frequency is modified.

Once the current signal level value P_{cur} becomes smaller than the pre-defined threshold, the multi-channel algorithm is triggered to begin with its calculations. The dark blue blocks in Fig. 5.3 illustrate the activated multi-channel algorithm. The algorithm starts by performing the four test constellations for the first frequency through measured signal levels according to [66]. After finishing the last test case, the frequency change is activated. Meanwhile, further algorithm calculations for the first frequency f_A are performed in parallel. By the time the calculations for frequency f_A are finished, the local oscillator and mixer are already set for the second frequency f_B . For this frequency, the four test constellations are performed as well. Then, the frequency change is re-triggered to ensure the frequency modification from f_B to f_A for the next period. Afterwards, the evaluation of the bit error rates is conducted. The optimization is based on choosing the phase combination leading to the minimum estimated average bit error probability over both ensembles. According to the calculated optimal phase combination, the micro-controller unit sets the phase shifters with the corresponding phases. The whole diversity period, including measures to accelerate the algorithm calculations, has a duration of approximately $366\mu\text{s}$. A more detailed investigation of the duration of the different algorithm parts will be presented in the section 5.3.

In order to get a clearer understanding of the multi-channel algorithm, an additional illustrative scenario is depicted in Fig. 5.4. It shows that the multi-channel algorithm could be triggered by starting from either f_A or f_B . The scenario begins with four consecutive cases (light blue blocks) where the algorithm is still not yet triggered since the signal level exceeds the threshold. Each block has duration of $100\mu\text{s}$, out of which approximately $60\mu\text{s}$ are reserved for the frequency change. The rest of the time ($40\mu\text{s}$) is utilized for signal level measurement.

5 Multi-Channel Algorithm for Antenna Diversity

Afterwards, the multi-channel algorithm is activated as the current signal level value P_{cur} drops below the pre-defined threshold. The first diversity period is triggered at the frequency f_A . At this frequency, the algorithm starts by performing the four test constellations through measured signal levels. After finishing the fourth test case, the frequency change is activated. In the meantime, further algorithm calculations for f_A are performed simultaneously.

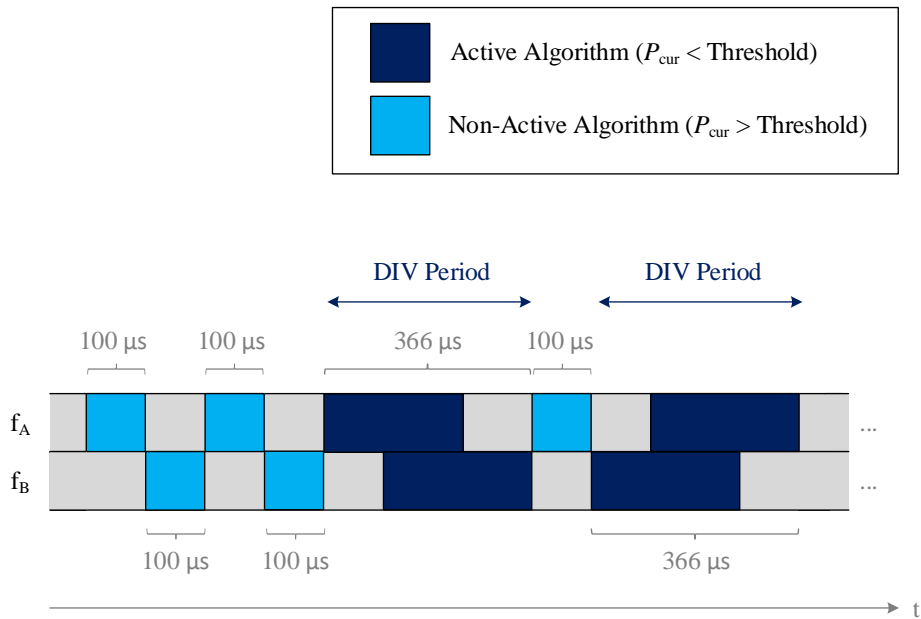


Figure 5.4: An illustrative scenario showing the timeline of the algorithm taking into consideration both frequencies

By the time the calculations for frequency f_A are accomplished, the local oscillator and mixer are already set for the second frequency f_B . The four test constellations are also performed for f_B as well. Afterwards, the frequency change is activated again to guarantee having the frequency f_A set for the next period. Then, the bit error evaluation and phase shifting based on the optimal phase combination takes place. The whole diversity period, including measures to accelerate the algorithm calculations, has a duration of approximately 366 μs .

The next period at the frequency f_A takes only 100 μs because the threshold is exceeded by the current signal level measurement. After that, the algorithm is triggered at frequency f_B and undergoes the same steps as the last diversity period with multi-channel algorithm. After presenting the timeline with the algorithm, a description of the algorithm parts upon its activation is introduced.

The powers $P_1(f)$ and $P_2(f)$, which are considered proportional to the squared absolute value of the complex wave amplitudes $A_1(f)$ and $A_2(f)$ respectively, in addition to the the power $P_s(f)$ of the sum $S(f)$ of these amplitudes are measured [66, 74]. Then, the antenna signal $A_1(f)$ is rotated by 90° in phase and added to the other antenna signal $A_2(f)$. Afterwards, the corresponding sum power $P_T(f)$ is measured. Fig. 5.5 depicts a corresponding arbitrary constellation of complex signals. The noise correction method presented in chapter 4.2 can also be applied in the measurements.

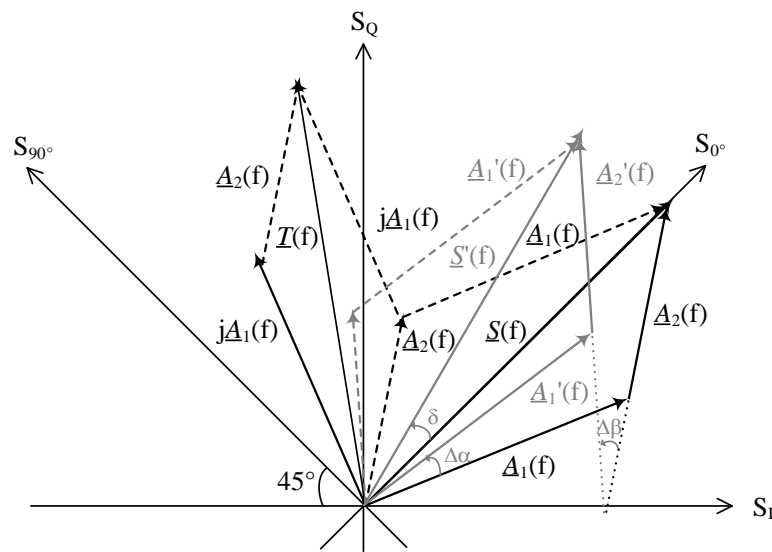


Figure 5.5: The complex signal diagram with the I-components and Q-components of the complex signal amplitudes.

In the following, the derivations are shown, which lead from the measured power values of the four test constellations towards a calculation of the SNR in all the different frequency channels in dependence to the possible phase shift constellations of the diversity circuit. From that a bit error estimation of the bit error rates is performed for low band and high band for its minimization to find the best phase constellation. All derivations are according to [64].

The signal components relative to a reference phase are calculated from the measured power values. The reference phase is transmitted regularly and is assumed to be synchronized to the SDARS receiver. The axis S_{0° in Fig. 5.5 is defined to point towards the direction of this phase. S_{90° is orthogonal to S_{0° . The variables $S_0(\Delta\alpha, \Delta\beta, f)$ and $S_{90}(\Delta\alpha, \Delta\beta, f)$, which represent the projections of the complex signal amplitudes on the S_{0° and S_{90° axes respectively, are calculated

as follows:

$$S_0(\Delta\alpha, \Delta\beta, f) = U(f)\cos(\Delta\alpha) + V(f)\cos(\Delta\beta) + W(f)(\sin(\Delta\alpha) - \sin(\Delta\beta)) \quad (5.1)$$

$$S_{90}(\Delta\alpha, \Delta\beta, f) = U(f)\sin(\Delta\alpha) + V(f)\sin(\Delta\beta) + W(f)(\cos(\Delta\beta) - \cos(\Delta\alpha)) \quad (5.2)$$

where $\Delta\alpha$ and $\Delta\beta$ represent the counterclockwise phase rotation of $A_1(f)$ to $A'_1(f)$ and $A_2(f)$ to $A'_2(f)$ respectively as depicted in Fig. 5.5. The introduced phases range from 0° to 315° in 45° -steps. This corresponds to the resolution of the variable phase shifters. The frequency dependent variables $C(f)$, $U(f)$, $V(f)$ and $W(f)$ are derived from the calculated powers according to the following equations:

$$C(f) = \frac{1}{S(f)} = \frac{1}{2\sqrt{P_s(f)}} \quad (5.3)$$

$$U(f) = C(f) \cdot (P_s(f) + P_1(f) - P_2(f)) \quad (5.4)$$

$$V(f) = C(f) \cdot (P_s(f) + P_2(f) - P_1(f)) \quad (5.5)$$

$$W(f) = C(f) \cdot (P_T(f) - P_1(f) - P_2(f)). \quad (5.6)$$

The angle of rotation δ from $S(f)$ to $S'(f)$ should ideally range between S_{-45° and S_{+45° in order to avoid the generation of bit errors in the QPSK modulated signal. If the level of one antenna is at least 6 dB lower than the other one, we obtain similar equations accordingly.

A coordinate rotation from the S_0 - S_{90} -reference frame to an orthogonal coordinate system ($S_I S_Q$) is applied. The aim of the coordinate rotation is to obtain the in-phase and quadrature components after IQ-demodulation. The mathematical projections $S_I(\Delta\alpha, \Delta\beta, f)$ and $S_Q(\Delta\alpha, \Delta\beta, f)$ of the rotated complex signals on the S_I and S_Q axes respectively are described by the following equations

$$S_I(\Delta\alpha, \Delta\beta, f) = (S_0(\Delta\alpha, \Delta\beta, f) - S_{90}(\Delta\alpha, \Delta\beta, f))/\sqrt{2} \quad (5.7)$$

$$S_Q(\Delta\alpha, \Delta\beta, f) = (S_0(\Delta\alpha, \Delta\beta, f) + S_{90}(\Delta\alpha, \Delta\beta, f))/\sqrt{2}. \quad (5.8)$$

Now the SNR of the I- and Q-channels are calculated accordingly. It is assumed that the external noises N_{e1} and N_{e2} , as depicted in Fig. 5.1, are statistically similar for both antennas 1 and 2 respectively. The same applies for the inserted noises N_{a1} and N_{a2} of the antenna amplifiers. Therefore, an average noise power P_N in each of the antenna paths is obtained.

By using the Q-function [75], the parameters $p_{\text{BE,I}}(\Delta\alpha, \Delta\beta, f)$ and $p_{\text{BE,Q}}(\Delta\alpha, \Delta\beta, f)$ can now be derived from the SNR values to evaluate the bit errors in the I- and the Q-channel respectively according to

$$p_{\text{BE,I}}(\Delta\alpha, \Delta\beta, f) = Q(S_I(\Delta\alpha, \Delta\beta, f)/\sigma_N^2) \quad (5.9)$$

$$p_{\text{BE,Q}}(\Delta\alpha, \Delta\beta, f) = Q(S_Q(\Delta\alpha, \Delta\beta, f)/\sigma_N^2) \quad (5.10)$$

where $\sigma_N = \sqrt{2P_N}$. Regarding the probability of a bit error in the I- or Q-channel, we obtain the total value of

$$p_{\text{total}}(\Delta\alpha, \Delta\beta, f) = \frac{1}{2}(p_{\text{BE,I}}(\Delta\alpha, \Delta\beta, f) + p_{\text{BE,Q}}(\Delta\alpha, \Delta\beta, f)). \quad (5.11)$$

A plot of p_{total} as a function of the parameters S_I and S_Q is shown in Fig. 5.6 and Fig. 5.7 as 2D and 3D respectively. It can be observed that as the phase rotating begins to exceed $\pm 45^\circ$, p_{total} tends to become larger than 0 until it reaches the maximum value of 1 at $\Delta\alpha = \Delta\beta = 180^\circ$, where both bits are erroneous and the QPSK symbol is received at the diagonally opposite quadrant of the received reference phase. Depending on $\Delta\alpha$, $\Delta\beta$ and the frequency dependent values $U(f)$, $V(f)$ and $W(f)$, the values of S_I and S_Q differ for each frequency band.

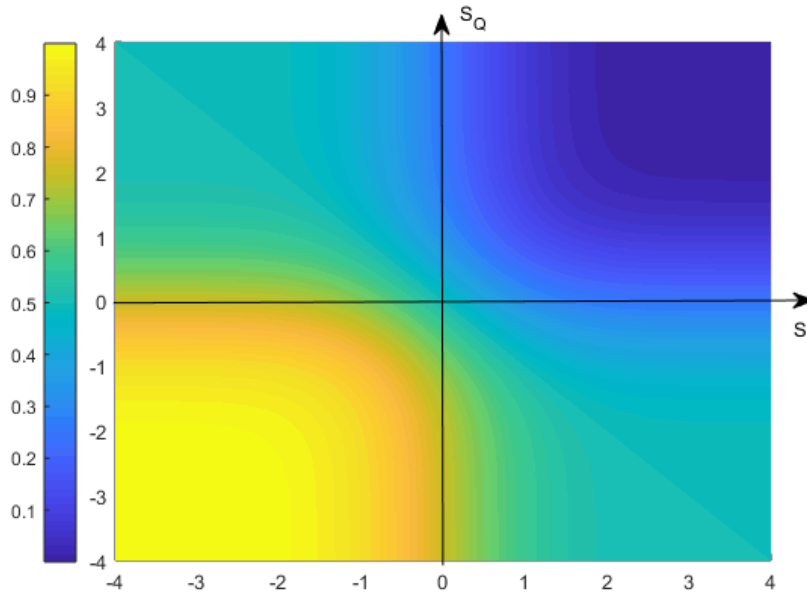


Figure 5.6: 2D plot of the function $p_{\text{total}}(S_I, S_Q)$.

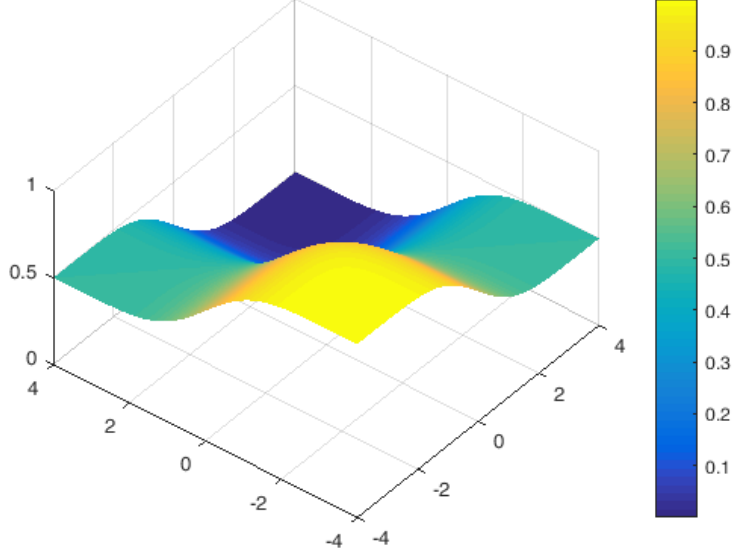


Figure 5.7: 3D plot of the function $p_{\text{total}}(S_I, S_Q)$.

In a next step, p_{total} is averaged over the two frequency bands f_A and f_B of both ensembles in order to obtain a good criterion for the estimation of the overall bit error probability. The following expression is obtained

$$p_{\text{eval}}(\Delta\alpha, \Delta\beta) = \frac{1}{2}(p_{\text{total}}(\Delta\alpha, \Delta\beta, f_A) + p_{\text{total}}(\Delta\alpha, \Delta\beta, f_B)). \quad (5.12)$$

Now $\Delta\alpha$ and $\Delta\beta$ are optimized in a way that $p_{\text{eval}}(\Delta\alpha, \Delta\beta)$ is minimized. As a result of the minimization, the phase shift values $\Delta\alpha_{\text{min}}$ and $\Delta\beta_{\text{min}}$ are then realized in the variable phase shifters of the antenna diversity circuit in order to obtain the improved signal-to-noise ratio for the SDARS radio.

In case the music channel is available in both frequency bands with an interleaver-delay like in the case of the SiriusXM low band with an interleaver-delay of 4 s, the currently determined total bit error probabilities of the two frequency bands must be multiplied by the average value of the mute probability $p_{\text{aver}}(f)$ of the respective other frequency band formed over this interleaver-delay [64]. The following expression is obtained

$$p_{\text{eval}}(\Delta\alpha, \Delta\beta) = \frac{1}{4}(p_{\text{BE,I}}(\Delta\alpha, \Delta\beta, f_A) \cdot p_{\text{aver,I}}(f_B) + p_{\text{BE,Q}}(\Delta\alpha, \Delta\beta, f_A) \cdot p_{\text{aver,Q}}(f_B) + p_{\text{BE,I}}(\Delta\alpha, \Delta\beta, f_B) \cdot p_{\text{aver,I}}(f_A) + p_{\text{BE,Q}}(\Delta\alpha, \Delta\beta, f_B) \cdot p_{\text{aver,Q}}(f_A)). \quad (5.13)$$

5.2 Mathematical Derivations

In this section, the derivations of the algorithm are presented according to [64]. The derivations of the antenna sum (A_1, A_2) will be presented at first and then the derivations of a single antenna.

5.2.1 Antenna Sum

The angle φ between A_1 and A_2 is shown in Fig. 5.8, which depicts the complex signal diagram with the I- and Q-components of the complex signal amplitudes.

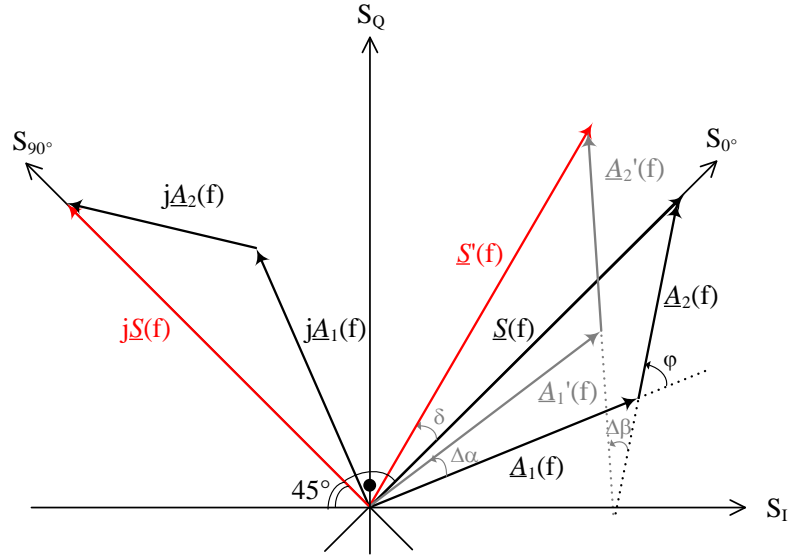


Figure 5.8: Complex signal diagram with the I- and Q-components of the complex signal amplitudes.

\vec{S}^{90° , $\vec{A}_1^{90^\circ}$ and $\vec{A}_2^{90^\circ}$ denote the anti-clockwise phase rotation of \vec{S} , \vec{A}_1 and \vec{A}_2 respectively by 90° . By calculating the scalar product of \vec{S}' and \vec{S}^{90° , the following is obtained:

$$\begin{aligned} \vec{S}' \cdot \vec{S}^{90^\circ} &= (\vec{A}_1' + \vec{A}_2') \cdot (\vec{A}_1^{90^\circ} + \vec{A}_2^{90^\circ}) \\ &= \vec{A}_1' \cdot \vec{A}_1^{90^\circ} + \vec{A}_2' \cdot \vec{A}_2^{90^\circ} + \vec{A}_1' \cdot \vec{A}_2^{90^\circ} + \vec{A}_2' \cdot \vec{A}_1^{90^\circ}. \end{aligned} \quad (5.14)$$

By expanding equation 5.14, we obtain:

$$\begin{aligned} \vec{S}' \cdot \vec{S}^{90^\circ} &= A_1^2 \sin(\Delta\alpha) + A_2^2 (-\sin(\varphi) \cos(\varphi + \Delta\beta) + \cos(\varphi) \sin(\varphi + \Delta\beta)) \\ &\quad + A_1 A_2 (-\sin(\varphi) \cos(\Delta\alpha) + \cos(\varphi) \sin(\Delta\alpha) + \sin(\varphi + \Delta\beta)). \end{aligned} \quad (5.15)$$

Equation 5.15 can be further expanded to:

$$\begin{aligned} \vec{S}' \cdot \vec{S}^{90^\circ} &= A_1^2 \sin(\Delta\alpha) + A_2^2 \sin(\Delta\beta) + A_1 A_2 (-\sin(\varphi) \cos(\Delta\alpha) \\ &\quad + \cos(\varphi) \sin(\Delta\alpha) + \sin(\varphi) \cos(\Delta\beta) + \cos(\varphi) \sin(\Delta\beta)). \end{aligned} \quad (5.16)$$

As a result the we get the following expression:

$$\begin{aligned} \vec{S}' \cdot \vec{S}^{90^\circ} &= \frac{1}{2}(S^2 + A_1^2 - A_2^2) \sin(\Delta\alpha) + \frac{1}{2}(S^2 + A_2^2 - A_1^2) \sin(\Delta\beta) + \\ &\quad + \frac{1}{2}(T^2 - A_1^2 - A_2^2)(\cos(\Delta\beta) - \cos(\Delta\alpha)). \end{aligned} \quad (5.17)$$

Equation 5.14 is simplified to:

$$S' S \sin(\delta) = \frac{1}{2}(U \sin(\Delta\alpha) + V \sin(\Delta\beta) + W(\cos(\Delta\beta) - \cos(\Delta\alpha))). \quad (5.18)$$

The variable S_{90} in equation 5.2 is derived from:

$$S S_{90} = \frac{1}{2}(U \sin(\Delta\alpha) + V \sin(\Delta\beta) + W(\cos(\Delta\beta) - \cos(\Delta\alpha))). \quad (5.19)$$

Therefore,

$$\begin{aligned} S_{90} &= \frac{1}{2S}(U \sin(\Delta\alpha) + V \sin(\Delta\beta) + W(\cos(\Delta\beta) - \cos(\Delta\alpha))) \\ &= \frac{1}{2\sqrt{P_S}}(U \sin(\Delta\alpha) + V \sin(\Delta\beta) + W(\cos(\Delta\beta) - \cos(\Delta\alpha))) \end{aligned} \quad (5.20)$$

where the factor $\frac{1}{2\sqrt{P_S}}$ in equation 5.20 is included in the parameter C according to equation 5.3.

Similarly, we can derive equation 5.1 by calculating the scalar product of \vec{S}' and \vec{S} , which is in phase with the S_0 axis, according to:

$$\begin{aligned} \vec{S}' \cdot \vec{S} &= (\vec{A}'_1 + \vec{A}'_2) \cdot (\vec{A}_1 + \vec{A}_2) \\ &= \vec{A}'_1 \cdot \vec{A}_1 + \vec{A}'_2 \cdot \vec{A}_2 + \vec{A}'_1 \cdot \vec{A}_2 + \vec{A}'_2 \cdot \vec{A}_1. \end{aligned} \quad (5.21)$$

By expanding equation 5.21, we obtain:

$$\begin{aligned} \vec{S}' \cdot \vec{S} &= A_1^2 \cos(\Delta\alpha) + A_2^2 \cos(\Delta\beta) + A_1 A_2 (\cos(\varphi + \Delta\beta) + \\ &\quad + \cos(\varphi) \cos(\Delta\alpha) + \sin(\varphi) \sin(\Delta\alpha)). \end{aligned} \quad (5.22)$$

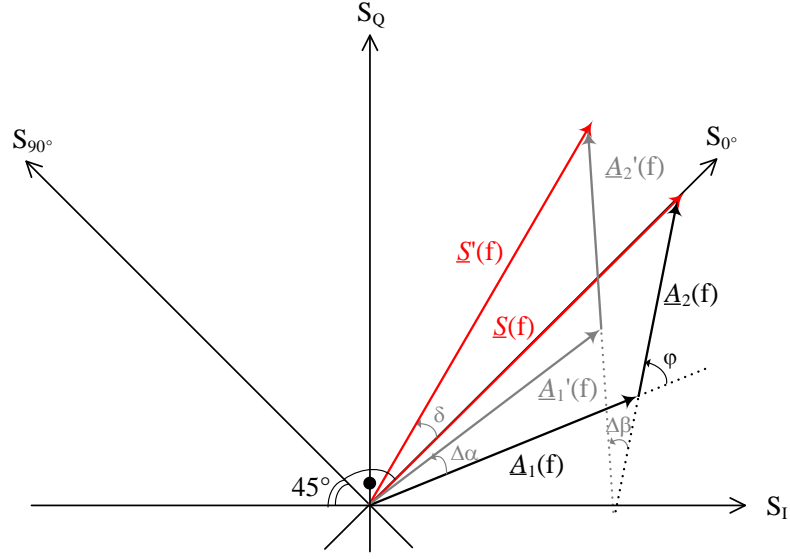


Figure 5.9: Complex signal diagram with the I- and Q-components of the complex signal amplitudes.

Equation 5.22 can be further expanded to:

$$\begin{aligned} \vec{S}' \cdot \vec{S} &= A_1^2 \cos(\Delta\alpha) + A_2^2 \cos(\Delta\beta) + A_1 A_2 (\cos(\varphi) \cos(\Delta\beta) \\ &\quad - \sin(\varphi) \sin(\Delta\beta) + \cos(\varphi) \cos(\Delta\beta) + \sin(\varphi) \sin(\Delta\alpha)). \end{aligned} \quad (5.23)$$

As a result the following expression is obtained:

$$\begin{aligned} \vec{S}' \cdot \vec{S} &= \frac{1}{2}(S^2 + A_1^2 - A_2^2) \cos(\Delta\alpha) + \frac{1}{2}(S^2 + A_2^2 - A_1^2) \cos(\Delta\beta) \\ &\quad + \frac{1}{2}(T^2 - A_1^2 - A_2^2)(\sin(\Delta\alpha) - \sin(\Delta\beta)). \end{aligned} \quad (5.24)$$

Equation 5.21 is simplified to:

$$SS' \cos(\delta) = \frac{1}{2}(U \cos(\Delta\alpha) + V \cos(\Delta\beta) + W(\sin(\Delta\alpha) - \sin(\Delta\beta))). \quad (5.25)$$

The variable S_0 in equation 5.1 is derived from:

$$SS_0 = \frac{1}{2}(U \cos(\Delta\alpha) + V \cos(\Delta\beta) + W(\sin(\Delta\alpha) - \sin(\Delta\beta))). \quad (5.26)$$

Therefore,

$$\begin{aligned} S_0 &= \frac{1}{2S} (U \cos(\Delta\alpha) + V \cos(\Delta\beta) + W(\sin(\Delta\alpha) - \sin(\Delta\beta))) \\ &= \frac{1}{2\sqrt{P_S}} (U \cos(\Delta\alpha) + V \cos(\Delta\beta) + W(\sin(\Delta\alpha) - \sin(\Delta\beta))) \end{aligned} \quad (5.27)$$

where the factor $\frac{1}{2\sqrt{P_S}}$ in equation 5.27 is included in the parameter C according to equation 5.3.

5.2.2 Single Antenna

If only one single antenna (e.g. antenna 1) is switched on, we calculate the scalar product of \vec{A}'_1 and \vec{S} , which is in phase with the S_0 , as follows:

$$\vec{S} \cdot \vec{A}'_1 = (\vec{A}_1 + \vec{A}_2) \cdot \vec{A}'_1 = (\vec{A}_1 \cdot \vec{A}'_1) + (\vec{A}_2 \cdot \vec{A}'_1). \quad (5.28)$$

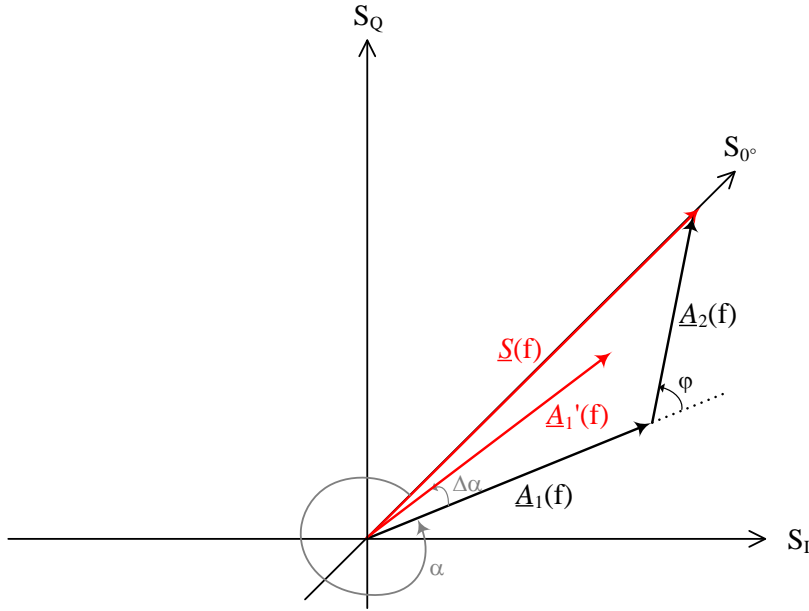


Figure 5.10: Complex signal diagram with the I- and Q-components of the complex signal amplitudes.

By expanding equation 5.28, we get:

$$\vec{S} \cdot \vec{A}'_1 = (A_1^2 \cos(\Delta\alpha) + A_1 A_2 (\cos(\varphi) \cos(\Delta\alpha) + \sin(\varphi) \sin(\Delta\alpha))) \cdot \sqrt{2}. \quad (5.29)$$

Equation 5.29 can be further expanded to:

$$\begin{aligned}
 \vec{S} \cdot \vec{A}'_1 &= (SA_1(\cos(\alpha + \Delta\alpha))) = SS_{0,\text{ant}1} \\
 &= \frac{1}{2}((S^2 + A_1^2 - A_2^2)\cos(\Delta\alpha) + \frac{1}{2}(T^2 - A_1^2 - A_2^2)\sin(\Delta\alpha)) \cdot \sqrt{2} \\
 &= \frac{1}{2}(U \cos(\Delta\alpha) + W \sin(\Delta\alpha)) \cdot \sqrt{2}. \tag{5.30}
 \end{aligned}$$

From equation 5.30, we obtain $S_{0,\text{ant}1}$ for antenna 1 according to:

$$\begin{aligned}
 S_{0,\text{ant}1} &= \frac{1}{2S}(U \cos(\Delta\alpha) + W \sin(\Delta\alpha)) \cdot \sqrt{2} \\
 &= \frac{1}{2\sqrt{P_S}}(U \cos(\Delta\alpha) + W \sin(\Delta\alpha)) \cdot \sqrt{2} \tag{5.31}
 \end{aligned}$$

where the factor $\frac{1}{2\sqrt{P_S}}$ in equation 5.31 is included in the parameter C according to equation 5.3.

Similarly, we calculate $S_{90,\text{ant}1}$ according to the following:

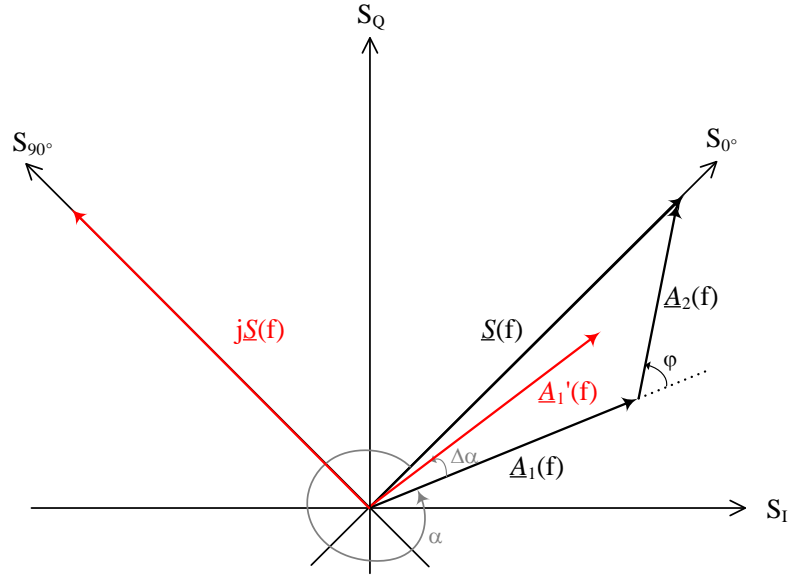


Figure 5.11: Complex signal diagram with the I- and Q-components of the complex signal amplitudes.

$$\vec{S}^{90^\circ} \cdot \vec{A}'_1 = (\vec{A}_1^{90^\circ} + \vec{A}_2^{90^\circ}) \cdot \vec{A}'_1 = \vec{A}_1^{90^\circ} \cdot \vec{A}'_1 + \vec{A}_2^{90^\circ} \cdot \vec{A}'_1 \tag{5.32}$$

By expanding equation 5.32, we obtain:

$$\vec{S}^{90^\circ} \cdot \vec{A}'_1 = (A_1^2 \sin(\Delta\alpha) + A_1 A_2 (\cos(\varphi) \sin(\Delta\alpha) - \sin(\varphi) \cos(\Delta\alpha))) \cdot \sqrt{2} \quad (5.33)$$

We obtain the following:

$$\begin{aligned} \vec{S}^{90^\circ} \cdot \vec{A}'_1 &= S A'_1 \sin(\alpha + \Delta\alpha) = S S_{90, \text{ant1}} \\ &= \frac{1}{2} (U \sin(\Delta\alpha) - W \cos(\Delta\alpha)) \cdot \sqrt{2} \end{aligned} \quad (5.34)$$

Thus:

$$\begin{aligned} S_{90, \text{ant1}} &= \frac{1}{2S} (U \sin(\Delta\alpha) - W \cos(\Delta\alpha)) \cdot \sqrt{2} \\ S_{90, \text{ant1}} &= \frac{1}{2\sqrt{P_S}} (U \sin(\Delta\alpha) - W \cos(\Delta\alpha)) \cdot \sqrt{2} \end{aligned} \quad (5.35)$$

where the factor $\frac{1}{2\sqrt{P_S}}$ in equation 5.35 is included in the parameter C according to equation 5.3.

For the single antenna 2 with angle $\Delta\beta$, the above derivations can similarly be applied.

In order to better visualize the algorithm parameters, a simulation was conducted with two co-phased antennas possessing the same level. P_N is chosen 3dB below the antenna levels. The phase $\Delta\alpha$ of antenna 1 ranges from 0° to 315° in 45° -steps where the iterations $i \in [0, 1]$ are multiples of 45° . The phase $\Delta\beta$ of antenna 2 also ranges from 0° to 315° in 45° -steps where the iterations $j \in [0, 1]$ are multiples of 45° .

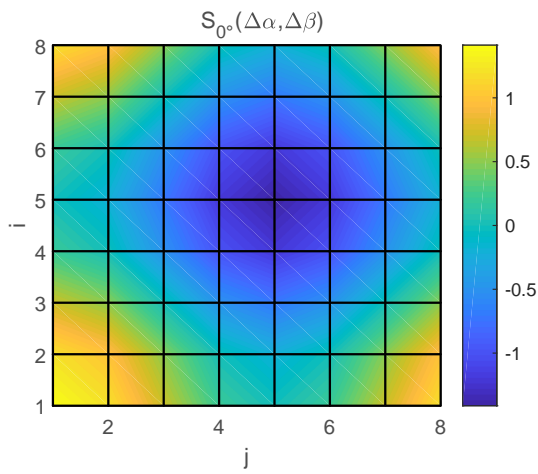


Figure 5.12: 2D plot of S_{0°

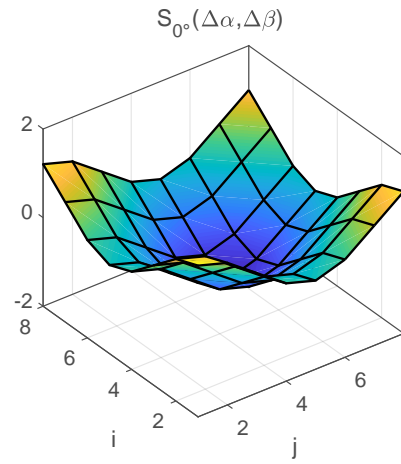


Figure 5.13: 3D plot of S_{0°

Fig. 5.12 and Fig. 5.13 illustrate the 2D and 3D plots of S_{0° respectively.

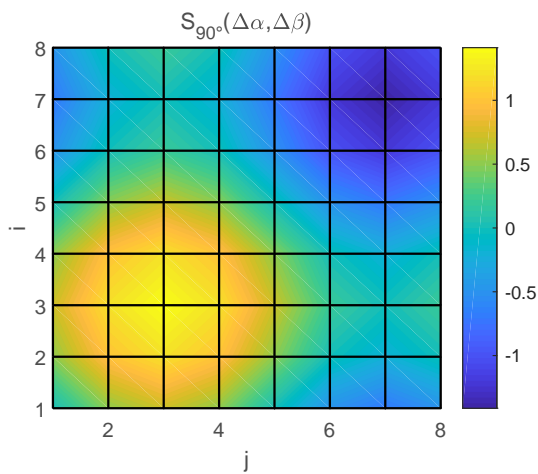


Figure 5.14: 2D plot of S_{90°

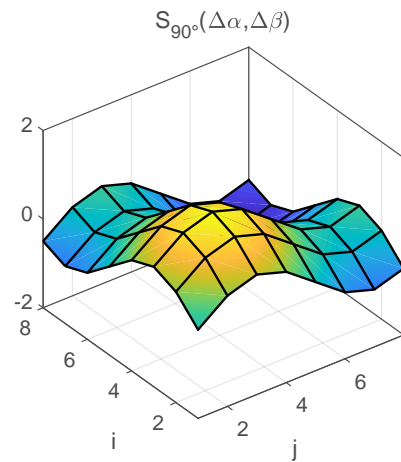


Figure 5.15: 3D plot of S_{90°

Fig. 5.14 and Fig. 5.15 illustrate the 2D and 3D plots of S_{90° respectively.

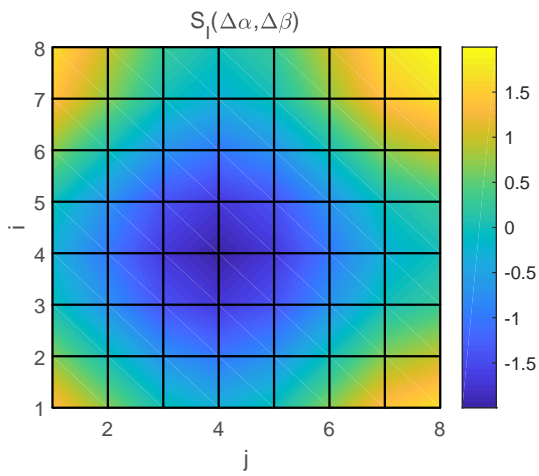


Figure 5.16: 2D plot of S_1

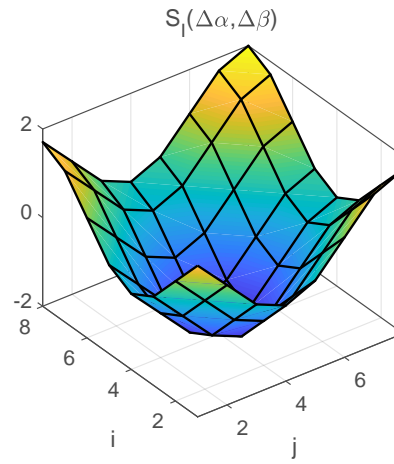


Figure 5.17: 3D plot of S_1

Fig. 5.16 and Fig. 5.17 illustrate the 2D and 3D plots of S_1 respectively.

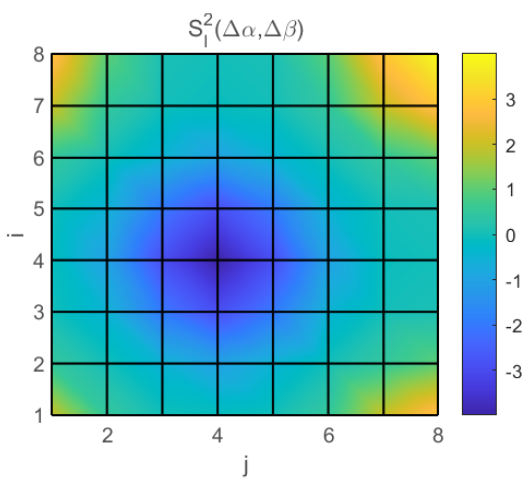


Figure 5.18: 2D plot of S_1^2

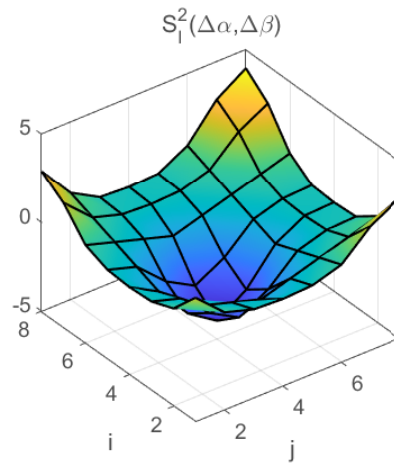


Figure 5.19: 3D plot of S_1^2

Fig. 5.18 and Fig. 5.19 illustrate the 2D and 3D plots of S_1^2 respectively.

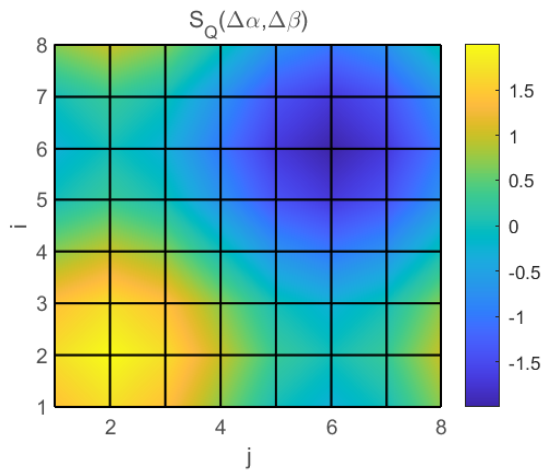


Figure 5.20: 2D plot of S_Q

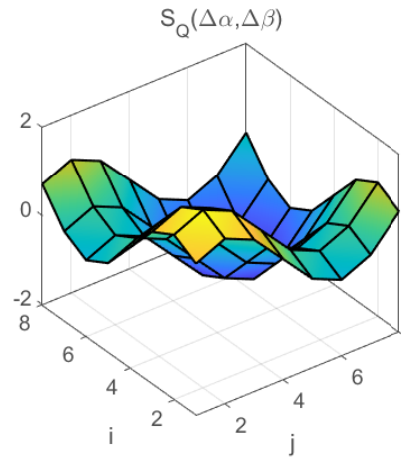


Figure 5.21: 3D plot of S_Q

Fig. 5.20 and Fig. 5.21 illustrate the 2D and 3D plots of S_Q respectively.

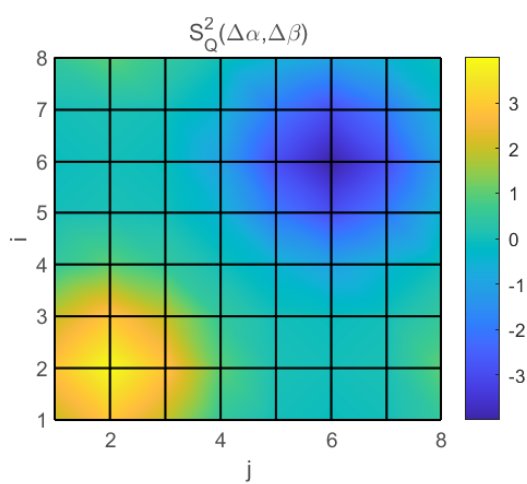


Figure 5.22: 2D plot of S_Q^2

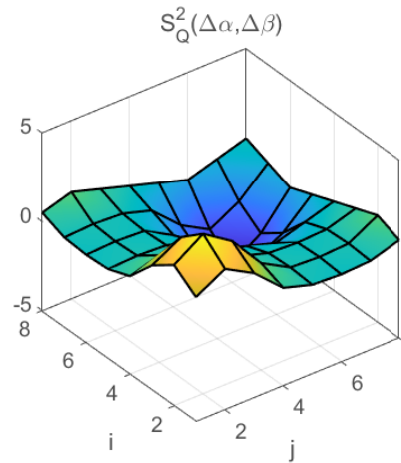


Figure 5.23: 3D plot of S_Q^2

Fig. 5.22 and Fig. 5.23 illustrate the 2D and 3D plots of S_Q^2 respectively.

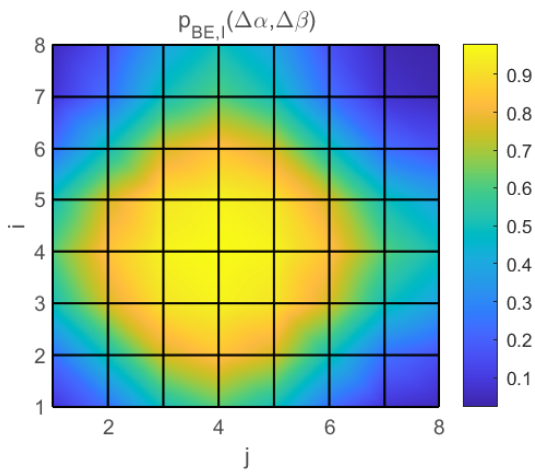


Figure 5.24: 2D plot of $p_{BE,I}$

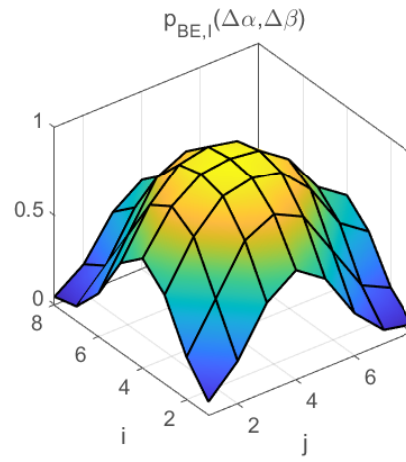


Figure 5.25: 3D plot of $p_{BE,I}$

Fig. 5.24 and Fig. 5.25 illustrate the 2D and 3D plots of $p_{BE,I}$ respectively.

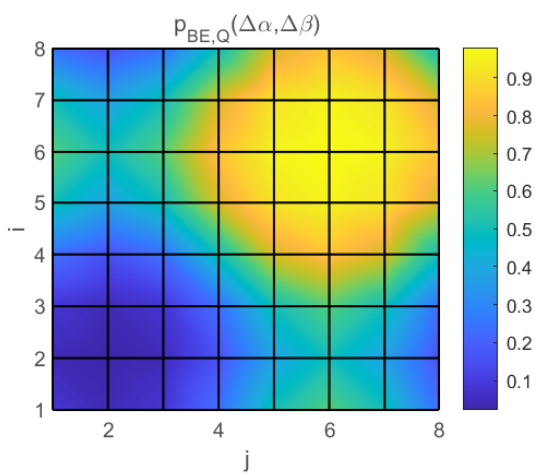


Figure 5.26: 2D plot of $p_{BE,Q}$

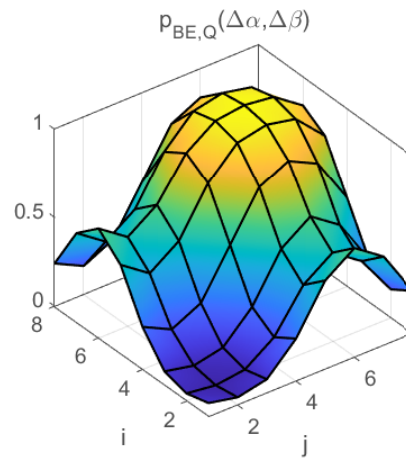


Figure 5.27: 3D plot of $p_{BE,Q}$

Fig. 5.26 and Fig. 5.27 illustrate the 2D and 3D plots of $p_{BE,Q}$ respectively.

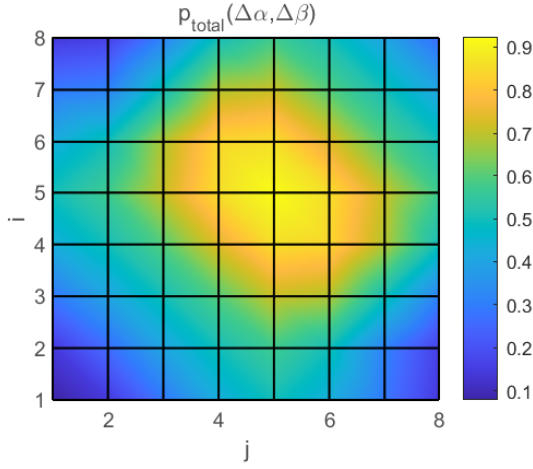
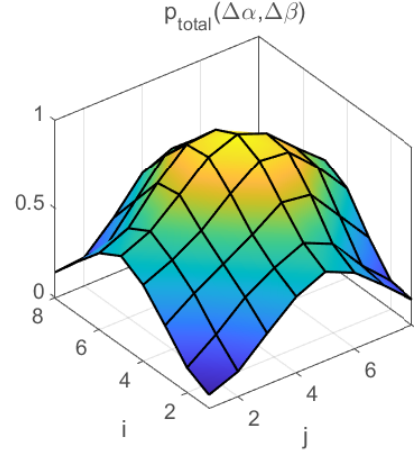

 Figure 5.28: 2D plot of p_{total}

 Figure 5.29: 3D plot of p_{total}

Fig. 5.28 and Fig. 5.29 illustrate the 2D and 3D plots of p_{total} respectively.

5.3 Measures for Algorithm Calculations Acceleration

To be able to utilize simple micro-controller units, efforts and investigations were performed in order to make the algorithm perform its calculations in an accelerated way avoiding a long processing time. In the diversity hardware demonstrator, the variable phase-shifters operate with a fine resolution of 45° , which means they can set the phase in 45° -steps. Table 5.1 lists the time durations for the different algorithm parts taking into consideration all eight phases ($0^\circ, \pm 45^\circ, \pm 90^\circ, \pm 135^\circ, 180^\circ$) which can be set by the phase shifters. If two antennas are considered this results in 64 possible phase combinations (8×8).

Algorithm Part	Duration [μs]
Measurement of P_{cur}	24
Calculation of all tests: $P_1(f), P_2(f), P_S(f)$ and $P_T(f)$	115
Frequency change	60
LUT reading of the tests' non-logarithmic values and of $C(f)$	3
Calculation of the variables $U(f), V(f)$ and $W(f)$	5
Calculation of $p_{total}(\Delta\alpha, \Delta\beta, f)$	150
High-band: $p_{eval}(\Delta\alpha, \Delta\beta)$ and setting the optimal phases	65
Low-band: $p_{eval}(\Delta\alpha, \Delta\beta)$ and setting the optimal phases	83

Table 5.1: The measured time durations for the different algorithm parts taking into consideration all 64 phase combinations (8×8).

The time durations in Table 5.1 were measured in the laboratory by means of an oscilloscope. The measurement of the current signal level including the comparison with the pre-defined threshold takes $24\mu\text{s}$. The calculation of all four test constellations $P_1(f)$, $P_2(f)$, $P_S(f)$ and $P_T(f)$ has an overall duration of $115\mu\text{s}$. The measurement results obtained from the test cases are logarithmic values. For this purpose the measured logarithmic values are converted to their corresponding linear power values through a look-up table. Reading the linear power values from this look-up table and the values of the variable $C(f)$ from another look-up table takes $3\mu\text{s}$ in total.

Regarding the frequency change, it takes approximately $60\mu\text{s}$ till the local oscillator is set. The duration of calculating the variables $U(f)$, $V(f)$ and $W(f)$ is $5\mu\text{s}$. One of the most time-consuming calculations in the multi-channel algorithm is the determination of the values of $p_{\text{total}}(\Delta\alpha, \Delta\beta, f)$. This takes $150\mu\text{s}$ when all 64 phase combinations (8×8) are taken into account. Concerning the calculation of $p_{\text{eval}}(\Delta\alpha, \Delta\beta)$ and setting the optimal phases leading to the minimum estimated average bit error probability over both ensembles, the whole process takes $65\mu\text{s}$ for the high-band. Regarding the low-band, this duration is higher ($83\mu\text{s}$) because of the additional multiplications due to the interleaver-delay.

In order to make the multi-channel algorithm more efficient and to reduce the calculation duration of some algorithm parts, some initial measures are applied. These initial measures include:

- the utilization of pre-calculated look-up tables (LUT) for variables such as $C(f)$ and for functions such as the Q -function instead of performing the time consuming calculations by means of the resources of the micro-controller unit.
- the deployment of bit-shifting instead of directly performing the multiplication and division operations in the algorithm for numbers which are a multiple of two.
- the triggering of the algorithm calculations (including the bit error rates) during the frequency change (frequency parallelization). Instead of waiting till the local oscillator is set and then performing further calculations, making use of simultaneous operations would be more time efficient. As long the further algorithm calculations take at least $60\mu\text{s}$ it is advantageous to simultaneously perform the frequency change in parallel.
- the reduction of the algorithm activity to just when it is necessary. This is accomplished by introducing shorter test intervals with a duration of $100\mu\text{s}$ (including the frequency change) whenever the current signal level is above the threshold.

In the following three test cases A , B and C are investigated, where different calculation acceleration measures are applied for the low-band and high-band.

5.3.1 SiriusXM High-Band Test Cases

In the following the test cases of the SiriusXM high-band are introduced.

Test Case A:

Fig. 5.30 depicts the timeline showing the durations of the different parts of the algorithm in a sequential way for one complete diversity period. All above mentioned acceleration measures except for the frequency parallelization are taken into consideration with the 64 phase combinations (8x8).

In the presented sequential mode of the algorithm, it can be noticed that waiting till the frequency change is totally accomplished costs the diversity algorithm a time duration of $120\mu s$ since the frequency is changed twice: from f_A to f_B and vice-versa. After each frequency change, further calculations with a duration of $158\mu s$ ($3\mu s + 5\mu s + 150\mu s$) are performed. This is reflected in the diversity period with a total duration of $755\mu s$, which is not considered low and should be further reduced.

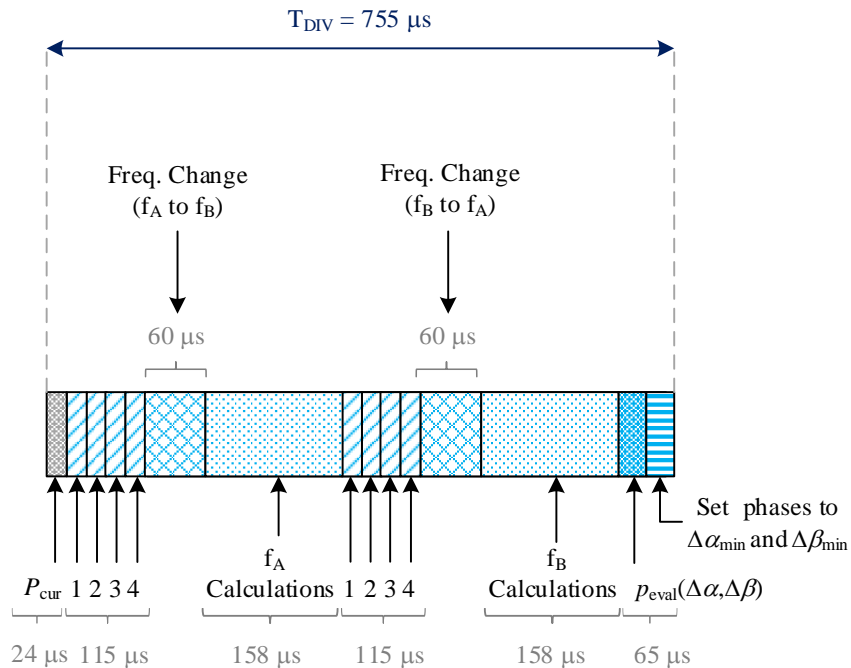


Figure 5.30: The timeline showing the durations of the different parts of the algorithm for one complete diversity period taking the 64 phase combinations into consideration (8x8) in addition to calculation acceleration methods except the frequency parallelization.

Test Case B:

In order to reduce the overall diversity period duration, the measure of triggering the further algorithm calculations during the frequency change is applied in this test case. Fig. 5.31 illustrates the timeline showing the durations of the different parts of the algorithm for one complete diversity period taking the 64 phase combinations into consideration (8x8) in addition to calculation acceleration methods including the frequency parallelization.

It can be clearly observed how the diversity period decreases from $755\mu\text{s}$ to $635\mu\text{s}$. Even though the duration is reduced due to frequency parallelization, it still can be noticed how the time consuming algorithm calculations with a duration of $158\mu\text{s}$ affect the overall period duration.

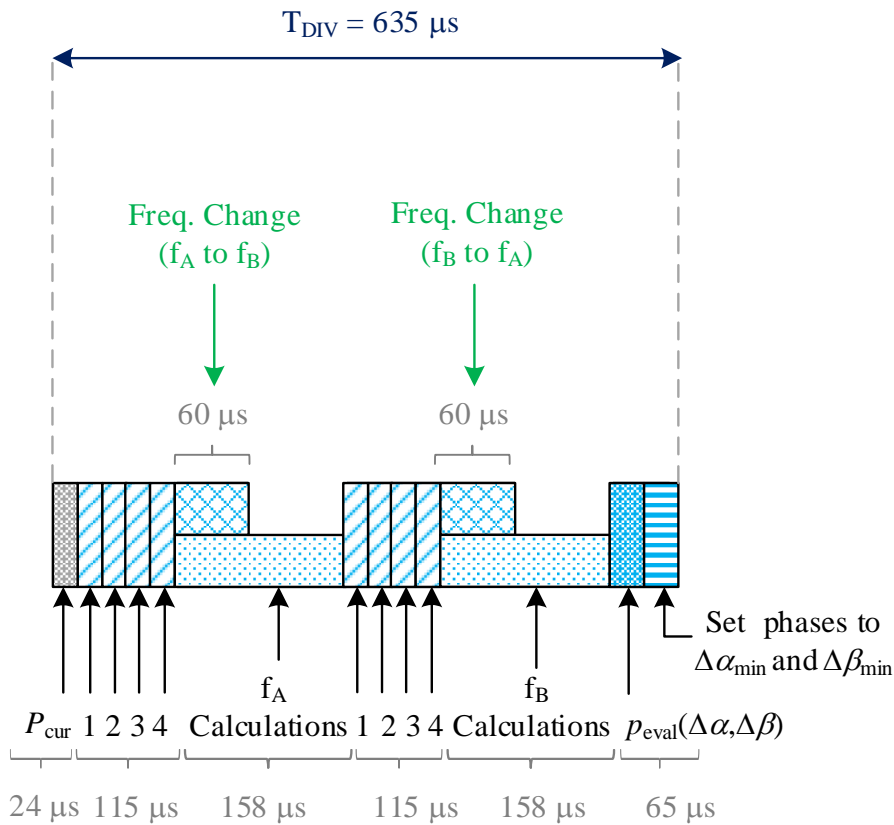


Figure 5.31: The timeline showing the durations of the different parts of the algorithm for one complete period taking the 64 phase combinations into consideration (8x8) in addition to frequency parallelization.

Test Case C:

In order to further reduce the processing time needed for one diversity period, it would make sense to accelerate the speed of the algorithm calculations which possess a duration of $158\mu\text{s}$. One can make use of the following two rules:

- **Rule 1:** $|\Delta\alpha - \Delta\beta| \leq 180^\circ$ must apply, which means the sum signal remains in the right half of the complex plane pointing towards the direction of the reference phase.
- **Rule 2:** Phases with the same sign are not allowed because the phase shifting of both antennas would be in the same direction (either clockwise or counter-clockwise).

$\Delta\beta \backslash \Delta\alpha$	-135°	-90°	-45°	0°	45°	90°	135°	180°
-135°	X	X	X	✓	✓	X	X	X
-90°	X	X	X	✓	✓	✓	X	X
-45°	X	X	X	✓	✓	✓	✓	X
0°	✓	✓	✓	✓	✓	✓	✓	✓
45°	✓	✓	✓	✓	X	X	X	X
90°	X	✓	✓	✓	X	X	X	X
135°	X	X	✓	✓	X	X	X	X
180°	X	X	X	✓	X	X	X	X

Table 5.2: The allowed and forbidden phase combinations after applying the two rules. (X) means at least one rule does not apply, and (✓) means both rules apply.

Table 5.2 summarizes all 64 possible phase combinations ($\Delta\alpha$ and $\Delta\beta$) and lists whether they obey both rules or not. If at least one rule is violated the table field is marked with the sign (X). The sign (✓) indicates that both rules are valid for the corresponding phase combination.

The use cases show that the $\Delta\alpha$ and $\Delta\beta$ combinations are reduced from 64 combinations to only 27 in the case of two switched antennas. There are seven combinations results from the phases 0° , $+45^\circ$ and -45° . There are ten further combinations if the phases $+90^\circ$ and -90° are included. If the phases $+135^\circ$ and -135° are taken consideration, eight further combinations are obtained. Finally, including the phase 180° yields two additional combinations. This results in 27 combinations in total. In the case of one antenna, a further reduction of the cases can applied for the combinations of the following three phases: 0° , $+45^\circ$ and -45° .

The time durations of the different algorithm parts in Table 5.3 correspond to the case where the three phases 0° , $+45^\circ$ and -45° are taken into account instead of all eight phases.

Algorithm Part	Duration [μs]
Measurement of P_{cur}	24
Calculation of all tests: $P_1(f)$, $P_2(f)$, $P_S(f)$ and $P_T(f)$	115
Frequency change	60
LUT reading of the tests' non-logarithmic values and of $C(f)$	3
Calculation of the variables $U(f)$, $V(f)$ and $W(f)$	2
Calculation of $p_{\text{total}}(\Delta\alpha, \Delta\beta, f)$	30
Calculation of $p_{\text{eval}}(\Delta\alpha, \Delta\beta)$ and setting the optimal phases	17

Table 5.3: The measured time durations for the different algorithm parts taking into consideration only the three phases 0° , $+45^\circ$ and -45° .

The significant time reduction can be observed in the part where $p_{\text{total}}(\Delta\alpha, \Delta\beta, f)$ is calculated. The duration decreases from $150\mu\text{s}$ in the case of all 64 phase combinations to only $30\mu\text{s}$. Moreover, there is additional reduction in the last part of the algorithm where $p_{\text{eval}}(\Delta\alpha, \Delta\beta)$ is calculated and the optimal phases are set. The time duration decreases from $65\mu\text{s}$ to only $17\mu\text{s}$. A minor reduction is also observed in the case of calculating the variables $U(f)$, $V(f)$ and $W(f)$. The time duration decreases from $5\mu\text{s}$ to $2\mu\text{s}$.

The algorithm parts which still possess an unmodified time duration include the measurement of the current signal level P_{cur} with $24\mu\text{s}$. Moreover, the durations of the calculation of all four test constellations as well as of the LUT reading of the tests' non-logarithmic values and of the variable $C(f)$ are $115\mu\text{s}$ and $3\mu\text{s}$ respectively.

Fig. 5.32 depicts the timeline showing the time durations of the different algorithm parts listed in Table 5.3 for one complete diversity period. All above mentioned acceleration measures (including frequency parallelization) are applied on the three phases 0° , $+45^\circ$ and -45° instead of all eight phases. A waiting time of $T_w = 25\mu\text{s}$ is included right after performing the algorithm calculations with a duration of $35\mu\text{s}$ ($3\mu\text{s} + 2\mu\text{s} + 30\mu\text{s}$) at the first frequency to make sure the local oscillator is correctly set after the time duration it needs ($60\mu\text{s}$). After being set on the frequency f_B , the four test constellations are performed in addition to the rest of the steps illustrated in Fig. 5.32. The overall diversity period is significantly reduced from $635\mu\text{s}$ in the case of test *B* to only $366\mu\text{s}$.

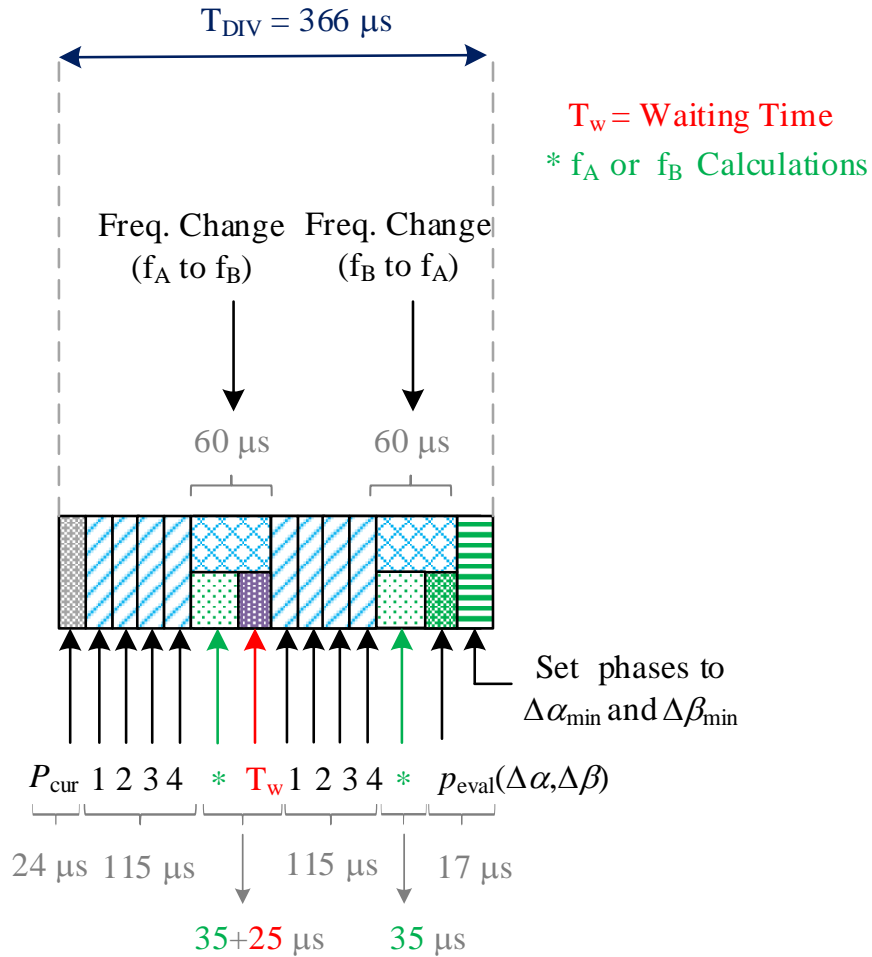


Figure 5.32: The timeline showing the durations of the different parts of the algorithm for one complete period taking the three phases 0° , $+45^\circ$ and -45° into consideration in addition to the acceleration measures (including frequency parallelization).

The influence of applying different acceleration measures on the overall diversity period duration can be clearly noticed in Table 5.4. All three test cases A, B and C are listed and compared with each other. Applying all the measures reduces the diversity period duration by more than a factor of two as can be seen in the table 5.4 where the diversity period duration is reduced from $755\mu s$ in test case A to $366\mu s$ in test case C. A comparison of the audio mutes duration between the test case B and test case C is presented in section 5.5.

Algorithm Acceleration Measure	Test A	Test B	Test C
Use of LUTs	✓	✓	✓
Use of Bit-Shifting	✓	✓	✓
Use of shorter Tests if ($P_{\text{cur}} > \text{Threshold}$)	✓	✓	✓
Use of Frequency Parallelization	X	✓	✓
Use of reduced Phase Combinations	X	X	✓
Diversity Period [μs]	755	635	366

Table 5.4: The differences in diversity period durations of the three different test cases *A*, *B* and *C* after applying various measures for the algorithm acceleration.

5.3.2 SiriusXM Low-Band Test Cases

Since initial investigations were performed on the SiriusXM low-band before performing further analysis on the high-band, one test case has been inspected for the low-band.

Test Case A:

Fig. 5.33 depicts the timeline showing the durations of the different parts of the algorithm in a sequential way for one complete diversity period. All above mentioned acceleration measures except for the frequency parallelization are taken into consideration with the 64 phase combinations (8×8).

In the presented sequential mode of the algorithm, it can be noticed that waiting till the frequency change is totally accomplished costs the diversity algorithm a time duration of $120\mu\text{s}$ since the frequency is changed twice: from f_A to f_B and vice-versa. After each frequency change, further calculations with a duration of $158\mu\text{s}$ ($3\mu\text{s} + 5\mu\text{s} + 150\mu\text{s}$) are performed.

It can be also observed that for the calculation of p_{eval} and for setting the optimal phases, it takes $83\mu\text{s}$ because of the additional multiplications due to the interleaver-delay. This is reflected in the diversity period with a total duration of $773\mu\text{s}$. Measurements inspecting the audio mutes duration with this test case are presented in section 5.5.

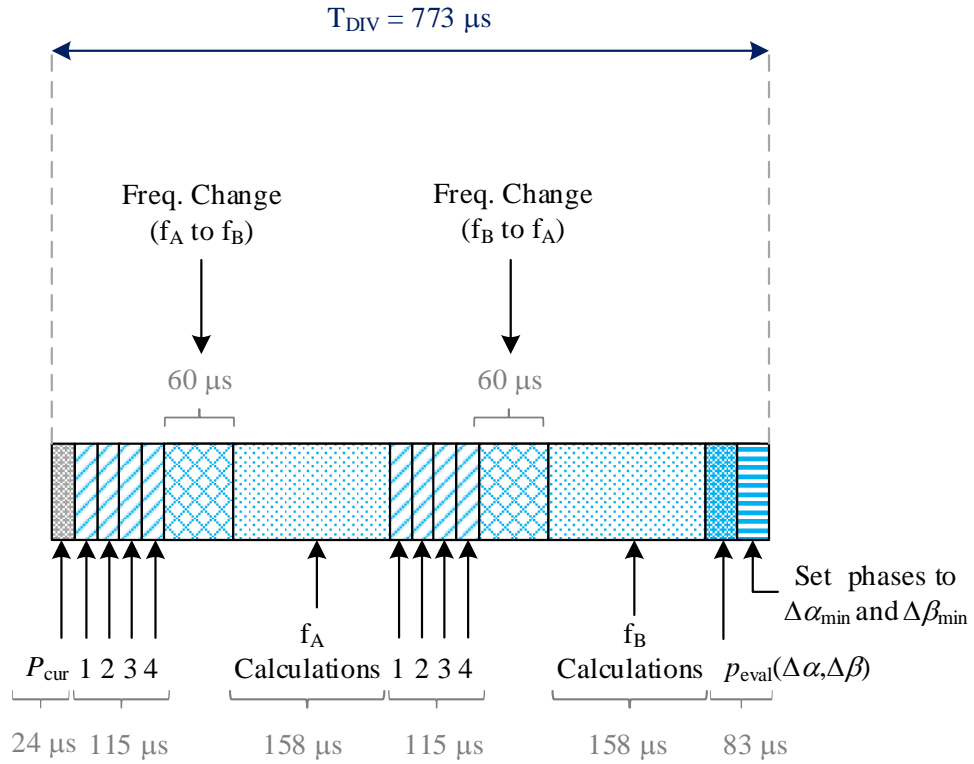


Figure 5.33: The timeline showing the durations of the different parts of the algorithm for the low-band for one complete diversity period taking the 64 phase combinations into consideration (8x8) in addition to calculation acceleration methods except the frequency parallelization.

5.4 Implementation

The following section deals with the micro-controller used to implement and verify the algorithm. The performance of the micro-controller defines how complex the algorithm can be. To be able to use simple micro-controllers, efforts were made to make the algorithm perform its calculations in a fast way through look-up tables for example. Two Atmel controllers, the ATxmega128A1 [76] and the SAM D21 J18A [77], are compared. The first one was used in previous SDARS diversity systems, but it was replaced by the SAM D21 controller since it is licensed and compliant to be utilized in vehicular applications. The main features of both micro-controllers are summarized in table 5.5.

Features	ATxmega128A1	SAM D21J
Flash-Memory	128 kB	256 kB
Supply Voltage	3.3 V	3.3 V
Operating Frequency	32 MHz	48 MHz
DFLL	up to 32 MHz	up to 96 MHz
GPIO Pins	78	53
Ports	A-F	A-B
Programming Interface	PDI	SWD
License (vehicles)	No	Yes

Table 5.5: Comparison between ATxmega128A1 and SAM D21J

5.4.1 SAM D21 Micro-Controller

The Atmel SAM D21 micro-controller used in the SDARS diversity system belongs to the family of ARM-based micro-chips. The ARM Cortex M0+ core developed by ARM is installed in a chip developed by Atmel, which contains all further features and wiring. The semiconductor chip is bonded to the pins of the TQFP and sealed with a polyamide package. This plastic housing protects the silicon semiconductor from mechanical forces and environmental influences such as high humidity.

The SAM D21 micro-controller is available in different versions, which makes it adaptable to various applications. For more complex tasks and algorithms, the most powerful micro-controller of the series, with 256 kB flash memory and 64 pins, is chosen.

The TQFP model shown in Fig. 5.34 is particularly suitable for first prototypes of PCBs. Short circuits on the board can be corrected or repaired by bridges. This is not possible with the UFBGA package shown in Fig. 5.35 since all the connections are situated on the bottom of the micro-chip. Therefore, in order to eliminate small errors in the circuit design, no completely new circuit board has

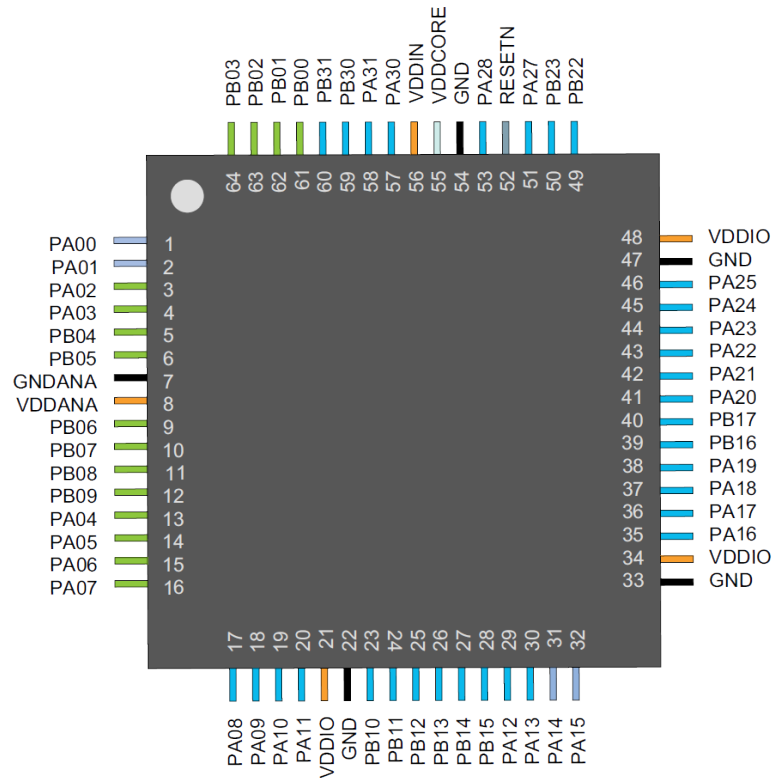


Figure 5.34: Pin configuration (TQFP) of the SAM D21 [77, p.13]

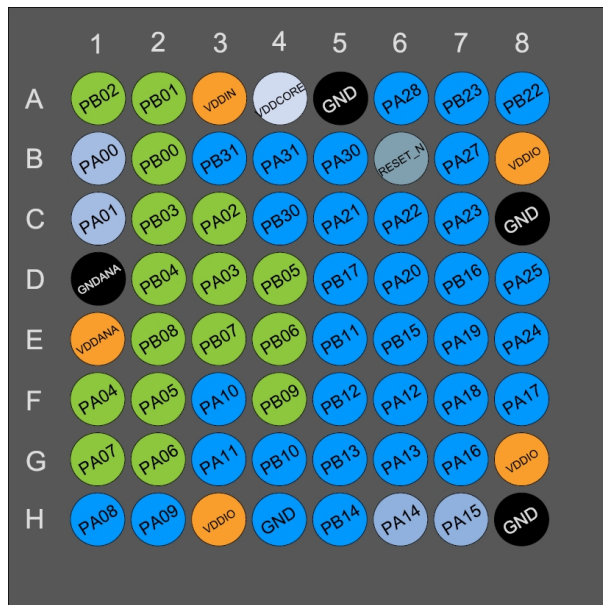


Figure 5.35: Pin configuration (UFBGA Package) of the SAM D21 [77, p.14]



Figure 5.36: An Atmel SAM D21 J18A micro-controller integrated in the PCB.

to be produced by using the TQFP version. This can be time and cost efficient. A photograph of an integrated SAM D21 micro-controller in a PCB is shown in Fig. 5.36

5.4.2 Micro-Controller PCB

Before integrating the micro-controller into the system, a test PCB is designed and manufactured to verify its functionality which includes controlling the phase shifters and switches as well as programming the oscillator to set the mixer frequency in the diversity system. The schematic illustration of the controller is divided into two parts: left and right (to the micro-controller) in order to better visualize the circuit diagram. The left part of the circuit diagram is illustrated in Fig. 5.37, whereas the right part is depicted in Fig. 5.38.

The PCB layout with the SAM DJ21 in the middle is depicted in Fig.5.39, and the manufactured PCB (top view) at the institute is shown in Fig. 5.40. If no short circuits are detected in the PCB, the MCU can be connected to a power supply after setting the supply voltage to +3.3V and limiting the supply current to 20 mA. Then, the programming interface can be started and individual functions and input/output pins can be tested. A test program is used for this purpose to verify if all registers are written correctly and the main clock is controlled properly. Everything else can now be added to the main program as desired.

5.4 Implementation

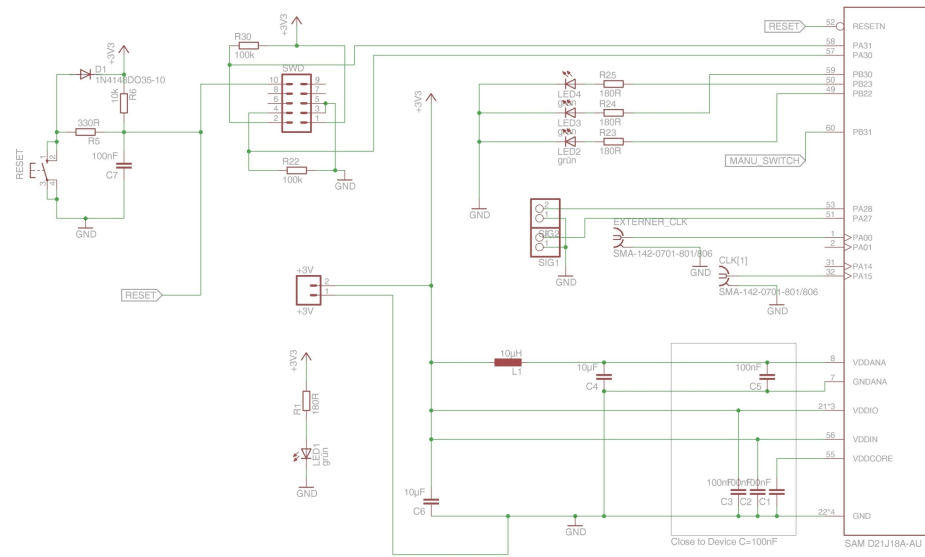


Figure 5.37: Circuit diagram left side

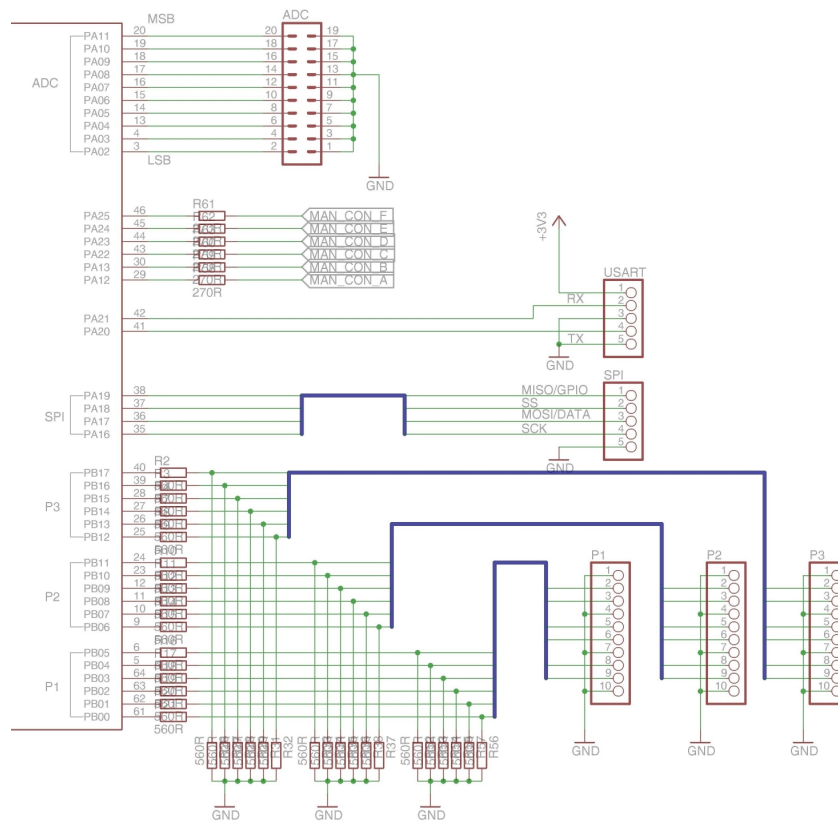


Figure 5.38: Circuit diagram right side

5 Multi-Channel Algorithm for Antenna Diversity

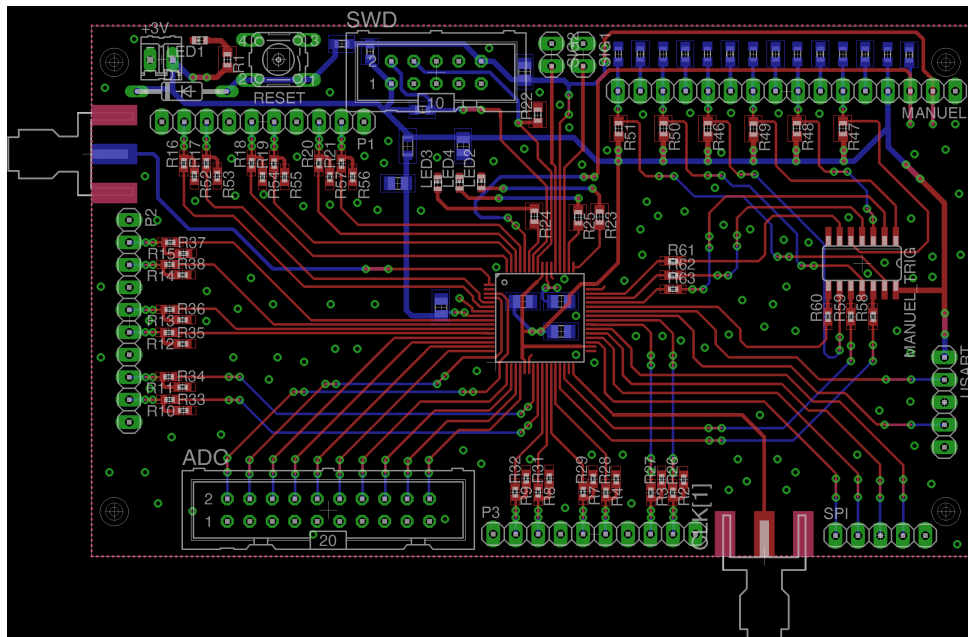


Figure 5.39: PCB Layout with the SAM DJ21 in the middle

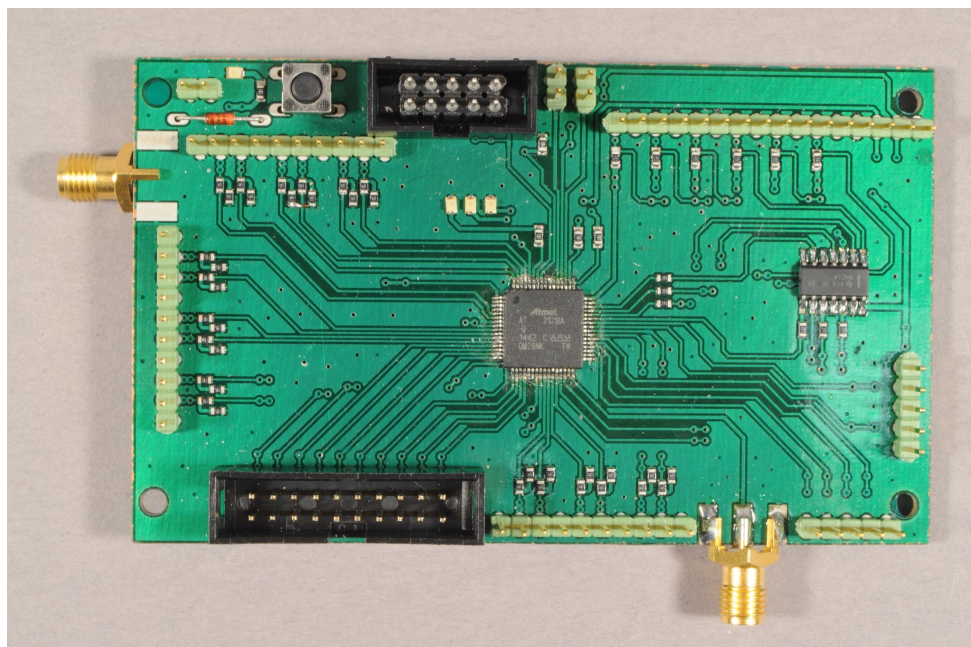


Figure 5.40: The implemented PCB (Top View)

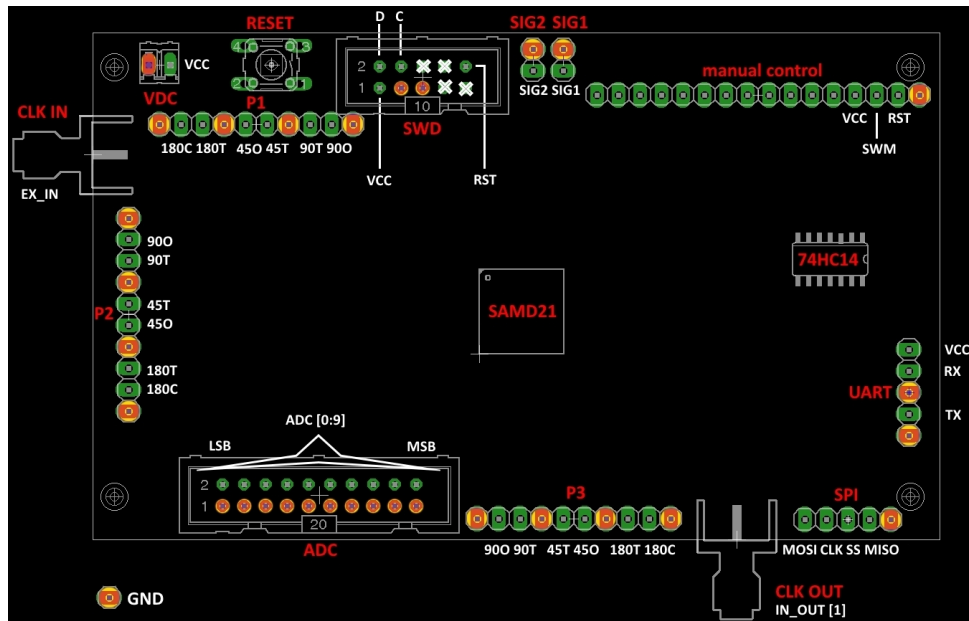


Figure 5.41: Pin configuration and connector of the PCB

The pin configuration is illustrated in Fig. 5.41. The PCB consists of multiple interfaces, which include SPI and USART (for debugging purposes).

The PCB connectors and their functionality are listed in table 5.6. Table 5.7 summarizes the utilized port allocation.

Table 5.6: PCB Connectors

P1-P3	Phase Control
SWD	Program and debug interface, Atmel-ICE debugger
VDC	Power Supply +3,3 V
CLK IN	Clock in
CLK OUT	Clock out
SIG1-2	GPIO pins that can be triggered for debugging
USART	Communications Interface PC
SPI	Local Oscillator Connection
ADC	ADC Input Connector
Manual Control	Interface for Manual Control

Table 5.7: Port allocation

PORT A	Function	PORT B	Function
PA00	CLK IN	PB00	P1 90O
PA01	GPIO	PB01	P1 90T
PA02	ADC[0] LSB	PB02	P1 45T
PA03	ADC[1]	PB03	P1 45O
PA04	ADC[2]	PB04	P1 180T
PA05	ADC[3]	PB05	P1 180C
PA06	ADC[4]	PB06	P2 90O
PA07	ADC[5]	PB07	P2 90T
PA08	ADC[6]	PB08	P2 45T
PA09	ADC[7]	PB09	P2 45O
PA10	ADC[8]	PB10	P2 180T
PA11	ADC[9] MSB	PB11	P2 180C
PA12	MC_A	PB12	P3 90O
PA13	MC_B	PB13	P3 90T
PA14	GPIO	PB14	P3 45T
PA15	CLK OUT	PB15	P3 45O
PA16	MOSI	PB16	P3 180T
PA17	SCK	PB17	P3 180C
PA18	SS	PB18	-
PA19	GPIO	PB19	-
PA20	USART TX	PB20	-
PA21	USART RX	PB21	-
PA22	MC_C	PB22	Stat_LED1
PA23	MC_D	PB23	Stat_LED2
PA24	MC_E	PB24	-
PA25	MC_F	PB25	-
PA26	-	PB26	-
PA27	SIG1/GPIO	PB27	-
PA28	SIG2/GPIO	PB28	-
PA29	-	PB29	-
PA30	SWD CLK	PB30	Stat_LED3
PA31	SWD DATA	PB31	SWM/GPIO

5.4.3 Micro-Controller Programming

The basic function of the ARM micro-controller has already been ensured with a basic program [78]. But since this program was adapted to the *Evaluation Board Atmel SAM D21 Xplained Pro*, it could not simply be adopted. So the code had to be re-adapted to the newly manufactured board. Two other important factors made it necessary to change the code: the synchronization of the controller and the analog-to-digital converter with 10 bit resolution in addition to the use of a new LO which was not utilized in previous diversity systems [79].

SPI Interface

The serial peripheral interface (SPI) is a serial data bus that can write and read data. There is only one line through which addresses and data are transmitted one after the other. It is possible to connect several devices and bring them into a hierarchy via a master-slave assignment.

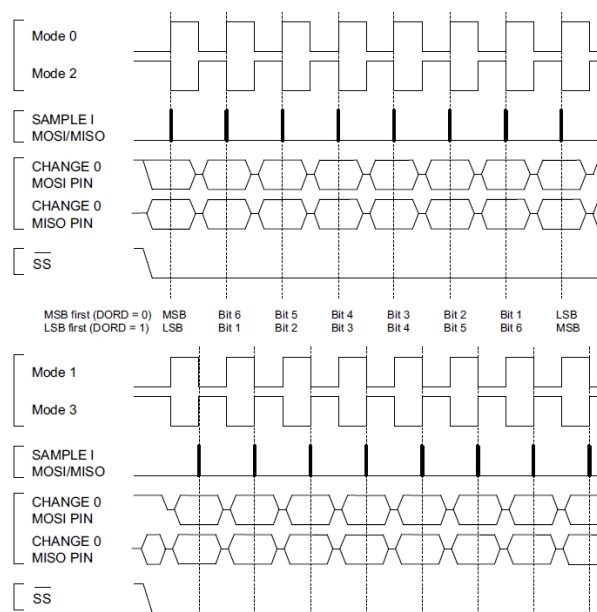


Figure 5.42: SPI Transfer Mode of SAM D21 [77, S.482]

There are different SPI modes, which differ in that the bit detection takes place either with a rising or falling clock edge and whether the clock line is high or low in idle mode, i.e. when nothing is transmitted. Moreover, either the MSB or the LSB can be sent first. The different possibilities are shown in Fig. 5.42.

Programming the local oscillator is performed via the SPI interface, so that the desired frequency is generated. The register description and the transferred

data during the process are described in [79]. The frequency of the local oscillator is set in the case of TDM1 to 2212.293 MHz in order to down-convert the RF signal into the intermediate frequency 110 MHz.

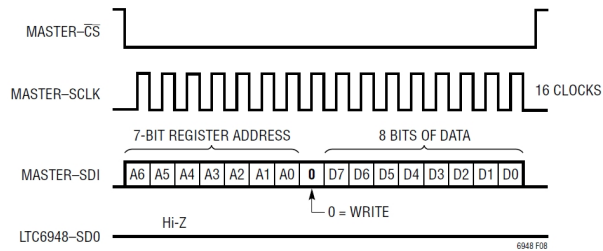


Figure 5.43: SPI Transfer Mode of LTC6948[80, S.21]

With the SAM D21 micro-controller any SPI mode can be used. The controller can be adapted to various integrated circuits or other micro-controllers. The mode of the local oscillator chip in Fig. 5.43 is crucial for the communication between the local oscillator and the MCU.

The modes are listed below:

- **CTRLB_MODE_SPI_MASTER:** the controller shifts into the SPI master mode, which is supplied by its internal clock source. In slave mode, it would depend on an external clock source
- **CTRLA_MODE:** can be used to set the SPI mode (Default: Mode (0))
- **CTRLA_DORD:** if this bit is set, the LSB is sent first (Default: MSB first)
- **CTRLA_CPOL:** is not set, otherwise the clock is reversed (Default: Clock Low idle)

The next step is to use the SPI port in a similar way to the USART, except that no direct output on the PC is possible here and thus an alternative test option must be used. The easiest way to do this is with the oscilloscope. The "Single Run" function is suitable to record the bit stream at the moment. Another advantage of the oscilloscope is that not only the data bit stream (yellow) can be displayed, but also the clock (blue) and the slave select (red) as depicted in Fig. 5.44. If the specified bit sequence is output in the correct clock and at SS on low, the SPI interface works.

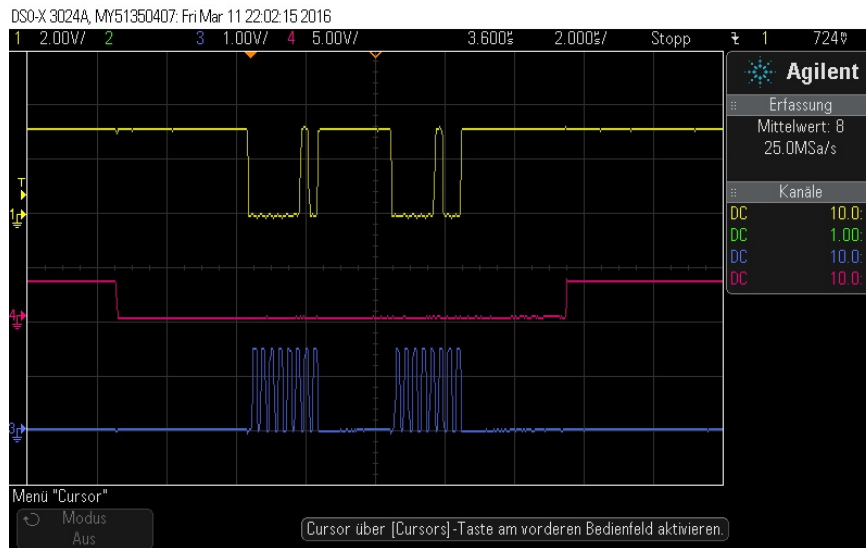


Figure 5.44: Register description of the local oscillator via SPI

USART

The test program adapted to the board also contains some routines with which the communication interfaces can be tested. First, the communication between computer and microcontroller is checked. For this purpose, the main program is adapted so that the USART (universal synchronous/asynchronous receiver/transmitter) routine is initialized. Once this has been done, any output can be programmed and read out in a subsequent test. If the default text is displayed in the output window on the computer, the USART connection works without problems.

Clocksystem

The SAM D21 micro-controller can be clocked with different frequencies. It is possible to use different internal oscillators or an externally supplied clock. The clock frequency can be multiplied by any internal DFLL. With the DFLL, a maximum frequency of 48 MHz can be achieved. To generate even higher frequencies, the controller has an implemented FDPLL that can reach frequencies from 48 MHz up to 96 MHz. Furthermore, the internal clock generators have a divider that can be programmed. This allows almost any frequency to be generated. The chip has different internal clock sources. Alternatively, the microprocessor can be given a clock, by a frequency generator or by a quartz oscillator. During the initiation of the controller, the internal 32 kHz clock source was used.

5.5 Measurements

The same test drive scenario introduced in 4.5.1 is taken into consideration in order to verify the multi-channel algorithm. For this purpose, recorded signals from the real fading scenario are analysed in the laboratory using the RF-signal playback unit presented in 4.5.2 in addition to a diversity system hardware demonstrator. The algorithm is programmed using the C-language on a MCU, which is responsible for steering the switches as well as the phase shifters of the diversity system.

5.5.1 SiriusXM High-Band

In one of the numerous measurement campaign scenarios, a micro-diversity antenna set consisting of two loop antenna structures is mounted on the front fender of the test drive vehicle as depicted in Fig. 5.45.



Figure 5.45: The micro-diversity antenna set composed of two loop antenna structures mounted on the front fender.

The audio mutes introduced in Table 1 are average values over five individual measurements for the two single antennas, for diversity optimized at one frequency (SAT1A or SAT1B) as well as for diversity deploying the presented multi-channel algorithm. The first single antenna yields an average mute duration of 11.89 s and the second one 19.85 s. Optimizing the algorithm at only the most suitable frequency (SAT1A) leads to a reduced mute duration of 1.88 s. This measurement requires a-priori knowledge of the frequency band at which the test channel is currently available. This is only possible in the laboratory and not in real scenario conditions.

Table 5.8: Comparison of average audio mute durations (each over five measurements) in a real fading scenario recorded on test drives in the USA for the cases of single antennas as well as antenna diversity. The micro-diversity antenna set was mounted on the car’s front fender.

	Audio Mutes [s]	Duration [s]	Availability [%]
Average (Ant1,2)	15.87	380	95.82
DIV SAT1A	1.88	380	99.50
DIV SAT1B	5.34	380	98.59
New Algorithm	2.43	380	99.36

Optimizing the algorithm at the other frequency (SAT1B) yields a mute duration of 5.34s. The results indicate that by optimizing diversity at both frequencies (SAT1A and SAT1B) by using the novel multi-channel algorithm, antenna diversity achieves a mute duration of 3.52s [74]. As can be noticed the mute duration is reduced to around 1/5 in comparison to the average single antenna (15.87 s). It is worth mentioning, that the improvement of the multi-channel algorithm was accomplished in the worst case scenario of reception through Satellite 1 because the measurements were conducted on the eastern side of the USA, where the SiriusXM frequency bands 1A and 1B with a distance of 10 MHz have only a weak correlation with each other in their fading behaviour. On the western side the correlation between the frequency bands 2A and 2B of the second satellite is considered higher. Therefore, it is expected that the multi-channel algorithm achieves even better results (closer to the ones of achieved by SAT1A).

Fig. 5.46 illustrates the audio mutes denoted by black dots for both single antennas as well as the diversity configuration with the new algorithm over a total time of 380 s. The introduced recordings correspond to individual measurements which have been selected to closely match the average mute durations in Table 5.8. A significant reduction of the number of mutes by the new algorithm in comparison to both single antennas can be observed.

The multi-channel algorithm improvement presented in Table 5.8 corresponds to the test case C introduced in section 5.3 (refer to Table 5.4), where all acceleration measures with only three phases (0° , $+45^\circ$ and -45°) are taken into account. The same investigation scenario as described above with the micro-diversity set mounted on the vehicle’s front fender is considered.

For inspecting the influence of the acceleration measures on the audio mutes duration, a comparison between the test case B and test case C is shown in Table 5.9. The test case B which includes all eight phases (0° , $\pm 45^\circ$, $\pm 90^\circ$, $\pm 135^\circ$ and 180°) taking frequency parallelization into account yields an audio mutes duration of 3.31s. The reduction of number of phases to three contributes to a reduction of the audio mutes duration as can be noticed in the test case C which

5 Multi-Channel Algorithm for Antenna Diversity

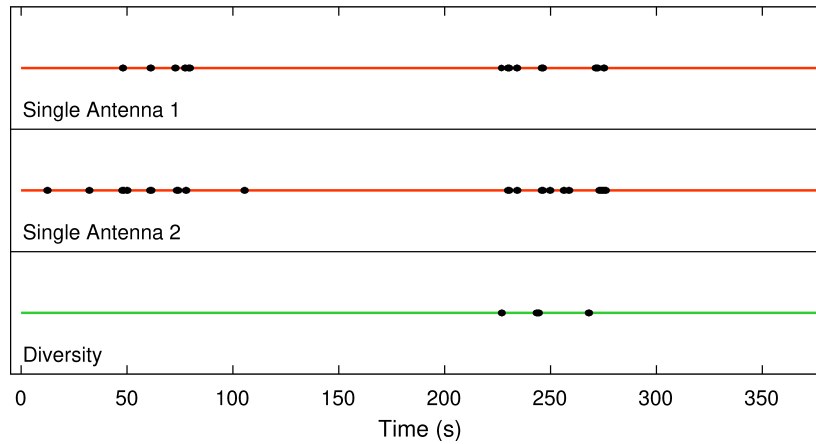


Figure 5.46: Measured audio mutes of individual measurements of the diversity antenna set's single antennas at one mounting point (front fender) in comparison to diversity with the multi-channel algorithm.

has an audio mute duration of 2.43s. This acceleration measure reduces the audio mutes time by almost 0.9s. In other words, reducing the diversity period duration from $635\mu\text{s}$ (test case *B*) to only $366\mu\text{s}$ (test case *C*) plays a big role in the audio mutes reduction which reflects in a better audio quality.

Table 5.9: Comparison of average audio mute durations in a real fading scenario recorded on test drives in the USA for the cases of single antennas as well as antenna diversity. The micro-diversity antenna set was mounted on the car's front fender. The test cases *B* and *C* are compared.

	Audio Mutes [s]	Duration [s]	Availability [%]
Test Case B	3.31	380	99.13
Test Case C	2.43	380	99.36

5.5.2 SiriusXM Low-Band

The initial investigations of the multi-channel algorithm were performed on the SiriusXM low-band. Measurements were conducted with the test case *A* introduced in section 5.3.2. In one of the various measurement campaign scenarios, a micro-diversity antenna set consisting of two loop antenna structures is mounted on the dashboard of the test drive vehicle as depicted in Fig. 5.47. The direction of the test drive was counter-clockwise with an overall test duration of 380 s.



Figure 5.47: A micro-diversity antenna system mounted on the dashboard

Table 5.10 shows a comparison of audio mute durations in a real fading scenario recorded on test drives in the USA for the cases of single antennas as well as antenna diversity. If the single antennas are directly connected to the receiver with TDM1 reception only, the average audio mutes duration of the single antennas is 110.9 s. If TDM2 reception only is activated, the average audio mutes duration of the single antennas is 297.95 s. In case both satellites are available, the average audio mutes duration is 41.4 s.

5 Multi-Channel Algorithm for Antenna Diversity

Table 5.10: Comparison of audio mute durations in a real fading scenario recorded on test drives in the USA for the cases of single antennas as well as antenna diversity. The micro-diversity antenna set was mounted on the car’s dashboard. The direction of the test drive was counter-clockwise with a total test duration of 380s.

	Audio Mutes [s]
Average (Ant1,2) with TDM1 only	110.9
Average (Ant1,2) with TDM2 only	297.95
Average (Ant1,2) with TDM1+2	41.4
DIV (All SATs available/Algorithm optimized on best TDM)	16.8
Multi-Channel Algorithm	17.4

If the scan-phase algorithm is optimized on the best TDM (in this scenario: TDM1), diversity yields a mutes duration of 16.8 s. By deploying the multi-channel algorithm as described in test case A (with all eight phases and without frequency parallelization), diversity yields 17.4 s. The huge difference in the reception quality between TDM1 only and TDM2 only (110.9 s against 297.95 s) can be noticed in this scenario.

90s out of the 380s recording (above) are analyzed. Within the 90s the performance difference between TDM1 and TDM2 is not so large like in the previous case. Table 5.11 lists the results for this case. If the single antennas are directly connected to the receiver with TDM1 reception only, the average audio mutes duration of the single antennas is 16.26 s. If TDM2 reception only is activated, the average audio mutes duration is 67.98 s. In case both satellites are available, the average audio mutes duration is 6.30 s. If the scan-phase algorithm is optimized on the best TDM (in this scenario: TDM1), diversity yields a mutes duration of 1.48 s. By deploying the multi-channel algorithm as described in test case A (with all eight phases and without frequency parallelization), diversity yields 1.37 s. The multi-channel algorithm shows in this case an improvement even though not all calculation acceleration measures are taken into account.

Table 5.11: Comparison of audio mute durations in a real fading scenario recorded on test drives in the USA for the cases of single antennas as well as antenna diversity. The micro-diversity antenna set was mounted on the car’s dashboard. The direction of the test drive was counter-clockwise with a total test duration of 90s.

	Audio Mutes [s]
Average (Ant1,2) with TDM1 only	16.26
Average (Ant1,2) with TDM2 only	67.98
Average (Ant1,2) with TDM1+2	6.30
DIV (All SATs available/ Algorithm optimized on best TDM)	1.48
Multi-Channel Algorithm	1.37

5.6 Satellite Monitoring

As previously mentioned, the algorithm determines which antenna phase combination leads to the minimum estimated bit error probability over both ensembles of the most suitable satellite.

In order to know which of the SiriusXM high band satellites has to be supported, the average signal levels of both satellites in line-of-sight (LOS) conditions are compared. This allows to determine the geographic location of the user, so that the algorithm can then accordingly optimize the ensemble of the satellite with the best SNR.

Fig. 5.48 depicts the upper band spectrum of SiriusXM between 2.3325 GHz and 2.3450 GHz. SNR_1 , SNR_2 , SNR_3 and SNR_4 correspond to the SNRs at the band 1A, 2A, 2B and 1B respectively.

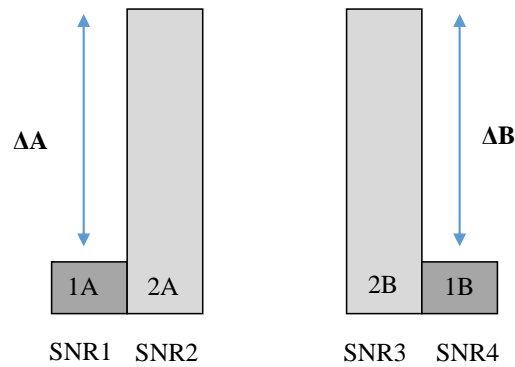


Figure 5.48: Parameter definitions for monitoring based on the SiriusXM upper side band

The parameter ΔA which is defined as the SNR difference between the bands 1A and 2A is calculated according to:

$$\Delta A = SNR_1 - SNR_2. \quad (5.36)$$

Similarly, the variable ΔB is calculated as follows:

$$\Delta B = SNR_4 - SNR_3. \quad (5.37)$$

Since ΔA and ΔB fluctuate according to the position of the vehicular receiver, it is necessary to investigate their possible variations and how they affect the SNR and the optimization of the diversity algorithm.

		ΔA		
		< -6dB	[-6dB,+6dB]	> +6dB
ΔB	< -6dB	SNR2 & SNR3	SNR1 & SNR2 & 2.SNR3	SNR1 & SNR3
	[-6dB,+6dB]	2.SNR2 & SNR3 & SNR4	SNR1 & SNR2 & SNR3 & SNR4	2.SNR1 & SNR3 SNR4
	> +6dB	SNR2 & SNR4	SNR1 & SNR2 & 2.SNR4	SNR1 & SNR4

Figure 5.49: Monitoring distinction of cases

Fig. 5.49 depicts which SNRs are taken into consideration according to the variations of ΔA and ΔB . Fig. 5.50 illustrates the corresponding scenarios introduced in Fig. 5.49.

It is clear that at the upper right and lower left corners, the scenarios would never take place. That is why they are excluded from the analysis. On one hand, if both ΔA and ΔB are lower than 6dB, the west satellite is utilized for optimization. On the other hand, if they do exceed 6dB, the east satellite is chosen.

If ΔA and ΔB do not show a large difference as the case in the middle of Fig. 5.50, the optimization is performed on the satellite 2, since optimizing all 4 bands is not time efficient and both bands 2A and 2B offer a higher correlation than 1A and 1B.

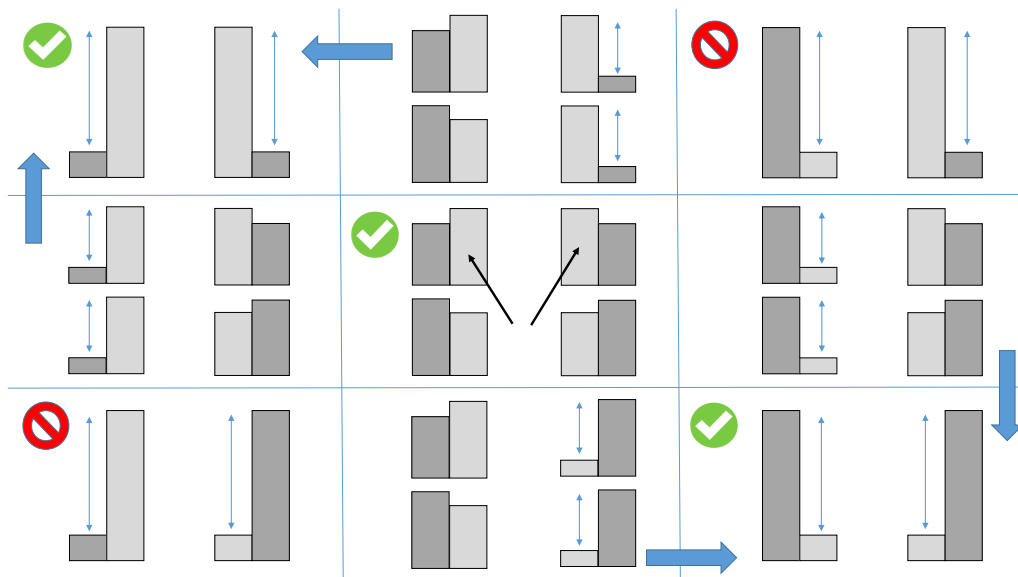


Figure 5.50: Monitoring scenarios

In order to deal with the above scenarios, a monitoring algorithm was implemented. The flowchart to perform the satellite monitoring is illustrated in Fig. 5.51.

Every 30 min the signal level P_{current} is monitored. The standard deviation σ , which is the square root of the variance σ^2 , is calculated according to:

$$\sigma = \sqrt{\sigma^2} = \sqrt{\frac{1}{N} \sum_{n=1}^N |P_{\text{current},i} - \mu|^2} \quad (5.38)$$

where N is the number of scalar observations (in our case 1000), $i \in [1,1000]$ and μ is the mean of $P_{\text{ANT},i}$

$$\mu = X = \frac{1}{N} \sum_{n=1}^N P_{\text{current},i}. \quad (5.39)$$

If the standard deviation is more than 1dB, it means that the level fluctuation is high and we have a NLOS scenario. So, a counter of 5 min is set and the verification it performed again till we end up in a LOS scenario where the level deviation is 1 dB at most.

In this case, the signal level of each single antenna is measured. Afterwards, the average values (X) of the two antennas for each band (1A, 1B, 2B and 1B) are calculated. Then, ΔA and ΔB are calculated. If the result is more than 6dB, the corresponding satellite is chosen. Otherwise satellite 2 in order to make use of the high correlation of band 2A and 2B.

Laboratory measurements showed that the standard deviation of the signal levels in LOS scenario signals is 1dB at most. Applying the monitoring algorithm on signals recorded on the east coast of the USA led to choosing satellite 1 for optimization as expected.

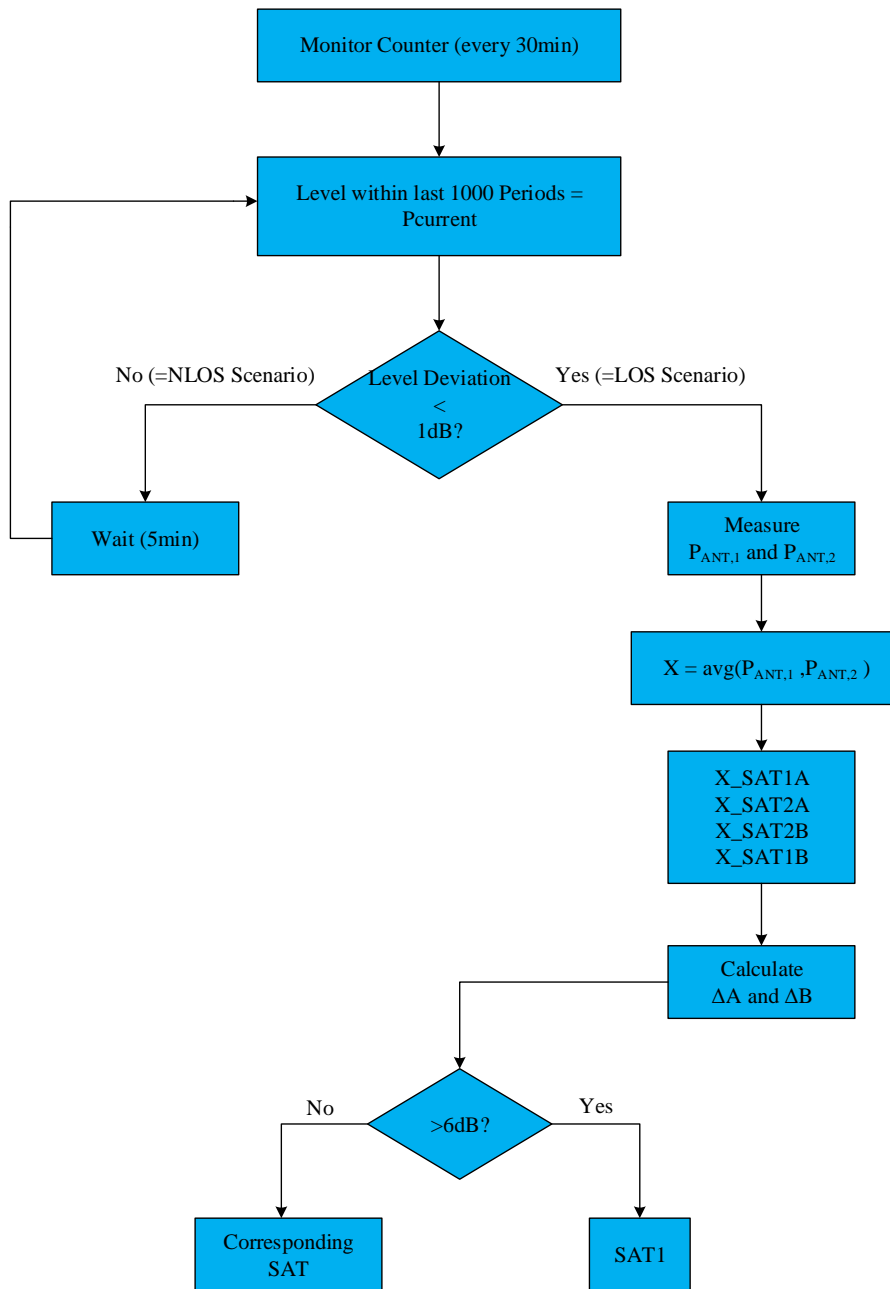


Figure 5.51: Monitoring Flowchart

6 Measurements with the Diversity System IC Chip

After presenting the advantages of applying the noise cancellation method and the multi-channel algorithm in chapters 4 and 5 respectively, measurements with a compact antenna diversity system with an integrated circuit (IC) are introduced for automotive reception of SDARS signals. The integrated circuit includes RF switches, phase-alignment and signal combining in addition to frequency conversion for level detection. It is considered the first IC for SDARS scan-phase antenna diversity, which includes all the diversity functions except for level detection and digital signal processing [81]. A compact hardware demonstrator is realized with the IC with a package size of just 9 mm by 9 mm. The characteristic values of the RF signal paths such as gain and variable phase shift are determined by means of laboratory measurements [81]. In this chapter, the compact diversity circuit is investigated in a real fading scenario on different antenna mounting positions and various system setups in order to show the significant improvement of the signal quality through scan-phase diversity in comparison to single antenna reception.

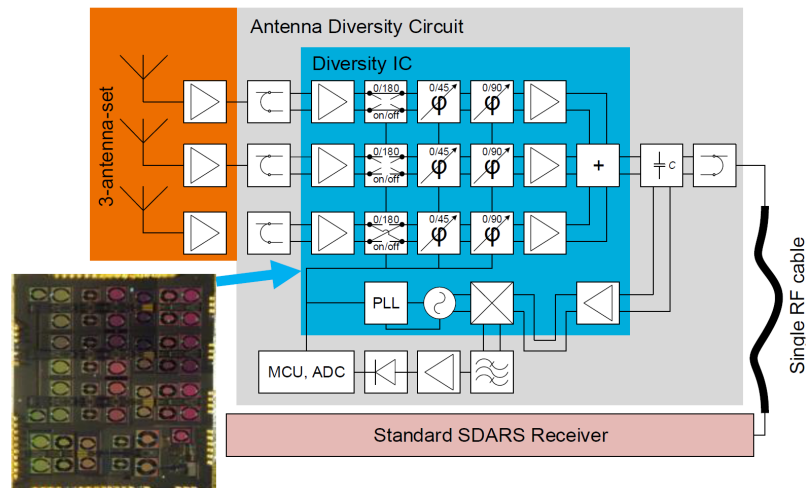


Figure 6.1: Block diagram of the scan-phase antenna diversity system with phase aligned selective RF combining and frequency down-conversion integrated inside the diversity IC. The rest of the components are implemented outside the IC. The image inset shows a photograph of the realized integrated circuit.

6.1 Satellite Radio Diversity Circuit

Fig. 6.1 depicts the block diagram of the scan-phase antenna diversity system with completely integrated silicon based microwave circuit. The fundamental RF components such as LNAs, switches, phase shifters and the power combiner are implemented inside the integrated circuit. Moreover, a programmable local oscillator (LO) as well as an active mixer are also integrated inside the IC [81]. They are utilized for the down-conversion in frequency range of a small fraction of the RF signal for level detection. The additional implementation of complex components from the level detection path inside the IC enables not only a lean design but also a cost efficient system. The few further system components in the level measurement path such as band-pass filter, logarithmic detector, analogue-to-digital converter (ADC) as well as MCU are implemented outside the integrated circuit.

6.1.1 Analysis of the RF Signal Path

In the following, the RF-signal path is described from the antenna amplifier through the diversity IC to the level detector. At each of the three input ports, a low-noise amplifier is preceded by a $0^\circ/180^\circ$ phase shifter. This phase shifter is also utilized as an antenna switch. Further phase shifter sections, which are switchable between $0^\circ/45^\circ$ and $0^\circ/90^\circ$, complete the capability to set eight different phase shifts in 45° steps for each individual antenna signal path. Afterwards, an active power combiner buffers the output signal and provides a perfect isolation between the signal paths. In all phase and switch settings, the measured isolation between all ports of the antenna diversity circuit (IC and external circuitry combined) is better than -25 dB [81].

The discrete baluns on the printed circuit board enable a conversion from the external unbalanced signals to the differential signaling inside the IC. A simple differential T-type junction found on the output port is utilized to split the signal into two paths. A balun converts the main output signal towards the receiver into a single ended signal. At all ports, the impedance matching is -12 dB or better independent of the switch and phase shifter settings [81].

Fig. 6.2 illustrates a photograph of the implemented hardware demonstrator of the antenna diversity circuit. In all signal paths, the achieved measured results for all discrete phase shift values do not deviate by more than $\pm 10^\circ$ [81]. Regarding the total IC gain, the input and output baluns and the output coupling circuit is in the range from -3.0 dB to $+0.2$ dB for all signal paths and all phase settings. An integrated LNA receives a small share of the signal power, which is then down-converted in frequency by an internal active mixer. An integrated programmable PLL from an external reference clock generates the LO for frequency down-conversion, and it is directly applied to the integrated mixer.

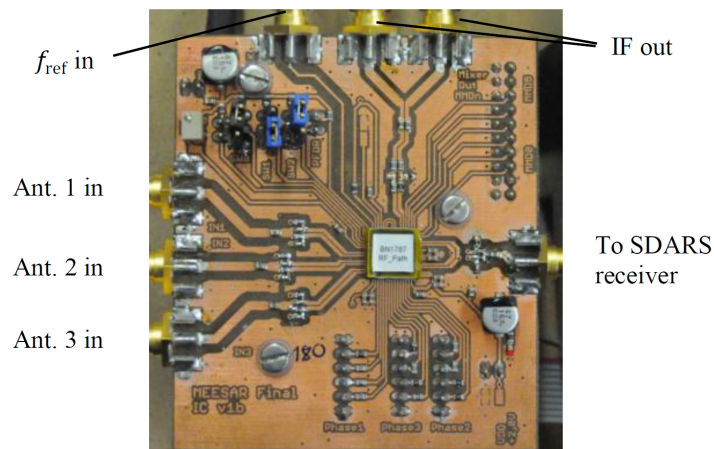


Figure 6.2: Photograph of the circuit board with the diversity integrated circuit. It contains the diversity IC with a size of 9 mm by 9 mm as well as the input and output baluns. Connectors for RF signal path control (bottom) as well as programming the PLL (top right and left) connect to the micro-controller unit.

The rest of the system components of the level measurement path at the intermediate frequency (IF) are not included inside the IC. Channel selectivity is ensured through a surface acoustic wave (SAW) filter with a center frequency of approximately 110.6 MHz and a 3 dB bandwidth of 1.4 MHz. The IF SAW filter acts as a balun in the level detection path. Afterwards, a single ended amplifier boosts the signal level so that even very small signal levels in fading scenarios can be measured with sufficient accuracy by the logarithmic detector, which converts the IF signal level to a DC voltage. The DC voltage is proportional to the input power in dBm. This voltage is read by means of an ADC, and the MCU calculates optimal signal path settings for the switches and phase shifters inside the IC from the measured signal level values [81].

The path loss between the transmitting satellite and the receiver is considered high [82] with a value of approximately 190 dB. Even in ideal LOS conditions only a signal level of approximately -70 dBm is achieved at the output port of a regular receiving antenna's LNA assuming a standard-conformal antenna characteristic and amplifier gain. A low noise figure of the overall reception system is paramount due to the low external noise temperature at 2.33 GHz [47]. Standard SDARS antenna LNAs are directly placed at the output ports of the passive antenna elements. The orange box in Fig. 6.1 depicts these LNAs with a gain of 27 dB and a noise figure of 0.6 dB. An overall noise figure of 0.65 dB and a gain of 25.9 dB is achieved combination with the antenna diversity circuit [81].

6.2 Diversity Measurements with initial IC Versions

In all following sub-sections, an external ADC is taken into consideration with initial IC versions, where frequency down-conversion was still not integrated within the IC. Measurements with an internal ADC within the MCU will be presented later in the sub-section 6.3.2.

6.2.1 Laboratory Setup with IC + Level Detection Test Board

The measurements in this sub-section were performed using the EHS signal recording and playback unit. This signal recorder is able to record different satellite signals in the field and then play them back in the laboratory for further analysis. To do this, the signal is down-mixed to an intermediate frequency during the recording and then up-mixed again during playback. Figure 6.3 illustrates the utilized EHS recording and playback unit.

Part (1) in Fig. 6.3 depicts the unit with the keyboard and monitor to operate it. Part (2) includes the power supply and the board with the components used for frequency up- and down-mixing. Part (3) shows the signal generators to feed the local oscillators in the frequency conversion board in (2).

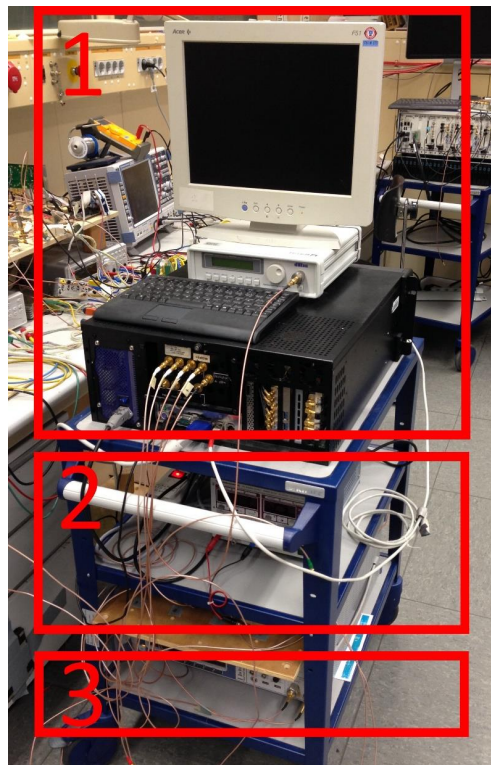


Figure 6.3: The EHS recording and playback unit

Attenuation of the Direct Path to the Receiver:

The SDARS signals are amplified by +15dB using LNAs before feeding the MEESAR PCB. The amplifiers however must not provide any additional amplification in the direction of the receiver. To implement this restriction, an attenuator is added before the receiver to compensate the generated gain as shown in Fig. 6.4.

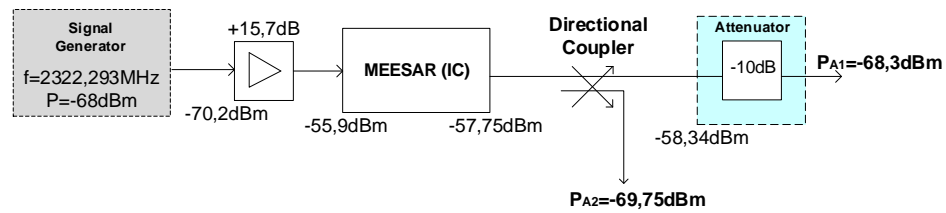


Figure 6.4: Signal path through the diversity system

The path of the third antenna in the MEESAR PCB was measured with a 0° phase shifter switched through. The signal generator was set to a power of $P = -68$ dBm and a frequency of $f = 2322.293$ MHz. Cable attenuation is of course taken into consideration. The used directional coupler does not split the signal symmetrically: a path is attenuated by about 1 dB and the other by 12 dB. This results in two different output powers, where P_{A1} is fed to the SDARS receiver and P_{A2} is supplied to the level detection.

Table 6.1: Measured power at the output of the MEESAR PCB

Phase	Power [dBm]
0°	-57.75
45°	-57.43
90°	-59.10
135°	-58.30
180°	-58.00
-135°	-57.54
-90°	-58.80
-45°	-58.22
Average Value	-58.14

The MEESAR PCB contains the phase shifters, switches and the combiner. The phase settings of the board lead to different attenuations. The output power for the different phase settings were measured and are summarized in Table 6.1.

The measurement campaign could only be carried out after the setup had been completely prepared, correctly programmed and optimized. All components were checked for their function so that a measurement could be performed in the overall system as depicted in Fig. 6.5.

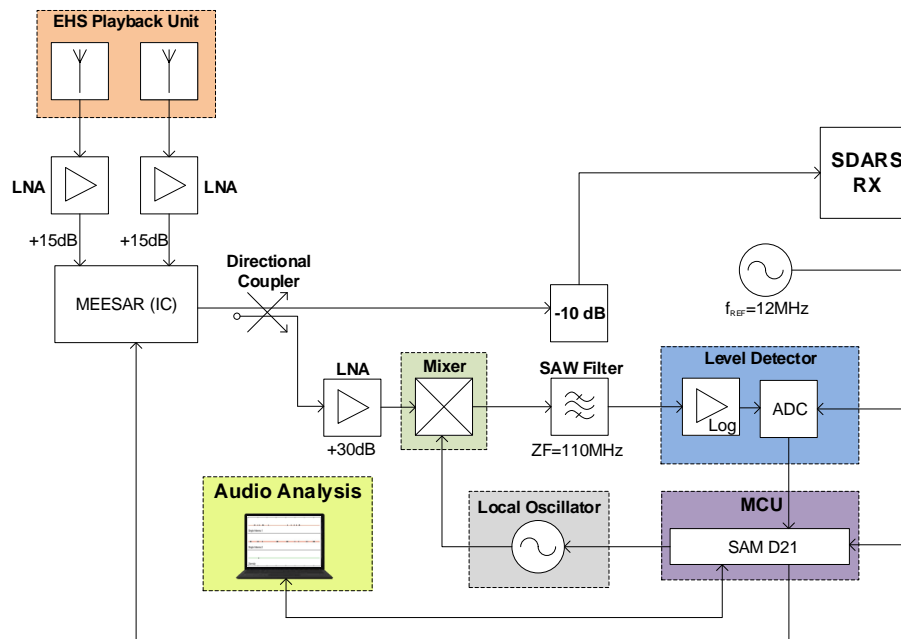


Figure 6.5: Block diagram of the lab setup

The played-back signals are amplified with +15 dB LNAs before feeding the MEESAR (IC) PCB. A small share of the output signal is amplified by 30dB, down-converted in frequency to 110 MHz and bandpass filtered by means of a surface acoustic wave filter. A logarithmic detector generates a voltage which is proportional to the signal level. This voltage is then converted to a digital value by means of an analog-to-digital converter (ADC). The micro-controller unit (MCU) reads these level measurement results and executes the diversity algorithm. The MCU controls the local oscillator for down-conversion, the phase shifters as well as the switches found within the MEESAR board. The other share of the signal, after the directional coupler, is attenuated by 10 dB before being led to the SDARS receiver. A laptop with an installed software is utilized to perform the audio analysis in order to investigate the performance of the diversity system and to prove its improvement in comparison to single antennas.

The implementation of the lab setup introduced in Fig. 6.5 is illustrated in Fig. 6.6. The corresponding system components (1) till (12), which are marked in red, are are fixated into a wooden board and are summarized in Table 6.2.

The used EHS recording and playback unit, as signal input for the system, is depicted in Fig. 6.3. Commercial SDARS receivers, which are deployed by the users in the USA, have been used during this measurement campaign. Concerning the phase display (3), the LEDs permit to better visualize the phase activity of the diversity algorithm.

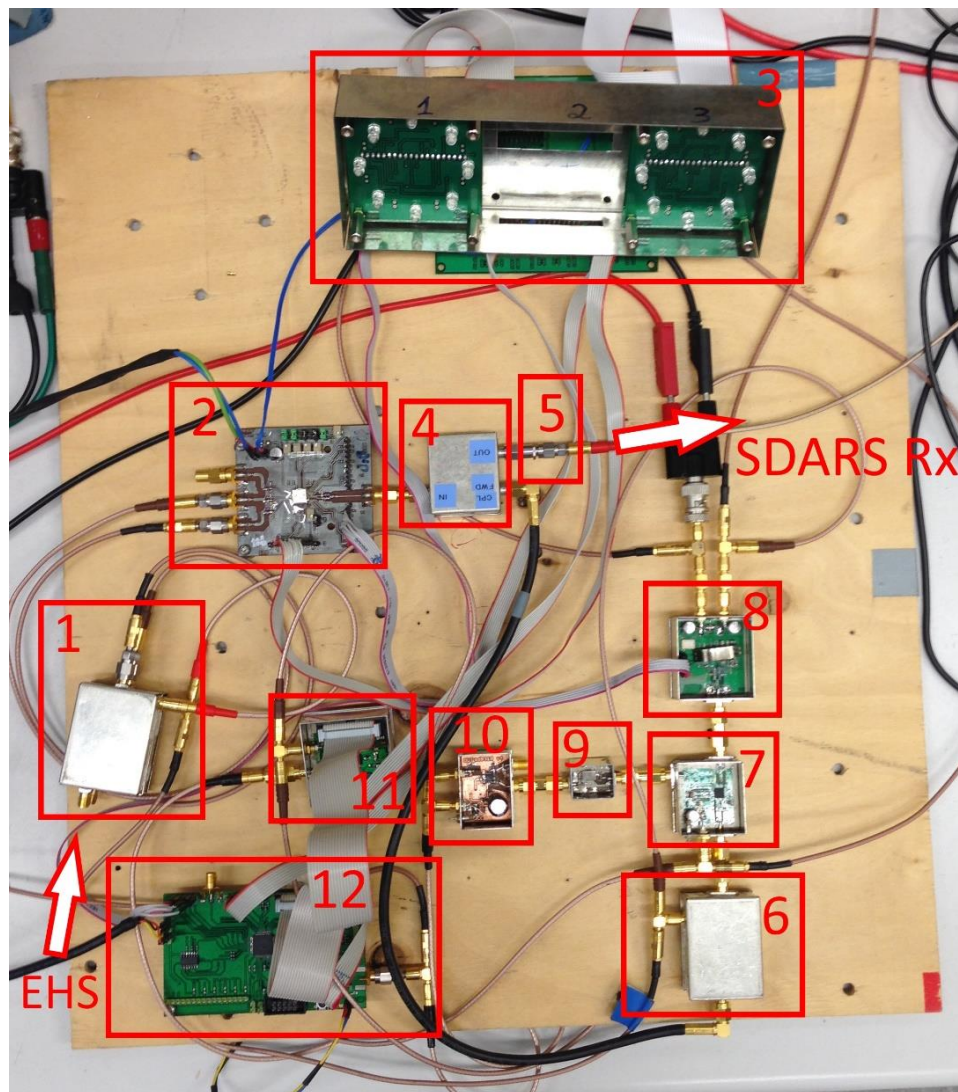


Figure 6.6: Lab setup including all components of the test board

Table 6.2: Components of the lab measurement board

Component	Description
(1)	2x LNAs (+15 dB)
(2)	Meesar IC
(3)	Display of the phases
(4)	Directional Coupler
(5)	Attenuator (-10 dB)
(6)	LNA (+30 dB)
(7)	Mixer
(8)	Local Oscillator
(9)	SAW Filter (110 MHz)
(10)	Logarithmic Amplifier
(11)	ADC (v6)
(12)	ARM MCU

Clocksystem:

The micro-controller SAM D21 can be clocked with different frequencies. There is the possibility to use different internal oscillators or even an external clock. The clock frequency can be multiplied by an internal DFLL as desired. With the DFLL, a maximum frequency of 48MHz can be achieved. To generate even higher frequencies (from 48MHz to 96MHz), the controller has an implemented Fractional Digital Phase Locked Loop (FDPLL). Furthermore, the internal clock generators have a divider that can be programmed. This allows almost any frequency to be generated. For this measurement campaign, an external square wave signal from a clock generator was utilized as main clock source. The clock generator was configured with a frequency of 12 MHz and the voltages $U_{\text{low}} = 0V$ and $U_{\text{high}} = +3.3V$.

ADC Characteristic-Curve:

Via USART connection to the audio analysis laptop, one can not only manually switch the antennas on and off, but also change the corresponding phases and perform a level measurement. Before performing the manual level measurement, a sine signal with known amplitude and frequency is generated by a signal generator. The logarithmic amplifier converts the sine signal into DC voltage, which is converted by the ADC into a digital value. To determine the ADC characteristic curve, input powers from -115 dBm to -48 dBm are fed into the measurement setup. The limits were chosen so that the lower values are within the noise range, and the upper ones reach the upper limit of the ADC.

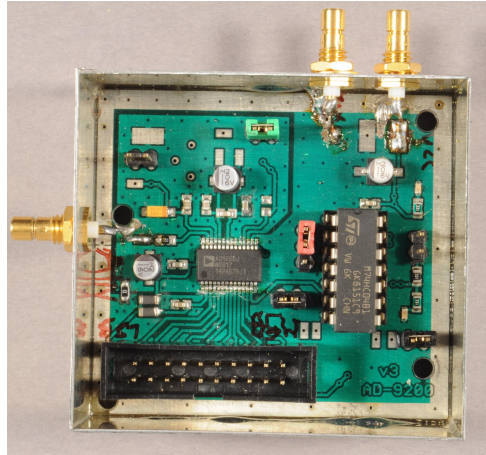


Figure 6.7: Circuit of ADC v3

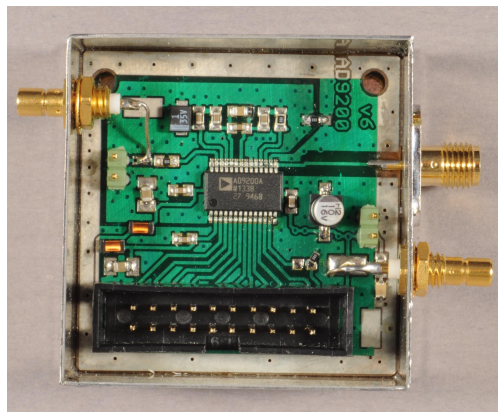


Figure 6.8: Circuit of ADC v6

Two ADC circuits were used for comparison. Both circuits have the same AD9200 chip from Analog Devices [83]. The ADC used has a 10-bit resolution and can thus generate levels from 0 to 1023. The chip is programmable by its external circuitry. In the setup used, input voltages from 0V to 2V can be achieved. The 0V cannot be reached completely, because the 30 dB amplifier also increases the noise level. The logarithmic amplifier has a minimum output voltage U_{\min} of 0.5V. The two circuits *v3* and *v6* differ mainly in the external circuitry. The version *v3* has an extensive circuit in order to adjust the run-time difference between the micro-controller and the ADC. This was completely removed in the newer version *v6*. The new ADC is operated with the same clock generator, so that no noticeable run-time difference is detected.

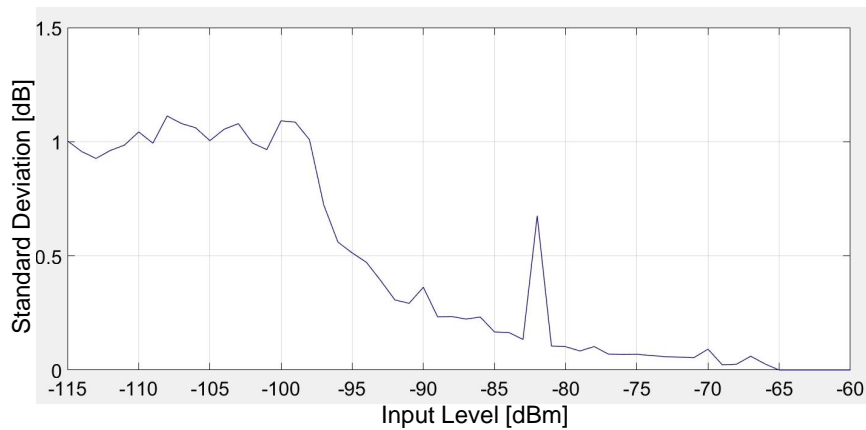


Figure 6.9: ADC v3 standard deviation of the characteristic curve

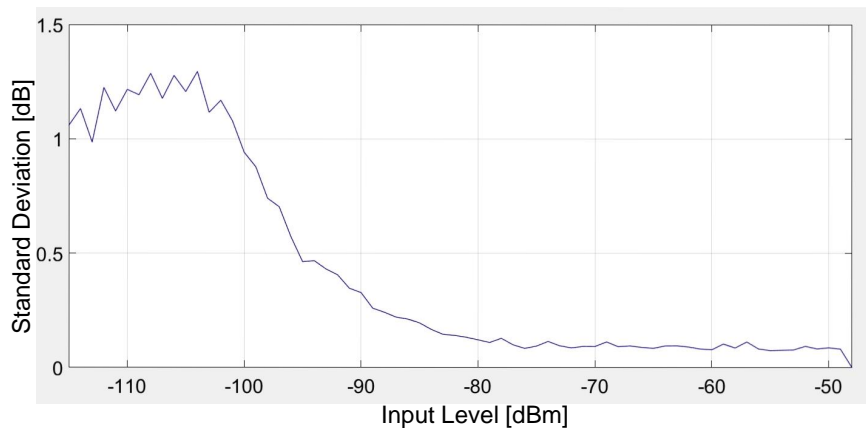


Figure 6.10: ADC v6 standard deviation of the characteristic curve

Because the wiring has been reduced in *v6*, unwanted additional noise sources disappear. In the previous version *v3*, these noise sources caused a distortion of the characteristic curve, which is clearly visible in the standard deviation. This source of error has been decimated by the new circuit as can be clearly noticed by comparing Fig. 6.9 and Fig. 6.10. With the old version of the ADC, the standard deviation at -78 dBm input level is considered high. This can contribute to phase errors and therefore deteriorate the audio availability of the system. Both characteristic curves are almost linear in the working range. The level values measured when determining the characteristic curve are used to calculate a LUT for the system. Fig. 6.11 and Fig. 6.12 show the characteristic curve and the linear ideal values for ADC v3 and ADC v6 respectively.

6.2 Diversity Measurements with initial IC Versions

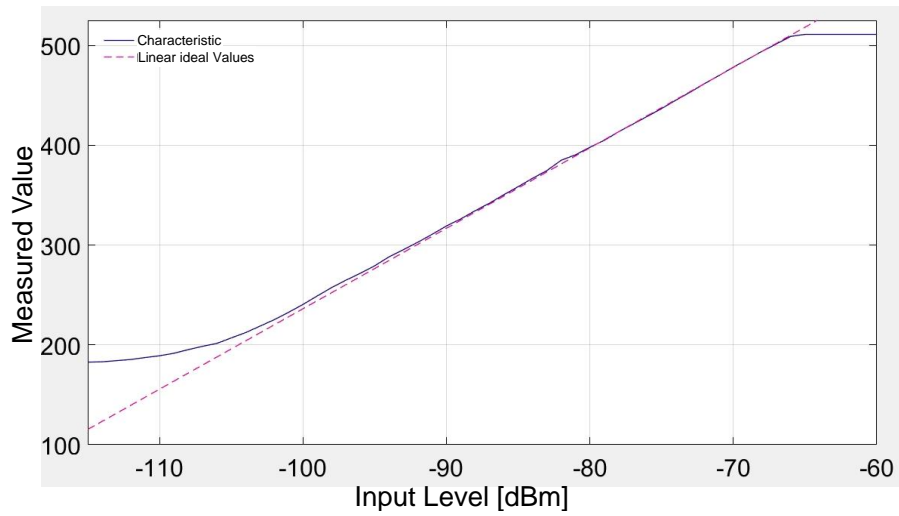


Figure 6.11: ADC v3 characteristic curve (solid) and the corresponding linear ideal values (dashed)

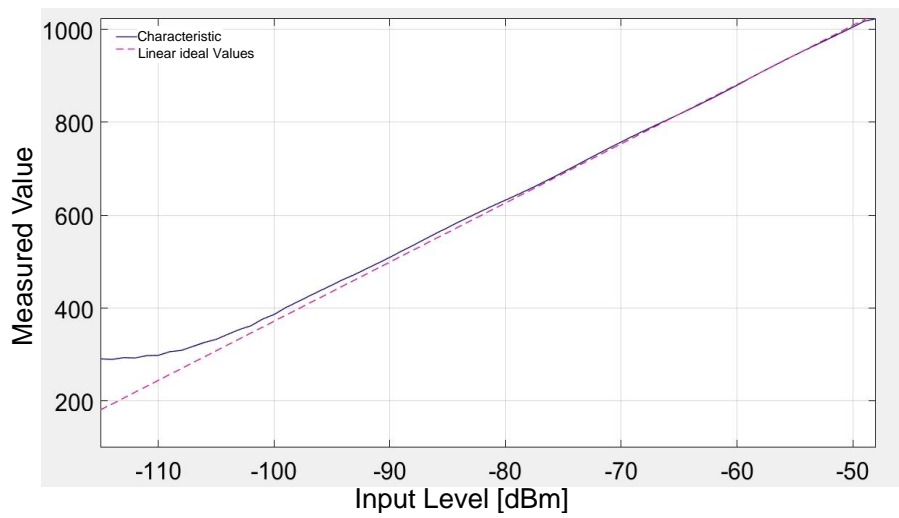


Figure 6.12: ADC v6 characteristic curve (solid) and the corresponding linear ideal values (dashed)

Sirius: Macro-Diversity Measurement

For the laboratory setup introduced in Fig. 6.6, a macro-diversity antenna set made up of two dislocated Sirius patch antennas mounted on the roof of the testing vehicle is taken into consideration. Figure 6.13 shows the patch antennas mounted on the vehicle, where one possesses an availability of 89.45% with 30.45s audio mutes over a testing time of 290s and the other one has an availability of 86.32% with 39.10s audio mutes over the same testing time.



Figure 6.13: Dislocated patch antennas on the rooftop of the vehicle

Measurements of the audio signal availability were taken for the two antennas of the macro-diversity set as individual single antennas and of the antenna diversity system. As the results given in Table 6.3 show, the mutes duration dropped from 34.78s to 5.27s showing an improvement in the audio availability from 88% up to 98.18%. This corresponds to a diversity efficiency of 1.78 when taking the best reference antenna (89.45% availability) into consideration.

Table 6.3: Average total audio mute duration of the single antennas as well as of the diversity system using the same input signals in a fading scenario.

	Audio Mutes [s]	Duration [s]	Avail. [%]	Mute Rate [%]
Single Ant.	34.78	290	88.00	12
DIV	5.27	290	98.18	1.82

This measurement campaign was one of the first to be performed with the initial MEESAR board along with the ARM micro-controller. Even though the diversity efficiency is below the expectation, further optimizations and improvements of the diversity efficiency are presented in the following sections.

6.2.2 Laboratory Setup with IC + Compact Level Detection PCB

The separate level detection components integrated on the test board introduced in section 6.2.1 are built into a single PCB to make the level detection system more compact. The main level detection components include:

Amplifier:

To linearly amplify the received satellite signals, the amplifier ERA-5XSM+ from Mini-Circuits [84] was utilized. This amplifier is suitable for applications with signals from 0 Hz to 4 GHz. It amplifies the signal with small fluctuations due to temperature changes. The amplifier requires a 5V power-supply with a current consumption of 85mA. During the system operation, it has been shown that the received signals can be amplified by approximately 10 dB.

Mixer:

The LTC5542 mixer from Linear Technology [85] was used as the mixer. This down-converter requires 1.6 - 2.7 GHz RF input signal and 1.7 - 2.5 GHz LO input frequency, making it ideal for the planned application. The mixed signal can be output in a frequency range of 5 - 500 MHz. The mixer requires a 3.3V power supply with a current consumption of 200 mA. The requirement was that the mixer outputs an IF of 110.592 MHz with a maximum fluctuation of 10 kHz.

Local Oscillator:

The LTC6948-3 local oscillator was used for the application. This local oscillator has already shown that a frequency change below 30 μ s is possible on average [79]. The LTC6948 series of local oscillators covers a wide frequency range from 373MHz to 6.39GHz. The LTC6948-3 is best suited for level measurement as the required LO frequencies can be set as center frequencies on the chip. The local oscillator requires a 3.3V supply at approximately 120mA and a 5V supply at approximately 48mA.

The following table shows the transmission frequencies of the SiriusXM satellites and the corresponding frequencies of the local oscillator to reach the required intermediate frequency of 110.592MHz. In addition to the transmission frequencies of the satellites, the frequencies of the terrestrial repeaters of the radio service are also listed.

Table 6.4: LO Frequencies for the SDARS system

	Satellite	Transmission Frequency	LO Frequency
Sirius	Sat1	$f_{RF1} = 2,322293$ GHz	$f_{LO1} = 2,211701$ GHz
	Terr.	$f_{RFT} = 2,326250$ GHz	$f_{LOT} = 2,215658$ GHz
	Sat2	$f_{RF2} = 2,330207$ GHz	$f_{LO2} = 2,219615$ GHz
XM	Sat1A	$f_{RF3} = 2,333465$ GHz	$f_{LO3} = 2,222873$ GHz
	Sat2A	$f_{RF4} = 2,335305$ GHz	$f_{LO4} = 2,224713$ GHz
	TerrA	$f_{RFTA} = 2,337490$ GHz	$f_{LOTA} = 2,226898$ GHz
	TerrB	$f_{RFTB} = 2,340020$ GHz	$f_{LOTB} = 2,229428$ GHz
	Sat2B	$f_{RF5} = 2,342205$ GHz	$f_{LO5} = 2,231613$ GHz
	Sat1B	$f_{RF6} = 2,344045$ GHz	$f_{LO6} = 2,233453$ GHz

SAW Filter:

As there are several signals at the output of the mixer apart from the desired mixed product, all irrelevant signals must be filtered out. Since only the intermediate frequency is interesting for the application, the SAW filter SF1056B from RFM (muRata) was used. The center frequency of the filter is 110.592MHz, which results in the intermediate frequency. The 3 dB bandwidth is 1.44MHz and the attenuation of the filter is, according to the data sheet [86], 10 dB maximum.

Logarithmic Amplifier:

The logarithmic converter is the AD8310 [87], a product of Analog Devices. The logarithmic converter converts signals up to 400MHz into a linear DC voltage. This logarithmic converter has a sensitivity range of -78dBm to 17dBm in which it operates linearly. The component requires a direct current of 8mA at a voltage supply of 3V.

Analog-to-Digital Converter:

The analog-to-digital converter AD9203 from Analog Devices was used in the application. This ADC has a resolution of 10 bits at a minimum sampling rate of 40MSPS. With a voltage supply of 3.3V, around 25mA are needed during operation.

Micro-Controller:

The SAM D21 J18A AUT micro-controller from Atmel was utilized. It also necessitates a power supply of 3.3V. It has a 256 kB flash memory and has a working frequency of 48MHz.

6.2.2.1 Preliminary Tests

Preliminary measurements for both the IC and level detection PCB are necessary in order to check the functionality of the single components. After that, diversity measurements can be conducted.

Figure 6.14 depicts both the IC and level detection PCB inside a protective case. This setup was used in order to perform measurement campaigns, which will be introduced later in this section.

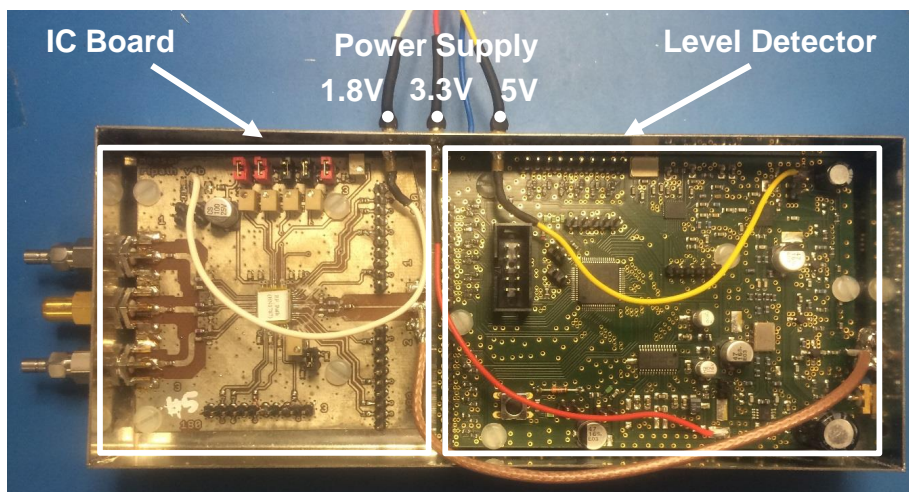


Figure 6.14: Measurement setup showing both the IC and level detection PCB

Level Detection PCB:

The spectrum as well as the signal power levels at the input and output of the system components were checked as an initial step. The measurements were carried out with the level detection board connected to the MEESAR board, since both boards are to be used together. The input 1 of the MEESAR board was fed with a lab-generated sine signal with the Sirius TDM1 frequency and with a constant power level of -50dBm .

Figure 6.15 illustrates the setup to perform the level measurements on the level detection PCB using a spectrum analyzer and a measuring probe. The following table gives an overview of the measurement points in Fig. 6.15 and the corresponding measurement results.

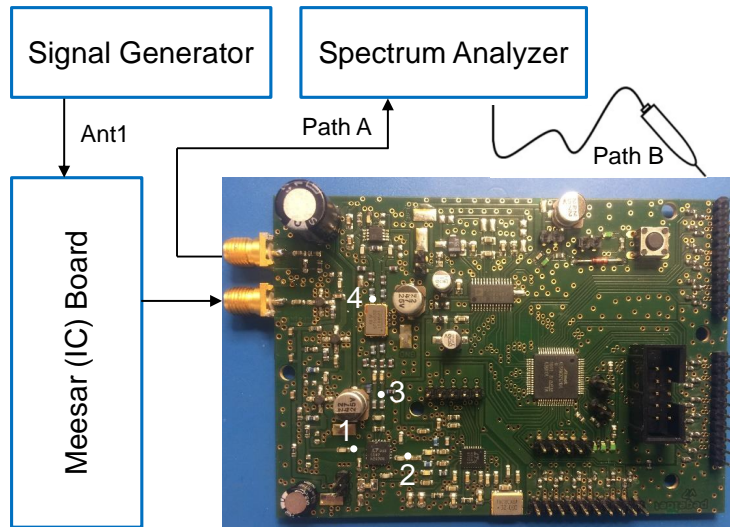


Figure 6.15: Preliminary test setup for the level detection PCB

Table 6.5: Measurement overview based on Fig. 6.15

Measuring Probe in Fig. 6.15 at	Description	Spectrum
Position 1	Mixer Input	Fig. 6.17
Position 2	LO Output	Fig. 6.18
Position 3	Mixer Output	Fig. 6.19
Position 4	SAW Output	Fig. 6.20

Figure 6.16 shows the spectrum at output of the level detection PCB using path A as introduced in Fig. 6.15. Figure 6.16 shows that of the -50dBm fed into the MEESAR board, only about 1 dB of power is lost. A power gain of 10 dB was actually expected at this measurement point. However, it was found that the power is attenuated by approximately 3 dB through the MEESAR board and the cables used in the laboratory have different attenuations of about 3.5 dB. It is worth mentioning there is a cable between the signal generator and the input of the IC board as well as another cable between the level detection PCB and the spectrum analyzer. For the measured power level in Fig. 6.16, only the cable for path A needs to be taken into account. In this case, it can be assumed that power level at the output of the level detector is around -47dBm .

It is now possible to investigate what happens to the signal at to the mixer input. Since the signal is running through two further amplifiers of 10 dB each, a significant power increase can be expected. The following measurements were

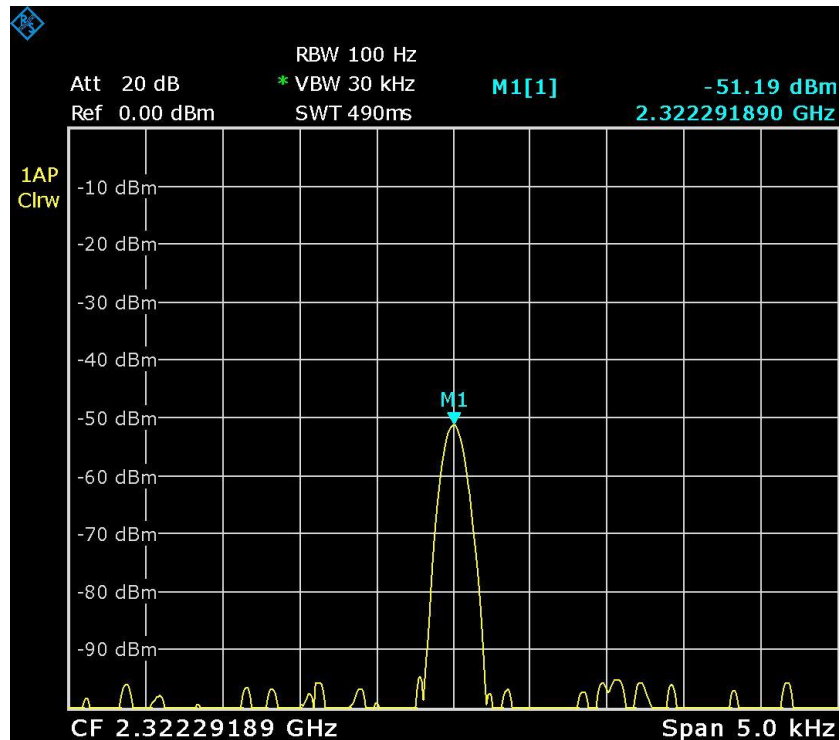


Figure 6.16: Spectrum at the output of the level detection PCB

made using the measuring probe, i.e. using path B in Fig. 6.15.

Figure 6.17 shows an increase in the signal power level. If the power level at the reference output of the PCB is about -47dBm, and two amplifiers are connected in series to the mixer input, a power level of -27dBm should be expected. However, Fig. 6.17 shows considerably less power at the mixer input.

One explanation is that the amplifiers do not amplify by the 10 dB as predicted in the data sheet and therefore component-related losses take place. Further losses are possible due to the measuring probe. The probe is located on the measuring point of the level detection PCB and the ground connection of the probe is held to the edge of the board by hand. The mass of the probe is therefore not correctly defined, which explains the small power losses.

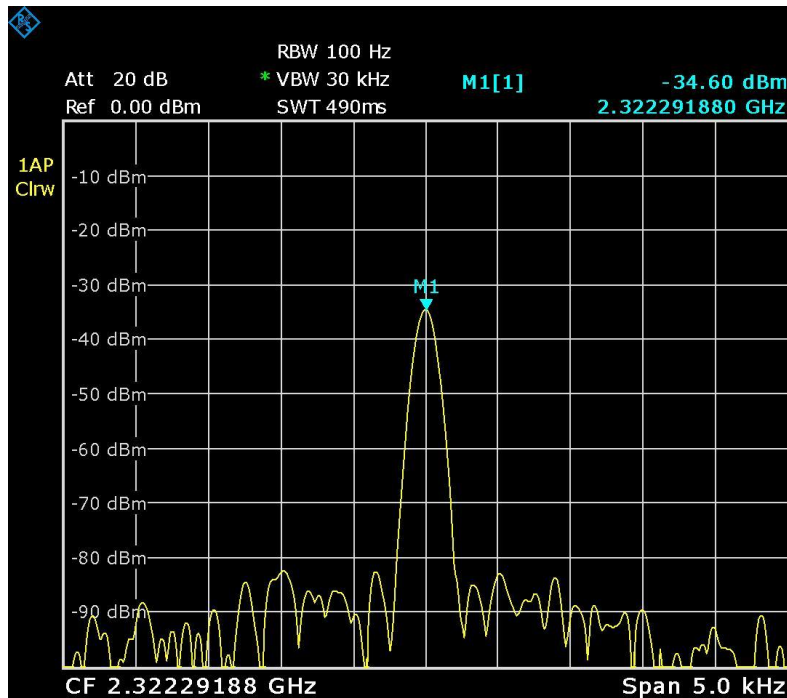


Figure 6.17: Spectrum at the input of the mixer (measurement point 1)

Figure 6.18 shows the spectrum of the signal generated by the local oscillator. A power level between 0dBm and 1dBm has been already measured at the LO output [79].

However, since the output could not be connected directly to the spectrum analyzer and the probe was also used, a small loss of power can be explained. It is also possible that this chip does not output exactly the same power as in previous measurements. However, this loss is minimal as the figure shows.

During the LO measurements, it could be noticed that the programmed frequency showed slight fluctuations. This happened whenever the PCB was not in operation for a longer period of time. So it can be assumed that the local oscillator needs a certain warm-up phase to run stable.

As soon as the board ran for two minutes, this phenomenon was no longer detectable. The local oscillator only fluctuated within its tolerance range of less than 1 kHz.

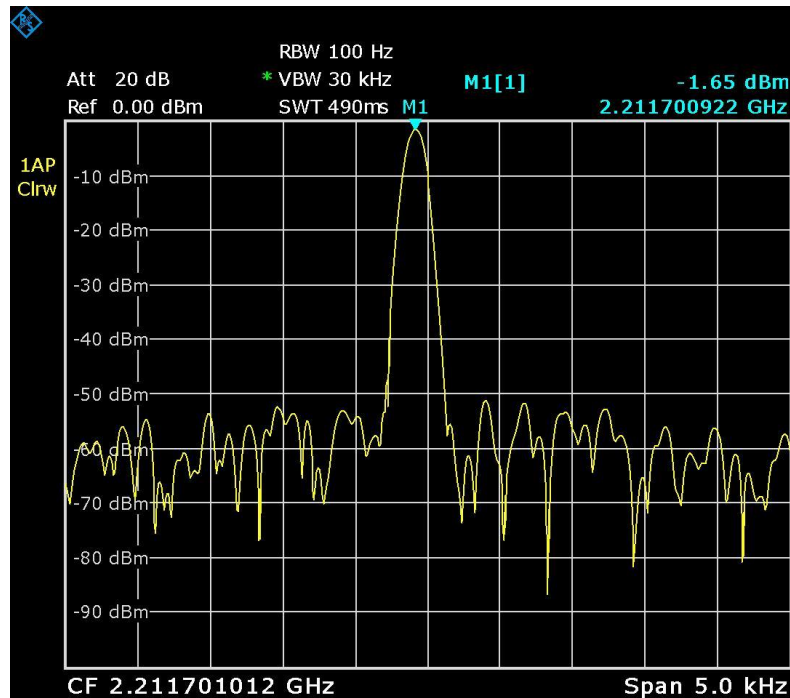


Figure 6.18: Spectrum at the output of the local oscillator (measurement point 2)

The two signals for the down-conversion are now available at the mixer. The intermediate frequency $f_{IF} = 110.592$ MHz should now be present at the output of the mixer. Figure 6.19 shows that the power level has reached an acceptable value of -17.28dBm. Of course there were additional undesired mixing products at the mixer output .

These products are suppressed by including a SAW filter at the mixer output. The intermediate frequency after the filter is shown in the Fig. 6.20. The intermediate frequency is exactly in the range that was expected. The deviation from 370 Hz is negligible. The maximum permitted frequency deviation of 10 kHz is not reached if the local oscillator frequency is set correctly. The figure also shows that the expected 10 dB power loss does not necessarily apply. Here the filter attenuated a little more than 5 dB.

In conclusion, it can be said that the components deliver the frequencies that were expected. Their power levels show negligible variations which do not affect the performance of the system.

6 Measurements with the Diversity System IC Chip

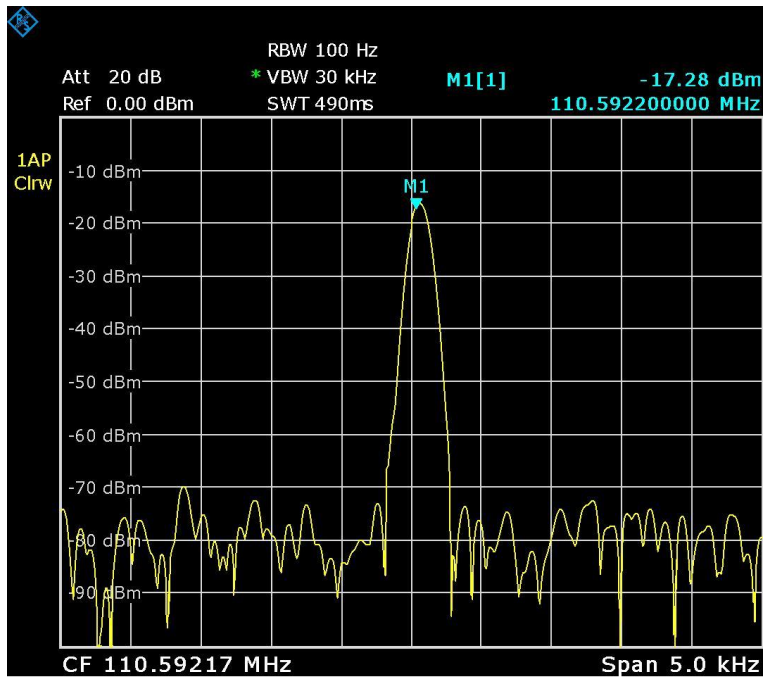


Figure 6.19: Spectrum at the output of the mixer (measurement point 3)

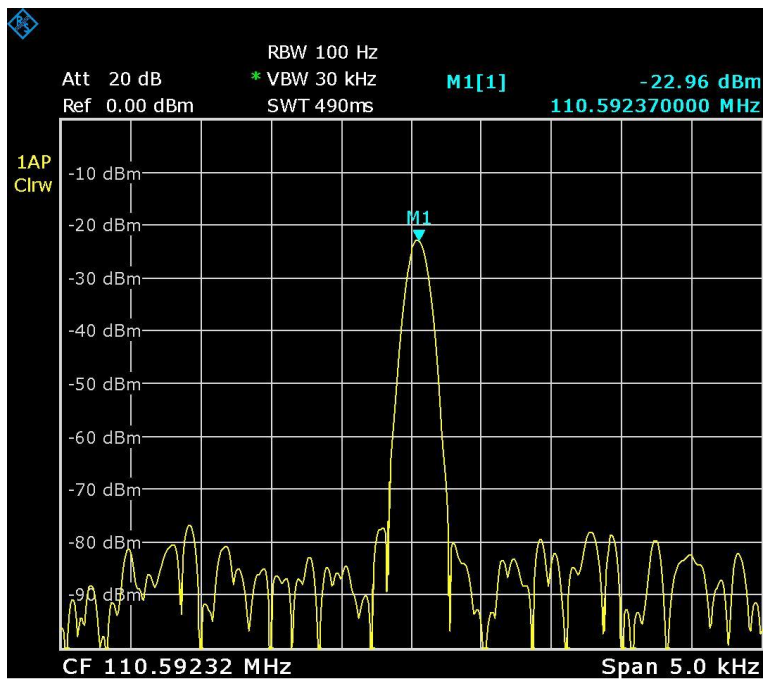


Figure 6.20: Spectrum at the output of the SAW filter (measurement point 4)

ADC Level Measurement:

To determine whether and how accurate the ADC works, a level measurement curve was generated and its standard deviation was determined. For this purpose, only the level detection PCB without the MEESAR board was utilized. A signal generator was set to the frequency of the Sirius TDM1 satellite and connected to the reference signal input of the level detector.

Via the USART-connection it is possible to perform various manual operations through the micro-controller. The MCU not only controls the phase shifters and switches of the IC-board but also is capable of configuring the LO frequency and displaying the result of ADC measurements.

For the level measurement, the range from -100dBm to -50dBm was considered, since experience has shown that the levels of the satellite signals can be expected within this dynamic range. In this area, the power level at the signal generator was manually increased (in steps of 1dB) and then the level measurement was performed. The ADC then passes to the MCU the level of the signal as a digital value. The micro-controller then transmits the result as a decimal number to the PC via the USART-connection.

The results of the level measurement curve and the corresponding standard deviation in dB are shown in Fig. 6.21 and Fig. 6.22 respectively. The level measurement curve shows a constant linear behavior starting from -90dBm. This curve is ideal for an ADC and should be considered for further applications.

However, the standard deviation is not particularly good up to an input level of -80dBm, where the fluctuation varies between 0.5dB and more than 1.5dB. The high deviations are caused by fluctuations in noise. From -80dBm to -70dBm, the standard deviation decreases further till it reaches around 0.1dB. For input levels larger than -70dBm, the standard deviation remains almost constant and does not exceed more than 0.1dB.

The accuracy of the level measurement curve of the ADC is important for the diversity algorithm. Out of the curve, a look-up-table (LUT) can be created, which in turn corrects the non-linearities. The LUT is stored in within the micro-controller.

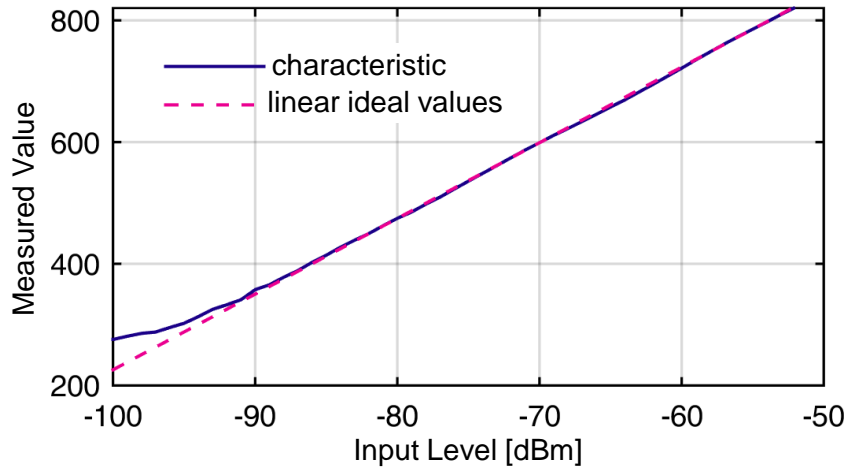


Figure 6.21: ADC level measurement curve of the level detector without the MEESAR board

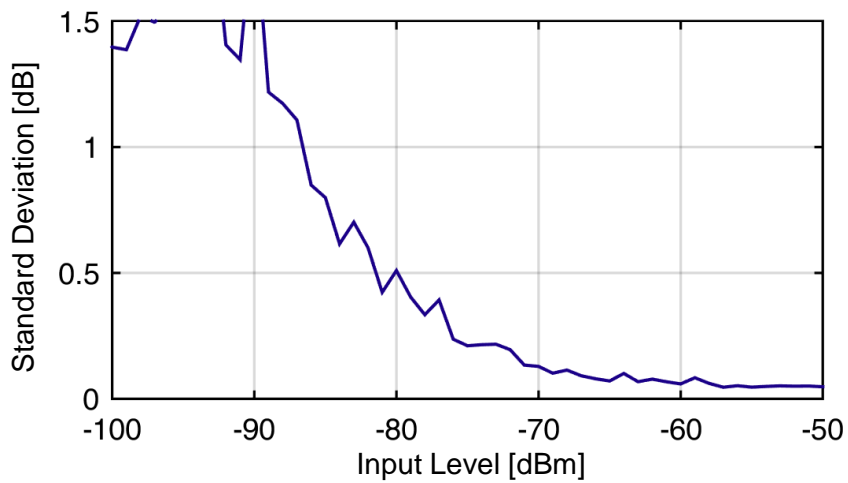


Figure 6.22: Standard deviation of the ADC level measurement curve of the level detector without the MEESAR board

Delay Time of the Logarithmic Level Measurement:

A capacitor with 470 pF is connected to the logarithmic output. This capacitor is necessary to smooth the output level of the logarithmic converter and to filter out high frequencies. The logarithmic converter does not immediately output the correct level as DC voltage as soon as the level at the input changes. It needs a certain time to output the correct level. This time must be taken into account in the at ADC.

A delay time must be initialized in the program so that the micro-controller waits until the correct level is applied to the input of the ADC and thus to the micro-controller. This delay time is directly related to the charging curve of the capacitor. Figure 6.23 shows the charge/discharge curve of the capacitor at the logarithmic converter (yellow curve). The charging and discharging time is 5 μ s each.

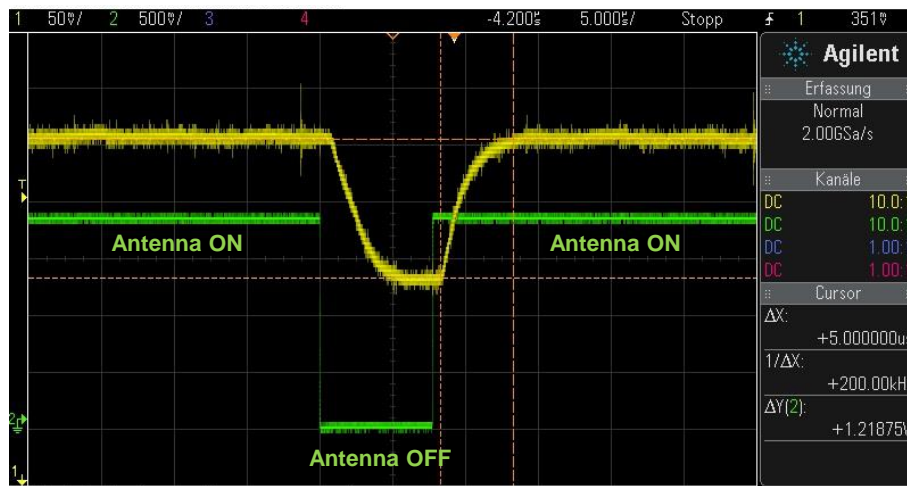


Figure 6.23: Charge/discharge curve (yellow) of the capacitor at the logarithmic converter

The green graph shows one of the pins controlling an antenna via the phase shifter. The antenna is at first switched on. After switching it off for a short time, the measured level changes and hence the capacitor discharges as can be seen in Fig. 6.23. The discharging process takes 5 μ s. After re-switching the antenna on, the measured level changes again, and the capacitor needs another 5 μ s before being re-charged. At this point the ADC can perform its task correctly, before handing over a digital value to the micro-controller.

Attenuation through the MEESAR (IC) Board:

In order to determine the attenuation of each antenna path for the different phases, an investigation was conducted. A sine signal with a constant power level of -50 dBm was fed by the signal generator at MEESAR board input. The output of the IC board was then connected via a cable to the input of the level detection board. In order to measure the level passing through both boards, a cable was led to the spectrum analyzer from the reference output of the level detector. The measurement setup corresponds to Fig. 6.15 using path A.

The version of the investigated IC board included amplifiers, phase shifters, switches and the combiner. Both the phase and the antenna path on the MEESAR board were modified manually while using the same sine signal at the input. The investigation results are summarized in the following table.

Table 6.6: Measured output power level through path A according to Fig. 6.15

Phase		Antenna	
Position	in °	Path 1	Path 3
0	135	-51.5 dBm	-51.0 dBm
1	90	-49.8 dBm	-51.3 dBm
2	45	-51.5 dBm	-51.3 dBm
3	0	-51.4 dBm	-52.0 dBm
4	-45	-52.0 dBm	-50.6 dBm
5	-90	-49.9 dBm	-51.3 dBm
6	-135	-51.8 dBm	-51.8 dBm
7	-180	-51.2 dBm	-52.4 dBm

In general, it can be noticed that the power level at the output is smaller than the power level at the input (-50 dBm). Antenna path 1 has a maximum difference of 2.2 dB regarding the measured power level at the different phases. This difference is 1.8 dB for the antenna path 3. Nevertheless, the attenuation caused by the MEESAR board can still not be deduced from the above measured values.

The calculation of the MEESAR board attenuation can however be performed by taking the system losses and gains shown in Fig. 6.24 into consideration. The measured power levels in the above table are going to be referred to as P_R in the following part.

Fig. 6.24 shows that the measurements were carried out with long cables which also have an attenuation that must be taken into account. The connecting cable between the boards is very short and can be neglected in the calculation.

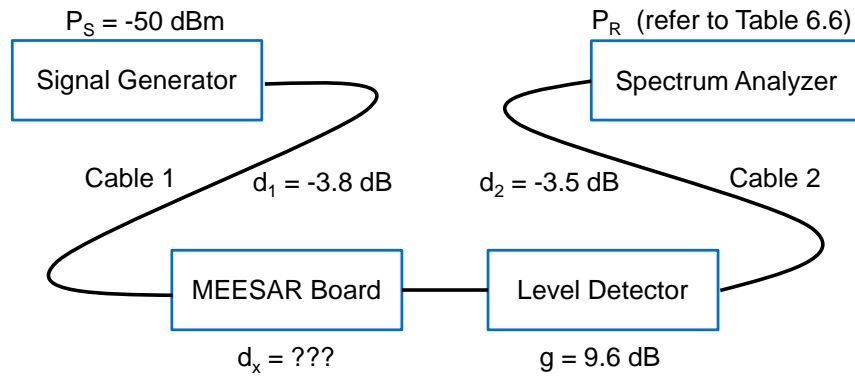


Figure 6.24: Setup to determine the attenuation of the MEESAR board

The MEESAR board attenuation d_x can be calculated as follows:

$$d_x = P_R - (P_S + d_1 + g + d_2), \quad (6.1)$$

where P_S is the generated input power level, d_1 and d_2 are the attenuation of cables 1 and 2 respectively, and g is the gain achieved by the level detection board. Equation 6.1 can be simplified because the input power, the attenuation of the cables and the amplification by the level detector remain constant. Hence, the following expression is obtained:

$$d_x = P_R - \underbrace{(P_S + d_1 + g + d_2)}_{-47.7 \text{ dBm}} \quad (6.2)$$

Since the attenuation d_x now only depends on the measured values in Table 6.6, the attenuation can be determined for each individual antenna path with the corresponding phase position. The results are listed in the table below.

Table 6.7: MEESAR attenuation results

Phase		d_x for Antenna	
Position	in °	Path 1	Path 3
0	135	-3.8 dB	-3.3 dB
1	90	-2.1 dB	-3.6 dB
2	45	-3.8 dB	-3.6 dB
3	0	-3.7 dB	-4.3 dB
4	-45	-4.3 dB	-2.9 dB
5	-90	-2.2 dB	-3.6 dB
6	-135	-4.1 dB	-4.1 dB
7	-180	-3.5 dB	-4.7 dB

There is a minimum attenuation of 2.1 dB for antenna path 1 and a minimum attenuation of 2.9 dB for antenna path 3. A maximum attenuation of 4.3vdB occurs for antenna path 1 and a maximum attenuation of 4.7 dB for antenna path 3. Although the attenuation of the MEESAR board is relatively low, it is not totally negligible. So in average, antenna path 1 has an attenuation of 3.44 dB and antenna path 3 an attenuation of 3.76 dB.

Due to the attenuation of the MEESAR board, a new ADC level characteristic curve was is measured. This time, the level measurement was done with the level detector in combination with the IC board. Due to the MEESAR board attenuation, the ADC level characteristic changes.

The ADC level measurement curve in Fig. 6.25 is for the antenna path 1 and phase position 0. The level measurement curve shows a constant linear behavior starting from -85dBm which is higher than the value shown by the level detector without the IC board (-90 dBm).

It was to be expected that the level measurement curve would be lower than the curve in Fig. 6.21, which is the case in the linear range. If we take the input level -60 dBm as an example, it can be clearly noticed that in Fig. 6.21 the measured value by the ADC is around 725. By taking the same input level of -60 dBm into consideration, we can see in Fig. 6.25 that the measured valued by the ADC is 675.

In the noise range, however, the level measurement curve is higher compared to the level measurement curve without the MEESAR board. If we take the input level -100 dBm as an example, it can be clearly noticed that in Fig. 6.21 the measured value by the ADC is around 280. By taking the same input level of -100 dBm into consideration, we can see in Fig. 6.25 that the measured valued by the ADC is 295.

This can be explained by the even worse standard deviation in this range by referring to Fig. 6.22 and Fig. 6.26. At the input level -80 dBm the standard deviation is 1dB, which is larger by 0.5 dB in comparison to the level detector without IC board. The standard deviation reaches the value 0.5 dB at around -85 dBm in Fig. 6.26. The standard deviation decreases till it reaches the value 0.1 dB at around -60 dBm input level. Just then, it remains constant at 0.1 dB.

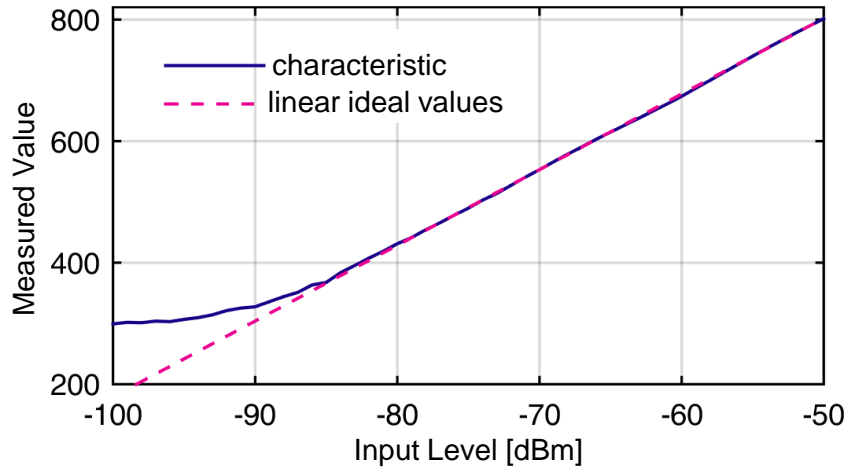


Figure 6.25: ADC level measurement curve of the level detector with the MEESAR board

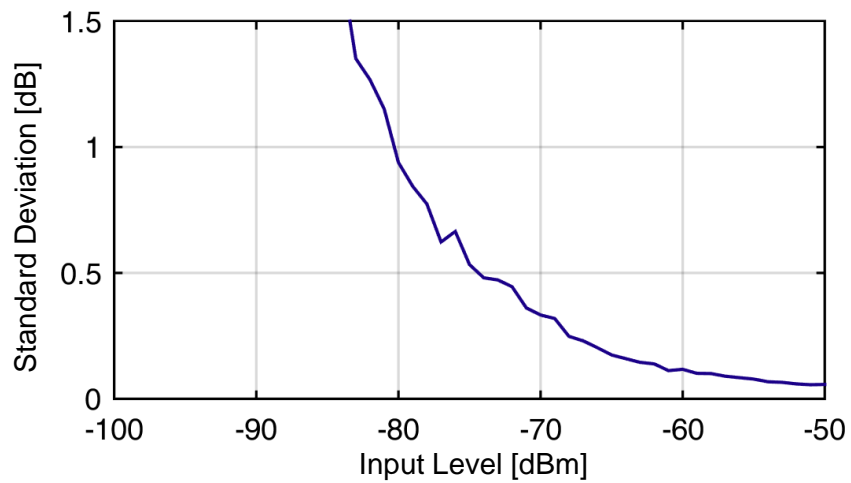


Figure 6.26: Standard deviation of the ADC level measurement curve of the level detector with the MEESAR board

Level Measurement with Pre-Amplifiers before the IC Board:

As will be later introduced, a setup is prepared by adding +15dB amplifiers at the MEESAR board input. For the audio analysis during the diversity measurements, the amplification is compensated with a corresponding attenuation at the level detector output.

Fig. 6.27 shows the setup in order to perform the measurement of the level curve with the pre-amplification at the antenna path 1. The exchange of data between the level detector and the analysis laptop is performed via an USART-connection.

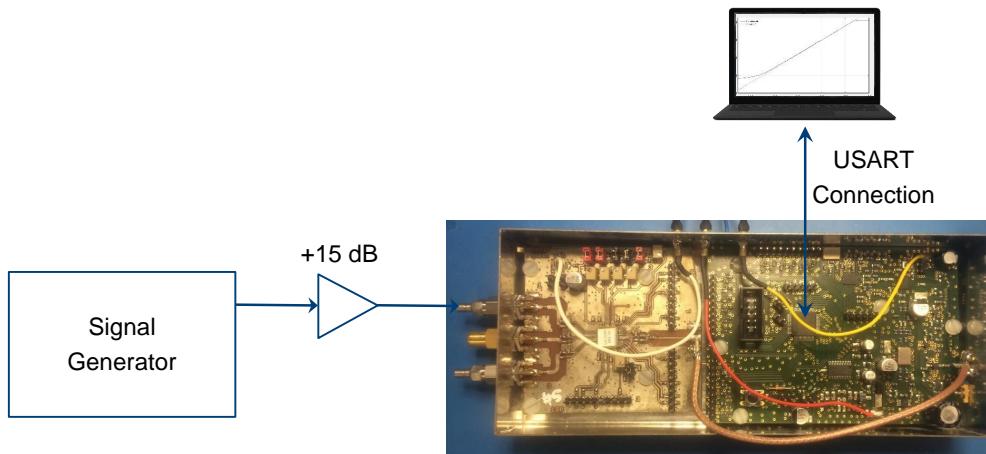


Figure 6.27: The setup to measure the level curve using pre-amplification before the MEESAR board

The level measurement curve shows a constant linear behavior starting from approximately -90 dBm. By taking the input level -60 dBm into consideration, we can see in Fig. 6.28 that the measured value by the ADC is around 820, which is higher than the value (675) delivered by the ADC in the non-amplified setup introduced in the previous section.

The standard deviation in dB is depicted in Fig. 6.29. The improvement is particularly noticeable in the low level (noise) range. A deviation of 0.5 dB is already achieved at an input level of -80 dBm. The deviation decreases further for the input level range from -80 dBm to -60 dBm to achieve a standard deviation of only around 0.04 dB. For input levels larger than -60 dBm, the standard deviation remains constant and low at 0.04 dB.

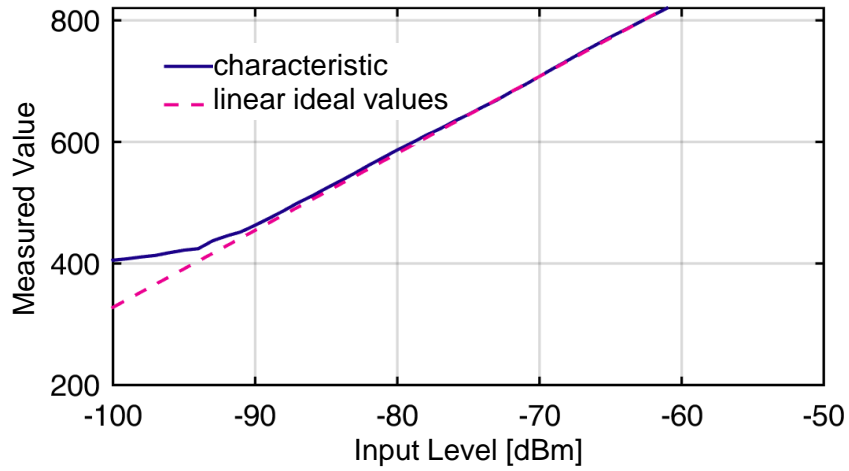


Figure 6.28: ADC level measurement curve of the level detector with the pre-amplified MEESAR board

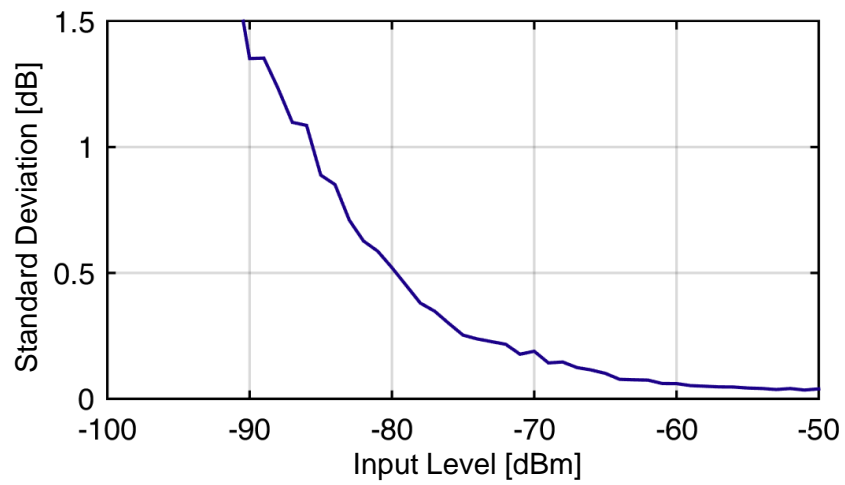


Figure 6.29: Standard deviation of the ADC level measurement curve of the level detector with the pre-amplified MEESAR board

Measurements with the internal ADC:

In order to make the level detector more compact, an investigation was conducted to observe how precise the ADC within the micro-controller is. If the internal ADC is accurate enough, the external ADC can be excluded from the level detector making the system even more cost-efficient.

A second level detection board was modified slightly by disconnecting the ADC (AD9203) from the power supply and by soldering the connection between the logarithmic converter and the micro-controller together, so that the MCU receives values directly from the logarithmic converter.

By this way, the internal ADC in the micro-controller should now be utilized instead of the previous external ADC. The program code was adapted accordingly to initialize the internal ADC. Apart from that, the measurement setup has not been further modified.

The internal ADC can be deployed with either 8-bit or 10-bit resolution. For this purpose, both possibilities were examined. Fig. 6.30 and Fig. 6.31 depict the internal ADC level measurement with a resolution of 8-bits and 10-bits respectively. Both measurements were performed with the +15 dB pre-amplified MEESAR board.

The level measurement curve of the internal 10-bit ADC is very similar to the behavior of the external ADC level measurement in Fig. 6.28. Both setups work with the same number of bits, which means that the levels are divided identically. The level curve of the 8-bit internal ADC is much flatter than the previous level curves, but just as linear as before.

Concerning the standard deviation of the 8-bit and 10-bit ADC shown in Fig. 6.32 and Fig. 6.33, there are noticeable differences. The internal 8-bit ADC generally shows a rather high standard deviation even in areas where the signal level is quite high. The internal 10-bit ADC is much better in comparison. However, the standard deviations of both internal ADCs show no improvement over the external AD9203. It can, nevertheless, be noticed that standard deviation of the 10-bit ADC is comparable to the standard deviation of the external ADC.

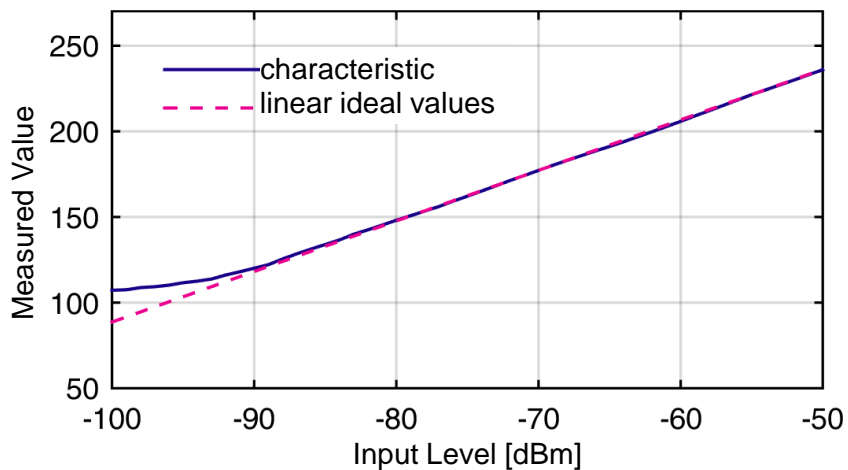


Figure 6.30: The internal ADC level measurement with a resolution of 8-bits and with the pre-amplified MEESAR board

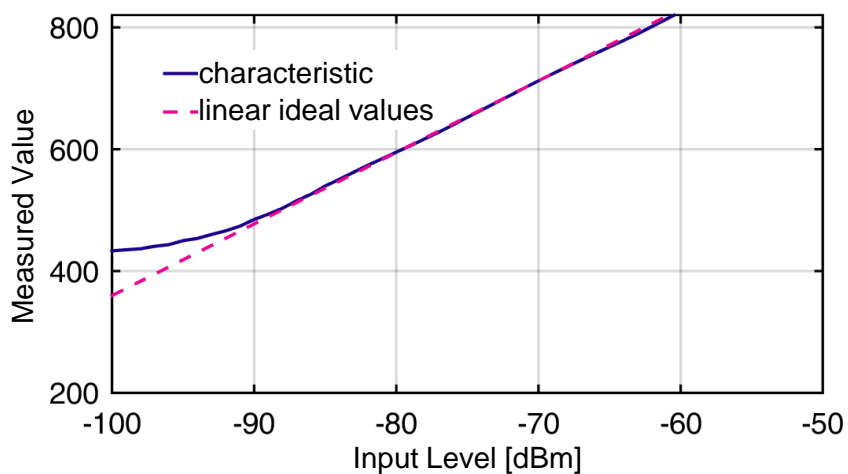


Figure 6.31: The internal ADC level measurement with a resolution of 10-bits and with the pre-amplified MEESAR board

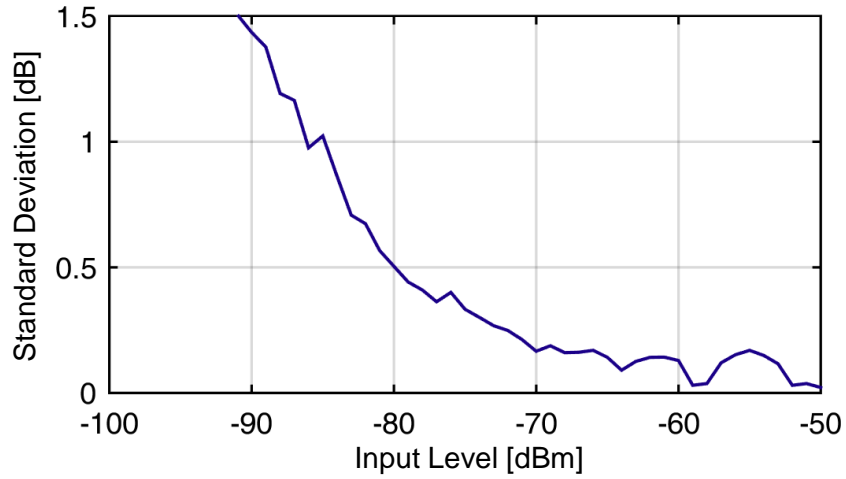


Figure 6.32: Standard deviation of the internal ADC level measurement with a resolution of 8-bits and with the pre-amplified MEESAR board

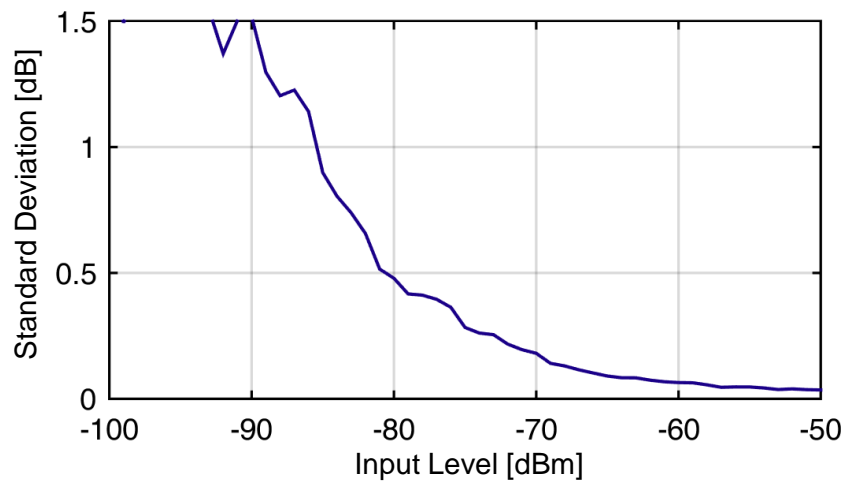


Figure 6.33: Standard deviation of the internal ADC level measurement with a resolution of 10-bits and with the pre-amplified MEESAR board

Diversity Measurements with the external ADC & no Pre-Amplification:

For the laboratory setup introduced in Fig. 6.34, a macro-diversity antenna set made up of two dislocated Sirius patch antennas mounted on the roof of the testing vehicle is taken into consideration. One antenna possesses an availability of 89.45% with 30.45s audio mutes over a testing time of 290s and the other one has an availability of 86.32% with 39.10s audio mutes over the same testing time. Standard after-market receivers for Sirius Satellite Radio have been used for the measurements.

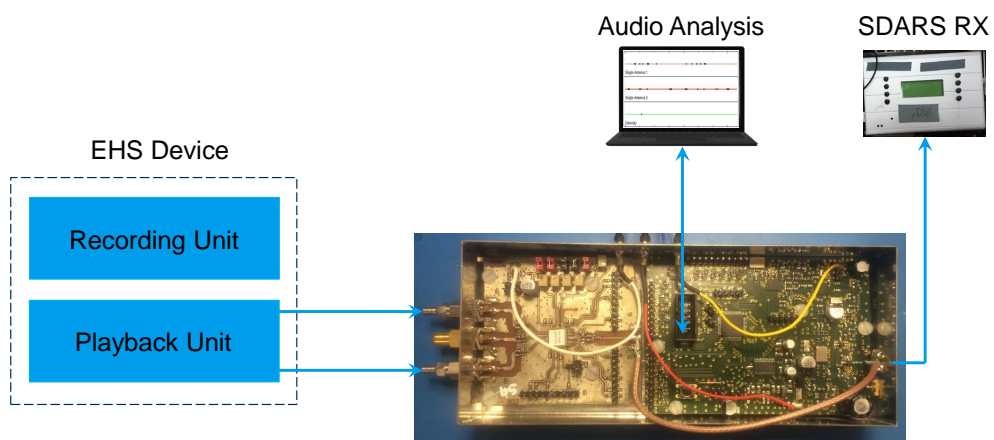


Figure 6.34: Laboratory setup to perform the diversity measurements with the external ADC and without pre-amplification at the MEESAR board input

Measurements of the audio signal availability were taken for the two antennas of the macro-diversity set as individual single antennas and of the antenna diversity system. As the results given in Table 6.8 show, the mutes duration dropped from 34.78s to 4.23s showing an improvement in the audio availability from 88% up to 98.54%.

This corresponds to a diversity efficiency of 1.88 when taking the best reference antenna (89.45% availability) into consideration.

Table 6.8: Average total audio mute duration of the single antennas as well as of the diversity system using the same input signals in a fading scenario.

	Audio Mutes [s]	Duration [s]	Avail. [%]	Mute Rate [%]
Single Ant.	34.78	290	88.00	12
DIV	4.23	290	98.54	1.46

Diversity Measurements with the external ADC & Pre-Amplification:

For the laboratory setup introduced in Fig. 6.35, a macro-diversity antenna set made up of two dislocated Sirius patch antennas mounted on the roof of the testing vehicle is taken into consideration. One antenna possesses an availability of 89.45% with 30.45s audio mutes over a testing time of 290s and the other one has an availability of 86.32% with 39.10s audio mutes over the same testing time. Standard after-market receivers for Sirius Satellite Radio have been used for the measurements.

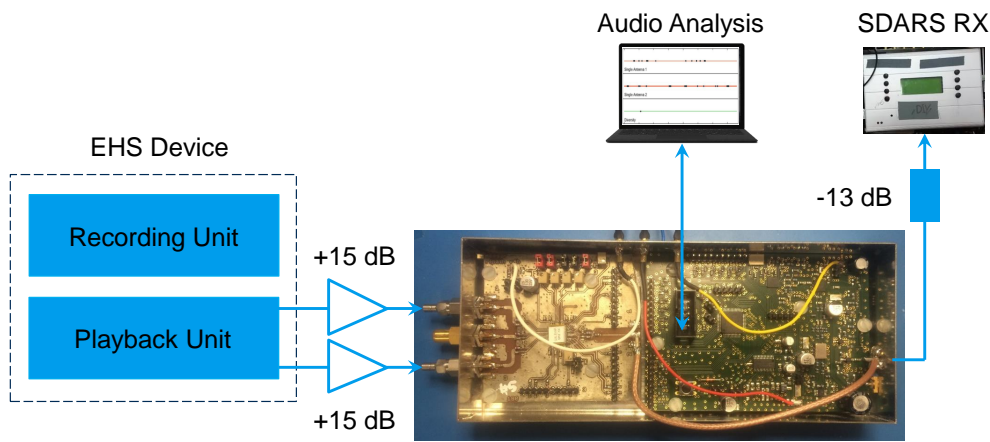


Figure 6.35: Laboratory setup to perform the diversity measurements with the external ADC and with pre-amplification at the MEESAR board input

Measurements of the audio signal availability were taken for the two antennas of the macro-diversity set as individual single antennas and of the antenna diversity system. As the results given in Table 6.9 show, the mutes duration dropped from 34.78s to 3.20s showing an improvement in the audio availability from 88% up to 98.90%.

This corresponds to a diversity efficiency of 2.00 when taking the best reference antenna (89.45% availability) into consideration.

Table 6.9: Average total audio mute duration of the single antennas as well as of the diversity system using the same input signals in a fading scenario.

	Audio Mutes [s]	Duration [s]	Avail. [%]	Mute Rate [%]
Single Ant.	34.78	290	88.00	12
DIV	3.20	290	98.90	1.10

Diversity Measurements with the 10-bit internal ADC & Pre-Amplification:

For the laboratory setup introduced in Fig. 6.36, a macro-diversity antenna set made up of two dislocated Sirius patch antennas mounted on the roof of the testing vehicle is taken into consideration. One antenna possesses an availability of 89.45% with 30.45s audio mutes over a testing time of 290s and the other one has an availability of 86.32% with 39.10s audio mutes over the same testing time. Standard after-market receivers for Sirius Satellite Radio have been used for the measurements.

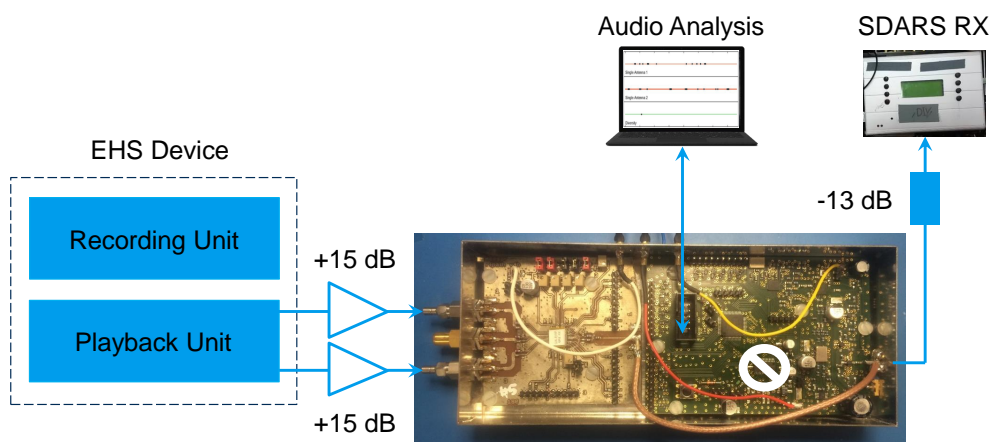


Figure 6.36: Laboratory setup to perform the diversity measurements with the 10-bit internal ADC and with pre-amplification at the MEESAR board input

Measurements of the audio signal availability were taken for the two antennas of the macro-diversity set as individual single antennas and of the antenna diversity system. As the results given in Table 6.10 show, the mutes duration dropped from 34.78s to 4.03s showing an improvement in the audio availability from 88% up to 98.61%.

This corresponds to a diversity efficiency of 1.90 when taking the best reference antenna (89.45% availability) into consideration.

Table 6.10: Average total audio mute duration of the single antennas as well as of the diversity system using the same input signals in a fading scenario.

	Audio Mutes [s]	Duration [s]	Avail. [%]	Mute Rate [%]
Single Ant.	34.78	290	88.00	12
DIV	4.03	290	98.61	1.39

6.3 Diversity Measurements with the advanced IC Version

For analysis of the system performance of the IC based antenna diversity with integrated frequency down-conversion, recorded signals by means of the equipment introduced in 4.5.2 from real fading scenarios as described in section 4.5.1 are utilized. In the following, the results of laboratory investigations with different setups are presented.

6.3.1 Laboratory Setup with external ADC

Fig. 6.37 describes the laboratory setup used in order to perform the measurements with the antenna diversity module including the IC. The IC consists of LNAs, RF switches, phase-alignment and signal combining components as well as the frequency conversion (PLL and mixer) for level detection.

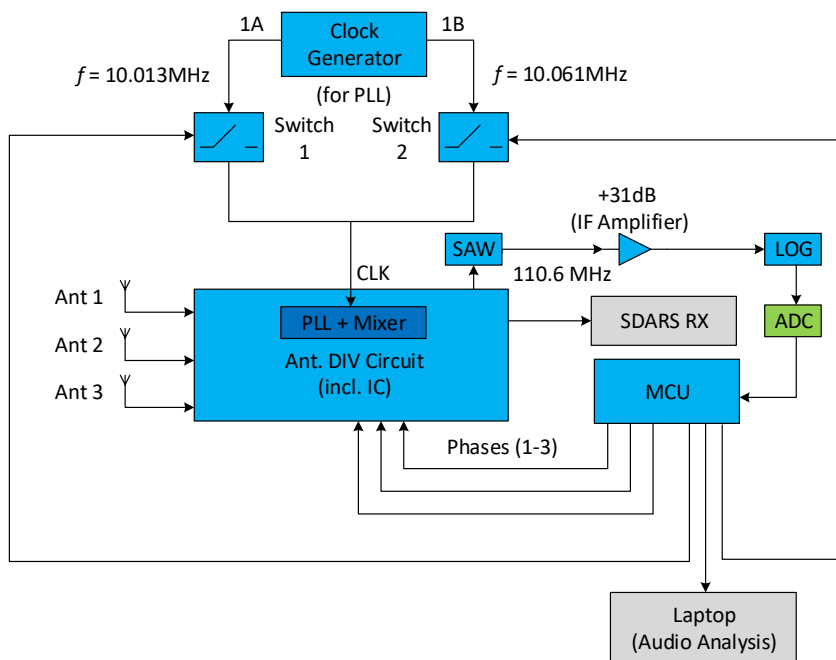


Figure 6.37: Measurement setup in the laboratory with an external ADC

An external reference clock for the PLL is used. A SAW Filter ensures the IF filtering at 110.6 MHz before the amplification with +31 dB. Preceding the MCU a logarithmic detector in addition to an ADC are inserted. The MCU controls the phases of the antenna diversity circuit as well as the switches after the external reference clock.

Fig.6.38 depicts the laboratory setup according to Fig. 6.37. It can be clearly observed that RF switches, phase shifters, combiners, LNAs, PLLs and mixers are no longer external components as they are integrated in the IC chip. Standard after-market receivers for XM Satellite Radio have been used for the measurements.

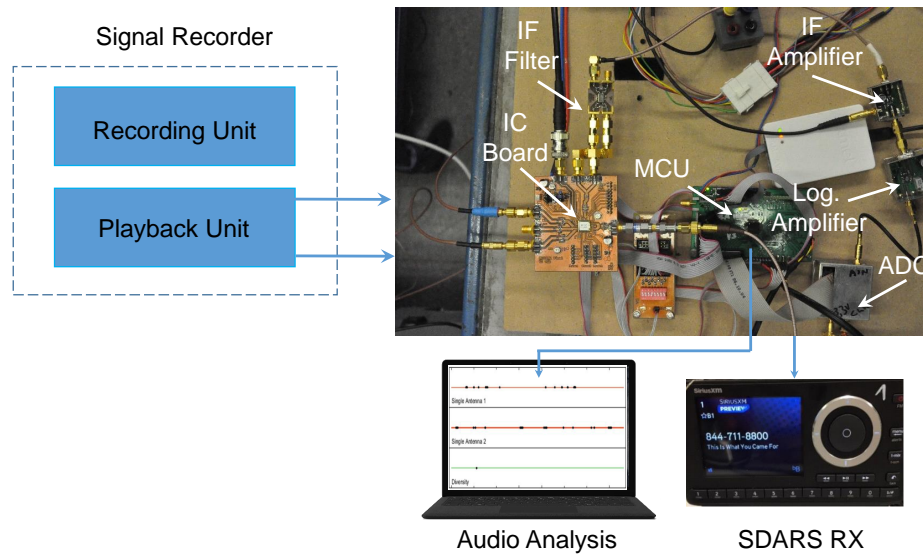


Figure 6.38: Lab Setup including all components

6.3.1.1 XM-SAT1A: Macro-Diversity Measurement

A measurement campaign has been performed using this laboratory setup. As the results given in Table 6.11 show, the mute duration dropped from 21.74s to 1.85s showing a significant improvement in the audio availability from 94.28% up to 99.51%.

Table 6.11: Average total audio mute duration of the single antennas as well as of the diversity system using the same input signals in a fading scenario.

	Audio Mutes [s]	Duration [s]	Avail. [%]	Mute Rate [%]
Single Ant.	21.74	380	94.28	5.72
DIV	1.85	380	99.51	0.49

6.3.2 Laboratory Setup with internal ADC

As a measure to reduce the number of components outside the antenna diversity circuit module, a micro-controller unit with an internal ADC has been utilized.

Fig. 6.39 describes the laboratory setup used in order to perform the measurements with the antenna diversity module including the IC. The IC consists of LNAs, RF switches, phase-alignment and signal combining components as well as the frequency conversion (PLL and mixer) for level detection.

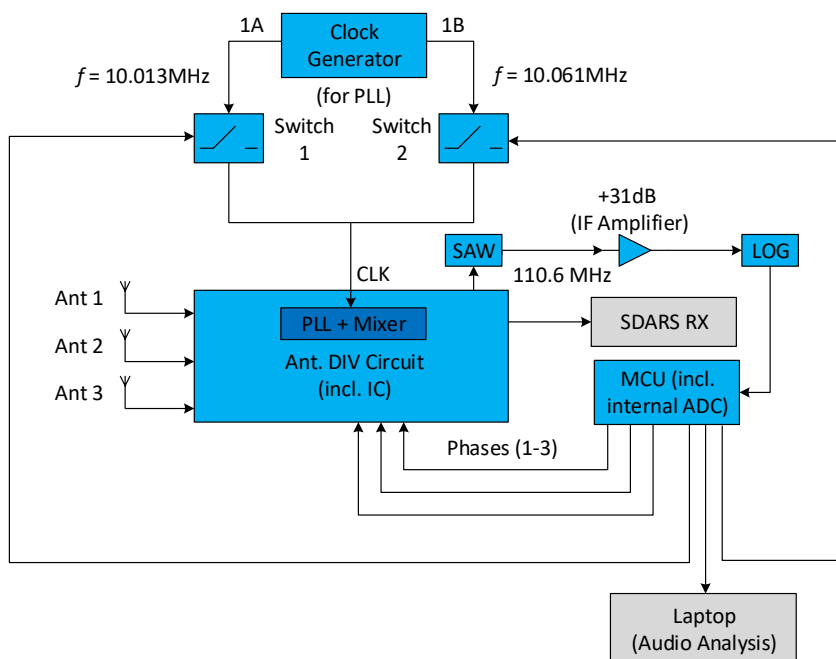


Figure 6.39: Measurement setup in the laboratory with an internal ADC

An external reference clock for the PLL is used. A SAW Filter ensures the IF filtering at 110.6 MHz before the amplification with +31 dB. Preceding the MCU a logarithmic detector is inserted. The MCU not only converts the analog signal into a digital one through its internal ADC but also controls the phases of the antenna diversity circuit as well as the switches after the external reference clock.

Fig.6.40 depicts the final laboratory setup according to Fig. 6.39. It can be clearly observed that RF switches, phase shifters, combiners, LNAs, PLLs and mixers are no longer external components as they are integrated in the IC chip.

6.3 Diversity Measurements with the advanced IC Version

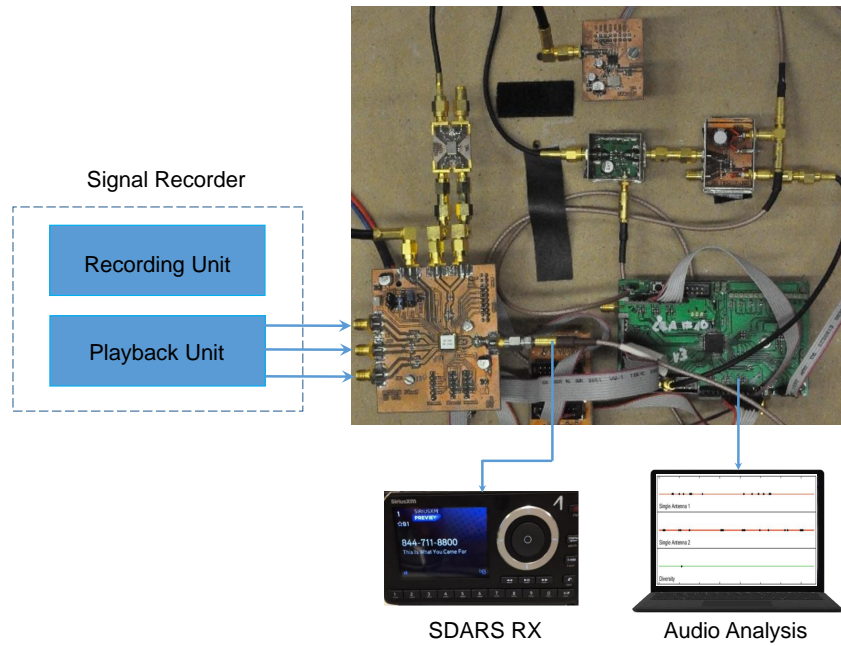


Figure 6.40: Lab Setup including all components

The only visible external components include the SAW filter, IF amplifier, the logarithmic detector, the micro-controller and the reference clock for the PLL inside the IC antenna diversity circuit. Even though the components are external they have small dimensions as shown in Fig. 6.41.

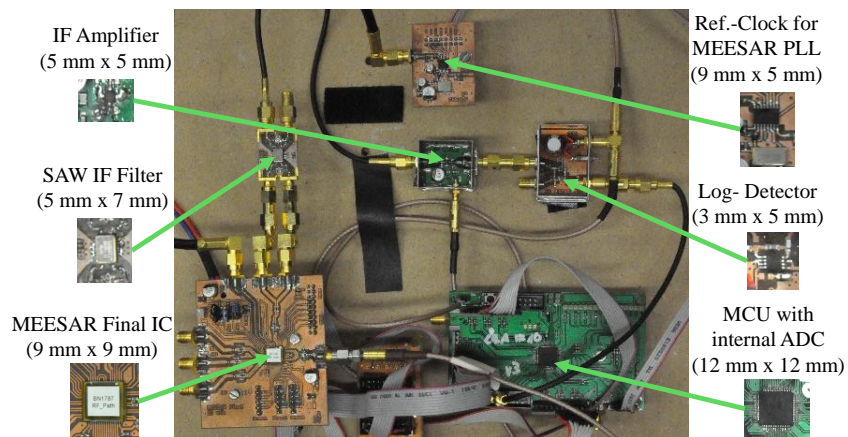


Figure 6.41: Lab Setup with the dimensions of the components

In the following, investigations including the fourth test constellation P_T with $\pm 45^\circ$ resolution in addition to the three-antenna algorithm are presented.

6.3.2.1 XM-SAT1A: Micro-Diversity Measurement

A micro-diversity antenna set made up of two loop antennas has been mounted on one of the side mirrors of the test vehicle. Standard after-market receivers for XM Satellite Radio have been used for the measurements.

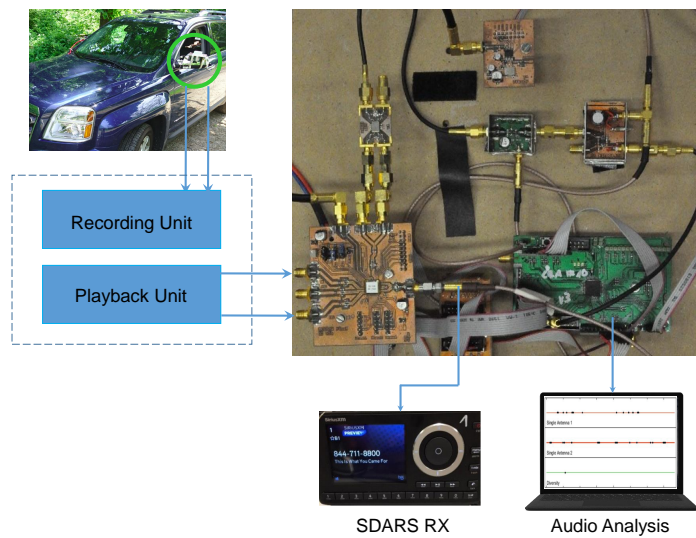


Figure 6.42: Laboratory setup for the micro-diversity measurement

Fig. 6.42 depicts the laboratory setup used to perform the measurement of the final IC. The signals have been played back and fed into the circuits inputs.

Measurements of the audio signal availability were taken for the two antennas of the micro-diversity set as individual single antennas and of the antenna diversity system. As the results given in Table 6.12 show, the duration of the audio mutes has dropped from 8.53s to 0.87s showing a significant improvement in the audio availability from 97.75% up to 99.77%.

Table 6.12: Average total audio mute duration of the single antennas as well as of the micro-diversity system using the same input signals in a fading scenario.

	Audio Mutes [s]	Duration [s]	Avail. [%]	Mute Rate [%]
Single Ant.	8.53	380	97.75	2.25
Diversity	0.87	380	99.77	0.23

6.3.2.2 XM-SAT1A: Macro-Diversity Measurement

Two dislocated reference patch antennas mounted on the hood of the car are taken into consideration. Standard after-market receivers for XM Satellite Radio have been used for the measurements.

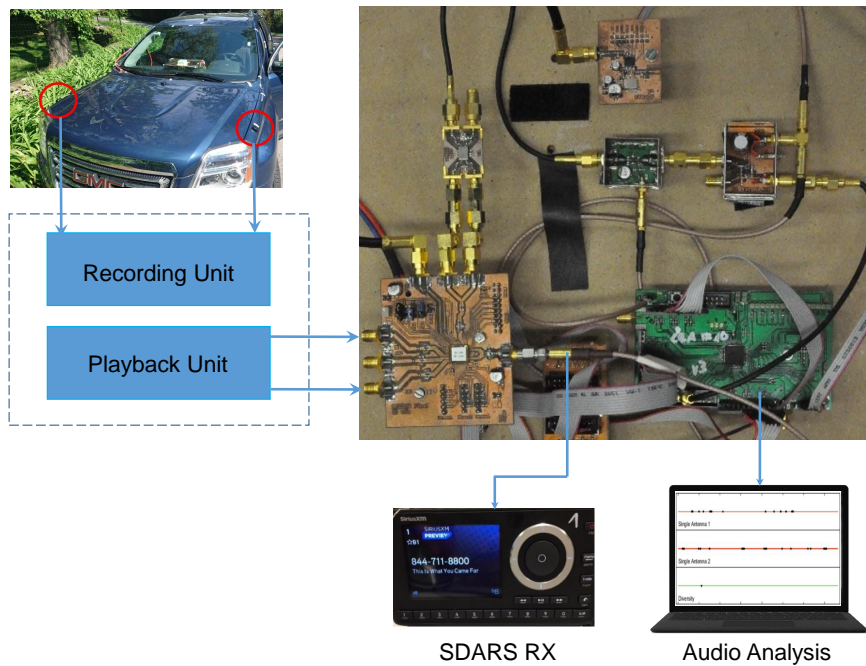


Figure 6.43: Laboratory setup for the macro-diversity measurement

Fig. 6.43 depicts the laboratory setup used to perform the measurement of the final IC. The signals have been played back and fed into the circuits inputs.

Measurements of the audio signal availability were taken for the two antennas of the macro-diversity set as individual single antennas and of the antenna diversity system. As the results given in Table 6.13 show, the duration of the audio mutes has dropped from 12.87s to 0.77s showing a significant improvement in the audio availability from 96.61% up to 99.79%.

Table 6.13: Average total audio mute duration of the single antennas as well as of the macro-diversity system using the same input signals in a fading scenario.

	Audio Mutes [s]	Duration [s]	Avail. [%]	Mute Rate [%]
Single Ant.	12.87	380	96.61	3.39
DIV	0.77	380	99.79	0.20

XM-SAT1A: Macro-Diversity Measurement / P_T with 45°

The previous measurements were performed using P_T with 90° resolution as already shown in equation 4.17. The phase of antenna 1 is rotated by $+90^\circ$ and then the sum with antenna 2 is calculated. The equation can also be described as follows:

$$P_{T,90} \sim |\underline{A}_1 \cdot e^{+j90^\circ} + \underline{A}_2|^2 \tag{6.3}$$

Further measurements were conducted using P_T with 45° resolution where the phase of antenna 1 is rotated by $+45^\circ$ and the phase of antenna 2 by -45° . Afterwards the sum is calculated. The equation is described as follows:

$$P_{T,45} \sim |\underline{A}_1 \cdot e^{+j45^\circ} + \underline{A}_2 \cdot e^{-j45^\circ}|^2 \tag{6.4}$$

Fig. 6.44 depicts the laboratory setup used to perform the measurement and verification of P_T with 45° resolution. The signals have been played back and fed into the circuits inputs.

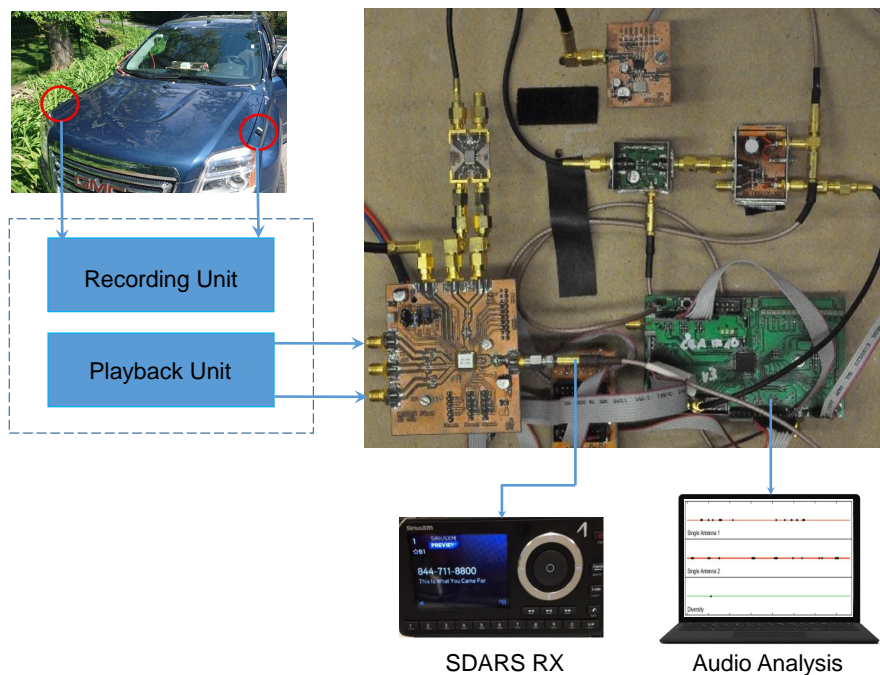


Figure 6.44: Laboratory setup for the macro-diversity measurement with 45° resolution of P_T .

Table 6.14: Average total audio mute duration of the single antennas as well as of the macro-diversity system with 90° and 45° resolution using the same input signals in a fading scenario.

	Audio Mutes [s]	Duration [s]	Avail. [%]	Mute Rate [%]
Single Ant.	12.87	380	96.61	3.39
DIV (90°)	0.77	380	99.79	0.20
DIV (45°)	0.48	380	99.87	0.13

As can be observed in Table 6.14, applying the 45° resolution instead of 90° contributed to a further improvement in the overall audio availability which increased from 99.79% to 99.87%.

The audio mutes represented by black dots for both single reference antennas as well as the diversity configuration with the 45° resolution over a total time of 380 s are depicted in Fig. 6.45. The presented recordings correspond to individual measurements which have been selected to closely match the average mute durations in Table 6.14. It can be clearly noticed how the number of mutes is reduced by diversity with 45° resolution in comparison to both single antennas.

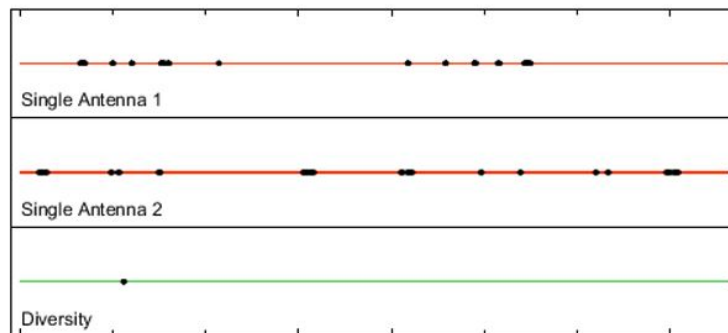


Figure 6.45: Measured audio mutes of individual measurements of the single reference antennas in comparison to diversity with 45° resolution.

6.3.2.3 Three Antenna Algorithm

In order to further increase the diversity efficiency and to benefit from all three antenna inputs of the antenna diversity system with integrated circuit a three antenna algorithm is investigated which can be a basis of the multi-channel algorithm presented in chapter 5 before. Out of the three available antennas Ant_1 , Ant_2 and Ant_3 , the one with the best SNR is defined to be the primary antenna (Ant_{prim}). One of the two remaining antennas is chosen to be the secondary antenna (Ant_{sec}). At first the initial (default) switching status is set as the phase aligned sum of the primary and secondary antenna.

The current antenna level is measured. If it exceeds a pre-defined diversity threshold (div_threshold), the switching status of the current antenna remains unmodified since the antenna level is satisfactory for reception and there is no necessity for any switching or phase alignment. Otherwise, the initialization of the three antenna algorithm is triggered.

The algorithm begins by performing a series of four test constellations in order to measure the power levels $P_{1,\text{prim}}(f)$ and $P_{2,\text{sec}}(f)$ of the primary and secondary antennas respectively. The powers $P_{1,\text{prim}}(f)$ and $P_{2,\text{sec}}(f)$, which are proportional to the squared absolute value of the complex wave amplitudes $A_{1,\text{prim}}(f)$ and $A_{2,\text{sec}}(f)$ respectively, as well as the power $P_s(f)$ of the sum $S(f)$ of these amplitudes are measured. Afterwards, the antenna signal $A_{1,\text{prim}}(f)$ is rotated by 90° in phase and added to the other antenna signal $A_{2,\text{sec}}(f)$. The corresponding sum power $P_T(f)$ is then measured. The frequency dependent variables $C(f)$, $U(f)$, $V(f)$ and $W(f)$ are derived from the calculated powers according to the equations 5.3, 5.4, 5.5 and 5.6 respectively. Consequently, the parameters $S_0(\Delta\alpha, \Delta\beta, f)$, $S_{90}(\Delta\alpha, \Delta\beta, f)$ are calculated according to the equations 5.1, 5.2 and $S_I(\Delta\alpha, \Delta\beta, f)$, $S_Q(\Delta\alpha, \Delta\beta, f)$ according to the equations 5.7 and 5.8. The parameters $p_{\text{BE},I}(\Delta\alpha, \Delta\beta, f)$ and $p_{\text{BE},Q}(\Delta\alpha, \Delta\beta, f)$ are derived from the SNR values to evaluate the bit errors in the I- and the Q-channel respectively according to equations 5.9 and 5.10. For the probability of a bit error in the I- or Q-channel, $p_{\text{total}}(\Delta\alpha, \Delta\beta, f)$ is derived in equation 5.11.

The estimation of the overall bit error probability $p_{\text{eval}}(\Delta\alpha, \Delta\beta)$ is calculated according to equation 5.12. Now we optimize $\Delta\alpha$ and $\Delta\beta$ in a way that $p_{\text{eval}}(\Delta\alpha, \Delta\beta)$ is minimized. As a result of the minimization, the phase shift values $\Delta\alpha_{\text{min}}$ and $\Delta\beta_{\text{min}}$ are then realized in the variable phase shifters of the diversity circuit in order to obtain the improved signal-to-noise ratio for the radio. Every 40 ms the error probability of the secondary antenna is checked to determine whether it does not exceed a pre-defined threshold (3_ant_thr). If the pre-defined threshold is not exceeded the secondary antenna Ant_{sec} switches to the third antenna. The time counter ($3_ant_counter$) is reset every 40ms. The flowchart of the three antenna algorithm is depicted in Fig. 6.46.

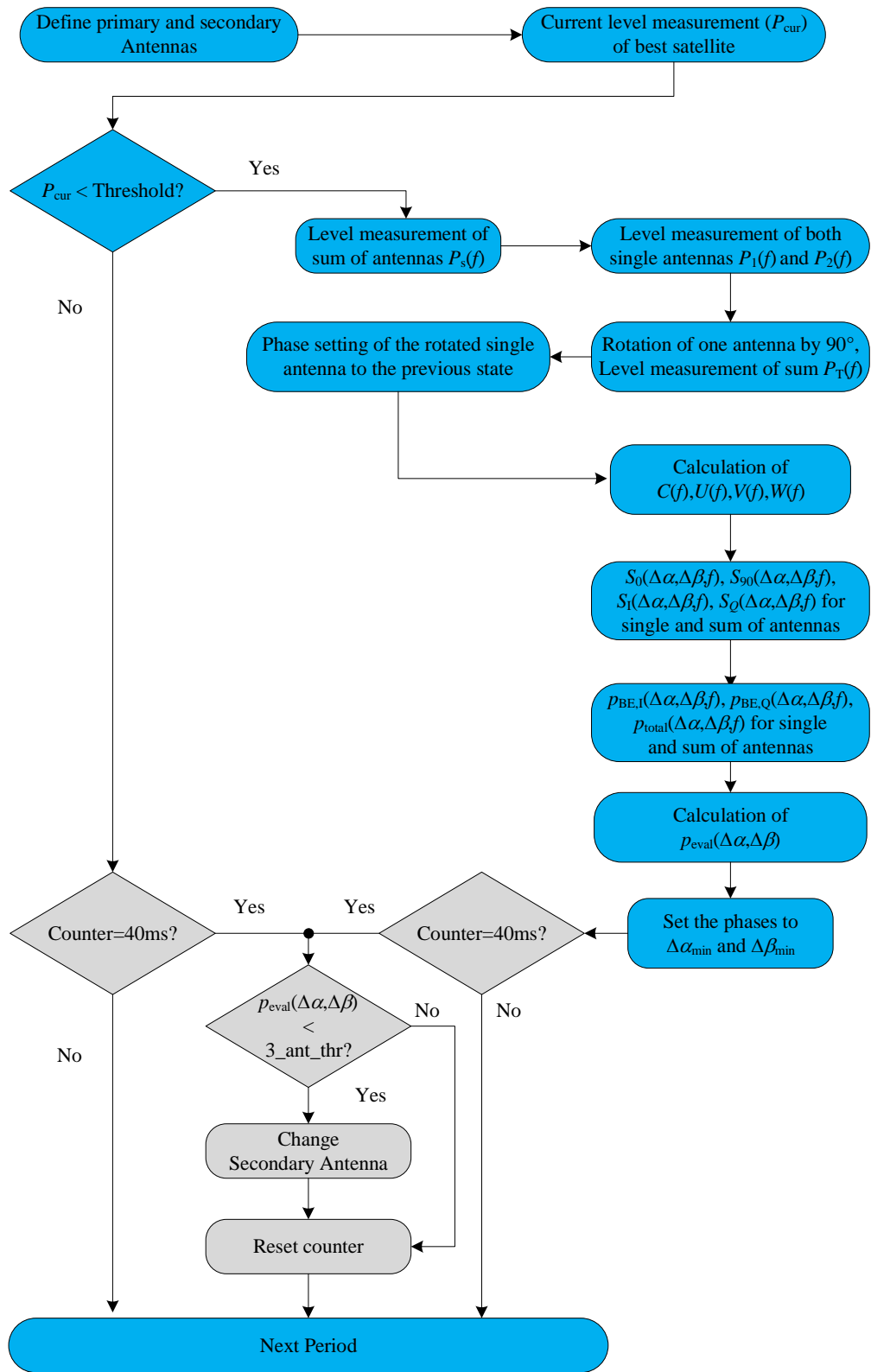


Figure 6.46: Flowchart of three antenna algorithm.

In order to verify the introduced algorithm, a measurement campaign in the laboratory was performed using recorded signals possessing a Rayleigh fading behavior from test drives in the USA. Fig. 6.47 illustrates the block diagram of the laboratory setup which was used during the test series to validate the three antenna algorithm.

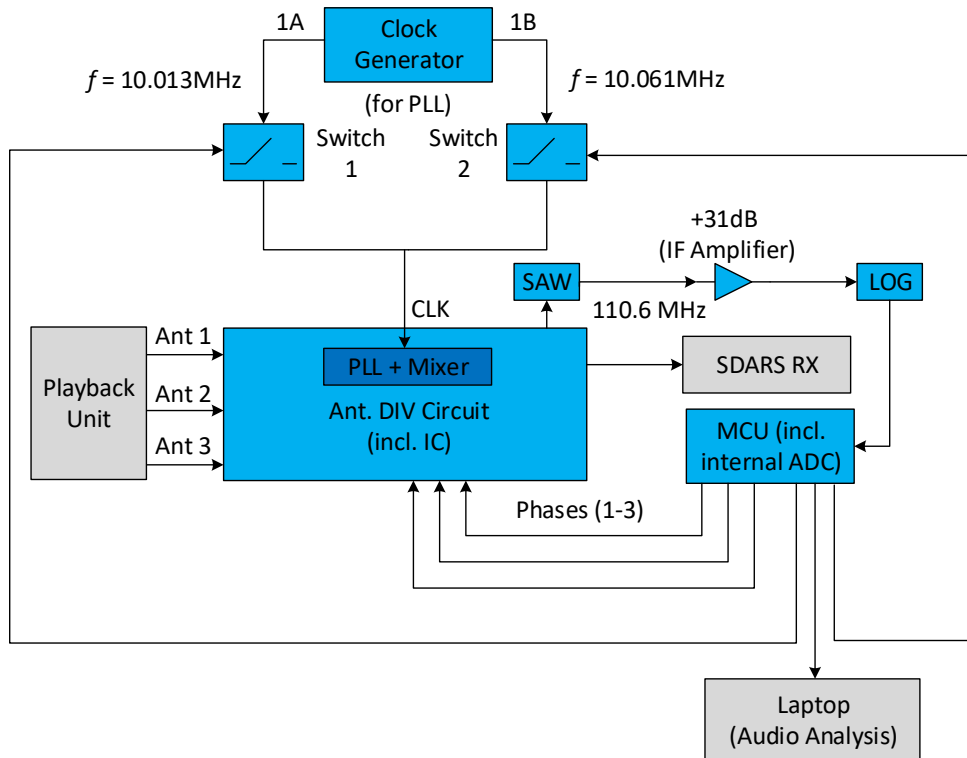


Figure 6.47: Block diagram of the laboratory setup for the 3 antenna algorithm

Signals from three reference patch antennas mounted on three dislocated positions on the fender of the car were played back from the signal playback unit and fed into the three inputs of the antenna diversity system with integrated circuit. A commercial SiriusXM SDARS receiver was utilized in addition to a laptop in order to perform the audio analysis of the investigated scenario. Fig. 6.48 depicts the used system scenario in the laboratory including all needed devices and components to conduct the verification and validity of the presented three antenna algorithm measurements.

The results of the measurement campaign are summarized in Table 6.15. The three antenna algorithm contributes to a significant improvement in the audio availability.

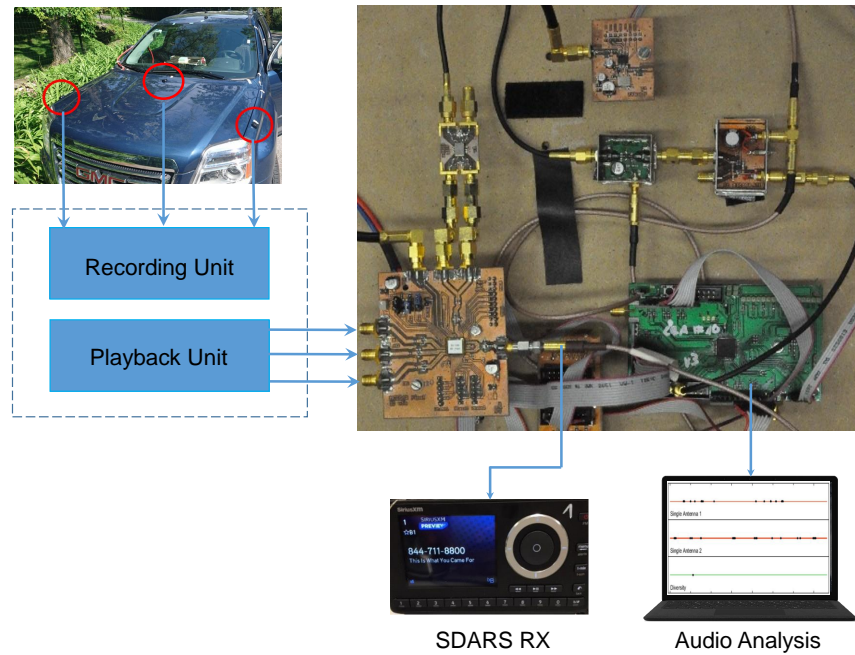


Figure 6.48: The laboratory system setup for the 3 antenna algorithm measurements

The three single patch antennas have an audio mute duration of 11.71s, 14.03s and 12.85s respectively which leads to an average audio mute duration of 12.87s for an overall test duration of 380s. By applying the three antenna algorithm the mute duration dropped to 0.1s only.

In other words, the signal availability increased from 96.61% to 99.99% which is basically a flawless audio reception underneath dense foliage. The diversity efficiency with respect to the average of the single antennas is 2.43.

It is worth mentioning, that the presented results are considered preliminary for initial investigations. The three-antenna algorithm is being further optimized.

Table 6.15: Diversity with 3 reference patch antennas on the hood of the car.

	Audio Mutes [s]	Duration [s]	Avail. [%]	DIV Efficiency
Ant. 1	11.71	380	96.92	–
Ant. 2	14.03	380	96.31	–
Ant. 3	12.85	380	96.62	–
Aver. (1,2,3)	12.87	380	96.61	1
Diversity	0.1	380	99.99	2.43

7 Conclusions

Multipath propagation in fast fading scenarios impose many challenges to guarantee full SDARS signal coverage. In this dissertation, the SDARS system behaviour and performance with antenna diversity in fast fading scenarios underneath dense foliage is investigated with emphasis placed on the steering algorithm of the antenna diversity system.

A channel model to investigate the wave propagation in a land mobile satellite channel along roadside trees has been presented and tested. The RCS of a leaf with all its orientations relative to the incident LHCP plane wave indicates a nearly unique pattern enabling simplified scattering models for the leaves. The results of a simulated virtual test drive using the introduced channel model are presented and compared to measured SDARS signals from real fading scenarios. For this purpose, measurements of recorded test drive signals are post-processed and further evaluated in the laboratory. A very good matching between the simulated and measured histograms of the received signal amplitudes is noticed, showing deviations of only around 0.01 in the probability density.

Moreover, an analysis of noise influence on the diversity performance for SDARS systems at 2.33 GHz and a method for correction of this influence in a diversity algorithm were investigated. Thereby the diversity performance can be improved by one order of magnitude at low SNR conditions without the necessity for additional hardware or even with reduced hardware complexity compared to an uncorrected system. Real scenario test drives underneath dense foliage have been conducted with standard patch antennas mounted on both front fenders of a test vehicle as well as with a micro-diversity antenna set mounted only on one mounting position on the fender. A statistical analysis shows severe multipath fading in the test track underneath dense foliage for single antenna signals and significant improvements by the antenna diversity system. All transmitted satellite signals have been evaluated in audio availability measurements by using standard single-input off-the-shelf SDARS receivers. In cases of low SNR the diversity system without noise correction reduces audio mutes by a factor of 3.5 to 7 depending on the utilized antennas. The noise correction method contributes to a reduction by a factor of approximately 16 to 40 compared to the average of the single antennas. Using antenna diversity this way, even for a critical unconventional mounting position of the antennas, results are equal to those of standard antennas on the ideal position on a car's roof top.

Furthermore, a multi-channel scan-phase algorithm for vehicular antenna diversity of SiriusXM satellite reception was presented. The algorithm is designed for different systems for the SiriusXM low-band as well as for the high-band. The algorithm supports the frequency bands of different satellites by taking into consideration their signal-to-noise ratio. For the SDARS reception optimization of frequency bands of the same satellite, but of different ensembles, the optimization is based on choosing the phase combination leading to the minimum estimated average bit error probability over both ensembles. For the case of the SiriusXM low-band, the interleaver-delay is additionally taken into consideration in the calculations. To be able to utilize simple micro-controllers, efforts were made to make the algorithm perform its calculations in a fast way. For accelerating the calculation speed of the algorithm various investigations were conducted. The acceleration measures include the utilization of pre-calculated look-up tables for algorithm variables and functions instead of performing the time consuming calculations by means of the resources of the micro-controller unit. Moreover, bit-shifting is deployed instead of directly performing the multiplication and division operations in the algorithm for numbers which are a multiple of two. Furthermore, the triggering of the algorithm calculations (including the bit error rates) during the frequency change (frequency parallelization) is applied. Instead of waiting till the local oscillator is set and then performing further calculations, making use of simultaneous operations is considered more time efficient, and it is advantageous to simultaneously perform the frequency change in parallel. Additionally, the algorithm activity is reduced to just when it is necessary. This is accomplished by introducing shorter test intervals with a duration of $100\mu\text{s}$ (including frequency change) whenever the current signal level is above the threshold. A further acceleration measure was the reduction of phase combinations. Only three phases (0° , $+45^\circ$ and -45°) instead of all eight are taken into consideration. Applying all mentioned acceleration measures contributes to a significant reduction of the diversity period duration by a factor of two. For the high-band case, the period duration decreases from $755\mu\text{s}$, where all eight phase are considered, to $366\mu\text{s}$ where only the three mentioned phases are taken into account. The new multi-channel algorithm is verified and validated by using antenna signals of a real scenario test drive which are recorded underneath dense foliage. Even in the case of a two-antenna micro-diversity antenna set mounted on one unconventional spot (front fender of a test vehicle), the algorithm leads to significant improvements in terms of reducing the duration of audio mutes in comparison to the single antennas mounted on the same position. Even in the worst case scenario of reception via satellite 1, where the SiriusXM frequency bands 1A and 1B with a distance of 10 MHz have only weak correlation with each other in their fading behaviour, the audio mute duration is reduced to approximately 1/7 in comparison to the single antenna. Applying the multi-channel algorithm on the SiriusXM low-band also showed improvements in audio quality even though not all acceleration methods were taken into account. Additionally, a three-antenna algorithm has been investigated.

The algorithms of investigation were tested in combination with different versions of SDARS diversity circuits which were designed and implemented at the Institute of High Frequency Technology of the University of Bundeswehr Munich. One important part was the testing and measuring of a new diversity IC within this work. The circuit consists of a single integrated RF combining, selection and frequency down conversion circuit in combination with few external components for level detection at lower frequencies. Based on the obtained level information a small micro-controller unit optimizes the settings of switches and phase shifters for the best RF output signal quality. Like for a conventional reception system the improved RF output signal is fed to any standard single antenna receiver by utilizing only one single RF cable. Diversity circuit measurements show the achievement of the desired phase accuracy of $< 10^\circ$, high de-coupling of the RF antenna paths and sufficient gain for the radio requirements. The new integrated diversity circuit is applied with different antenna diversity sets mounted on various positions on a test vehicle. In a fading scenario underneath dense foliage and in connection with a conventional SDARS receiver, antenna diversity yields a significant reduction of the overall mute duration compared to the average results with a single antenna.

Overall, the SDARS antenna diversity system has proven a significant performance improvement in terms of the signal reception quality in comparison to single antennas in areas characterized by a Rayleigh fast fading behaviour. The lean implemented multi-channel steering algorithm has reduced the audio mutes duration to approximately 1/7 in comparison to the single antenna in the worst-case scenario. SDARS diversity plays a big role in extending the application horizons of SDARS systems. The flexibility of SDARS systems due to antenna diversity can be further enhanced by making use of the following aspects and benefits:

- the use of new mounting positions (in vehicles) which are considered critical for single SDARS antennas
- the deployment of cost efficient as well as compact antenna diversity circuits by car manufacturers
- the guarantee of a larger link margin for SDARS reception which permits providing new regions in the northern USA with SDARS signals
- the use of the gain in the SNR via diversity in order to expand the coverage area and to offer further content for the SiriusXM subscribers by the service provider

Appendix

A Q-Function Table

x	$Q(x)$	x	$Q(x)$	x	$Q(x)$	x	$Q(x)$
0.00	0.5	2.30	0.010724	4.55	2.6823×10^{-6}	6.80	5.231×10^{-12}
0.05	0.48006	2.35	0.0093867	4.60	2.1125×10^{-6}	6.85	3.6925×10^{-12}
0.10	0.46017	2.40	0.0081975	4.65	1.6597×10^{-6}	6.90	2.6001×10^{-12}
0.15	0.44038	2.45	0.0071428	4.70	1.3008×10^{-6}	6.95	1.8264×10^{-12}
0.20	0.42074	2.50	0.0062097	4.75	1.0171×10^{-6}	7.00	1.2798×10^{-12}
0.25	0.40129	2.55	0.0053861	4.80	7.9333×10^{-7}	7.05	8.9459×10^{-13}
0.30	0.38209	2.60	0.0046612	4.85	6.1731×10^{-7}	7.10	6.2378×10^{-13}
0.35	0.36317	2.65	0.0040246	4.90	4.7918×10^{-7}	7.15	4.3389×10^{-13}
0.40	0.34458	2.70	0.003467	4.95	3.7107×10^{-7}	7.20	3.0106×10^{-13}
0.45	0.32636	2.75	0.0029798	5.00	2.8665×10^{-7}	7.25	2.0839×10^{-13}
0.50	0.30854	2.80	0.0025551	5.05	2.2091×10^{-7}	7.30	1.4388×10^{-13}
0.55	0.29116	2.85	0.002186	5.10	1.6983×10^{-7}	7.35	9.9103×10^{-14}
0.60	0.27425	2.90	0.0018658	5.15	1.3024×10^{-7}	7.40	6.8092×10^{-14}
0.65	0.25785	2.95	0.0015889	5.20	9.9644×10^{-8}	7.45	4.667×10^{-14}
0.70	0.24196	3.00	0.0013499	5.25	7.605×10^{-8}	7.50	3.1909×10^{-14}
0.75	0.22663	3.05	0.0011442	5.30	5.7901×10^{-8}	7.55	2.1763×10^{-14}
0.80	0.21186	3.10	0.0009676	5.35	4.3977×10^{-8}	7.60	1.4807×10^{-14}
0.85	0.19766	3.15	0.00081635	5.40	3.332×10^{-8}	7.65	1.0049×10^{-14}
0.90	0.18406	3.20	0.00068714	5.45	2.5185×10^{-8}	7.70	6.8033×10^{-15}
0.95	0.17106	3.25	0.00057703	5.50	1.899×10^{-8}	7.75	4.5946×10^{-15}
1.00	0.15866	3.30	0.00048342	5.55	1.4283×10^{-8}	7.80	3.0954×10^{-15}
1.05	0.14686	3.35	0.00040406	5.60	1.0718×10^{-8}	7.85	2.0802×10^{-15}
1.10	0.13567	3.40	0.00033693	5.65	8.0224×10^{-9}	7.90	1.3945×10^{-15}
1.15	0.12507	3.45	0.00028029	5.70	5.9904×10^{-9}	7.95	9.3256×10^{-16}
1.20	0.11507	3.50	0.00023263	5.75	4.4622×10^{-9}	8.00	6.221×10^{-16}
1.25	0.10565	3.55	0.00019262	5.80	3.3157×10^{-9}	8.05	4.1397×10^{-16}
1.30	0.0968	3.60	0.00015911	5.85	2.4579×10^{-9}	8.10	2.748×10^{-16}
1.35	0.088508	3.65	0.00013112	5.90	1.8175×10^{-9}	8.15	1.8196×10^{-16}
1.40	0.080757	3.70	0.0001078	5.95	1.3407×10^{-9}	8.20	1.2019×10^{-16}
1.45	0.073529	3.75	8.8417×10^{-5}	6.00	9.8659×10^{-10}	8.25	7.9197×10^{-17}
1.50	0.066807	3.80	7.2348×10^{-5}	6.05	7.2423×10^{-10}	8.30	5.2056×10^{-17}
1.55	0.060571	3.85	5.9059×10^{-5}	6.10	5.3034×10^{-10}	8.35	3.4131×10^{-17}
1.60	0.054799	3.90	4.8096×10^{-5}	6.15	3.8741×10^{-10}	8.40	2.2324×10^{-17}
1.65	0.049471	3.95	3.9076×10^{-5}	6.20	2.8232×10^{-10}	8.45	1.4565×10^{-17}
1.70	0.044565	4.00	3.1671×10^{-5}	6.25	2.0523×10^{-10}	8.50	9.4795×10^{-18}
1.75	0.040059	4.05	2.5609×10^{-5}	6.30	1.4882×10^{-10}	8.55	6.1544×10^{-18}
1.80	0.03593	4.10	2.0658×10^{-5}	6.35	1.0766×10^{-10}	8.60	3.9858×10^{-18}
1.85	0.032157	4.15	1.6624×10^{-5}	6.40	7.7688×10^{-11}	8.65	2.575×10^{-18}
1.90	0.028717	4.20	1.3346×10^{-5}	6.45	5.5925×10^{-11}	8.70	1.6594×10^{-18}
1.95	0.025588	4.25	1.0689×10^{-5}	6.50	4.016×10^{-11}	8.75	1.0668×10^{-18}
2.00	0.02275	4.30	8.5399×10^{-6}	6.55	2.8769×10^{-11}	8.80	6.8408×10^{-19}
2.05	0.020182	4.35	6.8069×10^{-6}	6.60	2.0558×10^{-11}	8.85	4.376×10^{-19}
2.10	0.017864	4.40	5.4125×10^{-6}	6.65	1.4655×10^{-11}	8.90	2.7923×10^{-19}
2.15	0.015778	4.45	4.2935×10^{-6}	6.70	1.0421×10^{-11}	8.95	1.7774×10^{-19}
2.20	0.013903	4.50	3.3977×10^{-6}	6.75	7.3923×10^{-12}	9.00	1.1286×10^{-19}
2.25	0.012224						

Figure A.1: Values of $Q(x)$ for $0 \leq x \leq 9$

B Q-Function Plot

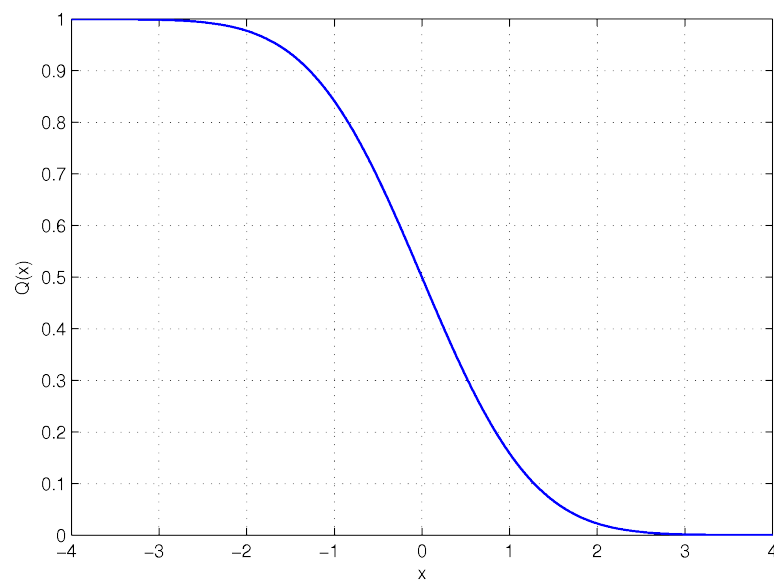


Figure B.1: Plot of $Q(x)$

Bibliography

- [1] D. E. Barié, S. Senega, L. Reiter, and S. Lindenmeier, "Concept Studies of Scanning and Combined Scan/Phase Antenna Diversity Systems for SDARS," *Frequenz*, vol. 62, no. 9-10, pp. 257–261, 2008.
- [2] S. Lindenmeier, D. E. Barié, L. Reiter, J. Hopf, and S. Senega, "Novel combined scan-phase antenna diversity system for SDARS," in *Antennas and Propagation Society International 2008*, pp. 1–4, AP-S, 2008.
- [3] S. Senega and S. Lindenmeier, "Antenna module with integrated scan-phase antenna diversity system for SDARS," in *Antennas and Propagation (EUCAP), 2012 6th European Conference on*, pp. 2807–2810, 2012.
- [4] S. Senega and S. M. Lindenmeier, "A Fast Switching Antenna Diversity System for Improved Mobile Reception of Digital Radio Signals of a Geostationary Satellite," in *Antennas and Propagation (EUCAP), Proceedings of the 5th European Conference on*, pp. 262–264, 2011.
- [5] S. Senega, D. Mueller, D. E. Barié, L. Reiter, J. Hopf, and S. Lindenmeier, "Investigation on the combination of a scan/phase antenna diversity system with a novel diversity antenna set," in *Antennas and Propagation Society International Symposium, 2009 (APSURSI)*, pp. 1–4, 2009.
- [6] H. H. Meinke and F. W. Gundlach, *Taschenbuch der Hochfrequenztechnik*. Berlin: Springer, 5 ed., 1992.
- [7] R. D. Briskman and R. J. Prevaux, "S-DARS broadcast from inclined, elliptical orbits," *Acta Astronautica*, vol. 54, no. 7, pp. 503–518, 2004.
- [8] S. J. Patsiokas, "XM Satellite Radio Technology Fundamentals," *SAE 2001 World Congress, Detroit, USA*, 2001.
- [9] S. DiPierro, R. Akturan, and R. Michalski, "Sirius XM Satellite Radio system overview and services," in *Advanced satellite multimedia systems conference (asma) and the 11th signal processing for space communications workshop (spsc), 2010 5th*, pp. 506–511, 2010.
- [10] C. Scarpa and E. Schell, "Method and Apparatus to jointly synchronize a legacy SDARS signal with overlay modulation," 2009. Patent US 20090168809.

Bibliography

- [11] G. A. Walker, E. A. DiBiaso, and Hiatt Jr., Michael L., "Method to minimize compatibility error in hierarchical modulation using variable phase," 2006. Patent US 2006027614 A1.
- [12] J. Smallcomb and P. Marko, "Method and system for hierarchical modulation and demodulation for digital radio," Patent US 20060239365. 2006.
- [13] G. C. Clark and J. B. Cain, *Error Correction Coding for Digital Communications*. New York: Plenum Press, 2 ed., 1982.
- [14] S. K. Koul and B. Bhat, *Semiconductor and Delay Line Phase Shifters*, vol. 2 of *Microwave and Millimeter Wave Phase Shifters*. Artech House, 1 ed., 1991.
- [15] J. Hagenauer and E. Lutz, "Forward Error Correction Coding for Fading Compensation in Mobile Satellite Channels," *Selected Areas in Communications, IEEE Journal on*, vol. 5, no. 2, pp. 215–225, 1987.
- [16] J. G. Proakis, *Digital Communications*. McGraw-Hill, 4 ed., 2001.
- [17] G. E. Corazza, "Digital satellite communications," 2007.
- [18] D. G. Brennan, "Linear Diversity Combining Techniques," *Proceedings of the IRE*, vol. 47, no. 6, pp. 1075–1102, 1959.
- [19] H. K. Lindenmeier, "Multi antenna scanning," *Potentials, IEEE*, vol. 11, no. 1, pp. 36–39, 1992.
- [20] T. S. Rappaport, *Wireless Communications: Principles and Practice*, ch. 6, pp. 325–330. Dorling Kindersley, 2009.
- [21] D. E. Barié, L. Reiter, and S. Lindenmeier, "Fast Switched Diversity for optimization of S-band SDARS reception," in *Wireless Technology Conference (EuWIT), 2010 European*, pp. 45–48, 2010.
- [22] S. M. Lindenmeier, L. M. Reiter, D. E. Barié, and J. F. Hopf, "Antenna diversity for improving the ber in mobile digital radio reception especially in areas with dense foliage," in *2007 2nd International ITG Conference on Antennas*, pp. 45–48, March 2007.
- [23] H. Bochmann and N. Eilers, "Empfaenger fuer Radiowellen mit mehreren Antennen," 1989. Patent 0 319 782 B1.
- [24] K. Wiedemann, "UKW-Autoradio mit Diversitykombinator," 1992. Patent 0 504 737 B1.
- [25] R. Shatara, *Combined Switched And Phase Aligned Multi-Antenna Diversity System for Signal-Error-Reduction in Mobile Receiving Systems*. Dissertation, Institut fuer Hoch und Hoechstfrequenztechnik, Universitaet der Bundeswehr Muenchen, 2005.

-
- [26] J. D. Parsons, M. Henze, P. A. Ratliff, and M. J. Withers, "Diversity Techniques for Mobile Radio Reception," *Radio and Electronic Engineer*, vol. 45, no. 7, pp. 357–367, 1975.
- [27] V. Rabinovich, N. Alexandrov, and B. Alkhateeb, *Automotive Antenna Design and Applications*, ch. 7.9, pp. 189–191. CRC Press, 2010.
- [28] D. Barié, S. Senega, L. Reiter, and S. Lindenmeier, "Concept studies of scanning and combined scan/phase antenna diversity systems for sdars," in *German Microwave Conference*, pp. 1–3, March 2008.
- [29] S. Senega, D. J. Mueller, L. M. Reiter, and S. M. Lindenmeier, "A Fast-Switching Diversity- and Beam-Forming-Circuit for S-Band Satellite Reception in Fading Scenarios," in *European Microwave Conference (EuMC)*, pp. 648–651, 2010.
- [30] A. Nassar, S. Senega, and S. Lindenmeier, "A time domain model for multipath wave propagation of satellite radio reception underneath dense foliage," in *2016 10th European Conference on Antennas and Propagation (EuCAP)*, pp. 1–4, April 2016.
- [31] Y. L. C. de Jong and M. H. A. J. Herben, "A tree-scattering model for improved propagation prediction in urban microcells," *IEEE Transactions on Vehicular Technology*, vol. 53, pp. 503–513, March 2004.
- [32] R. D. Briskman and J. V. Foust, "A new higher performance NGO satellite for direct audio/video broadcast," *Acta Astronautica*, pp. 914–921, 2010.
- [33] P. Crawford and R. Briskman, "Sirius Highly Inclined Orbit and Geostationary Earth Orbit Equivalent Isotropically Radiated Power," *Data supplied from SiriusXM for the dissertation of Dr.-Ing. Johannes Kammerer*, 2013.
- [34] S. Senega, L. Reiter, and S. Lindenmeier, "Dual-band scan-phase diversity system for american and european sdars," in *2013 IEEE Antennas and Propagation Society International Symposium (APSURSI)*, pp. 1272–1273, July 2013.
- [35] D. J. Mueller, *Kompakte Diversity-Antennen fuer den mobilen Empfang von Satellitensignalen*. PhD thesis, Universitaet der Bundeswehr Muenchen, Fakultae fuer Elektrotechnik und Informationstechnik, 2010.
- [36] H. H. Meinke and F. W. Gundlach, "H 2.1 Freiraumausbreitung: Taschenbuch der Hochfrequenztechnik," in *Springer*, p. H 4, 1992.
- [37] D. J. Müller, L. M. Reiter, D. E. Barié, and S. M. Lindenmeier, "Measurement and analysis of satellite digital audio signals in rayleigh fading scenarios," in *2008 IEEE Antennas and Propagation Society International Symposium*, pp. 1–4, July 2008.

Bibliography

- [38] S. Senega, D. J. Mueller, L. M. Reiter, and S. M. Lindenmeier, "Scan-Phase Antenna Diversity System for Improvements in SDARS Audio Availability at very low Signal-to-Noise Ratios," in *Antennas and Propagation Society International Symposium, 2010 (APSURSI)*, pp. 1–4, 2010.
- [39] C. D. Motchenbacher and J. A. Connelly, *Low-Noise Electronic System Design*, p. 422. New York: John Wiley, 1993.
- [40] H. Nyquist, "Thermal agitation of electric charge in conductors," in *Phys. Rev.* 32, pp. 110–113, 1928.
- [41] G. Vasilescu, *Electronic Noise and Interfering Signals*, p. 520. Germany: Springer Verlag, 2005.
- [42] W. Schottky, "Ueber spontane stromschwankungen in verschiedenen elektrizitaetsleitern," in *Annalen der Physik Band 362* *Annalen der Physik. Band 362*, pp. 541–567, 1918.
- [43] H. T. Friis, "Noise figures of radio receivers," *Proceedings of the IRE*, vol. 32, no. 7, pp. 419–422, 1944.
- [44] D. Pozar, *Microwave Engineering*. Wiley, 4 ed., 2011.
- [45] W. W. Mumford and E. H. Scheibe, *Noise Performance Factors in Communication Systems*, p. 89. Dedham: Horizon House - Microwave, 1968.
- [46] C. D. Motchenbacher and F. C. Fitchen, *Low-Noise Electronic Design*, p. 358. New York: John Wiley, 1973.
- [47] International Telecommunication Union - Radio Sector, *Recommendation ITU-R P.372: Radio Noise*.
- [48] U. Rohde and T. Bucher, *Communications Receivers*, p. 608. New York: McGraw-Hill, 1988.
- [49] H. Lindenmeier and J. Hopf, *Kurzwellenantennen*, p. 232. Heidelberg: Huethig Buch Verlag, 1992.
- [50] J. Kammerer, *Kompakte Ringantennen fuer satellitengestuetzte und terrestrische Uebertragungsdienste im Fahrzeug*. PhD thesis, Universitaet der Bundeswehr Muenchen, Fakultae fuer Elektrotechnik und Informationstechnik, Neubiberg, 2014.
- [51] I. Goncharova, *Compact Microwave Antennas and Antenna Combinations for Terrestrial and Satellite Services on Vehicles*. PhD thesis, Universitaet der Bundeswehr Muenchen, Fakultae fuer Elektrotechnik und Informationstechnik, Neubiberg, 2018.

-
- [52] J. Kammerer and S. Lindenmeier, "A new compact antenna combination with high efficiency for reception of SDARS- and GPS signals," in *Antennas and Propagation Society International Symposium, 2012 (APSURSI)*, pp. 1–2, 2012.
- [53] J. Kammerer and S. Lindenmeier, "Invisible antenna combination embedded in the roof of a car with high efficiency for reception of SDARS - and GPS - signals," in *Antennas and Propagation Society International Symposium, 2013 (APSURSI)*, pp. 2075–2076, 2013.
- [54] J. Kammerer and S. Lindenmeier, "Invisible Antenna Embedded in the Roof of a Car with High Efficiency for Reception of Satellite Digital Audio Radio Services (SDARS)," in *Antennas and Propagation (EUCAP), 2013 7th European Conference on*, pp. 1609–1611, 2013.
- [55] Jakes, Jr., William C., ed., *Microwave Mobile Communications*, ch. 5.1, pp. 310–313. John Wiley & Sons, 1 ed., 1974.
- [56] Lee, William C. Y, *Mobile communications engineering: Theory and applications*, ch. 10, pp. 347–380. New York: McGraw-Hill, 2nd ed. ed., 1998.
- [57] P. Mattheijssen, M. H. A. J. Herben, G. Dolmans, and L. Leyten, "Antenna-pattern diversity versus space diversity for use at handhelds," *IEEE Transactions on Vehicular Technology*, vol. 53, pp. 1035–1042, July 2004.
- [58] S. Lindenmeier, L. Reiter, J. Kammerer, and S. Senega, "Antenna technology for mobile satellite radio reception," in *Antenna Technology (iWAT), 2013 International Workshop on*, pp. 163–166, 2013.
- [59] S. Senega, D. E. Barié, D. Mueller, L. Reiter, and S. Lindenmeier, "Investigation on Improvements in SDARS Reception Quality with a Scan/Phase Antenna Diversity System," in *2009 German Microwave Conference*, IEEE, 2009.
- [60] S. Senega, A. Nassar, and S. Lindenmeier, "Compact scan-phase antenna diversity system for high driving speeds," in *European Microwave Conference (EuMC)*, pp. 1459–1462, 2015.
- [61] S. Senega and S. Lindenmeier, "Antenna Module with Integrated Scan-Phase Antenna Diversity System for SDARS," in *Antennas and Propagation (EUCAP), 2012 6th European Conference on*, pp. 2807–2810, 2012.
- [62] S. Senega, J. Kammerer, and S. Lindenmeier, "Scan-Phase Antenna Diversity for Digital Satellite Radio (SDARS) in a Single Automotive Side Mirror," in *2014 8th European Conference on Antennas and Propagation (EuCAP)*, pp. 3255–3259, 2014.
- [63] M. Eberhardt, *Ein neues Pegelmesskonzept fuer Satellitenradiosignale durch digitale Signalverarbeitung*. Master thesis, Universitaet der Bundeswehr Muenchen, 2011.

Bibliography

- [64] S. Lindenmeier, "Algorithmus zur bestimmung der besten schaltstellung fuer mehrere kanaele fuer sdars-diversity," *Internal Report*, 2017.
- [65] S. Senega, A. Nassar, and S. Lindenmeier, "Automotive antenna diversity system for satellite radio with high phase accuracy in low snr-scenarios," in *2017 47th European Microwave Conference (EuMC)*, pp. 46–49, Oct 2017.
- [66] S. Senega, A. Nassar, and S. Lindenmeier, "Automotive antenna diversity system for satellite radio with high phase accuracy in low snr-scenarios," in *International Journal of Microwave and Wireless Technologies*, vol. 10, pp. 578–586, Cambridge University Press, 2018.
- [67] D. J. Mueller, L. M. Reiter, J. F. Hopf, D. E. Barié, and S. M. Lindenmeier, "A Measurement System for Investigation and Evaluation of Diversity Antenna Combinations in Microwave Fading Scenarios," in *German Microwave Conference (GeMiC)*, 2008.
- [68] P. Loos, *Schaltlogik zur Verbesserung der Empfangsqualitaet von Satellitenradiosignalen*. PhD thesis, Universitaet der Bundeswehr Muenchen, 2010.
- [69] National Instruments, *Specifications: PXIe-5644 Reconfigurable 6 GHz Vector Signal Transceiver*, June 2017.
- [70] A. Bekaryan, H. J. Song, H. P. Hsu, and R. W. Wiese, "Parametric study of roof geometry and roof rack crossbar effects on the performance of multi-band vehicle antennas," in *IEEE 70th Vehicular Technology Conference*, Sept. 2009.
- [71] H. Lindenmeier, L. Reiter, J. Hopf, J. Brose, and R. Kronberger, *Elektronik im Kraftfahrzeug*. VDI Berichte, Nr. 1547, 2000.
- [72] S. M. Lindenmeier, L. M. Reiter, D. E. Barié, and J. F. Hopf, "Antenna Diversity for Improving the BER in Mobile Digital Radio Reception Especially in Areas with Dense Foliage," in *International ITG Conference on Antennas (INICA)*, pp. 45–48, 2007.
- [73] S. Senega, J. Roeber, A. Nassar, R. Weigel, C. Heuer, and S. Lindenmeier, "Characterization of a new integrated scan-phase antenna diversity circuit for automotive satellite radio reception," in *2016 46th European Microwave Conference (EuMC)*, pp. 1299–1302, Oct 2016.
- [74] A. Nassar, S. Senega, and S. Lindenmeier, "A multi-channel algorithm for antenna diversity of siriusxm high band satellite reception in vehicles," in *2018 48th European Microwave Conference (EuMC)*, pp. 312–315, 2018.
- [75] L. Impolito, *Satellite Communications Systems Engineering: Atmospheric Effects, Satellite Link Design and System Performance*, pp. 364–366. Wiley, 2008.

- [76] Atmel, "AVR XMEGA A1 Device Data Sheet," 2014.
- [77] Atmel, "Atmel SAM D21 Data Sheet," 2014.
- [78] S. Ruttor, *Implementierung eines Diversityalgorithmus auf einem ARM Mikrocontroller*. Bachelorarbeit, Universitaet der Bundeswehr Muenchen, Fakultae fuer Elektrotechnik und Informationstechnik, 2014.
- [79] T. Utesch, *Entwurf eines Lokaloszillators fuer schnelle Frequenzwechsel bei SDARS-Diversity*. Bachelorarbeit, Universitaet der Bundeswehr Muenchen, Fakultae fuer Elektrotechnik und Informationstechnik, 2014.
- [80] Linear Technology Corp., "LTC6946 Local Oscillator Data Sheet," 2014.
- [81] S. Senega, J. Roeber, A. Nassar, R. Weigel, C. Heuer, and S. Lindenmeier, "New compact antenna diversity with a fully integrated microwave circuit for automotive satellite radio reception," in *2018 48th European Microwave Conference (EuMC)*, pp. 1337–1340, 2018.
- [82] N. Geng and W. Wiesbeck, *Planungsmethoden fuer die Mobilkommunikation*. Springer Verlag, 1998.
- [83] Analog Devices, "AD9200 10-Bit, 20 MSPS, 80 mW, CMOS A/D Converter," 1999.
- [84] Mini Circuits, "ERA-5XSM+ Data Sheet."
- [85] Linear Technology Corp., "LTC5542 Mixer Data Sheet," 2010.
- [86] MuRata, "SF1056B Data Sheet," 2014.
- [87] Analog Devices, "AD8310 Data Sheet," 2010.

